Development of 3D printable SHCC for structural purposes

An experimental study on material design and material-system interactions

van Overmeir, A.L.

DOI
10.4233/uuid:627132e1-3c94-4f7a-b4b8-4c377c7cef0d

Publication date
2024

Document Version
Final published version

Citation (APA)
van Overmeir, A. L. (2024). *Development of 3D printable SHCC for structural purposes: An experimental study on material design and material-system interactions* . [Dissertation (TU Delft), Delft University of Technology]. https://doi.org/10.4233/uuid:627132e1-3c94-4f7a-b4b8-4c377c7cef0d

Important note
To cite this publication, please use the final published version (if applicable).
Please check the document version above.

DEVELOPMENT OF 3D PRINTABLE SHCC FOR STRUCTURAL PURPOSES

AN EXPERIMENTAL STUDY ON
MATERIAL DESIGN AND MATERIAL-SYSTEM INTERACTIONS

DEVELOPMENT OF 3D PRINTABLE SHCC FOR STRUCTURAL PURPOSES

AN EXPERIMENTAL STUDY ON
MATERIAL DESIGN AND MATERIAL-SYSTEM INTERACTIONS

Proefschrift

ter verkrijging van de graad van doctor
aan de Technische Universiteit Delft,
op gezag van de Rector Magnificus prof. dr. ir. T.H.J.J. van der Hagen,
voorzitter van het College voor Promoties,
in het openbaar te verdedigen op
10 december 2024 om 15:00 uur

door

Anne Linde VAN OVERMEIR

Master of Science, Architecture
Faculty of Architecture & the Built Environment

Master of Engineering, Structural eng.
Faculty of Civil Engineering & Geosciences

Technische Universiteit Delft, Delft, Nederland

geboren te Huizen, Nederland.

Dit proefschrift is goedgekeurd door de

promotor: prof. dr. ir. E.Schlangen
promotor: dr. B. Šavija
extern adviseur: dr. ir. F.P. Bos

Samenstelling promotiecommissie:

Rector Magnificus,	voorzitter
Prof. dr. ir. E. Schlangen,	Technische Universiteit Delft
Dr. B. Šavija,	Technische Universiteit Delft
Dr. ir. F.P. Bos,	Technische Universiteit München, Duitsland
Onafhankelijke leden:	
Prof. dr. ir. Gideon van Zijl	Stellenbosch Universiteit
Prof. dr. ir. Max Hendriks	Technische Universiteit Delft
Dr. ir. Jolien Van Der Putten	Witteveen+Bos
Dr. Vera Popovich	Technische Universiteit Delft

Keywords: 3DP-SHCC, concrete printing, fibre reinforcement, printability, fresh mechanical properties, particle size distribution,
Printed by: Ipskamp Printing, the Netherlands
Front & Back: Anne Linde van Overmeir

ISBN 978-94-6366-961-0

An electronic version of this dissertation is available at
http://repository.tudelft.nl/.

"Art is the antidote"

Patrick Brill

CONTENTS

SUMMARY

3D printing of concrete is an automated manufacturing technology being developed for the construction industry. The objective is that the technology can make the construction industry more time-, labour- and material-efficient as well as increase the formability of structural designs. 3D concrete printing has been in development for over a decade and the technology has recently made its introduction into the built world. That being said, there are still several challenges that call for attention before the technology can be widely implemented. One of the most distinct challenges is the reinforcement of the printed element. Concrete is by nature a brittle material, which is strong in compression but relatively weak in tension. Under loads that cause tensile forces, such as bending in beams, plain concrete can easily crack or even break completely. Traditionally, concrete is therefore reinforced with embedded steel reinforcement bars that prevent the concrete from brittle failure. In the application of 3DCP the implementation of steel rebars is not trivial, and thus alternative reinforcement methods are being developed.
Based on the concept of strain hardening cementitious composites (SHCC), one possible solution can be found in the development of 3D printable strain hardening cementitious composites (3DP-SHCC). SHCC is characterised by its ductility and its capacity to show strain hardening behaviour under uniaxial tensile loading. The combination of these two relatively new innovations imposes strict and occasionally contradicting requirements on the fresh and hardened mechanical properties. Where the 3DCP aspect of the material imposes requirements on the fresh mechanical properties, such as pumpability, extrudability and buildability, the strain hardening aspect requires very balanced and fragile criteria on the (micro)mechanical properties in the hardened state.

This PhD project ventures to incorporate SHCC into the 3-dimensional printing technology, with the underlying objective to systematically develop a printable strain - hardening cementitious composite for structural purposes.

- Optimisation of the particle size distribution formed the basis for developing a new 3DP-SHCC material. Grain size distribution analysis based on the "modified Andreasen and Andersen" model were performed on several dry-mix compositions to ensure the buildability and stability of the 3DP-SHCC in its fresh state. After this, four-point bending tests were carried out to verify the ductility in the hardened state. Two dry mixes were selected and further optimised with the addition of a viscosity modifier agent (VMA) and a super plasticiser (SP). Print speed trials and buildability tests were conducted to assess the printability of the final mix designs, followed by experimental testing of both the fresh and cured mechanical properties.
- To enable large-scale structural applications of 3DP-SHCC, various pumping strategies were evaluated, revealing bottlenecks such as the formation of fibre agglom-

erates and blockages. Individual components of the pumping system were tested and adjusted to achieve constant and adequate material flow as well as material stability throughout the printing process.

- The effect of the printing process on hardened mechanical properties underwent evaluation through two experimental studies. Firstly, an examination of the consistency of hardened mechanical properties was conducted across three nominally identical printing sessions. The second study focused on the different phases of one single printing session. It determined the influence of subsequent printing phases (mixing, pumping, extruding, and printing) on the hardened mechanical properties of the printed 3DP-SHCC elements.

- The fresh and hardened mechanical properties of a 3DP-SHCC matrix with various fibre types were evaluated in an experimental study. High variation in workability, ductility and strain hardening capacity was encountered.

- Finally, given the importance of the fresh mechanical properties of 3DP-SHCC, research was conducted on several fresh mechanical tests. The tests were evaluated for their applicability to 3DP-SHCC based on five criteria: Reliability, precision, un-ambiguity, reproducibility and feasibility.

The study successfully developed 3D printable SHCCs that meet the requirements on printability and strain hardening to the achieve ductility and strain hardening capacity of printed elements.

Furthermore, the study helps to understand the interaction between the printing system and the 3DP-SHCC. It highlights the implications the material has on the pumping system and how the printing process influences the hardened mechanical properties. It discusses the key parameters of fibre types and how these influence the fresh and hardened mechanical properties, and last but not least, it gives insight into fresh mechanical testing protocols for the high-yield stress 3DP-SHCCs.

All of these give a solid base for researchers to design fibre-reinforced printable composites, with required printability and strain hardening properties. In particular, it contributes to the design and tailoring strategies for high-performance strain hardening composites.

SAMENVATTING

Het 3D printen van beton is een geautomatiseerde productietechniek die wordt ontwikkeld voor de bouw. Het doel is om de bouwindustrie efficienter te maken wat betreft tijd, arbeid en materiaal, en tegelijkertijd de vormvrijheid van constuctieve ontwerpen te vergroten. Al ruim een decennium is de techniek van 3D beton printen (3DBP) in ontwikkeling en recent heeft het zijn intrede gemaakt in de bebouwde omgeving. Desalniettemin zijn er nog verschillende uitdagingen die aandacht behoeven eer de technologie op grote schaal kan worden geïmplementeerd. Een fundamentele uitdaging betreft het wapenen van geprinte betonelementen. Beton is van nature een bros materiaal, dat sterk is in compressie, maar relatief zwak in trek. Bij belastingen die trekkrachten veroorzaken, zoals buiging in balken, kan ongewapend beton gemakkelijk scheuren of zelfs volledig breken. Traditioneel is beton daarom gewapend met ingestortte stalen wapeningsstaven die voorkomen dat het beton bros breekt. Bij de toepassing van 3DBP is de implementatie van stalen wapeningsstaven niet triviaal en daarom worden alternatieve wapeningsmethoden ontwikkeld.

Gebaseerd op het concept van rekverhardende cementgebonden composieten (SHCC) kan een mogelijke oplossing worden geboden door de ontwikkeling van zelf-gewapend 3D-printbaar beton, ook wel 3D-printbare rekverhardende cementgebonden composieten (3DP-SHCC) genoemd. Deze composieten halen hun wapeningseigenschappen uit microvezels die in het verse beton worden gemengd. SHCC kenmerkt zich door zijn ductiliteit en zijn vermogen om rekverhardend gedrag te vertonen onder uniaxiale trekspanning. De combinatie van deze twee relatief nieuwe innovaties stelt strenge en soms tegenstrijdige eisen aan de mechanische eigenschappen. Om printbaar te zijn moet het materiaal voldoen aan verscheidene verse mechanische eigenschappen, zoals verpompbaarheid, extrudeerbaarheid en bouwbaarheid. Het rekverhardende aspect van het materiaal stelt nauwlettende eisen aan de (micro)mechanische eigenschappen in de uitgeharde toestand.

Dit doctoraatsproject beoogd de technologie van SHCC en 3D beton printen samen te brengen, met als onderliggend doel om op een industriele schaal een 3DP-SHCC te ontwikkelen voor constructieve doeleinden. Om dit na te streven zijn de volgende deelonderzoeken uitgevoerd:

- Optimalisatie van de korrelgrootteverdeling stond aan de basis voor het ontwikkelen van een nieuw 3DP-SHCC materiaal. Korrelgrootteverdelingsanalyses op basis van het "modified Andreasen and Andersen"model zijn uitgevoerd op verscheidene droogmix samenstellingen om de bouwbaarheid, stabiliteit van de 3DP-SHCC te waarborgen. Waarna vierpuntsbuigproeven zijn uitgevoerd voor het verifieren van de ductilitiet in uitgeharde fase. Op basis hiervan zijn twee droogmixen geselecteerd en verder geoptimaliseerd met toevoeging van een viscositeitsmodificerend middel (VMA) en een superplastificeermiddel (SP). Printsnelheidsproeven

en bouwbaarheidstesten werden uitgevoerd om de printbaarheid van de uiteindelijke mengsels te beoordelen, gevolgd door experimentele tests van zowel de verse als uitgeharde mechanische eigenschappen.

- Om grootschalige constructieve toepassingen van 3DP-SHCC mogelijk te maken, werden verschillende pompstrategieën geevalueerd, waarbij knelpunten, zoals de vorming van vezelballen en het ontstaan van verstoppingen, aan het licht kwamen. Individuele onderdelen van het pompsysteem werden getest en aangepast om een constante en toereikende materiaalstroom alsmede materiaalstabiliteit te bereiken gedurende het hele printproces.

- Het effect van het printproces op de uitgeharde mechanische eigenschappen werd geëvalueerd aan de hand van twee studies.In de eerste studie is de consistentie van het materiaal onderzocht dat was vervaardigd in drie aparte maar identieke printsessies. In de tweede studie is specifiek ingezoomd op de verschillende fasen van het printproces. Hierbij is de invloed van de opeenvolgende printfasen (mengen, pompen, extruderen en printen) op de mechanische eigenschappen van de 3DP-SHCC geprinte elementen onderzocht.

- Verschillende vezeltypes zijn geëvalueerd op hun invloed op de verse en uitgeharde mechanische eigenschappen, waarbij grote variatie in verwerkbaarheid, ductiliteit en rekuithardingscapaciteit werd gevonden.

- Tot slot is, gezien het belang van de verse mechanische eigenschappen van 3DP-SHCC, een onderzoek uitgevoerd naar verschillende verse mechanische testen. De testen werden geëvalueerd op hun toepasbaarheid voor 3DP-SHCC gebaseerd op vijf criteria: Betrouwbaarheid, precisie, eenduidigheid, reproduceerbaarheid en haalbaarheid.

Het onderzoek heeft succesvol 3D-printbare SHCCs ontwikkeld die voldoen aan de eisen voor zowel printbaarheid in verse staat als ductiliteit en rekverharding in uitgeharde staat. Bovendien draagt het onderzoek bij aan het begrip van de interactie tussen het printsysteem en de 3DP-SHCC. Het belicht de implicaties dat het materiaal heeft op het pompsysteem alsmede de invloed van het printproces op de uitgeharde mechanische eigenschappen. Het bespreekt het effect van verschillende vezeltypes op zowel de verse als uitgeharde mechanische eigenschappen en tot slot biedt het een overzicht van toepasbare testmethodes voor het vergaren van de verse mechanische eigenschappen van 3DP-SHCC's.

Dit alles legt een stevige basis voor onderzoekers om vezelversterkte printbare composieten te ontwerpen met oog voor de vereiste printbaarheid en ductiele eigenschappen. Het geeft duidelijke ontwerp-, optimalisatie- en evaluatie-strategieën voor hoogwaardige printbare rekverhardende cementgebonden composieten.

PREFACE

Before you lies the PhD thesis *"Development of 3D printable SHCC for structural purposes- An experimental study on material design and material-system interactions"*. The thesis provides a summary of the research conducted on the development of strain-hardening cementitious composites for use in 3D concrete printing. This study brought together everything I pursued during my academic career, combining my background in architecture and my love for concrete (an admiration sparked by the brutalistic architectural style), along with my theoretical knowledge of concrete technology gained during my structural engineering studies. The PhD project aimed to merge these aspects, developing a new material for an innovative technology that could potentially transform the way we construct our built environment. How exciting is that!

This dissertation results from the NWO Open Technology Program project *"High Performance 3D Concrete Printing – Systematic Development of a Printable Strain-Hardening Cementitious Composite for Structural Purposes"*, grant number 17251. The project ran as a collaboration between the Delft and Eindhoven Universities of Technology from 2019 until 2023. The project's main applicant was F.P. Bos, the co-applicants were E. Schlangen, T.A.M. Salet, and A.S.J. Suiker. The research was performed by S. Chaves Figueiredo (post-doc), K. Nefs (PhD candidate), and the author of this dissertation, and supervised by the applicants and B. Savija. Besides the main project funding provided by the Dutch National Science Foundation NWO, the project was financially supported by Witteveen+Bos consulting engineers, Saint Gobain Weber Beamix, and Kuraray. Their support is gratefully acknowledged. The project featured a User Committee, which consisted of representatives from the supporting companies as well as G. van Zijl of the University of Stellenbosch and C. Menna of the University of Naples Federico II. Their input and feedback are highly appreciated.

For more details on the material characterisation from micro to macro scale, including fibre pull-out tests and material application case studies, the complementary doctoral thesis produced during this project, *"Structural Engineering of 3D Printed Strain Hardening Cementitious Composites: From micro-scale analysis to application"* by K. Nefs is highly recommended.

Anne Linde van Overmeir
Wageningen, May 2024

1

INTRODUCTION

1

1.1. RESEARCH BACKGROUND

Three-dimensional concrete printing (3DCP) is one of the most common techniques of the additive manufacturing (AM) for concrete, in which the cementitious material is extruded layer upon layer, by a digitally controlled robot. This innovative construction method provides increased flexibility in architectural design, allowing for structural optimisation that leads to more slender and material-efficient structures, as shown in figure 1.1. Beyond its design advantages the technique potentially has economic benefits as it makes traditional formwork superfluous, which can speed up the production process and reduces formwork costs. However, despite the benefits that this additive manufacturing technique offers, it is not yet widely applied in practice, due to the multiple technical challenges [1–3], one being the mechanical properties of plain concrete, which is brittle by nature and lacks sufficient tensile strength. In traditional concrete this lack of tensile strength is overcome by the implementation of steel reinforcement. This provides the concrete with the required ductile behaviour needed to comply with modern building regulations, as it ensures structural integrity and safety. For 3DCP however, the implementation of steel reinforcement is not evident and researchers are developing alternative methods to reinforce printed concrete elements.

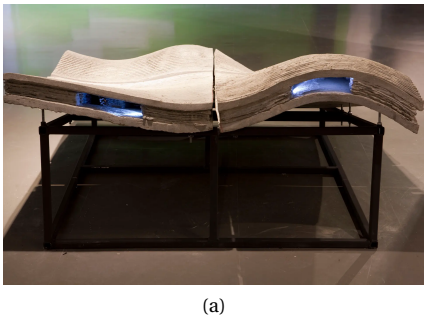

(a)

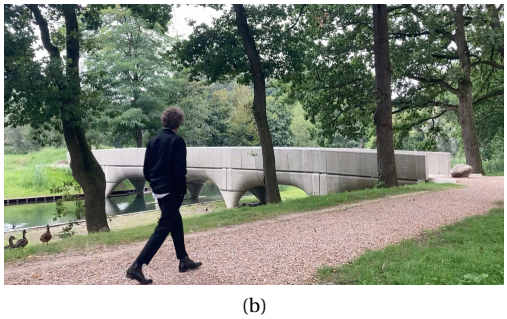

(b)

Figure 1.1: Case studies 3DCP
a) Double curved slab Loughborough University (2012) [4] b) The Bridge Project (2023) [5]

One of the alternative reinforcement methods is the development of strain hardening cementitious composites (SHCC) for 3D printing applications. SHCC, also known under the name ECC (engineered cementitious composite) is a relatively new kind of fibre reinforced material developed in the early ‘90s [6]. The material is characterised by its capacity to show strain hardening behaviour under uniaxial tensile loading and by its ductility under bending, see figure 1.2. These features are made possible by incorporating high-strength fibres into the cement matrix. The fibres are able to dissipate the fracture energy and distribute the cracks that form in the cement matrix as the material is stressed, which helps to prevent brittle failure under tensile loading [7].

3D printable SHCC (3DP-SHCC) as a new material type, combines two relatively new developments: 3D concrete printing and strain hardening cementitious composites. For the material to be successful, the 3DP-SHCC has to comply with many different and sometimes contradicting requirements, on fresh and hardened mechanical proper-

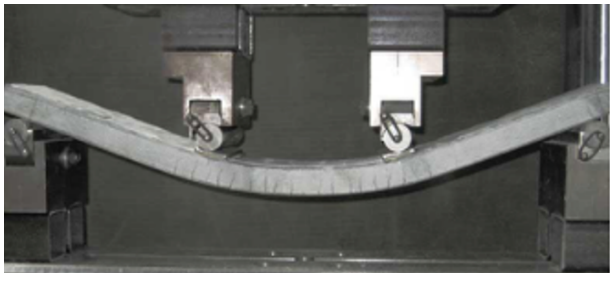

Figure 1.2: Ductile behaviour of SHCC in 4 point bending test [8]

ties, to achieve a well-printed object with strain hardening capacity. The printing system imposes requirements on the fresh and very early-age mechanical properties, while the strain hardening aspect is achieved by satisfying micro mechanical requirements in hardened state.

At the moment of starting the PhD project, a handful of studies had demonstrated the potential 3DP-SHCC [9–12]. The research focused mainly on demonstrating the viability of the new material, using different mixture designs and 3D concrete printing systems. A uniform method for designing, processing, and assessing these materials is still lacking.

1.2. AIM AND OBJECTIVE

The main aim of this PhD work is to systematically develop a strain hardening cementitious composite that is specifically tailored for large-scale 3D printing systems. Additionally, the objective is to provide valuable insights into the challenges associated with the development of 3D-printable strain hardening cementitious composites (3DP-SHCC), enabling future researchers to advance this technology in a targeted and well-informed manner. To achieve this overarching goal, five sub-objectives have been formulated and are outlined below:

- To develop a 3DP-SHCC material that meets the printability requirements in the fresh state and shows strain hardening behaviour in the hardened state.
- To evaluate and adapt the industrial-scale 3D printing system for the manufacturing of printed 3DP-SHCC elements.
- To determine the effect of the printing system on the mechanical properties of the material.
- To assess the usability of different fibre types for SHCC in 3D printing applications.
- To assess the applicability of rheological and fresh material tests for determining the fresh state properties of 3DP-SHCC.

1.3. SCOPE

Combining two exciting innovations to create a brand-new material opens up a world of possibilities. To limit the scope of the project the research presented in this thesis is

tethered by two distinct constraints.

Firstly, the research focuses on the development of a material for full-scale industrial printing systems in which structural elements can be manufactured. It is known from the literature that printing systems may affect mechanical properties [13, 14]. The research conducted in this thesis is limited to industrial-scale printing systems only. Secondly, the research will primarily focus on the tailoring of the material's printability properties in conjunction with large-scale printing systems. The goal of the research is therefore is not solely to improve the mechanical properties such as strain hardening and ductility, but to ensure these properties when printed.

1.4. THESIS OUTLINE

The main content of this thesis is composed of a literature review in chapter 2, which covers three main subjects. Firstly, it describes the knowledge on 3D concrete printing, printing systems and recent projects accomplished in this field. Secondly, it covers the concept behind strain hardening materials, and how they are developed, tested and applied in practice. And last but not least, the final section covers printable SHCCs that have been developed thus far.

In chapter 3 the development of a 3D printable SHCC is presented. The concept of optimised particle packing is proposed as the foundation of the material design. Initial mix designs were evaluated on ductility and the fresh mechanical properties of promising mix designs were tailored using viscosity modifiers agents (VMA) and super-plasticisers (SP) combined with the deployment of RAM extrusion tests. Finally, the mix designs were printed and analysed on their mechanical and material properties.

Chapter 4 reviews several pumping systems and presents a study into the optimisation of a pumping systems for 3D printable SHCC.

After understanding the effect of the printing system on the material, chapter 5 focuses on the tailoring of the 3DP-SHCC mix design for the final printing system. The chapter discusses the effect of four ingredients in the mix design for optimisation of both the fresh and hardened state properties.

With the 3DP-SHCC mix design developed in chapter 5, chapter 6 investigates the influence of the printing system on the mechanical properties of the printed SHCC elements. The chapter consists of two studies, the first being a consistency study, that investigates the variance in mechanical properties of printed SHCC manufactured in three identical but separate printing sessions. The second study investigates the effect of individual printing phases on the hardened state mechanical properties.

Chapter 7 presents a study on different fibre types and their effect on the hardened properties of SHCC.

A wide range of fresh mechanical and rheological tests are reviewed on their applicability for fresh 3DP-SHCC materials in chapter 8. For this study six commonly used fresh mechanical and rheological tests were selected. The rheology theory behind each test will be addressed, followed by an in-depth discussion on the usability of the test based on the acquired experimental data.

Finally, chapter 9 presents a final overview of the study and presents its main conclusions. Additionally, it provides some reflections and recommendations for future work.

Appendix A contains additional experimental research in which the influence of the

3D printing facility on the mechanical properties of hardened SHCC specimens is investigated. This research has been conducted on a material that was developed, separately from this PhD thesis, by Figueiredo et al. [10, 15].

2

LITERATURE REVIEW

This chapter provides a comprehensive review of all the factors integral to designing 3DP-SHCC. The performance of this new material is determined by restrictions that are set by both the material processing of 3DCP and the micro-mechanical concept of SHCC. This literature review is structured into three parts. Part one consists of a concise and evaluative review of 3DCP. It explores the various methodologies employed in 3DCP and elaborates on the primary printing technique. This section is followed by an introduction to the material SHCC providing insights into the micro-mechanical mechanisms that form the foundation of its strain hardening capacity. Finally, the literature review addresses the key material and system design factors that are encountered when combining these two innovations, 3DCP and SHCC.

2.1. INTRODUCTION INTO ADDITIVE MANUFACTURING IN CONSTRUCTION INDUSTRY

The construction industry, a vital global sector, is lagging when it comes to productivity. Where other industries ranging from retail to manufacturing were able to strongly develop their efficiency, the building industry has faced challenges in modernising [16]. One innovation that has been successful in industrial production technology is additive manufacturing, which uses computer-controlled material addition to fabricate objects. The technology enables the creation of lighter, stronger, and more complex-shaped parts and has been successfully integrated into industries such as manufacturing, computer technology, and medicine. Over the last decade, this method has also been introduced in the construction industry under the name: Digital fabrication of concrete.

2.1.1. DIGITAL FABRICATION OF CONCRETE STRUCTURES

Concrete is the most widely used building material globally. The raw materials for concrete (cement, sand and water) are widely available over the world and the material is powerful due to its strength, durability, and versatility in shaping. The development of digital fabrication of concrete has gained interest for several reasons. Firstly, traditional manufacturing methods, whether on- or off-site, involve labour-intensive processes for formwork construction and reinforcement positioning. Secondly, the production of cement is very energy intensive as cement is made by firing raw materials in a kiln to a temperature of 1300-1450 °C. As a consequence, concrete accounts for an estimated 4-8% of the global CO_2 output [17–19].

The development of digital fabrication can potentially offer economic benefits by speeding up production processes and reducing formwork costs. It may also provide environmental advantages through optimised material usage and minimising waste [2]. The development of 3D concrete printing has resulted in a large number of different manufacturing methods, which can be broadly divided into five groups: particle-bed 3D printing, shotcrete 3D printing, smart dynamic casting, formwork printing and 3D concrete printing.

Particle-bed 3D printing, also known as selective binding, refers to a 3D printing process characterised by the controlled introduction of a binding fluid into a particle bed [20]. The printed elements are formed by introducing a flowable binding fluid to a very thin layer of particles, after which a new layer of particles is deposited on top of the previous one and the sequence is repeated. The element is built up layer upon layer. This manufacturing technique allows for the printed element to always be self-supported by the full particle bed during its fabrication and curing. (figures 2.1a and 2.1b)

Shotcrete 3D Printing (SC3DP) is a method that integrates shotcrete technology with the versatility of robotic digital manufacturing [21, 22]. In SC3DP, the material is not extruded in layers as is often seen in 3D printing techniques, but rather the material is sprayed to create a 3-dimensional structure. The cementitious material is sprayed, with compressed air, from a nozzle that is controlled by a robotic arm with six degrees of freedom (figure 2.2a). The spraying technique offers several advantages including superior interlayer bonding and the ability to embed steel reinforcement.

Smart Dynamic Casting (SDC) is a robotic slip-forming technique that is specifically

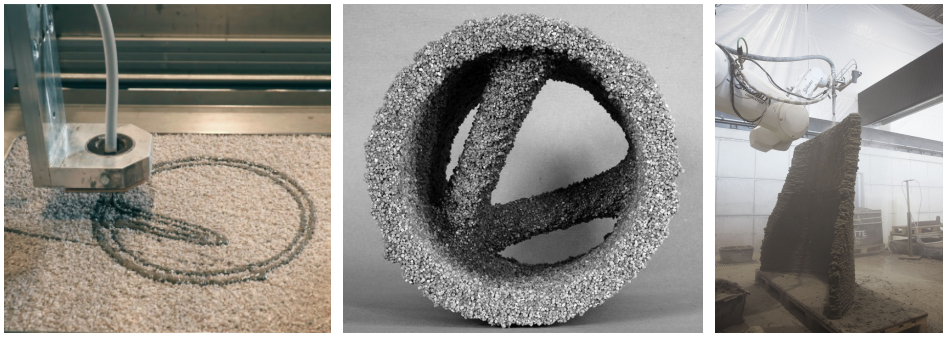

(a) (b) (c)

Figure 2.1: a-b) Particle bed 3D printing [23, 24] c) Shotcrete 3D printing [21]

designed for the prefabrication of custom, structurally optimised concrete and slender elements [25–27] (figure 2.1c). Essential to the technique is the dynamic formwork that can shape the fresh concrete in the desired form. In the automated process, the fresh and fluid concrete is poured in the formwork, by the time the formwork moves up and the concrete leaves the formwork, the concrete is set and able to carry its own weight. Therefore, the speed of the vertical movement of the formwork should be calibrated to the hydration time of the concrete.

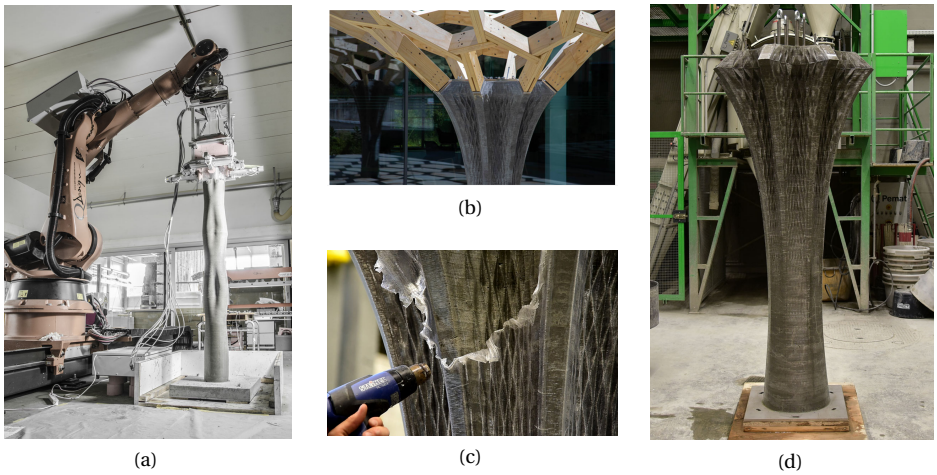

(a) (b) (c) (d)

Figure 2.2: a) Smart dynamic casting (ETH Zurich) [25] b-d) Egg shell column, (ETH Zurich) [28]

Another technique is Ultra-Thin 3D Formwork printing, also known as Eggshell [25, 28] (figure 2.2b - 2.2d). Here the focus is not on the digital manufacturing and shaping of the concrete, but on the printing of a thin and freeform mould. Simultaneously with the printing of the mould, the concrete is poured into the mould. After setting of the concrete, the thermoplastic material of the mould is removed using a heat gun.

Extrusion-based 3DCP is one of the most common techniques of additive manufacturing (AM) for concrete. The technique was developed in 2004 under the name "contour crafting" at the University of Southern California [29] and is applicable for large-scale structural elements. In this method, the cementitious material is transported employing a pump and extruded layer upon layer, through a nozzle that is digitally controlled by a robot. This is the technique used in the current thesis, and will be described in more detail in the coming paragraphs.

2.1.2. EXTRUSION-BASED 3D CONCRETE PRINTING

3DCP is an additive manufacturing technique that made tremendous progress over the last decades. Where other printing techniques are studied and used on a relatively small scale, 3DCP is researched globally by an increasing group of structural and civil engineering, material, and architectural research institutes. The technique has also been embraced by multiple industry parties. The knowledge gained on this specific concrete printing technique is enormous, and covers among others, printing systems ([30–32]), material development ([33–37] and durability studies ([38–40]). In recent years the technology has delivered multiple case studies [41] in the built environment that showcase its potential. The case studies vary from bridges to houses as can be seen in figure 2.3.

(a) (b)

Figure 2.3: Case studies 3DCP
a) Milestone house [42] b) The Striatus bridge [43]

Although strong development of the technique has taken place over the last two decades, there is one technical challenge that still needs to be overcome, which is reinforcement. Concrete, aside from being strong in compression and durable, is brittle by nature and lacks sufficient strength under tensile loading. In traditional concrete structures, this lack of tensile strength and ductility is overcome by the implementation of steel reinforcement. This provides the concrete with the required ductile behaviour needed to comply with modern building regulations, as it ensures structural integrity and safety. For 3DCP however, the implementation of steel reinforcement is not straightforward.

Without reinforcement, 3D concrete printing designs focus on elements subjected predominantly to compressive stresses. In this manner, brittle failure as a consequence of tensile forces can be avoided and structural integrity can be ensured [44]. However,

this "design in compression" concept counteracts one of the key advantages of 3D concrete printing, namely, the potential to reduce material usage through design optimisation [1–3].

Multiple studies therefore have been conducted on reinforcement methods for full-size printed concrete elements [44–47]. Among others, research trajectories were, the application of an external reinforcement frame [48](figure 2.4a), the use of post-tensioning pre-stressed reinforcement [4, 49] (figure 2.4b), the implementation of mesh reinforcement [46, 50](figure 2.4c), and the inline implementation of steel wires in the printed filaments [30] (figure 2.4d). However, these methods entail additional printing features or manual work, therewith counteracting the efficiency increase that the automated printing process may deliver, or are insufficient as an alternative to reinforcement.

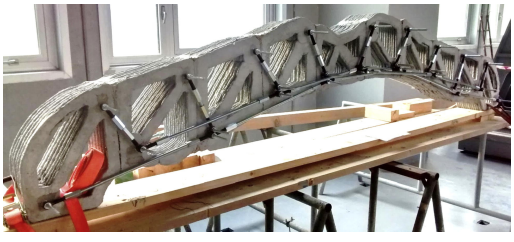

(a) Inside-out reinforcement [48]

(b) Post-tensioning of pre-stress cables [4]

(c) Mesh reinforcing method [46]

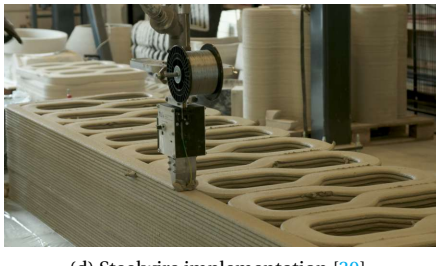

(d) Steelwire implementation [30]

Figure 2.4: Alternative reinforcement strategies in 3D concrete printing

2.2. SHCC

Another approach to improve the tensile strength and ductility of printed concrete is the development of a printable strain hardening cementitious composite (SHCC). SHCC, also known under the name ECC (engineered cementitious composite) is a special class of fibre-reinforced material. The material was developed in the early 1990s by V. Li [6]. SHCCs are characterised by their high tensile ductility (see figure 1.2) and strain hardening behaviour, which they derive from a small volume (1-2 vol%) of incorporated microfibres. The mechanical design of this engineered material finds its basis in the fracture mechanics concepts developed for fibre-reinforced cementitious composites.

Over the last decades research on SHCC material development and material appli-

cations [6, 51–55] has been conducted all over the world. In this period also a new name was introduced for the material namely, "strain hardening cementitious composite" (SHCC) under which the material is generally referred to in Europe and Asia. While there may be some regional preferences for the use of one term over the other, ECC and SHCC are used interchangeably in the literature, and both terms are recognised and widely used in research around the world.

The characteristic properties of SHCC are the result of the formation of multiple microcracks when the SHCC element is subjected to increasing tensile stress, which is achieved by the incorporation of micro fibres as self-reinforcement. The performance of these fibres, and their ability to bridge microcracks in the brittle cementitious matrix, strongly depends on micromechanics of the bond between the fibre and the matrix. The interaction between matrix, fibre and matrix/fibre interface is essential in order to obtain a cementitious composite with strain hardening behaviour [7].

Due to the importance of the fibre within this material concept, considerable research has been conducted on different fibre types and their applicability for SHCC. Typically, SHCCs are polyvinyl alcohol (PVA) fibres [56, 57] or polyethylene (PE) fibres [58, 59]. Besides these two commonly used fibres, research has also been conducted on other types of polymer fibres such as poly(p-phenylene-2,6-benzobisoxazole) (PBO) and aramide fibres [59, 60], steel fibres, [61, 62] and natural fibres [63, 64]. Finally, research has also been carried out on hybrid fibre mix designs [65–68]. Hybrid fibre mixtures combine steel fibres with synthetic and/or natural fibres within one SHCC material design, and are mainly used in strain hardening Ultra high-performance concrete (SH-UHPC), or Ultra high-performance SHCC, (UHP-SHCC)

2.2.1. MICRO-MECHANICAL SYSTEM

The mechanical concept behind SHCC is as follows: as soon as the concrete matrix develops its first microcrack, the fibres take over the tensile force. When the fibres manage to bridge the crack, the force equilibrium of the concrete element is restored. When the force increases further, the concrete will crack at a different location, and there the same mechanism takes place. This happens repeatedly until the tensile force within the material is higher than the fibre bridging capacity of the already-formed cracks. At that moment a crack will localise and the material finally fails. A typical stress-strain curve of the strain hardening behaviour and the multiple cracking is presented in figure 2.5.

For a material to display this mechanism, it must comply with two micro-mechanical requirements:

Strength criterion:

$$\sigma_{tensile,fibre} > \sigma_{tensile,matrix} \tag{2.1}$$

The strength requirement states that the matrix cracking strength should be lower than the maximum fibre bridging capacity of the existing cracks [6].

Energy criterion:

$$J_b' > J_{tip} = \sigma_0 \delta_0 - \int_0^{\delta_0} \sigma(\delta)\, d\delta \tag{2.2}$$

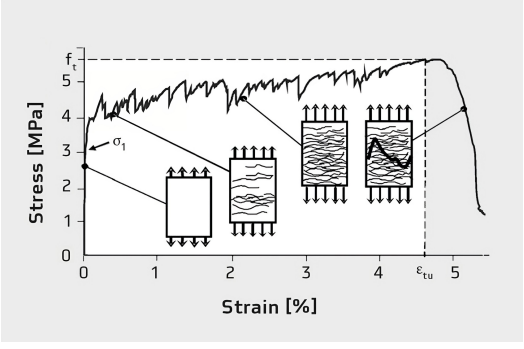

Figure 2.5: Typical stress-strain behaviour of SHCC (adapted from [69])

The energy requirement describes the energy balance in the crack extension process. It ensures that the fibre is able to build up enough complementary energy that it can bridge the matrix crack. When the fibre/matrix interface is too weak, the fibres are pulled out, but when the interface is too strong, the fibres break. In both cases the complementary energy will be too low to create a steady state crack and the composite will likely show strain softening behaviour. For strain hardening behaviour it is essential that the fibre has just enough freedom to deform: only then can it build up a high complementary energy which is needed to get a steady state crack and therewith its strain hardening behaviour [6].

2.3. 3D PRINTABLE SHCC

The unique properties of SHCC make it an attractive choice for applications in additive manufacturing. With its ability to undergo tensile strain, SHCC enhances design flexibility in 3D concrete printing, enabling more complex and optimised structural designs that promote material-efficient construction methods. As the fibres are embedded in the fresh material mixture, the material is regarded as self-reinforcing therewith ensuring the benefits of the automated printing process.

Furthermore, 3D printable SHCC (3DP-SHCC) can give solutions for printed concrete elements that rely on post printing reinforcement techniques. Currently, printed concrete structures often rely on post-tensioning systems for reinforcement [4, 49]. While this generates beneficial compressive stresses in the printed concrete, it also introduces tensile splitting stresses perpendicular to the direction of reinforcement [70]. For such specific structural elements, SHCC emerges as a compelling material candidate due to its ability to withstand the tensile splitting forces arising from prestressing, thereby ensuring structural integrity.

In addition to post-tensioned reinforcement, alternative research on reinforcing methods of 3D printed concrete elements is still ongoing. A recent study by Hass et al. [71] examines the performance of automated integrated helical reinforcement within 3D printed structures. Previous research has shown that SHCC can improve the bond with rebars due to the confinement effect of the fibre bridging capacity [72–74]. With the upscaling of reinforcement within 3D printed structures, SHCC can play a pivotal role not only

by optimising the performance of reinforcing bars but also in enhancing the durability of these reinforced structural elements, thanks to the reduced crack width attributed to SHCC.

2.3.1. MATERIAL DESIGN

The design of a printable cementitious mortar/concrete comes with requirements on the fresh material and mechanical properties to be printable. This has best been described by Le [33] who states that for a material to be applicable for 3D concrete manufacturing it must meet the following four requirements: pumpability, extrudability, buildability and open time. **Pumpability** is the requirement that is involved with pumping the mixture through a hose toward the extrusion nozzle. It requires certain fresh material properties, such as low viscosity, thixotropy and limited aggregate size, to achieve sufficient and consistent material flow. Furthermore, the mixture should remain stable and not segregate under pumping pressure, which can lead to system blockage [6, 75]. Regarding **extrudability**, the mixture should be stable when the layer is extruded from the nozzle, with limited cross-sectional deformation and imperfections [3]. Then there is the requirement of **buildability**, which specifies that the layer should be able to resist its own weight as well as the weight of subsequently added layers. **Open time** is the period between the mixing of the mortar and the loss of printability. This loss of printability is related to the time-dependent increase of the yield strength due to the formation of hydration products.

When not complying with these requirements, failure modes like blockage, buckling failure, plastic collapse and tearing can occur (see figure 2.6).

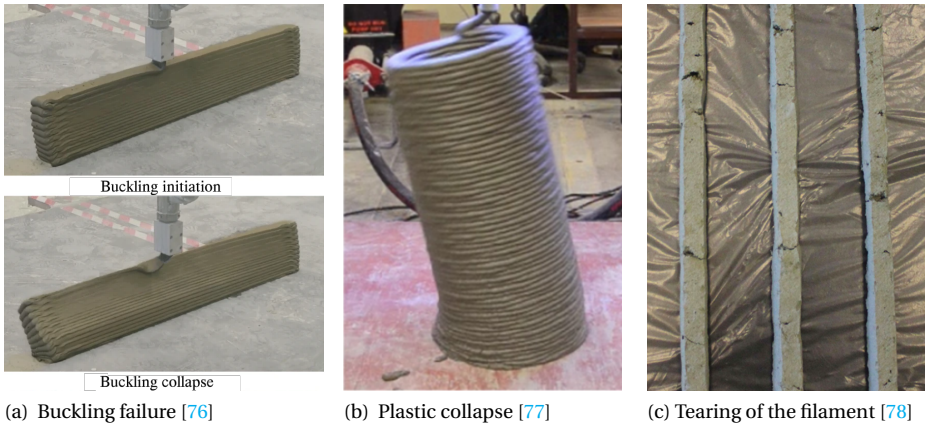

(a) Buckling failure [76] (b) Plastic collapse [77] (c) Tearing of the filament [78]

Figure 2.6: Possible failure modes that can occur during 3D concrete printing.

To achieve the required fresh mechanical parameters to comply with the printability requirements, concrete admixtures like superplasticizers, viscosity modifiers, retarders, and accelerators can be used [79, 80].

However, tailoring fresh properties of 3DP-SHCC with admixtures can jeopardise the strain hardening capacity in hardened state, as reported by Figueiredo et al. [10, 15].

The study aimed to develop a SHCC, suitable for 3D printing, by refining the rheological properties of a known SHCC mix design (M6), originally designed by Zhou et al. [56]. The developed 3DP-SHCC satisfied the requirements of pumpability, extrudability and open time, but showed insufficient buildability for 3D printing applications. Furthermore, the strain hardening behaviour of the composite in hardened state had decreased significantly compared to the original M6 mix design. Due to the adjusting of the rheological properties, by adding superplasticizers (SP) and viscosity modifier agents (VMA), the tensile strain at maximum stress decreased from 3.3% to 0.26% and the flexural deformation was reduced from 3.8 mm to 2.75 mm.

This illustrates the two big challenges in designing 3DP-SHCC: 1) The contradicting requirements for pumpability and buildability, a general issue for mortars designed for 3DCP. 2) Ensuring printability without jeopardising the strain hardening capacity in hardened state.

For pumpability, a material with low yield stress and low viscosity is preferred to facilitate material flow, where the buildability requirement calls for high yield stress and elasticity to prevent buildability failures such as buckling failure and plastic collapse [81].

A solution to these contradicting requirements can to a certain extent be found in the structural build-up behaviour of the material and hence the material composition and the particle packing of the granular ingredients [82]. In the first period after the deposition of a printed layer, two phenomena occur in the material: particle flocculation and nucleation of calcium silicate hydrates (C-S-H). In a few seconds after deposition, flocculation occurs in which the particles in the fresh mortar form a network of interacting particles (flocs) that can resist stress. Additionally, early hydration products (C-S-H phases and ettringite) form bridges between cement particles that have flocculated [83]. Both phenomena can be influenced by the choice of raw materials and the particle packing.

The choice of raw material and particle packing also influences the hardened mechanical properties. A fibre embedded in a strong and dense matrix might not be able to build up enough complementary energy to bridge a crack, as explained in section 2.2.1. Furthermore, rheological properties of the fresh 3DP-SHCC can influence the dispersion of the fibres during mixing. To achieve robust strain hardening capacity, the fibres must be evenly present throughout the material [84].

2.3.2. TEST METHODS

FRESH MECHANICAL PROPERTIES

Due to the importance of fresh mechanical properties, multiple characterisation methods have been developed and assessed for the analysis of the fresh properties of printable mortars[85–88]. These tests encompass a range of areas, including penetration, compression, shear failure, rotational behavior, non-destructive assessment, in-line testing, and capillary rheometry. Penetration tests, such as the Vicat test [87] and continuous penetration test [89], have been used to measure the penetration resistance of the printable material. Compressive tests play a vital role in assessing the structural integrity and strength of 3DCP. Two notable tests in this category are the squeeze flow test [90] and the Unconfined Uniaxial Compression Test (UUCT) [78, 87, 91–94]. Shear failure tests, including the Direct Shear Test [87], examine the shear behavior and resistance of

the printable concrete. Rotational tests utilising rheometers [86] and viscometers provide insights into the flow and viscosity characteristics of the printing materials. This includes tests such as the amplitude sweep test, the controlled shear rate test and the hysteresis loop test. Capillary rheometry, specifically the Ram Extrusion Test [10, 86, 95], has been employed to assess the flow behavior and extrudability of printing materials. Non-destructive tests such as the Ultrasonic Wave Transmission Test (UWTT) [87, 94] and Ultrasonic Pulse Velocity Test [91] have been used to evaluate the strength development over time and the integrity and quality of 3DCP. In-line testing methods, such as buildability tests [10, 76, 96], slug tests [97], and open time tests [86], have been utilised to monitor and optimise the printing process parameters in real-time.

The addition of fibres in any cementitious suspension has a strong effect on the rheology [84, 98–101]. In general, it is agreed that the addition of fibre reduces workability depending on fibre content, specifications and distribution and that the reduction in workability is due to both fibre-matrix and fibre-fibre interactions [102].

The influence of the fibres on the fresh mechanical properties of SHCC also affects the testing methods that can be used to measure the fresh material properties. High fibre volume mixtures can cause several issues when performing fresh material tests, such as segregation, blockage and fibre alignment. But also the general high viscosity of (printable) SHCC can affect the reliability of the results. A study by De Franca et al, [103] concludes that a rheometer-controlled shear rate test with a ball-measuring setup was affected by the high viscosity of the material, as it caused channels with reduced material behind the rotating ball, which impaired the results.

HARDENED MECHANICAL PROPERTIES

Besides the fresh mechanical properties, the determination of the hardened mechanical properties of the printed concrete elements is also important. For traditional concrete construction, standardised norms, such as the European EN-12390 [104], offer guidelines for testing material and mechanical properties. These norms ensure the reliability and performance of concrete in various applications. For concrete, standard test methods are described for compressive strength, flexural strength, tensile splitting strength, direct shear strength, elastic modulus, density and others.

For SHCC, additional mechanical tests are needed to assess the ductility and strain hardening capacity. The uniaxial tensile test (UTT), also known as the direct tensile test, is the most intuitive method for testing and evaluating the strain hardening capacity of SHCC. In this test, a specimen is subjected to axial tensile strain, while continuously measuring the resisting force. The tensile strain causes multiple cracks in the specimen until the cracks localise and the specimen ultimately fails. The UTT is relatively difficult to conduct as it is sensitive to specimen flaws, eccentric loading, size effects and strain rates [105, 106]. Consequently, establishing meticulous test protocols is crucial for obtaining accurate measurements.

The four-point bending test has also been used to investigate the mechanical properties of SHCC. While this test can not assess the strain hardening capacity of the material, it can assess the flexural strain capacity, which is a prerequisite for achieving strain hardening [107, 108]. On a smaller mechanical scale, fibre pull-out tests [109, 110] and Crack mouth opening displacement (CMOD) tests [111, 112] provide insights into the mechanical behaviour of individual fibres and cracks.

For printed structures, the existing standards designed for cast concrete are not entirely applicable. This is because printed concrete test specimens have unique features that are logically absent in the standards for traditional concrete, such as the anisotropy of the material due to the layer-by-layer build-up. Consequently, when evaluating the hardened properties of 3D-printed concrete, all loading directions relative to the layer interface must be tested to achieve a full understanding of the material. In this regard, the RILEM Technical Committee ADC (Assessment of Additively Manufactured Concrete Materials and Structures) discussed several adapted tests and specimen preparation protocols for (unreinforced) 3DCP materials [113].

2.3.3. INTERACTION BETWEEN MATERIAL AND PRINTING SYSTEM

When it comes to any material, researchers and structural engineers rely on the mechanical properties retrieved from experiments as a basis for structural analysis. Unfortunately, full-scale concrete printing sessions are too time- and material-intensive for quick feedback on material adjustments. So, to keep the iteration time during material development reasonably short, researchers often conduct preliminary experiments on cast specimens. In recent years, however, multiple research papers have reported discrepancies between cast and printed specimens [50, 114–117]. Le et al. [114] presented thorough research into material and mechanical properties for both cast and printed specimens. They found that the density of the printed specimens was 4.5 % higher, and also the flexural strength increased from 11 MPa (cast) to 13-15 MPa (printed). However, lower values were reported for compressive strength (5-30%) for the printed specimens. This reduction in compressive strength for printed elements is often found in literature, where contradicting reports can be found for the density. A recent study of Seo et al. [116], analysed the density and compressive strength of different mixtures and curing methods. They concluded that the density of the cast specimens showed a small increase for multiple specimen types.

When using SHCC for 3D concrete printing, these differences seem to be even more pronounced as multiple researchers have reported high deviations in flexural and tensile deformation capacity between cast and printed specimens [10, 15, 118], with reductions of 25% to 38% of the tensile strain capacity.

The tensile ductility of SHCC exhibits a higher degree of variability compared to other properties. Increased ductility is linked to saturated cracking, where fine cracks with close spacing uniformly form along the tensile specimen. However, unsaturated cracking, characterised by clusters of cracks interspersed with uncracked specimen segments, is commonly observed. This is primarily attributed to the significant variation in cracking strength among different parts of the tensile member. Segments with higher cracking strength may not undergo cracking before ultimate failure occurs in sections with lower strength. The full deformation capacity of SHCC may not be fully realised. The variation in cracking strength can be attributed to two main factors: 1) the distribution of matrix inherent flaws, (entrapped air voids, of insufficient mixing) and 2) the variation of fibre content due to insufficient mixing or the formation of fibre agglomerates.

Numerous phenomena have the potential to influence the material and its mechanical properties throughout the printing process. Consequently, cast specimens do not necessarily provide a reliable indication of the actual behaviour of printed material. In

the field of 3D concrete printing, it is generally agreed that the interlayer between the subsequently extruded filaments can affect the mechanical performance of the printed element. The quality of the adhesion between two subsequent layers depends on both the fresh material properties and printing setting such as time-gap (interlayer time), [114, 115, 119], print speed [115] nozzle height [120], moisture content [121] and the structuration rate of the material [122, 123].

The influence of pumping on the material and mechanical properties of concrete has been the subject of a considerable number of studies [124–126]. The overview given by Li et al. [124] on the effect of pumping on concrete mixtures reports changes in rheological properties and air void content. Shen et al. [126] concludes that pumping may accelerate the hydration process causing a reduction in both the dormant period and the setting period up to 27 and 28 %, respectively. Shen argues that this is the main cause for the increase in the dynamic yield stress observed in pumped concrete.

In the domain of printable fibre-reinforced composites (FRC), which includes SHCC, the micro-fibres may also play a substantial role in the observed variations of mechanical properties between cast and printed composites. Hambach and Volkmer [13] found that fibre alignment within a printed fibre-reinforced element can be achieved when the ratio of fibre length/nozzle diameter is larger than one. Similar to this approach, Me et al. [14] printed FRC using a narrow nozzle diameter, ensuring that the fibres were positioned vertically within the nozzle before extrusion. The evaluation of the mechanical properties was done in the three principal orthogonal directions and compared to conventionally cast specimens created from the identical FRC mix. In the cast specimen, the assumption is made that the fibres are arranged in a random manner. The research concludes that fibre alignment was achieved and that it strongly affected the mechanical properties in different directions. Figueiredo et al. [15] investigated the orientation of the fibres from a beam which was printed with a nozzle bigger than the maximum fibre length, (fibre length: 8 mm, rectangular nozzle size: 10x50 mm). In this scenario, it was found that the extrusion process orientated the fibres diagonally outwards with respect to the printing direction.

In addition to fibre orientation, fibre agglomeration, the clustering or grouping together of individual fibres within a material, has been reported for printable SHCC [127, 128]. Fibre agglomeration can strongly affect the robustness of SHCC performance, especially its tensile strain capacity [7, 129].

3

3DP-SHCC WITH OPTIMISED PARTICLE SIZE DISTRIBUTION

This chapter investigates the role of the particle size distribution (PSD) in relation to the buildability properties of the mixture in the fresh state and strain hardening properties in the hardened state. To this end, 6 SHCC mixtures were designed based on optimal particle packing with the application of the Modified Andreasen and Andersen Model. The two mix designs that showed the highest displacement at maximum stress when subjected to four point bending were selected for further development of their fresh state rheological properties. This was achieved by the addition of a viscosity modifying agent (VMA) and a superplasticizer (SP) and through material analysis by means of ram extrusion tests. Further fresh material characterisation on the final two 3DP-SHCC mix designs was attained by the deployment of uniaxial unconfined compression tests (UUCT), Vicat tests and buildability tests. After successful printing of the two SHCC composites, the compressive strength, the 4-point bending strength and the uniaxial tensile strength and strain at maximum stress were determined at an age of 28 days. The research shows that optimisation of the PSD in a 3DP-SHCC mix design results in an improvement of the buildability, but can result in decreased pumpability and strain hardening capacity.

[1]

[1]The research presented in this chapter has to a large extent been published in A.L. van Overmeir, S.C. Figueiredo, B. Šavija, F.P. Bos & E. Schlangen, Design and analyses of printable strain hardening cementitious composites with optimised particle size distribution Construction and Building Materials , 324, 126411 (2022)[95].

3.1. INTRODUCTION

In literature it is suggested that the solution to the contradicting printing requirements can to a certain extent be found in the structural build-up behaviour of the material and hence the material composition and the particle packing of the granular ingredients [82]. The current research focuses on the material design of 3DP-SHCC and aims to find a systematic approach to design a printable and strain hardening cementitious composite.

To this end, 6 mixtures were designed based on optimal particle packing. These six mixtures were mechanically tested on flexural strength and deflection capacity by use of a 4-point bending test. The two mix designs that showed the best performance were selected for further tailoring of their fresh state rheological properties. This was done by the adding of VMA and (additional) SP and the rheological properties were quantified by means of a ram extruder. Further fresh material characterisation of the final mixtures was achieved by the deployment of uniaxial unconfined compression tests (UUCT) and Vicat tests. Subsequently, both mixtures were subjected to a printing trial including a buildability test, to observe their performance on the printability requirements; pumpability, extrudability, buildability and open time. The beams resulting from these printing sessions have been subjected to mechanical tests at an age of 28 days, to assess their compressive strength, 4-point bending strength and uniaxial tensile strength and strain. The underlying hypothesis is that the PSD optimised mix designs yield good buildability properties and show strain hardening behaviour under uniaxial tensile loading.

3.2. THEORY

Fresh concrete can be characterised as a yield stress fluid, meaning that it behaves as a solid when the applied stress is below a critical yield stress, and as a liquid when a stress is applied above this critical value [80, 130]. Additionally, the rheological properties of fresh concrete mixtures are dependent on its flow history. For fresh concrete, it can be stated that with increasing time in a state of rest, the critical yield stress to initiate flow increases. This is due to the build-up of a stress-transferring structure between particles, a phenomenon called thixotropy.

Thixotropy is governed by two main mechanisms: re-flocculation and structuration. Re-flocculation is a physical process resulting from interparticle forces that grow structurally stable flocs and structuration is related to the formation of early hydration products of the cementitious particles [82]. In relation to re-flocculation, research has been conducted on the influence of particle size distribution (PSD). When the structurally stable flocs settle in an optimally packed particle microstructure, it will enhance the yield shear stress of the material which will result in better buildability for 3DCP [77]. Studies on the influence of PSD by the use of small-scale particles like nano-clay and silica fume show that the thixotropic behaviour increases when these particles are used [77, 131, 132]. Additionally, good particle size packing also enables the design of a stable mixture that will resist dynamic segregation during pumping [133].

Thus, for the development of a printable SHCC mix design that is sufficiently buildable, the optimisation of the particle packing is an important objective. To achieve sufficient particle packing the relative volumes of the ingredients must be determined accordingly. This can be achieved by the use of a particle packing model. In the literature, two types of particle packing models can be defined namely, *discrete models* that take into account discrete size classes of two or more particles and *continuous models* that assume that all possible sizes are present in the particle distribution system [134]. In the context of concrete mix design, continuous models are preferred, as they can easily represent the continuous character of a mix design's particle size distribution. The modified Andreasen and Andersen (A&A) model, developed by Funk and Dinger, [135] is a continuous model that takes into account a minimum and a maximum particle size. This model has been widely applied to optimise the particle packing for different types of concrete, including self-

compacting concrete (SCC) [133, 136], SH-UHPC, [137], UHPC [138], sustainable concrete [139] and printable mortars [140]. The modified A&A model is given in Eq. 3.1 and 3.2.

$$P_{tar}(D) = (D^q - D^q_{min})/(D^q_{max} - D^q_{min}) \tag{3.1}$$

$$P_{mix}(D) = \sum(v_i * PSD_i) \tag{3.2}$$

D	= Particle size [μm]
D_{max}	= Maximum particle size [μm]
D_{min}	= Minimal particle size [μm]
q	= Distribution modulus [-]
$P_{tar}(D)$	= Ideal volume fraction of particles smaller than D
$P_{mix}(D)$	= Real volume fraction of particles smaller than D
v_i	= Volume of mix ingredient i
PSD_i	= Specific particle size distribution of mix ingredient i

In the modified A&A particle packing model, the parameter q defines the curvature of the particle size distribution of the mix design. In general, high values of q (0.4 - 0.6) result in less workable mixtures that contain limited fines and a high fraction of aggregates.

Combining equations 3.1 and 3.2 together with a least square analysis results into the most optimal composition of the mix, given the chosen distribution modulus.

3.3. MATERIALS

For the development of a printable SHCC mix design that has sufficient buildability, the optimisation of the particle packing was taken as the backbone of the research.

The methodology of mix design and selection is as follows:

1. Six trial mixtures are designed using the modified A&A particle packing model.
2. Based on mechanical properties retrieved from a 4-point bending test, two of the designed trial mixes are selected for further development.
3. These two mix designs are developed further by adding of VMA and SP to improve the rheological properties.
4. The improved mix designs with the most optimal rheological properties are then selected and renamed as mix A and mix B.
5. Fresh rheological properties are determined by means of ram extrusion tests, unconfined uniaxial compression tests, and Vicat tests.
6. Printing sessions are conducted, covering buildability tests and printing of the beams from which specimens are extracted.
7. Hardened mechanical and material properties of the printed material are determined by means of compression tests, 4-point bending tests, uniaxial tensile tests and CT scans.

Binders used in this study are: CEM I 42.5 N, CEM I 52.5 R, Blast furnace slag (BFS) and Silica fume (SF). SF has been used to increase small particle fraction, therewith aiming to increase the thixotropic behaviour. CEM I 52.5 R has been added to the research to bridge the gap in particle size range between SF and BFS. Particle size distribution curves were either received from the material suppliers or measured by means of laser diffraction spectroscopy with a DIPA-2000 particle analyzer. Fillers consist of Limestone powder (LS), Sand 125 - 250 [μm], Sand 250 - 500 [μm] and Sand 500 - 1000 [μm]. To safeguard the strain hardening capacity of the 3DP-SHCC, no fillers with a size of >1000 [μm] were used in this research.

For the material research two groups of binders and three groups of fillers were defined. The commonly used Polyvinyl Alcohol (PVA) fibre was added to achieve strain hardening capacity [7]. Specifications on the mechanical properties of the specific RECS15 fibre can be found in table 3.2.

Table 3.1: Binder and filler groups

Binder groups	**BCS:**	BFS + CEM I 42.5 N + SF
	BCCS:	BFS + CEM I 42.5 N + SF + CEM I 52.5 R
Filler groups	**250:**	LS + Sand 125 - 250
	500:	LS + Sand 125 - 250 + Sand 250 - 500
	1000:	LS + Sand 125 - 250 + Sand 250 - 500 + Sand 500 - 1000

Table 3.2: Fibre specifications

		PVA (RECS15)
Tensile strength	[MPa]	1600
Modulus of elasticity	[GPa]	41
Ultimate strain	[%]	6
Length	[mm]	8
Diameter	[μm]	40
Aspect ratio	[L/D]	200
Density	[kg/m3]	1.3

With the use of the Modified A&A Model [141] the optimal particle size composition of all six combinations between binder and filler groups was calculated. The study utilised a maximal particle size (D_{max}) for Mix A and Mix B of 250 μm and 500 μm, respectively and a D_{min} of 0.05 μm. For the distribution modulus q a value of 0.25 was chosen, based on the findings of Ragalwar et al. [138, 142] on the most optimal q-value for UHPC-SHCC.

The particle size distribution of the raw materials and the mix design BCCS1000 are presented in figures 3.1a & 3.1b respectively. The final composition of the six dry material designs; BCS250, BCS500, BCS1000, BCCS250, BCCS500 and BCCS1000 can be found in table 3.3.

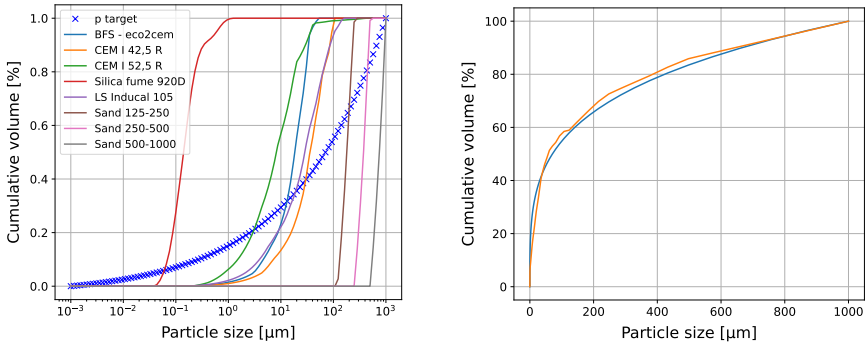

(a) Raw materials

(b) Mix design BCCS1000

Figure 3.1: PSD design with modified Andreasen and Andersen model with a) The PSD of the individual raw materials, b) Particle packing design for BCCS1000 with, in orange the optimised PSD of mix design BCCS1000, and in blue the p-target curve for a q-value of 0.25.

Table 3.3: Mix composition [g/dm^3]

		BCS			BCCS		
		250	**500**	**1000**	**250**	**500**	**1000**
Binder	Blast furnace slag	314	377	225	132	226	131
	CEM 1 42,5 N	483	458	500	478	502	522
	CEM 1 52,5 R	-	-	-	173	132	144
	Silica fume	70	51	40	60	41	39
Filler	Limestone powder	447	195	25	496	251	85
	Sand 125-250 μm	284	286	212	299	297	209
	Sand 250-500 μm	-	263	219	-	226	222
	Sand 500-1000 μm	-	-	231	-	-	235
Suppl.	Water	347	355	305	337	360	334
	Superplasticizer	1.73	1.77	1.53	1.69	1.8	1.67
	PVA (vol%)	2	2	2	2	2	2
Ratio	F/B	0.85	0.87	0.85	0.9	0.86	0.9
	w/b	0.4	0.4	0.4	0.4	0.4	0.4
	sp/b	0.2%	0.2%	0.2%	0.2%	0.2%	0.2%

The mixing was done on a Hobart A200-N planetary mixer, at a constant low speed (60 rpm). The procedure was kept the same for all 6 mix designs and consisted of the following steps:

- 2 Minutes: Mixing all dry materials, including fibers and SP.
- 1 Minute: Adding of water while mixing.
- 3 Minute: Mixing of wet material.

In a later stage of the material development the methyl hydroxyethyl cellulose based VMA, Tylose MHS 15002 P6 was incorporated in the mix design. For these mixes adjustments were done to the mixing procedure.

- 2 Minutes: Mixing all dry materials, including fibers , SP and $\frac{1}{3}$ of the VMA.
- 1 Minute: Adding of water while mixing.
- 1 Minute: Mixing of wet material.
- Add: $\frac{2}{3}$ of the VMA.
- 2 Minutes: Mixing of wet material.

The mixing procedures described above differ from the mixing process of general SHCC, where the fibres are added in the slurry phase. 3DP-SHCC is a very dough-like mixture, compared to normal SHCC. Due to this high viscosity of the fresh slurry, it is very difficult to disperse the fibres sufficiently when added in dough-like phase. The mixing procedure was therefore adjusted accordingly.

The developed mix designs have been cast and tested on 7-day flexural strength by means of a 4-point bending test with the aim to assess their deflection capacity and their potential strain hardening behaviour. The performed 4-point bending test was chosen as it gives, in comparison to the uniaxial tensile test, more quantifiable data on mixes that do not have strain hardening capacity. Therefore the test is able to distinguish between a wider range of mix designs, with higher or lower strain hardening capacity. The method utilised for the 4-point bending test and information on the specimen sizes and curing conditions can be found in section 3.4.

Table 3.4: 4-point bending test results, preliminary research

	BCS250	BCS500	BCS1000	BCCS250	BCCS500	BCCS1000
Maximum flexural stress [MPa] (RSD)	10.77 (4.4%)	6.42 (12%)	5.76 (14%)	10.05 (10%)	9.08 (34%)	6.10 (22%)
Deflection at max. stress [mm] (RSD)	3.94 (18%)	3.22 (21%)	2.63 (20%)	1.66 (7%)	1.88 (82%)	1.47 (27%)

The results of the preliminary research on the mix designs with optimised PSD can be found in table 3.4. Of the mix designs that showed flexural hardening behaviour, Mix BCS250 and Mix BCS500 showed the highest deflection capacity. These two mix designs have therefore been selected for further development of rheological properties, followed by the characterisation of their fresh and hardened properties. This was done by an elaborate experimental program, described in section 3.4.

3.4. TEST METHODS

3.4.1. OVERVIEW EXPERIMENTAL PROGRAM

As described in section 3.3, the selected mix designs BCS250 and BCS500 were developed further to tailor their rheological properties with respect to the printing requirements. This has been done by the employment of a ram extrusion test.

Afterwards, the two mix designs, Mix A and Mix B, were subjected to a full printing session and an experimental program to assess their material and mechanical properties in fresh and hardened state. For the assessment of the fresh material and mechanical properties, the mixtures were subjected to the following experiments: ram extrusion test, UUCT, open time test and buildability test.

The printed composites have been subjected to the following hardened mechanical tests: Compression test, 4-point bending test and uniaxial tensile test. Additionally, the 4-point bending test was conducted on cast specimens to compare the mechanical performance of the cast and the printed material. To consider the printing and building direction within the test specimens the definition of specimen coordination was used in accordance with the RILEM Technical committee ADC (Assessment of Additively Manufactured Concrete Materials and Structures) [113]. An overview of these definitions is given in figure 3.2. In these definitions, the first letter indicates the axis of the applied load, the second indicates the orientation of the specimen.

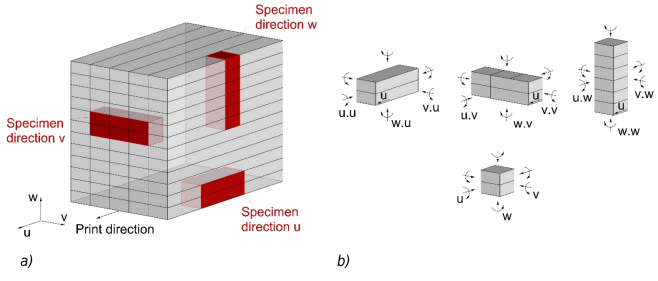

Figure 3.2: a) Definition of the orientations of 3D printed specimens b) Examples of specimen orientations related to the loading direction [113]

Finally, a material assessment was done using computed tomography (CT) to get insight into the internal micro-structure of a material, such as porosity over height and pore size.

3.4.2. FRESH PROPERTIES

RAM EXTRUSION TESTS

To achieve the rheological properties required for adequate pumpability and buildability, mix designs BCS250 and BCS500 were further developed with the incorporation of VMA and SP. To this end, the ram extrusion test method was deployed according to the procedure of Figueiredo et al.[10]. This ram extrusion method makes use of the non-linear Benbow-Bridgwater model for measurement data fitting and parameter determination as defined in equation 3.3 [143–145] .

$$P = P_1 + P_2 = 2\ln\left(\frac{D}{d}\right)(\sigma_0 + \alpha V^m) + \frac{4L}{d}(\tau_0 + \beta V^n) \tag{3.3}$$

P	= Total pressure drop [kPa]
P_1	= Pressure drop in the die entry [kPa]
P_2	= Pressure drop in the die land [kPa]
σ_0	= Bulk yield stress [kPa]
α	= Parameter characterising speed in the die entry [kPa.s/mm]
V	= Extrusion speed in the die land [mm/s]
D	= Barrel diameter [mm]
d	= Die diameter [mm]
τ_0	= Shear yield stress [kPa]
β	= Parameter characterising speed in the die land [kPa.s/mm]
L	= Die length [mm]
m & n	= non linear fitting coefficients

By varying VMA to binder ratios and adapting the SP to binder ratio accordingly, the contribution of these additives to the rheological properties of the 3DP-SHCC has been assessed.

To determine the fresh mechanical properties *bulk yield stress* and *shear yield stress*, each mixture variant has been extruded through three different die lengths at 4 different speeds. Per die length, a new batch of material was prepared to test the material at consistent age. Per die, a minimum of four ram extrusion tests were conducted, of which the average value was used for fitting of the Benbow-Bridgwater model. Results of these tests can be found in section 3.5.1. Based on these results, the decision has been made to continue the research with two mixtures namely, mix BCS250 consisting of a VMA/binder ratio of 0.6% and a SP/binder ratio of 0.4%, and mix BCS500 consisting of a VMA/binder ratio of 0.3% and a SP/binder ratio of 0.3%. Throughout the rest of the chapter these mixtures will be addressed as Mix A and Mix B, respectively. When including the new values for VMA and SP to the composition as given in table 3.3 the final composition of the two 3DP-SHCC mix designs are as presented in table 3.5 here below.

Table 3.5: Final composition Mix A and Mix B [g/dm^3]

	BFS	CEM 42,5N	SF	LS	Sand 125-250	Sand 250-500	Water	PVA	SP	VMA
Mix A	314	483	70	447	284	-	347	26	3.47	5.20
Mix B	377	458	51	195	286	263	355	26	2.66	2.66

UNIAXIAL UNCONFINED COMPRESSION TEST

In this research, a modified uniaxial unconfined compression test (UUCT) was used to determine the green compressive strength of the printable mortar. The method has been developed by Wolfs et al. [78] and is based on the traditional UUCT standard for soil specimens, ASTM D2166 [146]. This modified UUCT is well accepted in the field for the quantification of fresh properties of 3DP mortars [87, 92, 93].

During the test, the deformation of the specimen is captured with an optical camera. With the use of National Instruments Vision Builder, the optical data is post-processed and the load-dependent cross-sectional area is obtained. When the UUCT is performed at several time intervals after mixing, it can characterise the initial compressive strength and its development over time. Meanwhile, also the initial apparent Young's modulus and its time development can be obtained from the acquired data.

The UUCT is performed on a cylindrical specimen with a diameter of 70 mm and a height of 140 mm. The specimens are made with the use of a steel mould that on the inside is covered with baking paper, to avoid the fresh material to stick. The specimen was removed from the mould seconds prior to the testing of the specimen. The specimen is then placed in an Instron 5967 testing system, where a load cell with a 70 mm diameter loading plate is used to transfer the vertical compressive force onto the specimen. The test was performed in displacement-controlled mode, with a displacement rate of 0.5 mm/s. The test is carried out at t = 5, 15, 30, 60 and 90 minutes after mixing.

INITIAL SETTING TIME

The open time of the mixtures was examined by means of a Vicat penetration test. From an average of three specimens, the initial setting time of mix A and B was equal to ± 3h30 and ± 4h30, respectively.

PRINT FACILITIES AND SETTINGS

The printing facilities at the Delft University of Technology use a gantry system for creating the contour of the printed elements. The gantry system in Delft is illustrated in figure 3.3a, and is able to print a volume of [1 x 0.6 x 0.35] m^3. The printing facilities are equipped with a PFT Swing M pump, which is connected to a 5 m hose provided with a down flow nozzle. The hose has a diameter of 25 mm, and the nozzle has a rectangular cross-section of [40 x 14] mm^2. A separate A200-N Hobart planetary mixer is used for preparing the 3DP-SHCC.

PRINTING SESSION

A printing session has been conducted, composed of a buildability test and the printing of five beams of 800 mm length per 3DP-SHCC mixture. The beams consist of three 5-layer high beams and two 4-layer high beams and are printed in a back and forth printing routine as is presented in figure 3.3b.

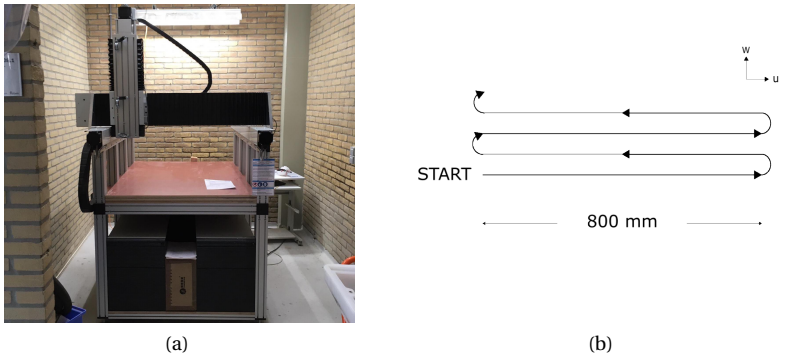

(a) (b)

Figure 3.3: a) Printer facilities at TU Delft b) Printing routing

For the full printing session, 7 batches of 3.5 litres each were mixed as described in section 3.3. As the material is prepared in multiple batches, the printing session could start after sufficient material was prepared. After the preparation of each batch, the material was placed into the pump reservoir and covered with a plastic foil to prevent the mixture from dehydrating. After the preparation of a sufficient amount of material, the printing session started with a buildability test, using the printing settings as provided in table 3.6. For both mix A and B, the buildability test started 40 minutes after the preparation of the first batch of material.

Table 3.6: Printing settings

	Printing speed [mm/s]	Pumping speed [r.p.m.]
Mix A	20	72
Mix B	30	60

BUILDABILITY TEST

The buildability test is another method to characterise the fresh material properties of the 3DP-SHCC. This test differs from the other tests utilised for the determination of fresh mechanical properties, as it characterises the material after completing the full printing procedure, instead of directly after mixing. In this study, the buildability of the material was tested by printing a slender wall in subsequent layers of 800 mm length until it fails or the maximum element height of the printer gantry is reached. Failure of the wall can occur either by plastic collapse or due to elastic buckling [76, 147]. From the achieved layer height, the compressive yield stress and the apparent Young's modulus at time of collapse (from mixing) are calculated based on the theory provided by [96].

The apparent Young's modulus at time of failure t=T can be calculated with:

$$l_{cr} = n_{layers} \cdot h_{layer} \cdot 10^{-3} \tag{3.4}$$

$$D_0 = \frac{l_{cr}^3 \cdot (\rho \cdot g \cdot b)}{(l_{cr}^*)^3} \tag{3.5}$$

$$E_{t=T} = \frac{12 \cdot D_0 \cdot (1 - \upsilon^2)}{h_{layer}^3} \tag{3.6}$$

The compressive yield stress at of failure t=T can be calculated with:

$$l_p = n_{layers} \cdot h_{layer} \cdot 10^{-3} \tag{3.7}$$

$$\sigma_{c,t=T} = \frac{l_p \cdot \rho \cdot g}{l_p^*} \tag{3.8}$$

n_{layers}	=	Number of layers [-]
h_{layer}	=	Layer height [mm]
b	=	Width of layer [mm]
ρ	=	Density [kg/m^3]
g	=	Gravity [m/s^2]
l_{cr}	=	Critical buckling length [m]
l_{cr}^*	=	Dimensionless critical buckling length [-] = 1,99 for calculation E at time t=T (not considering stiffness curing rate)
D_0	=	Initial bending stiffness [Nm]
υ	=	Poissons ratio [-]
$E_{t=T}$	=	Young's Modulus at time of collapse t=T [MPa]
l_p	=	Plastic collapse length [m]
l_p^*	=	Dimensionless plastic collapse length [-] = 1 for calculation σ_c at time t=T (not considering strength curing rate)
$\sigma_{c,t=T}$	=	Compressive yield stress at time of collapse t=T [kPa]

3.4.3. HARDENED PROPERTIES: 4-POINT BENDING TEST

To determine the flexural strength and the deflection capacity of the cast and printed specimens, four-point bending tests were conducted. The slab-shaped specimens with a size of 30 mm (b) x 8 mm (h) x 150 mm (l) were tested after 28 days of curing. The specimens have been cured at 20 °C with a relative humidity of 97% prior to testing. The printed specimens were extruded from the printed beams, with careful consideration of the interlayer zone locations. The height of one single layer within the printed beam was ± 14 mm, enabling the extraction of test specimens without the presence of an interlayer zone.

All specimens were tested in orientation **v.u** (load perpendicular to the printing plane) [113], see paragraph 3.4.1. The 4-point bending tests were conducted using an Instron 8872 servo-hydraulic testing system, with an effective load span of 120 mm, and the spacing between the span rods of 40 mm. These tests were executed in displacement-controlled mode with a testing speed of 0.01 mm/s.

To measure the effective displacement during testing, two linear variable differential transformers (LVDTs) were positioned on the steel components of the test set-up. It's important to note that the vertical displacement measurements were obtained by averaging the measurements from these two LVDTs. Considering their placement the retrieved values relate to the displacement of the two middle rods. In figure 3.4 the full test set-up is presented.

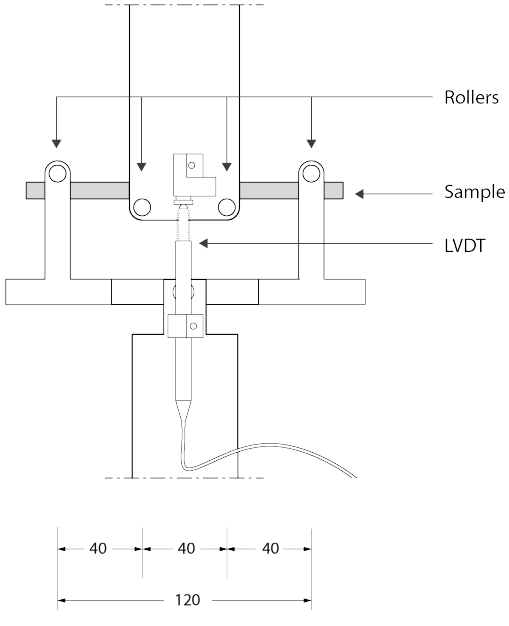

Figure 3.4: 4-point bending test setup, measurements in mm [148]

3.4.4. HARDENED PROPERTIES: COMPRESSION TEST

For the compression test, cubes with an edge of 35 mm (± 1mm) were sawn from the 5-layer high 3DP-SHCC beams. All test specimens have been cured at 20 °C with a relative humidity of 97% prior to testing. The cubed specimens were measured and weighed prior to testing to determine their apparent density. The compression test was conducted in a servo-hydraulic machine and

performed with a constant load rate of 2.0 kN/s, in accordance with ASTM-39 [149]. The printed specimens were tested in orientation **w** (load perpendicular to printing plane) and orientation **v** (load perpendicular to the printing direction), as defined by the RILEM Technical committee ADC (Assessment of Additively Manufactured Concrete Materials and Structures) [113] (figure 3.5). Per orientation, a minimum of 5 specimens were tested on compressive strength at 7, 14 and 28 days after printing.

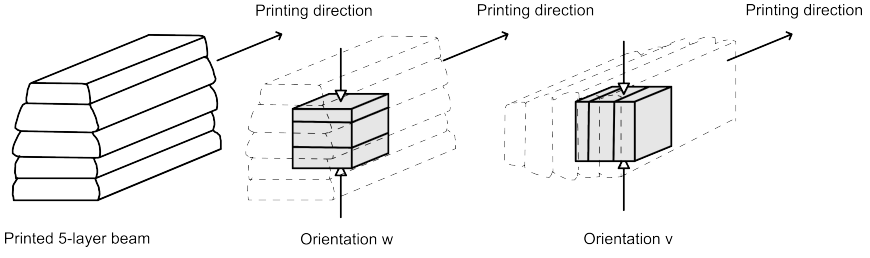

Figure 3.5: specimen orientation of compression test

3.4.5. HARDENED PROPERTIES: UNIAXIAL TENSILE TEST

After seven days in the curing room, specimens were sawn from printed SHCC beams using a wet stone saw with a diamond powder coated blade. The specimens had a rectangular shape with the following dimensions: 20 mm [w] x 40 mm [h] x 250 mm [l] (figure 3.6a). Fibre-reinforced concrete was cast on both outer ends with the use of a custom-made mould (see figure 3.6b)) to create a dog-bone shaped test specimen. Therewith ensuring the tensile failure to occur in the region with a smaller cross-section, which was monitored during testing. An elaborate description on the specimen preparation and test method can be found in the author's previous work [150]. After 24 hours the specimens were demoulded and placed back into the climate chamber to cure until testing.

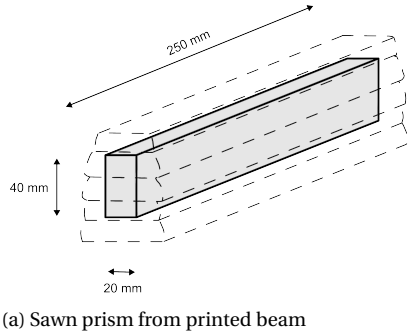

(a) Sawn prism from printed beam

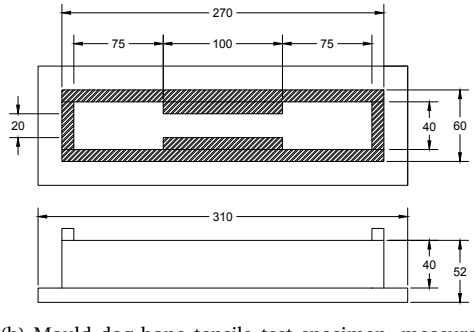

(b) Mould dog-bone tensile test specimen, measurements in mm [150]

Figure 3.6: Tensile test specimen preparation

The uniaxial tensile tests were carried out 28 days after printing in an Instron machine making use of the deformation-controlled mode. The displacement rate was set to 0.5 μm/s, resulting in a strain rate of 5 microstrain/s. Two LVDT sensors were utilised to measure the vertical displacement, the average value of the two sensors was used to control the vertical displacement of the tensile test. The full test set-up can be viewed in figure 3.7.

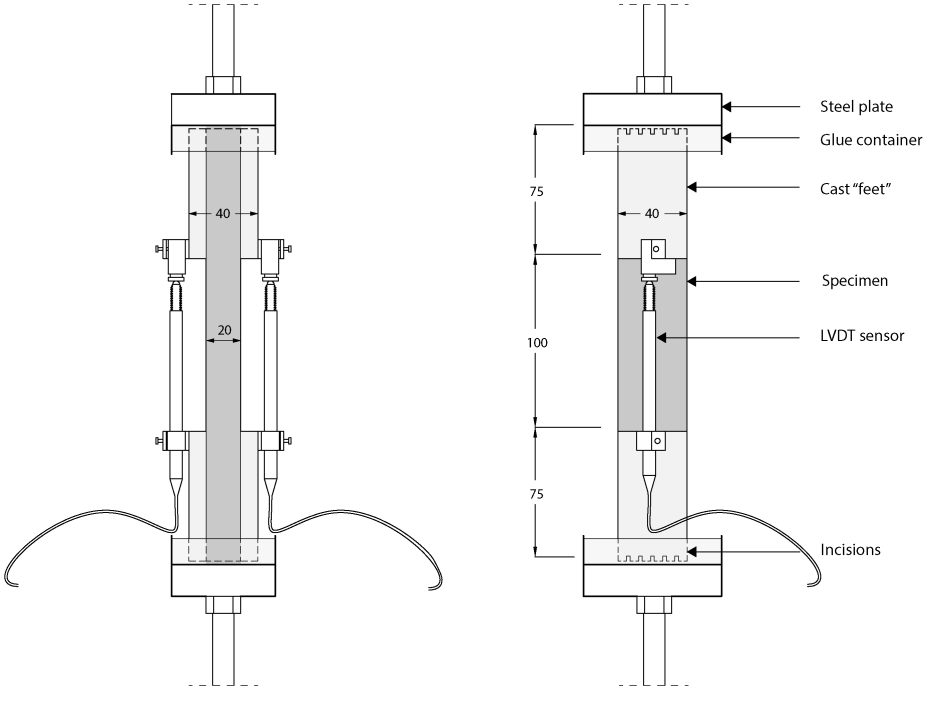

Figure 3.7: Test set-up of tensile test, measurements in mm

3.4.6. MATERIAL PROPERTY: POROSITY

To get insight in the air void content, the air void distribution and the presence of initial flaws in the printed strain hardening cementitious composites, two 20 mm diameter cores and two 40 mm diameter cores were extracted from the printed SHCC beams. The specimens were subjected to X-ray CT scans with a Phoenix Nanotom X-ray. The 20 mm diameter specimens were scanned with a resolution of 10μm/pixel over a height of 20 mm. The scan was performed on the height of the second and the third layer. The acquired data was analysed for the determination of the air void content and distribution by the method that previously has been reported by van Overmeir and Figueiredo [15, 150].

The 40 mm diameter cores were scanned with a resolution of 22.5 μm/pixel and the resulting images have been post processed with the use of VG studio software. The images were used to detect initial flaws, such as big entrapped air voids and the presence of fibre agglomerates.

3.5. RESULTS AND ANALYSIS

3.5.1. FRESH PROPERTIES

The ram extrusion test results that are presented in table 3.5.1 show positive correlation between the bulk yield stress and the increase of the VMA to binder ratio. This trend is more pronounced for Mix A which contains more superplasticizer. The final design of Mix A and Mix B (shown in bold) have a bulk yield stress of 8.5 N/mm^2 and 4 N/mm^2, respectively.

Table 3.7: Results ram extrusion tests

	VMA/b	SP/b	σ_0,	α	m	τ_0	β	n	
	%	%	kPa	-	-	kPa	-	-	
BCS250	0.30	0.40	1.14	4.07	0.60	0.15	0.10	0.45	
	0.45	0.40	3.54	16.40	0.33	1.06	1.00	0.56	
	0.60	**0.40**	**8.50**	**29.29**	**0.40**	**1.331**	**0.99**	**0.45**	**Mix A**
BCS500	**0.30**	**0.30**	**3.96**	**5.93**	**0.50**	**0.59**	**0.22**	**0.61**	**Mix B**
	0.45	0.30	6.77	10.23	0.41	0.52	0.53	0.50	
	0.60	0.30	7.99	30.95	0.34	2.01	0.171	0.69	

To visualise the fit of the Benbow Bridgwater model on the retrieved data, a 3D image plot of the average measured data and the model fit of Mix A is presented in figure 3.8.

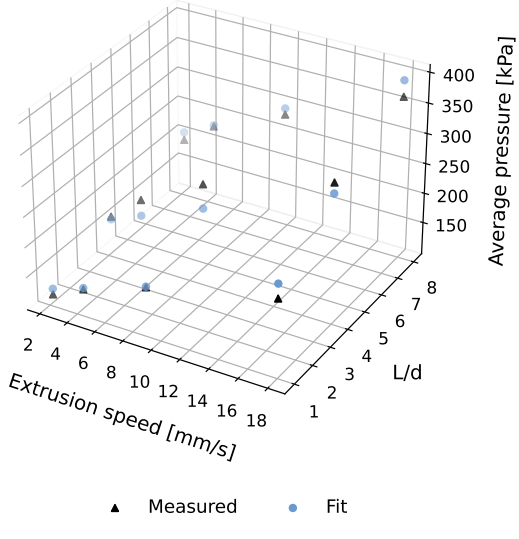

Figure 3.8: Benbow Bridgwater 3D model fit on measured data for Mix A

Images of the test on mix A can be found in figures 3.9 and 3.10. The UUCT measures the compressive strength of the fresh composite at a given time. The average stress strain curve from the three tested specimens, are presented in 3.11a and 3.11b for Mix A and Mix B, respectively. The images and stress strain curves display that the fresh printable SHCC specimens have a different failure mechanism than printable mortars with no, or very small amounts, of fibres [78].

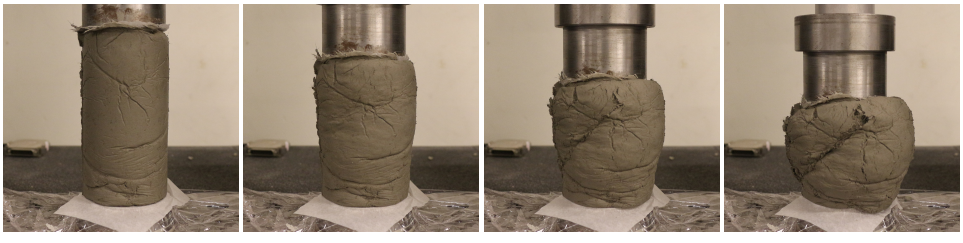

(a) 0% strain (b) 13.7% strain (c) 27.8% strain (d) 42.1% strain

Figure 3.9: Images of UUCT for Mix A (60 minutes) with increasing vertical strain

In this comparison two observations stand out, first one being the higher strain at maximum stress for the printable SHCC specimens. Where the printable mixtures presented in [78] showed maximum stresses from ± 0.2 strain (at age of 5 min) to ± 0.12 strain (at age of 90 min), the 3DP-SHCC mixtures report maximum stresses from ± 0.4 (at age of 5 min) to ± 0.2 strain (at age of 90 min). The second observation that can be made is the difference in failure that occurs for the specimens of 60 and 90 minutes. Where the low fibre content printable mortars display clear failure planes that correspond with failure planes of hydrated concrete under compressional force [94], the SHCC specimens do not show these clear failure planes and the shape of failure is closer to those seen in the younger specimen.

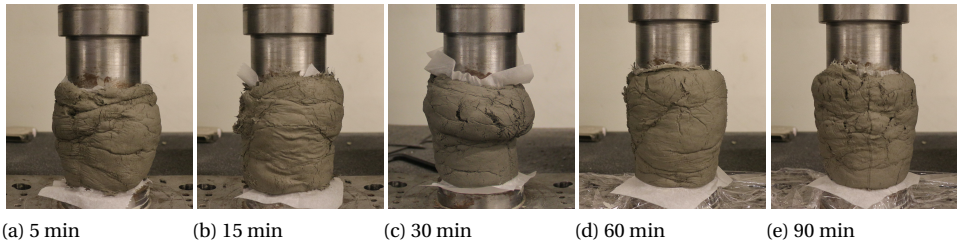

(a) 5 min (b) 15 min (c) 30 min (d) 60 min (e) 90 min

Figure 3.10: Images of UUCT for Mix A of different ages with a constant vertical strain of 27.8%

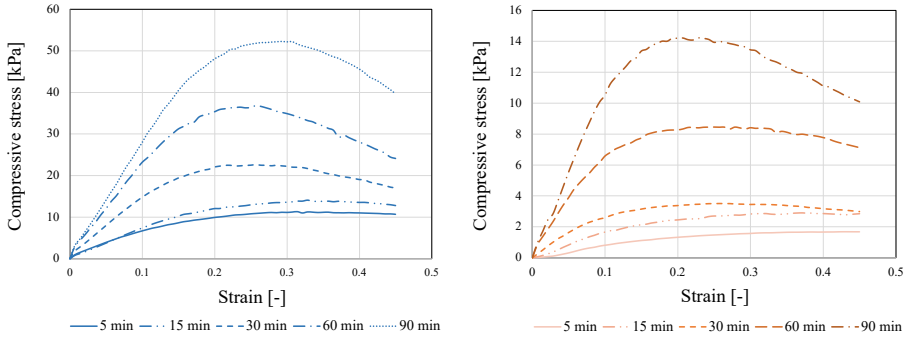

(a) Mix A (b) Mix B

Figure 3.11: Average stress strain curve of the uniaxial unconfined compression test

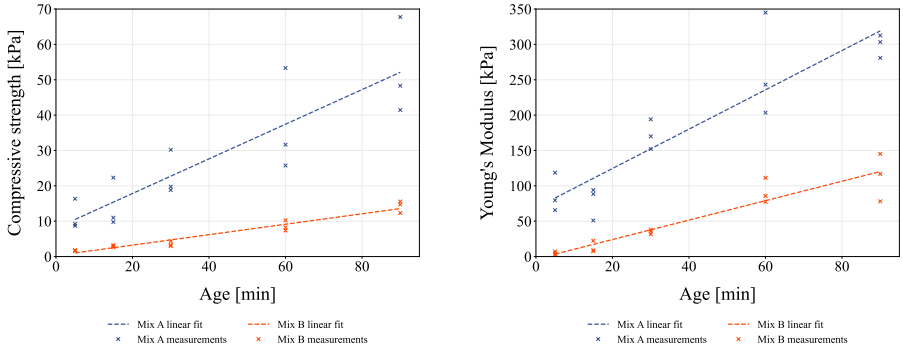

(a) Development of compressive strength over time (b) Development of Young's modulus over time

Figure 3.12: Fresh mechanical property results from uniaxial unconfined compression test

By performing the UUCT at multiple time intervals, the development of the compressive strength over time has been obtained, these are presented in figures 3.12a. By post-processing of the retrieved compressive stress values and their associated strain, the apparent Young's moduli could be determined. The results thereof are depicted in figure 3.12b. Based on the results of the UUCT, the compressive strength and the apparent Young's modulus for both material compositions, a function can be defined for the first hours of the concrete after mixing. For Mix A this leads to equations 3.9 and 3.10. In all equations the parameter t is set in minutes and σ and E are set in kPa.

$$\sigma_c(t) = 0.49 \cdot t + 8.04 \tag{3.9}$$

$$E(t) = 2.89 \cdot t + 66.26 \tag{3.10}$$

The Mix B the development of the compressive strength and apparent Young's modulus over time are represented in equations 3.11 and 3.12.

$$\sigma_c(t) = 0.15 \cdot t + 0.55 \tag{3.11}$$

$$E(t) = 1.26 \cdot t \tag{3.12}$$

A striking result emerges from the trendline subjected to the average apparent Young's modulus values of Mix B, that predicts an initial Young's modulus of approximately zero for t=0.

The compressive strength of Mix A at t=0 was found to be 8.04 kPa, which is almost equivalent to the bulk yield stress that resulted from the ram extrusion test, namely 8.5 kPa. This can not be stated for Mix B, where the compressive strength at t=0 of 0.55 kPa deviates strongly from the 3.96 kPa found in the ram extrusion analysis.

Both mixtures have been successfully printed on the printing facilities of Delft University of Technology. For Mix A, the buildability test showed no failure at maximum height capacity of the printing gantry. The first 10 layers were printed with a consistent material flow and stable layer shape, as can be observed in figure 3.13a. The additional five layers (layers 10-15) show inconsistent and often excessive material flow, resulting in thicker layers consisting of wrinkles. This is most probably caused by the stiffening of the material in the pump reservoir. The maximum height of 210 mm was achieved in 9.5 minutes, which relates to a vertical wall growth velocity of 0.368 mm/s.

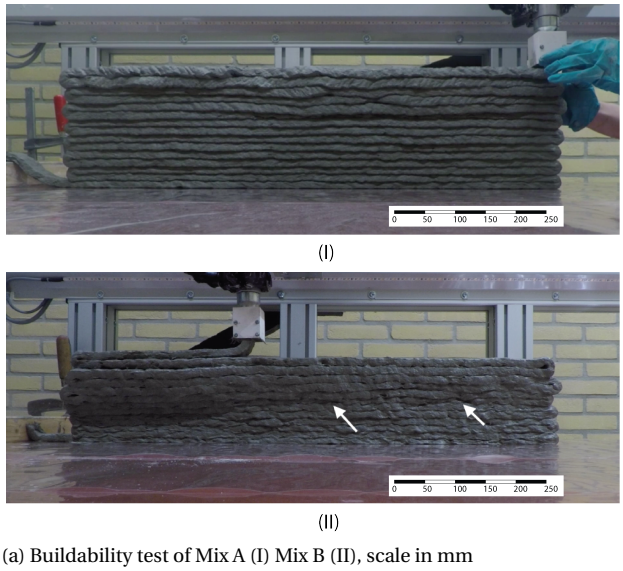

(a) Buildability test of Mix A (I) Mix B (II), scale in mm

(b) Top view Mix B, circles indicate air voids behind fibre agglomerates

Figure 3.13: Images of printing trial

Mix B showed buckling failure at the beginning of the 13th layer after 6 minutes and 10 seconds, which yields to a wall growth velocity of 0.508 mm/s. All layers that were printed had a consistent material flow, nevertheless irregularities in layer shape can be observed in image II of figure 3.13a. This was due to the presence of fibre agglomerates in the printed layers. These fibre agglomerates are the result of the segregation of the material during the pumping phase, as no segregation was observed after the mixing phase. Additionally, the printed layers showed lack of material directly extruded after the location of the fibre agglomerate (in perspective of the moving nozzle). This is visible in the top view image of the printed elements in figure 3.13b.

With the use of the equations 3.4 - 3.8 and the time of failure (T) the minimal yield stress ($\sigma_{c,t=T}$) and elastic stiffness ($E_{t=T}$) at time of failure can be calculated. These values are presented in table 3.8. The table also provides the corresponding yield stress ($\sigma_{c,t=T}$) and elastic stiffness ($E_{t=T}$) values at time of failure in accordance with the equations that were deducted from the strength development curves in figures 3.12a and 3.12b.

Table 3.8: Fresh properties from buildability test and UUCT

	Material age at time of failure T [min.sec]	**Buildability test**		**UUCT**	
		$E_{t=T}$ [kPa]	$\sigma_{c,t=T}$ [kpa]	$E_{t=T}$ [kPa]	$\sigma_{c,t=T}$ [kpa]
Mix A	49.30	≥ 158.5	≥ 4.1	209.3	32.2
Mix B	43.20	103.0	≥ 3.6	54.6	6.8

Cross analysing the data of the UUCT with the calculated mechanical properties at time = T from the buildability test two things stand out. Firstly, the elastic stiffness of Mix B calculated from the buildability test is almost double the value that was found with the UUCT namely, 103.0 and 54.6 respectively. This offset is beyond the standard deviation that was found in the UUCT data. In effect, with the lower value for the Young's modulus determined with the UUCT, the buildability test would have resulted in buckling failure at the 11th layer. This contradicts the findings from the buildability test, where buckling failure occurred at a height of 13 layers. As the buildability test did not result in failure for Mix A, the buildability test only resulted in a minimum elastic stiffness of 158.5 kPa. This is in correspondence with the 209.3 kPa that was found for Mix A in the UUCT, which would have resulted in a maximum building height of 17 layers.

Secondly, the UUCT values for the compressive strength are significantly higher than needed for the achieved height. This has been visually confirmed, as no plastic deformation was observed at the lower layers during execution of the buildability test.

3.5.2. HARDENED PROPERTIES

From the four-point bending test, all specimens showed flexural hardening in orientation v.u. (load perpendicular to the printing bed), as shown in figure 3.14. From the supplied graphs it can be observed that the cast composites out-performed the printed composites in terms of flexural strength and the associated ductility. For the printed specimens the flexural strength was reduced by 22.4% and 16.9% for Mix A and Mix B, respectively, in comparison with cast specimens. The reduction in deflection capacity stands out even more, with a reduction of 63.1% and 42%. All average values of the four point bending test and the relative standard deviation are presented in table 3.9.

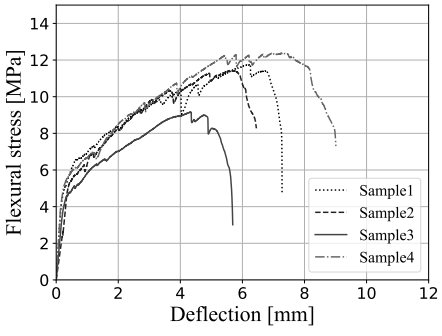

(a) Mix A, cast @ 28 days

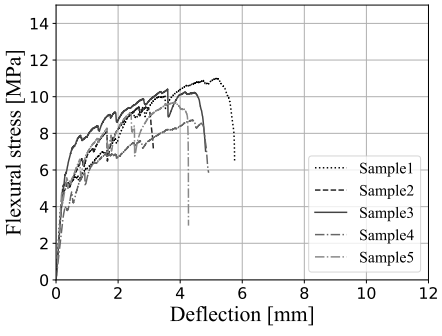

(b) Mix B, cast @ 28 days

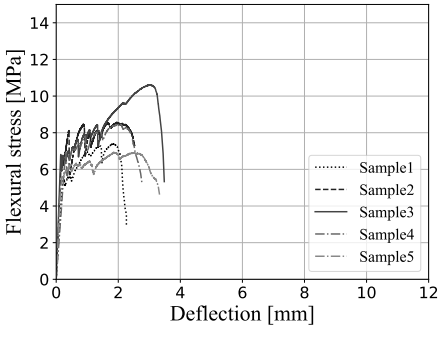

(c) Mix A, printed @ 28 days

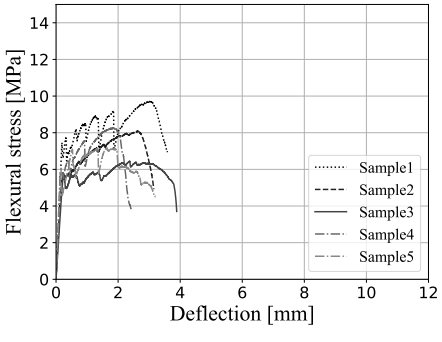

(d) Mix B, printed @ 28 days

Figure 3.14: 4-point bending: Flexural stress - deflection curves

Table 3.9: 4-point bending average values and relative standard deviation

	Mix A			Mix B		
	Cast	Printed	Printed/	Cast	Printed	Printed/
	28 days		Cast	28 days		Cast
Maximum flexural stress [MPa] (RSD)	11.18 (13%)	8.68 (23%)	-22.4%	9.56 (9%)	7.94 (15%)	-16.9%
Displacement at max. stress [mm] (RSD)	5.8 (19%)	2.14 (23%)	-63.1%	3.93 (24%)	2.28 (26%)	-42.0%

The results from the compression test are presented in figure 3.15. From the 28 days test results it can be concluded that Mix B has a a 10% higher compressive strength than Mix A. This result was expected as Mix B contains more sand. Additionally, the orientation of the specimen did not significantly influence the compressive strength. For the two tested orientations the differences are small and seem to fall within the error margin. However, when looking at the compressive strength development over time, as shown in figures 3.15a and 3.15b, it can be concluded that the

compressive strength values of orientation v are systematically higher than orientation w. This holds for both Mix A and Mix B.

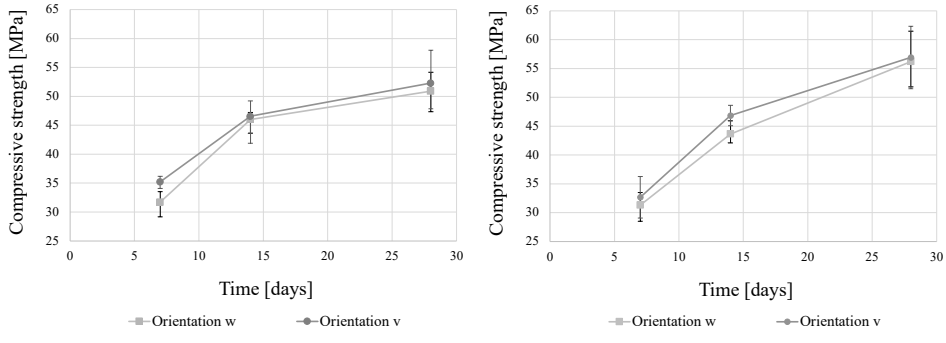

(a) Mix A (b) Mix B

Figure 3.15: Compressive strength development over time

In figure 3.16 the tensile stress-strain curves of the uniaxial tensile tests, performed in orientation **u**, are plotted. What stands out from figure 3.16a is the high scatter in results from Mix A, where only two specimens show strain hardening behaviour up to a strain of 1,5%. In test results of Mix B, presented in figure 3.16b illustrates that none of the specimens show strain hardening. This was to be expected after the formation of the fibre agglomerates during the printing procedure.

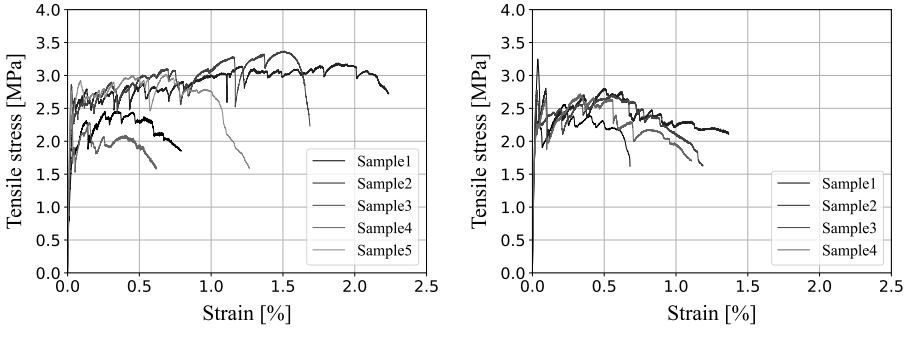

(a) Mix A (b) Mix B

Figure 3.16: Stress strain diagram uniaxial tensile tests of a) Mix A and b) Mix B

After specimen failure, the fracture surfaces of the specimens were inspected and it was found that a majority of those fracture surfaces contained big entrapped air voids. An image of one of these fracture surfaces and corresponding failure crack is presented in figure 3.17. These entrapped air voids were found, in various amounts, in all tested specimens of Mix B and in the specimens of Mix A, except for specimens 2, 3 and 5. It is therefore plausible that these initial flaws are responsible for the lack of (Mix B) or variety in (Mix A) strain hardening response of the printed specimens.

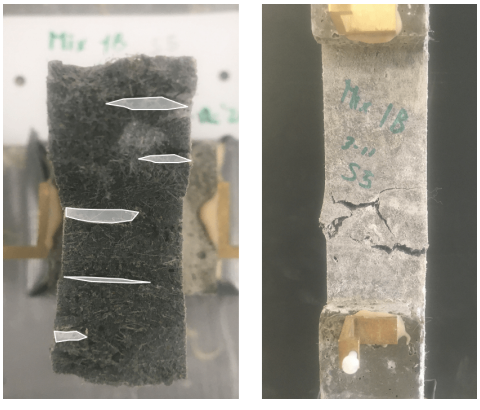

Figure 3.17: Entrapped air voids visible on fracture surface of uniaxial tensile test specimen 3, Mix B

3.5.3. MATERIAL PROPERTIES

Results of the air void content and distribution of the 20 mm diameter specimens are shown in figures 3.18a and 3.18c. In these figures, the interlayer between the second and third layer is indicated with a black dashed line. From the porosity curves one main aspects stand out, being the high variation of the air void content over the specimen height, for both mixtures, even though the average air content of composite A and composite B is similar, namely 5% and 6% respectively. For Mix A, the air void content across the layer height varies between 3.5 and 9.8%. Mix B shows an even stronger variation, between 2.2 and 14.8%. In figures 3.18b and 3.18d the average pore diameter over height is presented for Mix A and Mix B, respectively. From these results, no clear relation was found between the average pore diameter and the presence of the interlayer. Figure 3.18d does present a higher average pore size in the centre of the analysed layers two and three. This, on the first hand, doesn't correspond with the low air void content measured on that height. A possible explanation is that there is one big entrained air void and just a few smaller air voids, which leads to an increase of the average pore diameter but doesn't necessarily result in higher overall porosity.

The presence of big entrapped air voids has also been confirmed by the images retrieved from the CT scan of the 40 mm diameter specimens. A set of these images has been selected to illustrate these imperfections and can be found in figure 3.19. On the cross sectional images zones of poor homogeneity can be observed for Mix B. The areas as marked in figure 3.20b and 3.20c are of a lighter grey, indicating a denser material. Furthermore, they possess very thin and narrow air voids and are often surrounded by big entrapped air voids. When we take into consideration the observed fibre agglomerates during the printing session of Mix B and the air voids that subsequently followed these fibre agglomerates in the printed filament, as was shown in figure 3.13b, it is likely to assume that these fibre agglomerates are present in the composite. Furthermore, it can be stated that this segregation during printing has led to significant imperfections that resulted in an inhomogeneous and non strain hardening material.

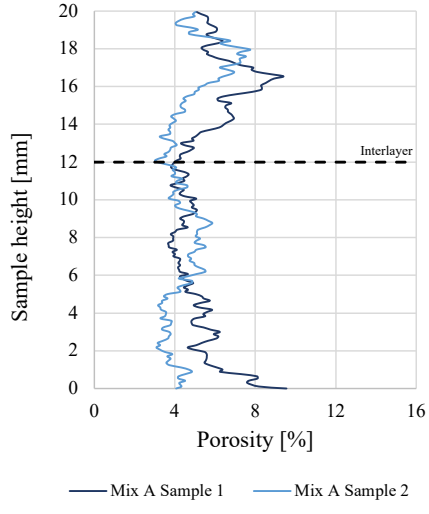

(a) Porosity over height, Mix A

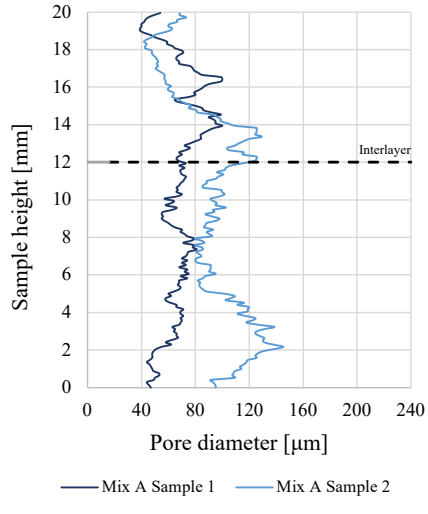

(b) Average pore size over height, Mix A

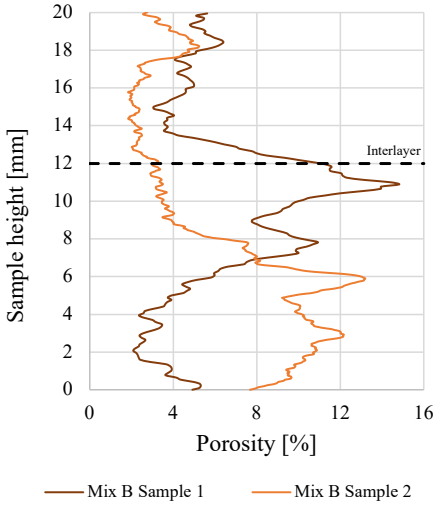

(c) Porosity over height, Mix B

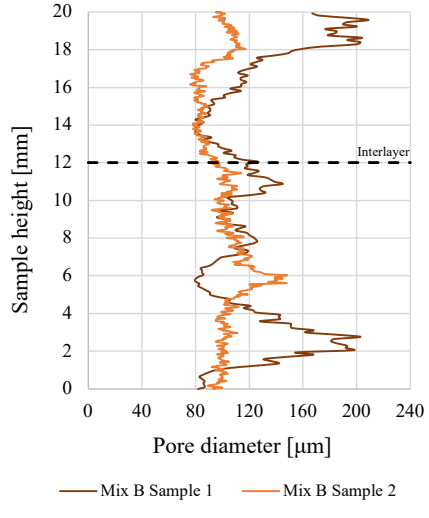

(d) Average pore size over height, Mix B

Figure 3.18: Air void analysis

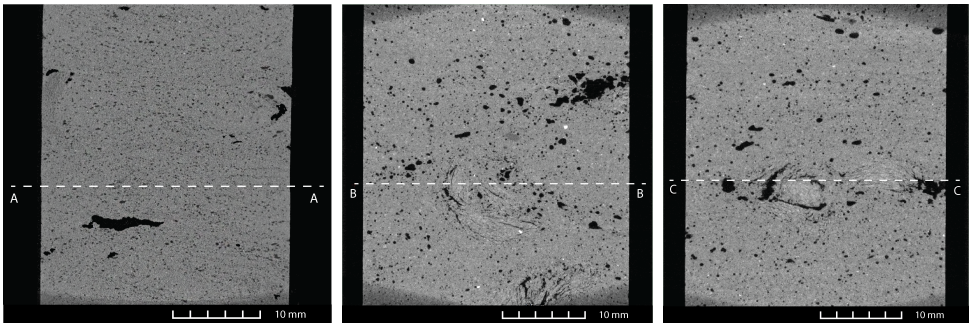

(a) Mix A, specimen 1 (b) Mix B, specimen 1 (c) Mix B, specimen 2

Figure 3.19: CT scan images

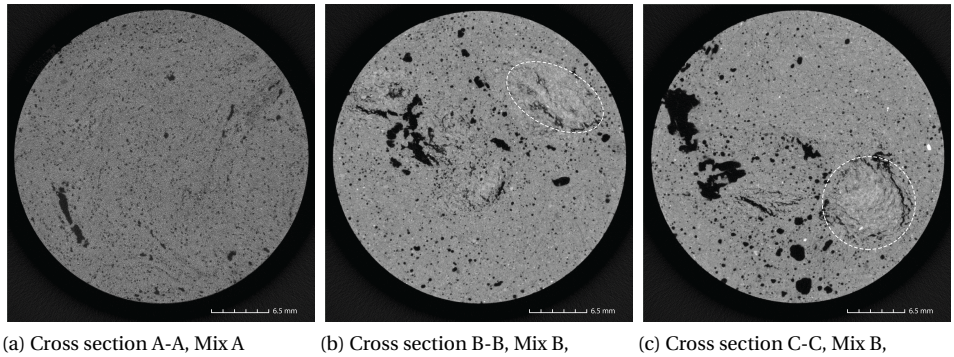

(a) Cross section A-A, Mix A (b) Cross section B-B, Mix B, circle indicates a fibre agglomerate (c) Cross section C-C, Mix B, circle indicates a fibre agglomerate

Figure 3.20: Cross sectional images

3.6. DISCUSSION

The partial objective of the conducted research was to achieve a printable mixture that met all four requirements for printability, namely: **Pumpability**, **Extrudability**, **Buildability** and **Open time**, by optimising the PSD.

Overall it can be stated that Mix A performed well in regards to extrudability, buildability and open time, but underperformed in terms of pumpability, due to the stiffening of the material in the pump reservoir. The same observation can be made for Mix B, only here the pumpability was poor due to material segregation. This segregation was an unexpected outcome of the printing trial, especially because a smooth and stable fresh 3DP-SHCC was achieved after mixing. The segregation resulted in the formation of fibre agglomerates that led to inconsistent material flow and contributed to the weak strain hardening behaviour in the hardened state. There are two possible causes for this segregation. On the one hand, it is possible that the segregation is caused by the high pressure cavity pump, where the geometry of the transport screw (in the material reservoir) and that of the rotor/stator in the pump may lead to formation of fibre agglomerates. The pump configuration used in this research is presented in figure 3.21.

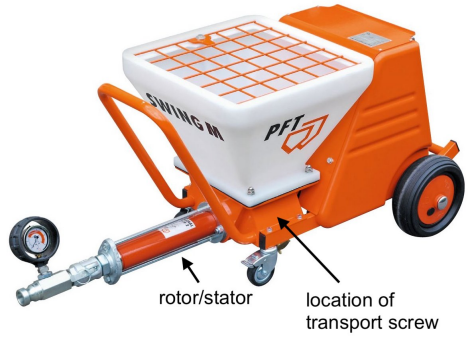

(a) PFT pump, TU Delft

(b) Rotor/stator

(c) Transport screw

Figure 3.21: Printing pump and its specific components

On the other hand, the challenge may lie in the material design, since Mix A remained much more stable during the pumping process than Mix B. To the best of author's knowledge, no literature on the topic of 3DP-SHCC has discussed segregation during the pumping process. Therewith it should be noted that the use of a high pressure cavity pump for the application of 3DP-SHCC is not yet widely investigated.

Another interesting observation was the presence of air voids within the extruded layer. These big air voids were not observed during the printing trial but were revealed after analysing the fracture planes of the tensile test specimens.

This phenomenon was also observed by Figueiredo et al [151], after conducting a printing trial on another type of 3DP-SHCC with the PFT Swing M pump. The hypothesis of Figueiredo et al. that states that the design of the transport screw causes these air voids to be entrained into the material, is in line with the findings of this research. Therewith, it should be emphasised that the pump geometry is of great importance when 3PD-SHCC is used for printing applications.

The segregation and entrapment of air voids are the two main reasons for the lack of (consistent) strain hardening results of Mix A and Mix B. For Mix A, the specimens with no or limited amount of entrapped air voids were able to achieve strain hardening behaviour under tensile loading. Mix B, that besides the entrapped air voids, also contained fibre agglomerates due to segregation, showed no strain hardening behaviour under tensile loading.

Relating the strain hardening performance under tensile loading to other research conducted

on the development of SHCC for 3D printing as drawn up by Li et al [152], we see that Mix A and Mix B underperform. However, it should be noted that the results presented by Li, are mostly based on specimens printed with the use of caulk guns or Archimedes screw pumps. Comparing Mix A with the two other PVA reinforced composites that have been printed with the use of a high pressure cavity pump [10, 15], the strain capacity under tensile loading has improved. Where Figueiredo et al. reported an average strain at maximum tensile stress of 0.26% and 0.15%, the results of Mix A demonstrate an average deformation of 0.91%. Mix B, with an average deformation at maximum tensile stress of 0.13%„ clearly demonstrates a weak strain hardening performance.

In regard to the experimental program, an interesting outcome resulted from the cross correlation of the UUCT and the buildability test. In the buildability test of Mix B, it was indeed found that the wall failed due to elastic buckling, as was predicted by the Suiker model [76] on the bases of the UUCT data. However, the wall clearly outperformed the expected printing height, based on the same UUCT data. This finding was unexpected and suggests that UUCT, whom were performed on only mixed and not printed fresh specimens, underestimates the development of the Young's modulus of the printed material over time. This result may be explained by the fact that only the time is considered when estimating the building height, but the additional effects due to printing, such as the adding of energy and the entrainment of air, are not. Furthermore, the experimental program used the initial 4-point bending tests to select the two mix designs with the highest potential for strain hardening behaviour. In this selection procedure, the influence of the fresh properties and the effect on the fibre dispersion, was not considered. In this phase of the mix designs, the mixtures contained no VMA and all six mixes showed low viscosity and were easy to cast. Therefore, it is assumed that the influence of the fresh properties on the 4-point bending test results are minimal.

3.7. CONCLUSIONS

The present study was designed to determine the effect of optimal particle size distribution on the buildability of 3D printable strain hardening cementitious composites.

- The optimisation of the particle size distribution can indeed contribute to the buildability performance of 3DP-SHCC. Both Mix A and Mix B have sufficiently high initial compressive yield stress σ_0 and therewith showed no plastic failure during buildability tests.
- The Young's modulus has shown to be the critical fresh mechanical parameter for both Mix A and Mix B. For Mix B, this was found during the buildability test where the wall failed due to elastic buckling and this was supported by the Suiker Model based on the UUCT data. For Mix A no failure occurred during the buildability test, but here also the Suiker model indicated the Young's modulus to be the critical fresh property.
- From the research it can be stated that Mix A has potential for the practical application of 3D printing. The mixture showed good stability during pumping phase and tested specimens without entrained air voids showed tensile strain capacity up to 1.85%.
- The strain hardening capacity of the printed elements was compromised by the air voids entrapped during the pumping phase.
- 3DP-SHCC is sensitive to dynamic segregation in the pumping phase, yielding the formation of fibre agglomerates, resulting in inconsistent fibre distribution throughout the specimens, and limiting the strain hardening capacity.
- The pump geometry has proven to be a crucial element in the printing process of 3DP-SHCC. Further research on the influence of the pump geometry on the segregation of 3DP-SHCC is an essential next step in the development of SHCC for 3D printing applications.

4

TAILORING OF THE PUMPING SYSTEM FOR 3DP-SHCC

The interaction between pumping systems and printing materials is crucial in extrusion-based 3DCP. Pump-induced material segregation and temperature fluctuations can result in blockages and altered material and mechanical properties. Introducing 3DP-SHCC adds complexity due to increased yield stress and viscosity from fibre incorporation. Additionally, traditional SHCC is known to be sensitive to segregation and the formation of fibre agglomerates, affecting both fresh and hardened state properties. This chapter presents a study to optimise the printing systems for 3D printing SHCC (3DP-SHCC), where specific pump types and components are assessed for pumpability and material stability. The study reveals that the choice of pumping system significantly influences both the flow rate, air void content, and material stability of 3DP-SHCC. Progressive cavity pumps emerge as the most suitable option, providing customisable components that can be selected/designed in compliance with the specific material properties of 3DP-SHCC.

4.1. INTRODUCTION

In extrusion-based 3DCP, the interaction between the pumping system and the designated printing material plays a crucial role in achieving the required printability and mechanical properties. It has generally been found that the pumping system can cause material segregation that can lead to blockage of the printing system [33], and temperature increases which can affect the final material properties [151, 153]. Deploying strain hardening cementitious composites (SHCC) as a printing material introduces a new set of complexities. The incorporation of fibres into a cementitious paste increases both the yield stress and the plastic viscosity [103, 154]. This addition of fibres to a 3D printable mortar results in a substance exhibiting a dough-like consistency characterised by relatively high viscosity [10]. Consequently, these materials can be prone to entrapped air voids introduced by transport screws [151]. Additionally, they demand a higher input of pumping energy to facilitate flow, which can lead to temperature elevation within the pumping system and, consequently, within the material being pumped. From the literature on "plain" SHCC it is known that the material is sensitive to segregation and the formation of fibre agglomerates. Both these phenomena can affect the fresh and hardened state properties of SHCC. Improper dispersion of the fibres can negatively impact the flow characteristics of fresh concrete, and poorly dispersed fibres in the hardened state can severely limit the otherwise beneficial effects of fibres [155].

Mix B, as presented in chapter 3, shows several of these issues, namely, fibre agglomerates and entrapped air voids. In a research project of the Delft University of Technology (TUD) together with Eindhoven University of Technology (TUe) (available in appendix A) it was shown that these imperfections are not solely caused by the material design; strong differences were found in the mechanical properties of the same material when printed on two different printing systems. It was proposed that the deviations were a result of both the difference in the mixing routine and the pumping system.

Herein, the optimisation of the pumping system for 3D printing SHCC is presented. It will review the effects of several pump types and specific pump components on pumpability and material stability.

4.2. BACKGROUND

Following the development of Mix A and the successful initial print at TUD, as has been described in chapter 3, it was decided to carry out a printing trial at the large-scale printing facility of the TUe [156]. This gantry system printing system is able to print volumes up to [9 x 4.5 x 2.8] m^3. Additional specifications on the printing facilities can be found in Appendix A.

Before proceeding with the main study of this chapter, challenges encountered during this printing trial are briefly discussed. In the first attempt, a M-tec P-20-connect progressive cavity pump was utilised, equipped with a D4-1/2 rotor-stator and a transport screw TS_1 (see figures 4.5, and 4.7). A start was made with the printing of a 12-layer high 800 mm long beam. However, after completing just 5.5 layers, the system became blocked, no more material was extruded from the nozzle, and the filament broke, as indicated as (a) in figure 4.1. Prior to the complete blockage,

Figure 4.1: Filament breakage indicated with (a) and printing irregularities (b & c) during printing at TUe

the beam had already exhibited irregularities related to inconsistent material flow, such as reduced beam length and narrow filament, indicated as (b) and (c), respectively, in figure 4.1. At the end of the printing trial, the hose came loose from the nozzle-hose connection, as can be seen in figure 4.2b. While disassembling the complete printing system, it was discovered that multiple fibre agglomerates had accumulated within the connection linking the rotational nozzle and the hose. Specifically, the fibre agglomerates were situated in front of a perforated pipe. The grid-shaped openings in the pipe were intended to facilitate material flow during nozzle rotation. The full nozzle hose connection including the gridded pipe is presented in figures 4.2a - 4.2c. To reduce the accumulation of fibres the connection was altered to improve material flow. The revised design of this nozzle connecting pipe is presented in figure 4.2d.

4.3. RESEARCH METHODOLOGY

The research was structured into three distinct lines of inquiry. The first section involves a comprehensive review of five pumps, followed by an evaluation of the transport screws in the second section. Finally, the third section focuses on testing various rotor-stators. This research follows a 'select and continue' methodology, meaning that each section will present its own sub-conclusion, and the subsequent section will build upon the decisions made in the previous part.

Throughout all phases of this research, Mix A and the mixing routine described in chapter 3 were used. All pump tests were conducted with a pump setting of 120 RPM, this value holds for both the transport screw and the rotor-stator.

4.3.1. PUMP TYPES

For the assessment of the pump types, three progressive cavity (PC) pumps, one peristaltic pump, and an automated caulk gun were evaluated, as presented in figure 4.3. The specifics of each pump are presented in table 4.1. These pumps were assessed on four points: ability to efficiently pump the material, achieve an adequate material flow, material stability during pumping, and their overall ease of use.

Type	Flow	Motor			Conveying	
	[l/min]	[kW]	[V]	[Hz]	d [m]	h [m]
Makita DCG140	0-28*	-	14.4	-	-	-
Verderflex Dura 25	0-20	1.5	230	50	-	-
PFT Swing M	1-9	1.5	230	50	20	-
M-tec P-20-connect	3-24	4	400	50	40	20
M-tec duo-mix-connect	2-22	5.5	400	50	60	30
* unity [mm/s]						

Table 4.1: Specifications of the assessed pump types

AUTOMATED CAULK GUN

The automated caulkgun (Makita DCG140) with a volume capacity of 0.75 litres was coupled to ABB robot arm (IRB 1200-5/0.9) to establish an automated printing process, as shown in figure 4.3a. The caulk gun consisted of a bespoke nozzle, a cylindric material reservoir, and an automated piston that pushes the material through the reservoir and nozzle. The material is carefully fed into the canister and compacted with a bespoke rod to eliminate the entrapment of air.

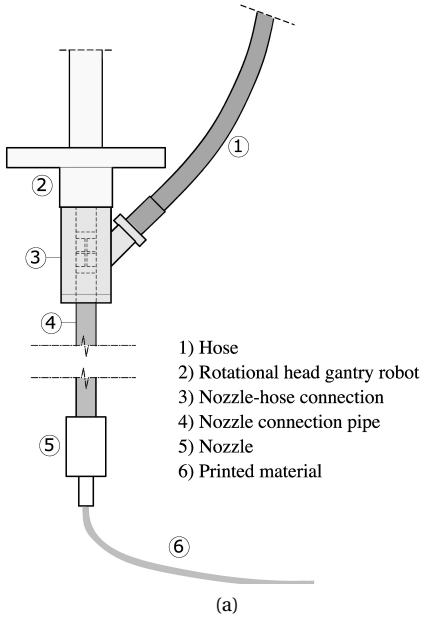

(a)

(b)

(c)

(d)

Figure 4.2: Adjustments to nozzle connection pipe: a) Overview of nozzle-hose connection b) Loose hose at the location where blockage occurred c) Original perforated nozzle connection pipe d) New nozzle connection pipe

(a) (b) (c) (d) (e)

Figure 4.3: Assessed pump types a) Makita DCG 140 b) Peristaltic pump [157] c) PFT Swing M [158] d) M-tec P20-connect [159] e) M-tec duo-mix-connect [159]

PERISTALTIC PUMP

The peristaltic pump (Figure 4.3b) is also called a flexible tube pump. In this pump type, a rubber flexible tube is located inside a circular housing. The material is pushed through the hose by rollers that are attached to the rotor, these rollers squeeze the tube as it passes, creating a vacuum that draws fluid through the tube. The pump gets its name from the human process of swallowing (peristalsis), as the method of advancing a fluid is similar. Peristaltic pumps do not have a built-in material reservoir, the material is drawn from an external reservoir, such as a mixing bowl or plastic container. For this research, a Verderflex Dura 25 peristaltic pump was used.

PROGRESSIVE CAVITY PUMP

Three progressive cavity (PC) pumps were tested, the PFT Swing M pump, the M-tec duo-mix-connect and the M-tec P20-connect, as can be viewed in 4.3. These PC pumps differ in terms of size, material transport orientation (vertical or horizontal), and equipment (transport screws and rotor-stators)

The principle behind a progressive cavity pump is that a helical rotor (stainless steel) turns inside a helical stator (elastomeric material). The cavities progress along the stator while the rotor turns, moving a constant volume of material through the pump. The principle is further visualised in figure 4.4.

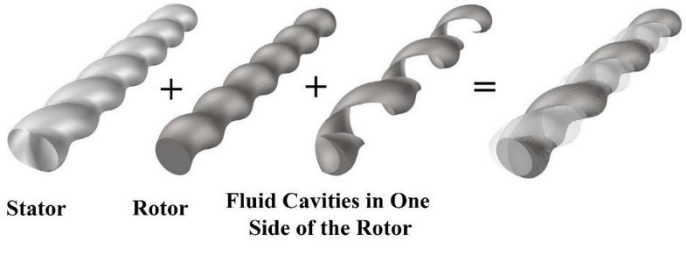

Figure 4.4: 3D configuration of pump rotor, stator and fluid cavities in one side of the rotor [160]

The duo-mix-connect is unique among this group of PC pumps. The pump is designed not only to pump material but also to efficiently mix a dry mix with water. Therefore, the dry mix can be fed into a large reservoir, and the pump is connected to a water source. After mixing, the material is transferred to a small reservoir that is connected to the PC pump.

In this study, SHCC was premixed in the same manner as for the other pumps. The fresh composite was then fed into the small reservoir with a transport screw that is connected to the rotor-stator. This method has been successfully deployed for the 3D printing of SHCC by Figueiredo et al.[15, 151].

PUMP TYPE: RESULTS

The assessment of the pumping trials will be shortly discussed per pump. An overview of the findings can be found in table 4.2.

Caulk gun

The automated caulk gun was effective in printing the material with a relatively low printing speed of 10 mm/s. The extruded layers maintained a consistent shape; however, there was inadequate alignment between consecutively printed layers. Throughout the printing process with the Makita extruder, the cylindrical reservoir required frequent refilling due to its limited volume capacity of only 0.75 L. This makes the pump impractical for printing sessions. Notably, the refilling procedure was observed to be sensitive to air entrapment, leading to increased void content and porosity.

Peristaltic pump

The peristaltic pump provides relatively low flow and pressure capability in combination with the tested material. There was some material flow, but insufficient for achieving the minimal printing speed required for 3D concrete printing. This observation aligns with the general consensus that peristaltic pumps are more suitable for low-viscosity fluids [161]. Unfortunately, due to the poor pumpability and the inadequate material flow it generated, the pump could not be assessed on the other criteria.

PC pump: FPT Swing M

The printing session using the FPT Swing M proved to be successful. The pump was capable of transporting the material with a sufficient flow rate, allowing for a printing speed of 20 mm/s. The pump is fitted with a 38-litre material reservoir which makes the pump practical for longer printing sessions.

However, it was observed that the material displayed some instability during the pumping process. This resulted in the entrapment of air voids and a slight presence of fibre agglomerates within the printed filaments.

PC pump: M-tec P-20-connect

Effective 3DP-SHCC printing was achieved using the P-20 pump (with revised nozzle connection), attaining a notable printing speed of 25 mm/s. The material proved highly pumpable, ensuring a consistent material flow. The printed material displayed some air pockets and fibre agglomerates.

The advantages of the P-20 include its substantial 100-liter material reservoir, which facilitates more extended printing sessions. However, this also displayed a downside.

It was observed that the material experienced stiffening within the reservoir, resulting in the arching phenomenon, in which the material creates a self-supported dome-like construction above the transport screw. To ensure material flow in the reservoir, the material had to be agitated manually regularly.

PC pump: M-tec duo-mix-connect

Among the three PC pumps, the M-tec duo-mix-connect showed the poorest performance. While the pump managed to transfer the material with sufficient material flow, this flow was highly irregular. This can be attributed to the method used for feeding the material into the small reservoir.

Type	Pumpability	Printing speed	Material stability	Usability
Makita DCG140	xx	x	xx	o
Verderflex Dura 25	o	o	o	o
PFT Swing M	xxx	xx	x	xx
M-tec P-20-connect	xxx	xx	x	xx
M-tec duo-mix-connect	x	xx	x	o

Table 4.2: Specifications of the assessed pump types.
Where xxx = very good xx = good x = sufficient and o = poor or could not be assessed

As the pump is designed to handle dry mixes, the premixed SHCC was fed directly into the small reservoir that contains the transport screw and is directly connected to the rotor/stator. It is worth noting that this procedure is impractical when printing larger elements. Furthermore, this procedure of feeding the material directly into the small reservoir comes with safety risks, as the material is manually fed into an unprotected reservoir in which a transport screw is continuously rotating. Unfortunately, the pump could not be assessed for other criteria due to the inadequate material flow it generated.

PUMP TYPE: CONCLUSION

For the pumping of 3DP-SHCC, the optimal choice is a PC pump due to its ability to handle highly viscous materials while maintaining sufficient material flow. Among the options considered, both the PFT Swing M and the M-tec P-20-connect offer good pumpability, adequate printing speed, and high usability.

However, it is important to acknowledge that both of these pumps exhibited some issues related to the entrapment of air voids and fibre agglomerates. It is expected that these imperfections can vary depending on the specific transport screw and rotor-stator configurations used. In that aspect the M-tec P-20-connect stands out by providing the flexibility to interchange these components, offering the opportunity to make bespoke configurations for specific material designs.

Therefore the subsequent research studies, into the transport screw and rotor-stator, will be assessed in combination with the M-tec P-20-connect.

4.3.2. TRANSPORT SCREW

During the conducted research in the previous section and in chapter 3 the hypothesis arose that the transport screw may be the underlying cause for the entrapped air voids and the formation of fibre agglomerates. When the transports screw rotates through the material and advances the material towards the rotor-stator, the screw blades cut through the material. Due to the high viscosity of printable SHCC, and the slow recovery of the material (as will be discussed more in detail in chapter 8), entrapped air pockets can be introduced during this stage.

This section therefore investigates four transport screw designs, which can be viewed in 4.5.

TS_1 is featured with eight small paddles distributed over its full length. TS_2 is the original transport screw of the P-20 pump. For the design of TS_3 it was chosen to reduce the amount of cutting edges of the transport screw blades and therefore TS_3 was fitted with half-circle round blades. TS_4 is designed as an Archimedes screw, eliminating almost all cutting edges.

The transport screws were tested in combination with the M-Tec P-20-connect and with its original rotor-stator (D4-1/4). The pumped material was assessed on the number of fibre agglomerates. The pumped material was cast directly into three prisms (40x40x160 mm^3) of a styrofoam mould. After the casting, the fresh material was (prism by prism) manually sifted through by hand, taking apart every manually tangible fibre agglomerate (see figure 4.6). These were then counted per filled beam, in which B1 is the first beam that was filled and B3 the last.

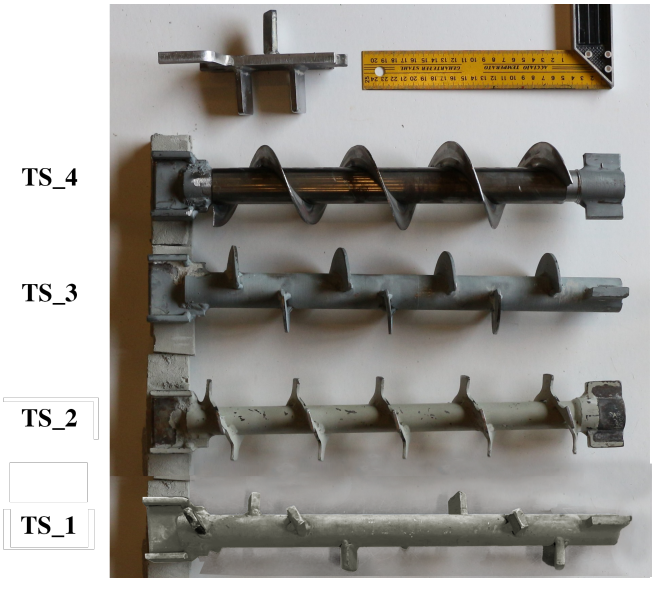

Figure 4.5: Transport screws, in the top left the transport screw of PFT Swing M is presented for reference.

(a) Collection of pumped materials and filling of the moulds

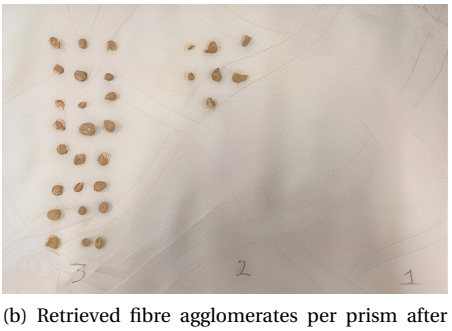

(b) Retrieved fibre agglomerates per prism after material inspection.

Figure 4.6: Transport screw test for fibre agglomerations

TRANSPORT SCREWS: RESULTS

Table 4.3 presents the number of fibre agglomerates per transport screw, clearly illustrating the significant influence of the transport screw on fibre agglomerate formation.

Type	Number of fibre agglomerates		
	Prism 1	Prism 2	Prism 3
TS_1	0	9	31
TS_2	0	7	24
TS_3	0	7	23
TS_4	0	0	2

Table 4.3: Number of fibre agglomerates found per prism, for all reviewed transport screws

Additionally, an interesting trend appears from the data, showing that the number of fibre agglomerates increases from B1 to B3, suggesting that prolonged pumping results in a larger number of fibre agglomerates.

The most favourable performance, characterised by the lowest number of fibre agglomerates, was observed for the Archimedes screw of TS_4, which featured very few cutting edges. Along the cutting edges of transport screws TS_1-TS_3, fibre agglomerates were observed, indicating that these edges accumulate fibres while moving through the material. These observations confirm that the cutting edges of the transport screw contribute to the formation of fibre agglomerates.

Nevertheless, it is worth noting that the design of TS_4 has a drawback. Due to its geometry, the transport screw does not actively agitate the material. This lack of agitation, and therefore reduced energy input, may lead to additional material stiffening in the reservoir, particularly when handling highly viscous materials. Potentially this could lead to the arching phenomena, in which the material forms a dome-like construction above the transport screw, resulting in insufficient material transport to the rotor-stator.

TRANSPORT SCREWS: CONCLUSION

Based on the results in the previous section, TS_4 was selected for the subsequent research into the rotor-stator.

4.3.3. ROTOR-STATOR

Like with transport screws, most PC pumps offer the possibility to exchange the rotor-stators, which are available in numerous models. For this study, four rotor-stators were selected that differ in geometry in terms of pitch length (distance between adjacent threads), helix angle (the angle at which the threads are spiralled in the rotor), and profile (shape of the rotor's threads). In figure 4.7 the selected rotor-stators are presented, and in table 4.4 the specifications of the pumps are listed.

Type	Colour	Flow rate (@ 200 RPM) [l/min]	Max grain size [mm]
D8-2	Dark blue	17	3
D7-2.5	Light blue	12	5
D4-1/2	Grey	4	2
D4-1/4	Black	4	2

Table 4.4: Specifications of the different rotor-stator's as presented in figure 4.7

The rotor-stators underwent evaluation based on two criteria: the formation of fibre agglomerates and material flow. The pumping trials were conducted in combination with the previously selected M-tec P-20 connect and the Archimedes-shaped transport screw, TS_4.

Figure 4.7: The selection of rotors/stators that were assessed, from left to right: D8-2, D7-2.5, D4-1/2, D4-1/4

Two batches of 3.5-litre material were mixed in an A120N Hobart planetary mixer, after which the material was weighed to assess the density. Subsequently, the material was pumped into a bucket for a duration of two minutes. The retrieved volume was also weighed. By dividing this value by the found density, the flow rate of the pump system was determined.

Building upon the findings from the previous section, which indicated that with increasing pump time the formation of fibre agglomerates increased, it was decided to collect the material after these two initial minutes. For this, the same methodology was deployed with the styrofoam mould and beams B1-B3.

ROTOR-STATOR: RESULTS

Table 4.3 presents the results from the rotor-stator assessment. The values obtained for the flow rate show a correlation with the rotor-stator cavity sizes and the maximum material flow as specified in table 4.4. However, this latter does not hold for rotor-stators D4-1/2 and D4-1/4. These two components are specified to have a similar material flow, but in the pumping of the 3DP-SHCC mix design, D4-1/2 pumps more than double the volume of its counterpart. Based on the flow rate, the potential printing speed varies between 8.2 mm/s for the D4-1/4 to 34 mm/s for D8-2.

Cavity pump	Density	Flow rate	Potential printing speed	Fibre agglomerates		
	kg/m^3	m^3/s	mm/s	B1	B2	B3
D8-2	2137.7	0.03814	34	0	0	0
D7-2.5	2137.9	0.03172	28	1	0	1
D4-1/2	2139.3	0.02016	18	1	2	1
D4-1/4	2108.3	0.00921	8.2	2	2	3

Table 4.5: Test results of rotor-stators

Upon reviewing the number of fibre agglomerates, it becomes evident that coarser rotor-stators result in reduced formation of these fibre agglomerates. This may be attributed to alterations in the shear forces introduced by the various rotor-stators. However, this specific aspect has not been explored within the scope of this research.

ROTOR-STATOR: CONCLUSION

The coarsest rotor-stator, D8-2, with the highest flow rate, suitable for printing the composite at ± 34 mm/s, and a minimal number of fibre agglomerates, presents the most promising results.

4.3.4. CONCLUSIONS

The present study was designed to optimise the pumping system for 3DP-SHCC. From the conducted experimental research the following conclusions can be drawn:

- The pumping system has a strong influence on the flow rate and the material stability of 3DP-SHCC.
- Progressive cavity pumps are the most suitable for processing the highly viscous 3DP-SHCC material. The pumps are able to generate a sufficient flow rate to facilitate 3D printing. Furthermore, most progressive cavity pumps allow for the exchange of components, offering the opportunity to make custom-made configurations for specific material designs.
- The transport screw design has a significant effect on the entrapment of air voids and the formation of fibre agglomerates.
- The number of cutting edges present in the blade of a transport screw plays a role in the formation of fibre agglomerates.
- The Archimedes-shaped transport screw (TS_4) displayed the lowest number of fibre agglomerates.
- The design of the rotor-stator has a significant influence on the flow rate of the material. In terms of fibre agglomerates, the rotor-stator displayed a smaller role than the design of the transport screw.

Throughout the rest of the thesis, the custom-made pump configuration was used, which contained the M-tec P20-connect, a D8-2 rotor-stator, and transport screw TS_4.

5

TAILORING FRESH AND HARDENED STATE PROPERTIES OF 3DP-SHCC

This chapter investigates the influence of raw materials and additives, such as silica fume, limestone powder, viscosity modifying agents and water, on the fresh and hardened mechanical properties of printable SHCC, by improving on a previously developed mixture presented in chapter 3. The fresh material mixtures were subjected to slump flow tests to analyse their potential for 3D printing. In hardened state, the mixtures were tested on their compressive strength and flexural strength to assess their potential for strain hardening capacity. Finally, two mixtures were selected for printing. The mixtures were assessed on print quality and buildability by the deployment of a buildability test. Furthermore, the printed elements were mechanically tested at 28 days, on compressive strength, flexural strength and uniaxial tensile strength and strain. It was concluded that the silica fume content and water-to-solid ratio are relevant variables for 3DP-SHCC optimisation. The study has yielded two 3DP-SHCC mix designs that display significant strain hardening capacity and good printability properties.

[1]

[1] The research presented in this chapter has to a large extent been published in A.L. van Overmeir, B. Šavija, F.P. Bos & E. Schlangen, 3D printable strain hardening cementitious composites (3DP-SHCC), tailoring fresh and hardened state properties Construction and Building Materials , 403, 132924 (2023) [148].

5.1. INTRODUCTION

Designing 3DP-SHCC presents a challenge as it must meet both strength and energy criteria to achieve the desired strain hardening capacity, while also satisfying the four printability requirements imposed by the printing process. An experimental study presented by Figueiredo et al. [10, 15] highlighted the complexity of this subject. The study aimed to tailor the rheological properties of a well-performing SHCC mix design [56] to make it applicable for 3D concrete printing, but the developed material was insufficient with regard to the strain hardening capacity and buildability, see figure 5.1a. The study presented in chapter 3 also indicated the difficulty to comply with the imposed criteria. Although some specimens showed clear strain hardening behaviour, the mechanical tests revealed that the composite's matrix was too strong to ensure robust strain hardening capacity. In general, SHCC reinforced with PVA fibres have a compressive strength of approximately 40 MPa after 28 days [9, 56, 152, 162, 163]. The two mix designs developed in chapter 3 resulted in a compressive strength that was 25% higher, with average compressive strengths of 51 and 56 MPa.

Furthermore, the improvement in buildability resulted in a reduction of pumpability and print quality. One of the issues that was found was the arching phenomenon [164, 165] that occurred in the hopper of the pump. From bulk material handling, this phenomenon is known to occur in funnels and hoppers. In the current chapter, the term arching refers here to the spontaneous formation of an arch-like supported mass of bulk material in a reservoir pump during gravitational flow. If a material has a high initial yield stress or presents high thixotropic behaviour, it may not flow down in the reservoir at the moment that the material underneath is transported toward the rotor-stator by the transport screw. Instead, the bulk material will form a self-supported arch, and no material will be transported towards the rotor-stator, resulting in large air voids, under-extrusion, and ultimately source material depletion. Secondly, the print quality was reduced, as a result of over-extrusion. This phenomenon has repeatedly been reported for 3DCP [166, 167] and is mostly observed during the printing of corners and other curved sections. Over-extrusion occurs when the volumetric flow rate of the material is too high for the programmed robot speed. However, here, over-extrusion was observed sporadically during the printing of straight lines, see figure 5.1b. Therefore, it can be concluded that the reduced print quality was due to inconsistent material flow which can result from variations in viscosity due to temperature change or irregular pumping rates due to arching effects.

The current study aims to further optimise the 3D printable mix design that was developed in chapter 3. The research methodology was based on insights obtained from this prior study which highlighted two main issues. Firstly, the high initial yield stress adversely affected the printability of the composite material. Secondly, the dense and strong composite matrix resulted in an overly strong fibre/matrix interface, which led to a reduction in the strain hardening capacity of the composite. Therefore, this research focuses on one hand on the reduction of the initial stiffness of the material to improve pumpability and extrudability. Simultaneously, the research aims to increase the strain hardening capacity by improving the matrix fracture toughness by reducing the fibre/matrix interface bond [6, 56]. A proper fibre/matrix interface bond allows for a bigger critical opening δ_0 [6, 7] and potentially also a higher maximum bridging strength σ_0, therewith increasing the complimentary energy needed for the energy requirement (Equation 2.2).

The research consists of an extensive material survey (Phase 1) which studies the effect of different material adaptions on the mechanical properties in fresh and hardened state. Based on the material survey, two mix designs were selected that had the potential to produce high-quality printed objects and exhibit strain hardening properties. These selected mixes were then subjected to further testing (Phase 2), including the 3D printing of multiple beams and a buildability test, to evaluate their pumpability, extrudability, and buildability. Specimens were extracted from the printed beams and used to determine hardened mechanical properties.

(a)

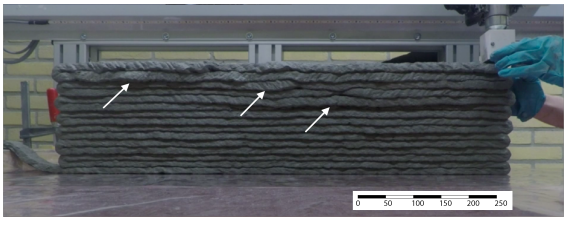

(b)

Figure 5.1: a) Failure due to a combination of plastic collapse and elastic buckling [10] b) Poor print quality due to overprinting (white arrows) as a result of inconsistent material flow [95]

5.2. METHODOLOGY

5.2.1. RESEARCH DESIGN

This research has been conducted in two phases. Phase 1 covers a large experimental program on fresh and hardened state properties, to evaluate mix designs presented in table 5.3. This experimental program consists of a slump flow table test, a compression test, and a 4-point bending test. At the end of Phase 1, two mix designs (later to be renamed as Mix C and Mix D), which showed the highest potential for application in 3D printing, were selected for further investigation in Phase 2.

Phase 2 consists of a cast and printed evaluation of the two selected mix designs. In cast form, the two mix designs were subjected to unconfined uniaxial compression tests (UUCT) test to evaluate the development of fresh state compression strength and Young's modulus over time, and a uniaxial tensile test, to assess the strain hardening capacity in the hardened state. For the assessment of the printed mixtures, a printing session was conducted, that consisted of a buildability test and subsequently the printing of six 5-layered beams. Test specimens were extracted from the beams for the assessment of the compressive strength, the flexural strength and deflection, and the tensile strength and associated strain. An overview of the research design can be found in figure 5.2.

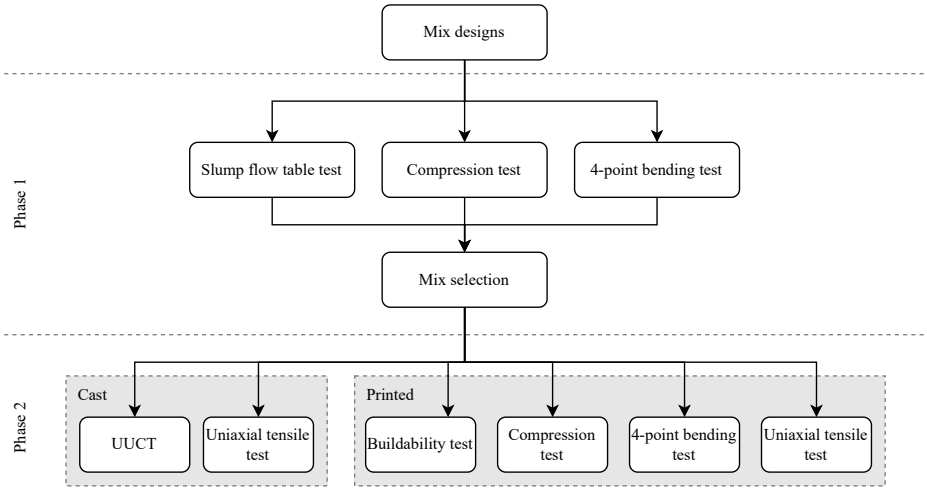

Figure 5.2: Research design flow chart

5

5.2.2. MATERIALS

This research builds upon Mix A, the 3DP-SHCC mix design from chapter 3. The mix was developed with an optimised particle size distribution based on the modified Andreasen and Andersen (A&A) model [141]. Founded on the mechanical and material properties presented in chapter 3, it was concluded that Mix A showed potential as a 3DP-SHCC material, but further development of the mix design was needed to improve its pumpability and strain hardening capacity.

In a first attempt to improve the mix design, Mix A is adjusted on two aspects. Firstly, the VMA to binder ratio was reduced from 0.6% to 0.4% to reduce the high initial yield stress which complicated the pumping phase.

Secondly, the binder to filler ratio (B/F ratio) was adapted, to reduce the matrix compressive strength and improve the strain hardening capacity of the printed elements. This was done by limiting the boundary condition related to the accepted range of B/F ratios within the modified A&A model. After rerunning the optimisation algorithm this second adjustment led to a binder to filler ratio of 0.92 (where Mix A had a f/b of 0.85). When we relate this to B/F ratio to "plain" printable cement mortars, where aggregate/filler volumes fractions of 60% [168] to 75% [169] are reported, the new B/F ratio is rather low. However, the volume fractions of aggregates and fillers in SHCC are generally much lower than fibre reinforced concretes or conventional concrete, to reduce matrix toughness to comply with equation 2.2. Therefore, in this context it is more appropriate to relate this ratio to the B/F ratio of general SHCC found in literature [152] and here indeed that these ratios are well in line.

These two alterations, and the corresponding mixture composition can be found under the name Mix V in table 5.3. As will be shown, these alterations caused a reduction in uniaxial compressive strength and an increase in flexural bending capacity with respect to Mix A. Mix V is therefore chosen as the starting point for this study.

In Phase 1, four mix design variables were analysed, starting with the Blast furnace slag (BFS) / Limestone (LS) ratio. Zhou et al [56] studied the influence of BFS/LS ratio on the tensile strain hardening capacities of SHCC mixtures and showed that, as the limestone powder content increases, the compressive strength is reduced, while the flexural deflection capacity and the tensile

strain capacity first increase and then decrease.

Secondly, the effect of the silica fume to Portland cement ratio was studied. Silica fume, due to its very small particle size and spherical shape, has a strong influence on the fresh mechanical properties of cement mortars. Ferraris et al. [170] reported that the use of silica fume strongly increases the viscosity of fresh cement mortar. Geng et al. [171] and Liu et al. [172] investigated the effect of silica fume (SF) in 3D printing mortars and found that the initial yield stress and thixotropy of the mortars increased with increasing silica fume content. In terms of hardened properties, silica fume improves the particle packing of the mortar which leads to a denser material with a higher compressive strength [173, 174]. Researchers also studied the use of silica fume in the context of SHCC. Hou et al. [175] found that the increase of silica fume content enhanced the compressive strength of SHCC with PVA fibres. However, excessive amounts of silica fume (>5%) resulted in the loss of tensile strain capacity and an increase in the crack width. The increase in the matrix fracture toughness and alterations in fibre/matrix bond weakened the energy balance of the composite during the cracking phase, which is unfavourable for meeting the energy criterion presented in equation 2.2.

The third variable was the water-to-solid (W/S) ratio, which strongly influences the fresh mechanical properties like static and dynamic yield stress, viscosity and thixotropy. Furthermore, an increase in W/S ratio generally reduces the compressive strength and fracture toughness [175]. Finally, the effect of a reduction in additive content was investigated. Additives, such as viscosity modifying agents (VMA) and super-plasticizers (SP), are often used in SHCC [84] to optimise rheological properties and ensure sufficient fibre dispersion. In 3DCP mortars, additives are used to tailor the fresh mechanical properties to realise good printability and buildability behaviour [79]. In this research, a proportional reduction of VMA and SP was investigated to see whether the amounts of additives could be reduced without affecting the fresh and hardened mechanical properties of the composite. In table 5.1, an overview is given of the variables, the range in which they were tested, and their hypothesised effect on the composite.

Table 5.1: Overview research parameter

Serie	Adjustment	Range	Hypotheses
V	Reducing: BFS / LS ratio	0.7 → 0.35	Similar PSD so it will not significantly affect the rheology, but due to the reduction of binder it is expected that it will reduce compressive strength and improve bending and strain hardening capacity
X	Reducing: SF / CEM I ratio	0.1425 → 0.0575	Reduce static yield strength and compressive strength and improve bending and strain hardening capacity
L	Increasing: Water / solid ratio	0.22 → 0.24	Reduce static yield strength and compressive strength
	Reducing: VMA / binder [%] SP / binder [%]	0.45 → 0.40 0.40 → 0.35	As the VMA and SP are both reduced limited effects on the fresh and hardened state mechanical properties are expected

To limit the number of mix designs and steadily iterate towards a new printable SHCC, this research uses a *"select and continue"* approach where the most promising mix design of one parameter investigation was selected as the base material for the next step of the study. For example, the first parameter variation was the adjustment of the BFS to LS ratio which was investigated in the V series. The best results from this series (including mix V) were shown by mix V_2. Therefore,

mix V_2 was chosen as the starting point for the X-series, in which the SF/CEM ratio was varied. A full overview of the mix iteration can be found in figure 5.3; the mixes indicated in green were selected as the base mix for the future series, the mixes indicated in bold are the materials that were chosen for the elaborate material evaluation in Phase 2. A full overview of the material parameters can be found in table 5.2, and the mix compositions can be found in table 5.3.

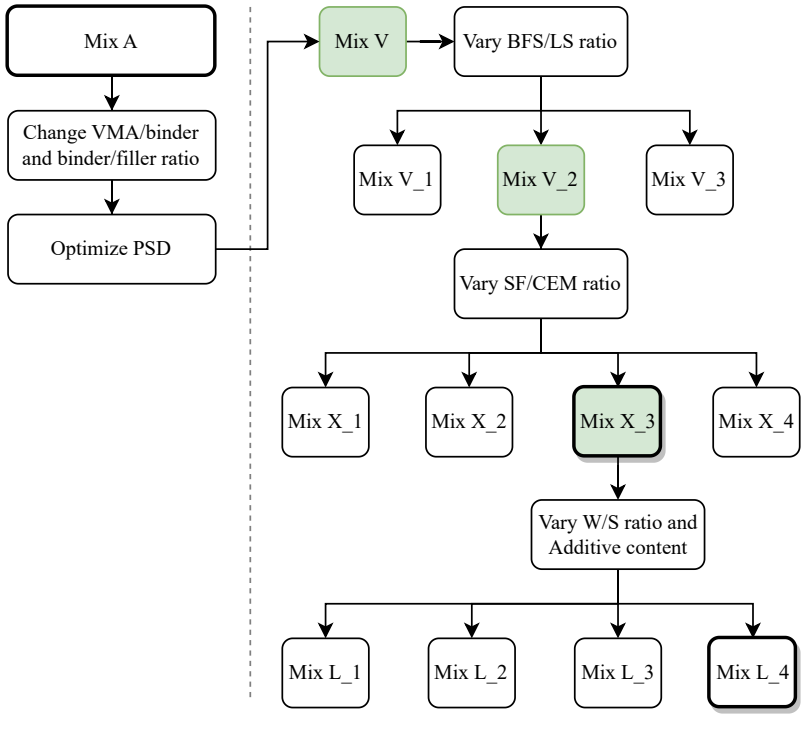

Figure 5.3: Mix design flow chart of Phase 1
Mixes indicated in green were selected as the base mix for the future series, the mixes indicated in bold were chosen for the elaborate material evaluation in Phase 2.

All mixtures were prepared in volumes of 3.5 litre according to the following mixing routine:

- 2 Minutes: Mixing all dry materials, including the fibres, SP and 1/3 of the VMA.
- 1 Minute: Adding of water while mixing.
- 1 Minute: Mixing of wet material.
- Add the remaining 2/3 of the VMA.
- 2 Minutes: Mixing of wet material.

Compared to traditional SHCC, 3DP-SHCC is a very dough-like mixture. Due to the high viscosity of the fresh slurry, it is difficult to disperse the fibres sufficiently when 100% of the VMA is added in the beginning. As sufficient fibre dispersion is essential for a robust performance of SHCC, the mixing procedure prescribes to add the VMA in two phases.

Table 5.2: Parameters, ratios per mix

	BFS/LS	SF/CEM 1	Water/Solid	VMA/ binder	SP/ binder
M A	0.7	0.1425	0.22	0.60%	0.40%
Mix V	0.7	0.1425	0.22	0.45%	0.40%
Mix V_1	0.55	0.1425	0.22	0.45%	0.40%
Mix V_2	0.45	0.1425	0.22	0.4%	0.40%
Mix V_3	0.35	0.1425	0.22	0.45%	0.40%
Mix X_1	0.45	0.13	0.22	0.45%	0.40%
Mix X_2	0.45	0.1	0.22	0.45%	0.40%
Mix X_3	0.45	0.07	0.22	0.45%	0.40%
Mix X_4	0.45	0.0575	0.22	0.45%	0.40%
Mix L_1	0.45	0.07	0.23	0.45%	0.40%
Mix L_2	0.45	0.07	0.24	0.45%	0.40%
Mix L_3	0.45	0.07	0.23	0.40%	0.35%
Mix L_4	0.45	0.07	0.24	0.40%	0.35%

Table 5.3: Material composition [g/dm^3]

	BFS	CEM I 42,5 N	SF	LS	Sand <250 um	Water	PVA vol%	VMA	SP
Mix A	329	506	73	468	298	364	2	5.46	3.65
Mix V	348	470	67	499	318	374	2	3.98	3.54
Mix V_1	300	470	67	546	318	374	2	3.77	3.35
Mix V_2	263	470	67	584	318	374	2	3.6	3.2
Mix V_3	220	470	67	627	318	374	2	3.41	3.03
Mix X_1	263	470	61	584	318	373	2	3.57	3.18
Mix X_2	263	470	47	584	318	370	2	3.51	3.12
Mix X_3	263	470	33	584	318	367	2	3.45	3.06
Mix X_4	264	470	27	583	318	365	2	3.43	3.05
Mix L_1	263	470	33	584	318	384	2	3.45	3.06
Mix L_2	263	470	33	584	318	400	2	3.45	3.06
Mix L_3	263	470	33	584	318	383	2	3.06	2.68
Mix L_4	263	470	33	584	318	400	2	3.06	2.68

The raw materials used in this study are: CEM I 42,5 N, Silica fume (SILMIX®), Blast furnace slag (ECO2CEM), Limestone powder (Inducal 105), River sand (GEBA, D90=0.17 mm), SP (Melflux 2651F), VMA (Tylose MHS). The mixtures were reinforced with RECS15 Poly-vinyl-alcohol fibres (PVA), supplied by Kuraray GmbH. The specifications of these fibres can be found in section 3.3.

5.3. EXPERIMENTS

For all the cast and printed elements that were tested in hardened state, the same curing procedures were applied. Directly after printing the printed elements were covered with foil. After one day of curing the printed and cast elements were moved to the fog room with a temperature of 20 °C with a relative humidity of 97%. One week after casting/printing, the elements were sawn into specimen size, as specified per test, after which they were placed back in the fog room. Finally, the specimens were removed from the fog room one day before testing.

5.3.1. SLUMP FLOW TABLE TEST

For the assessment of the rheological properties the slump flow table test, as specified in EN 1015-3 [176], was utilised. This test makes use of a circular rigid flow table that drops 15 times (without significant friction) over a height of 12.7 mm. The table has a weight of 4.35 kg and a diameter of 255 mm. The material is filled into a smooth cone, that has a height of 60 mm high, a top diameter of 70 mm and a bottom diameter 100 mm. The total volume of the tested material is 351.1 mm3. The full test set-up can be viewed in figure 5.4a.

The test is performed at multiple ages to assess the reduction in workability of the fresh 3DP-SHCC mortar. Specifically, the test was carried out at t = 5, 10, 15, 20, 25 and 30 minutes, where t=0 is the moment of adding of the water during the mixing procedure. During testing, a camera was positioned in top-view as can be seen in figure 5.4b. Subsequently, image analysis was used to accurately determine the mean spread diameter of the material. Due to the very minimal slump that these materials show directly after lifting of the mould, this parameter was not included for analysis within this research.

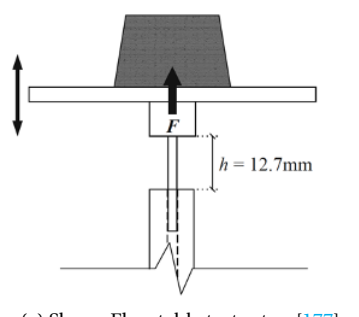

(a) Slump Flow table test setup [177]

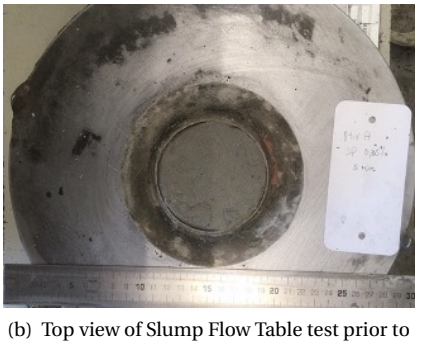

(b) Top view of Slump Flow Table test prior to testing

Figure 5.4: Slump Flow Table test

A variation of this test principle has been utilised by Cho et al. [177] to test fresh mixtures on their applicability for 3D printing. They concluded that mortar is printable when the diameter stays within the range of 130-180 mm. They suggested that materials with a larger diameter after testing will result in insufficient buildability. Stiffer materials with a spread diameter <130 mm are likely to be difficult to pump and to result in reduced printing quality such as filament tearing. It must be noted that Cho et al. conducted their research according to the ASTM C230 guidelines, which has a different cone shape, resulting in a volume reduction of 16.7%. From research conducted by Shamir et al. [178], on a mini-slump flow test, it is known that the changed cone type results in a smaller flow diameter with a correlation factor of 0.917. Additionally, the research conducted by Cho et al. was performed with a mortar without fibres. Due to these two differences in the experimental method, the range as suggested by Cho et al. is herein regarded as an indication only.

The slump flow table test does not directly measure the yield stress of a material, but it gives an indication of the workability which can be related to the yield stress. Therefore, a concrete mixture with a high slump flow value (high spread diameter) is considered to have a low yield stress and vice versa. Additionally, the test does not supply information on the thixotropy of a material; two materials with the same slump flow can result in significantly different building heights. Models to correlate slump tests [179] and slump flow table tests [180] to the static and dynamic yield stress

have been proposed, but will not be regarded in the context of this study.

5.3.2. COMPRESSION TEST AND APPARENT DENSITY

The determination of the compressive strength and apparent density took place 28 days after the casting and the printing of the specimens in accordance with the test methodology described in 3.4.4. The values that are displayed in the result section are the averages of six specimens, for both the cast and the printed specimens.

5.3.3. 4-POINT BENDING TEST

The 4-point bending tests were performed to determine the flexural strength and associated deflection of the cast and printed specimens at an age of 28 days. The experiments were conducted in the same manner as described in section 3.4.3.

In Phase 2, the average flexural toughness (T_f) of the cast and printed specimens was calculated in accordance with the method proposed by Kim et al. [107]. This method is applicable for the deflection hardening behaviour observed in strain hardening cementitious composites and gives an indication on the energy absorption capacity of the mix designs [108, 181].

For materials with deflection hardening the flexural toughness signifies the deformation energy (J) stored within the test volume of the specimen (m^3). The flexural toughness is quantified by the area underneath the load–deflection (Nm) curve [108, 148]. The load was normalised for the standard specimen test volume of (30 x 8 x 120 mm^3 (bxhxl)). The flexural toughness was assessed at two specific points along the load-deflection curve; the limit of proportionality (LOP) and the modulus of rupture (MOR), where MOR is defined as the point where deflection softening initiates subsequent to reaching the maximum load. Effectively, the flexural toughness at LOP ($T_{f,LOP}$) is quantified by the area under the curve up to the LOP point, while $T_{f,MOR}$ represents the energy stored within the material until the moment of rupture occurs. All relative parameters are presented in figure 5.5.

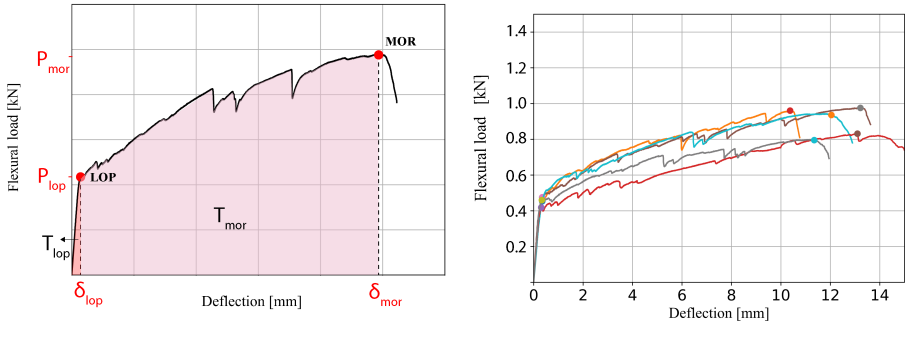

(a) (b)

Figure 5.5: Flexural Toughness a) Theory b) LOP (limit of proportionality) and MOR (modulus of rupture) data points of multiple specimens

5.3.4. UNCONFINED UNIAXIAL COMPRESSION TEST

The Unconfined Uniaxial Compression Test (UUCT) was used to determine the development of the fresh state compression strength and the apparent Young's modulus of the printable mix design. The UUCT is performed on a cylindrical specimen with a diameter of 70 mm and a height

of 140 mm. The specimens are made with the use of a steel mould covered with baking paper on the inside to avoid sticking of the fresh material. The specimen is demoulded one minute prior to testing. The specimen is then placed in a Instron 5967 testing system, where a load cell with a 70 mm diameter loading plate is used to transfer the vertical compressive force onto the specimen. The tests were performed in displacement-controlled mode at a rate of 30 mm/min. The material was tested over the first hour of hydration, with the time intervals: t= 10, 20, 30, 45 and 60 minutes, and a specimen size of three specimens per time interval. Here, t=0 minutes is defined as the time of water addition in the mixing procedure.

During the test, the deformation of the specimen is captured with an optical camera. With the use of National Instruments Vision Builder, the optical data is post-processed and the load-dependent cross-sectional area is obtained. The Unconfined Uniaxial Compression Test is used to measure the initial yield strength and its change over time, by testing the mix designs at various intervals after mixing. The initial apparent Young's modulus (and its development in time) was be calculated based on the compression stress and strain of the elastic part of the stress-strain curve (measured at 5% strain). The two obtained linear trendlines can, together with the buildability model proposed by Suiker [96], be used to predict the achievable building height in a buildability test.

5.3.5. BUILDABILITY TEST

A buildability test was carried out by printing a slender wall in subsequent layers of 800 mm length. During the test, two cameras were orientated towards the front and the side of the wall, to register the layer-by-layer build-up until failure. Failure can occur because of plastic collapse or elastic buckling, but also due to a combination of the two mechanisms [76, 147]. The achieved building heights were compared with the predicted heights retrieved from the UUCT.

For the mechanical tests on the printed material, six beams with a height of five layers and a length of 800 mm were manufactured. For the buildability test and printing of the beams, the gantry system 3D printer of the TU/e with the pump set-up as described in section 4.3.4. The pump was connected to a 5-meter-long hose with a 25.4 mm diameter and a downflow nozzle with a rectangular cross-section of [40 x 14] mm^2. The material was mixed in batches of 3.5 litres with an A200-N Hobart planetary mixer.

Initially, a single layer filament was printed at different speeds and constant pumping pressure, whereby the width of the filaments was measured to select the optimal printing speed. Subsequently, the Buildability test was conducted, followed by the printing of the six 5-layer high beams. Both were printed with a back-and-forth printing routine, as shown in chapter 3, figure 3.3b.

5.3.6. UNIAXIAL TENSILE TEST

The uniaxial tensile tests were carried out 28 days after casting and printing on dog-bone-shaped specimens. For the full description of specimen preparation and test methodology, consult section 3.4.5.

From the findings obtained from the uniaxial tensile tests, the tensile toughness values were quantified by the area underneath the tensile stress–strain curve (N/mm^2). The point where the modulus of rupture is reached within tensile test specimens is often less evident and doesn't always overlap with $\sigma_{t,MAX}$ (as was the case for the flexural specimens). Therefore the definition of $\sigma_{t,MOR}$ was further specified as: The tensile stress at the last crack before strain softening starts to occur, given that $\sigma_{t,MOR} > \sigma_{t,LOP}$.

5.4. RESULTS AND DISCUSSION PHASE 1

5.4.1. SLUMP FLOW TABLE TESTS

The results of the slump flow table tests that are presented in figure 5.6 show the effect of the design parameters on the workability of the different mixes.

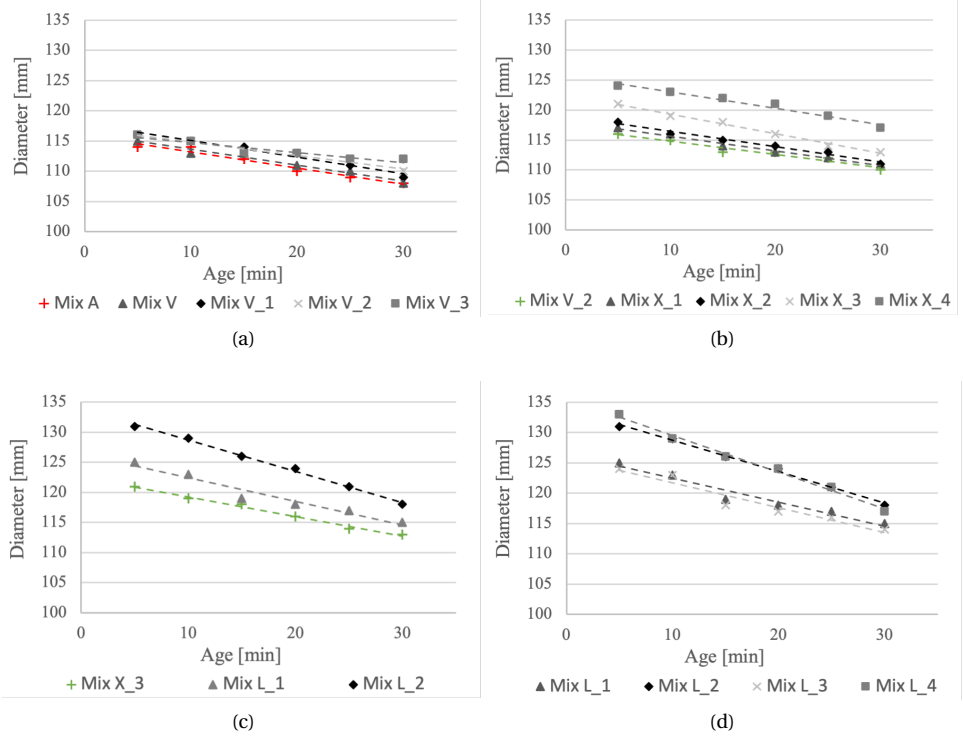

Figure 5.6: Slump flow diameter of a) The V-series, b) X-series c) the L-series (W/S) and d) the L-series (Additive content), the mixes shown in green represent the selected material from the previous series, as indicated in figure 5.3

The results of the V-series, namely Mix V - V_3 (BFS/LS) (figure 5.6a), confirm that adjusting the BFS/LS ratio has a limited effect on the initial flow. All mixtures, when tested directly after mixing (t = 5 min), show a diameter of ± 116 mm, meaning that the diameter of the material increased by only 16% over the course of the 15 drops. The differences between the mixtures become more pronounced when the material becomes older. The mixtures with a high BFS/LS ratio (i.e., higher binder/filler content) show a steeper downward slope over time than those with lower BFS/LS ratios. This can indicate that early hydration products, as a result of the higher binder content, already affect the slump flow diameter within the first half hour. The results of the X-series reveal that the reduction of silica fume to cement content results in an increased slump flow diameter. This suggests a decrease in the initial yield stress of the material, as supported by the literature [92, 93]. In contrast to the V-series, the graphs of the X-series (figure 5.6b) remain parallel to each other, indicating that the change of silica fume content does not affect the rate at which the workability decreases over time. Within the L-series, mixes X_3, L_1, and L_2 show the results of the

increasing water-to-solid ratio from 0.22 to 0.23 and 0.24, respectively. As anticipated, this modification significantly affected the final diameter of the slump flow table test, with an increase of ± 4% per 0.01 increase of W/S ratio (figure 5.6d). Upon examination of the impact of reducing the additive content (VMA and SP) in comparable proportions (i.e., L_1 vs L_3 and L_2 vs L_4), it can be concluded that there is no substantial impact on the material response to the slump flow table test. The variations observed are within the margin of error, as can be observed in figure 5.6c

When the flow diameters are juxtaposed with the recommendations of Cho et al, [177], it is found that only mix designs L_2 and L_4 comply with their requirement of minimal flow conditions in order to achieve good printing quality.

5.4.2. COMPRESSION TEST

The compression test results with their standard deviations are presented in figure 5.7. For comparison, the results of the selected material from the previous series were included in each bar chart.

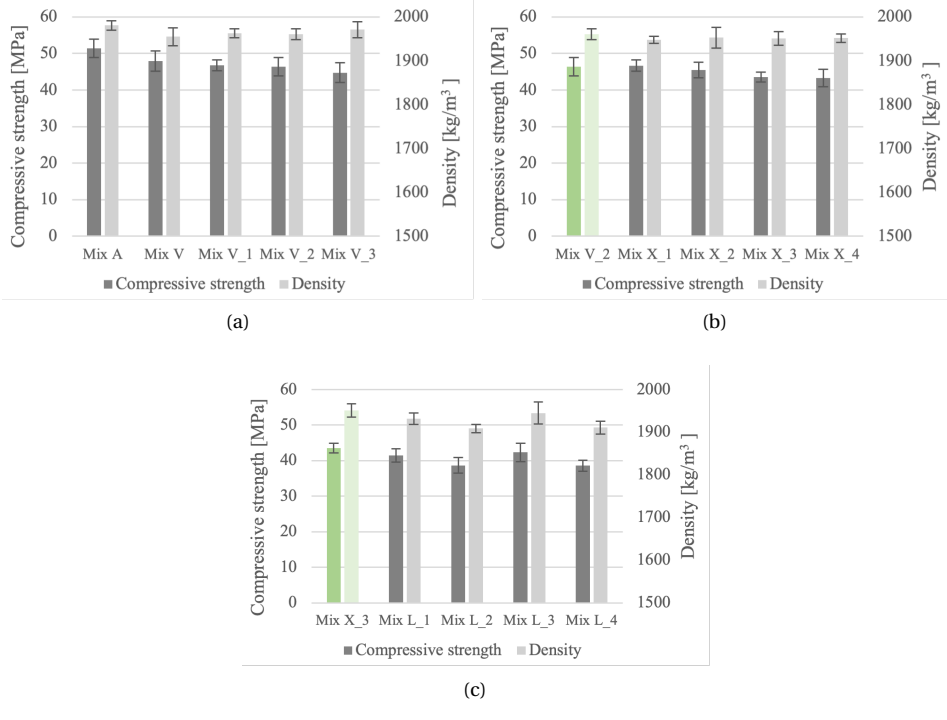

Figure 5.7: Compression strength and apparent density of a) The V-series, b) X-series and c) the L-series, the mixes shown in green represent the selected material from the previous series, as indicated in figure 5.3

All modifications of the initial Mix A resulted in a decrease in compressive strength, except for the mix designs where the VMA and SP were adjusted. For the V-Series, the compressive strength reduced from 47.93 MPa to 44.71 MPa for Mix V and Mix V_3, respectively. In the X series, the compressive strength further decreased, with a compressive strength of 46.7 MPa for mix X_1 containing a 13% silica fume to 43.5MPa when the silica to cement ratio was reduced to 5%. The

largest reduction in compressive strength was achieved through adjustment of the w/s ratio, with a decrease from 44.09 MPa (Mix X_3) to 38.69 MPa (Mix L_4).

5.4.3. 4-POINT BENDING TEST

The results of the 4-point bending test conducted in Phase 1 are presented in table 5.4. All the mix designs exhibited flexural hardening in orientation v.u. Overall, it can be concluded that the modifications made to the mix designs resulted in a reduction of the maximum flexural strength and an increase of the deflection at maximum flexural stress compared to Mix A. Specifically, the reduction in binder-to-filler ratio resulted in a strongly reduced maximum flexural strength from 11.19 MPa to 8.95 MPa, for Mix A and Mix V respectively. At the same time, it significantly improved the deflection capacity from 5.8 mm to 8.42 mm, an increase of 45%.

Table 5.4: 4-point bending average results and standard deviations

	Maximum flexural stress [MPa]			Deflection at max. flexural stress [mm]		
		STD	RSTD [%]		STD	RSTD [%]
Mix A	11.18	± 1.41	12.6	5.80	± 1.13	19.5
Mix V	8.95	± 0.82	9.2	8.42	±1.39	16.5
Mix V_1	8.81	±1.94	22.1	7.72	± 1.29	16.7
Mix V_2	9.11	± 1.37	15.1	8.00	± 1.92	24.0
Mix V_3	8.47	± 1.02	12.0	5.82	± 0.71	12.2
Mix X_1	8.98	± 1.20	13.4	8.87	± 1.07	12.1
Mix X_2	9.57	± 1.38	14.4	7.24	± 1.89	26.1
Mix X_3	10.83	± 1.07	9.9	9.85	± 0.38	3.8
Mix X_4	10.51	± 1.24	11.8	9.61	± 1.29	13.4
Mix L_1	9.53	± 1.03	10.8	9.78	± 1.83	18.7
Mix L_2	8.59	± 0.79	9.2	9.83	± 1.85	18.9
Mix L_3	8.45	± 1.00	11.8	9.71	± 2.25	23.2
Mix L_4	9.02	± 0.81	9.0	11.91	± 1.25	10.5

The results of the V-series show that the adjustment of the BFS/LS ratio has limited influence on the flexural strength of the composites. The flexural strength displayed a minimal reduction from 8.95 MPa to 8.47 MPa for Mix V (BFS/LS = 0.7) and Mix V_3 (BFS/LS = 0.35), respectively. In line with the findings of Zhou et al. [56] the deflection capacity decreased for Mix V_3, the mix design with the highest limestone powder content. Where Mix V-V_2 displayed deflection capacities around 8 mm ± 0.35. Mix V_3 achieved an average deflection of 5.82 mm. The X-series, with reduced silica fume-to-cement ratio, shows a clear improvement in flexural strength and deflection capacity. Mix X_3 and Mix X_4 exhibit similar flexural properties, with a strength of 10.65 ± 0.18 MPa and a deflection capacity of 9.7 ± 0.15 MPa. However, Mix X_3 stands out with low RSTD values of 9.9% and 3.8%, respectively. The decrease in silica fume content likely led to a lower matrix density and weakened the bond between fibres and the matrix. The mechanical properties acquired from the L-series, show that the increase of w/c ratio directly affects the flexural strength of the material, reducing from 10.83 MPa for Mix X_3 (w/c=0.22) to 8.59 MPa for Mix L_2 (w/c=0.24). Interestingly, the results show that the flexural deflection capacity was not affected by the w/c ratio. The highest deflection capacity was found for Mix L_4, with a deflection at maximum stress of 11.91 mm. Overall, when the results of the 4-point bending tests are related to the compressive strength results, it can be concluded that specimens with reduced compressive strength display a higher flexural deflection capacity. It is expected that the theory of Hou et al. [35] applies here.

The theory states that the lower compressive strengths relate to lower matrix fracture toughness, which can improve the energy balance in the crack extension process.

5.5. CONCLUSIONS PHASE 1

The main objective of Phase 1 was to improve the material properties of 3DP-SHCC by adjusting 4 parameters subsequently. From the experimental results the following conclusions can be drawn.

- The BFS/LS ratio adjustment (V-series) has no significant influence on the workability of the fresh material directly after mixing. However, this adjustment in binder/filler ratio does affect the workability over time. As expected, the reduced BFS/LS ratio decreased the compressive strength of the hardened composite. The flexural strength was stable for all mixes the V-series but the deflection capacity significantly reduces for the lowest BFS/LS ratio.
- Reducing the SF/CEM I (X-series) ratio strongly affects all the studied mechanical properties. The slump flow diameter clearly reduced with decreasing SF/CEM I ratio, as did the compressive strength. In the 4-point bending test, a lower SF/CEM I ratio resulted in an increase of flexural deflection capacity and therewith the maximum flexure strength also increased. Thus, this parameter has proven to be very effective for finetuning both fresh and hardened mechanical properties.
- The increase in W/S (L-series) ratio resulted in a reduction of the compressive and flexural strength, however it did not affect the flexural deflection capacity. As expected, the change in W/S ratio did strongly impact the slump flow diameter, with an increase of ± 4% per 0.01 increase of W/S ratio.
- Interestingly, the reduction of the additives (L-series) did influence the mechanical properties of the material. A decrease in compressive strength and a small increase in deflection capacity was found. As expected, the reduction of the VMA and SP in similar proportions did not lead to any significant change in workability.

5.5.1. MATERIAL SELECTION FOR PHASE 2

Based on the research conducted in Phase 1, Mix X_3 and Mix L_4 were selected for further investigation into their fresh and hardened properties. Both mixes show good flexural properties in combination with a compressive strength of ± 40 MPa and improved workability. However, when looking in detail, the differences in the mechanical properties are quite pronounced, which makes it relevant to compare them under printing conditions. Where Mix X_3 displayed a relatively high compressive and flexural strength (43.6 MPa and 10.84 MPa) in combination with a very low associated standard deviation, Mix L_4 performed optimal in the flexural deflection capacity (11.91 mm) but showed lower compressive and flexural strength (38.6 MPa and 9.02 MPa). And even though the two mixtures both display a larger slump flow diameter than Mix A, the difference in diameter between Mix X_3 and Mix L_4 is still significant (10%). In the continuation of this chapter, Mix X_3 will be referred to as Mix C, and Mix L_4 will be referred to as Mix D. An overview of the mechanical test results, including the flexural stress - deflection curves from the 4-point bending test, can be found in figures 5.8-5.10.

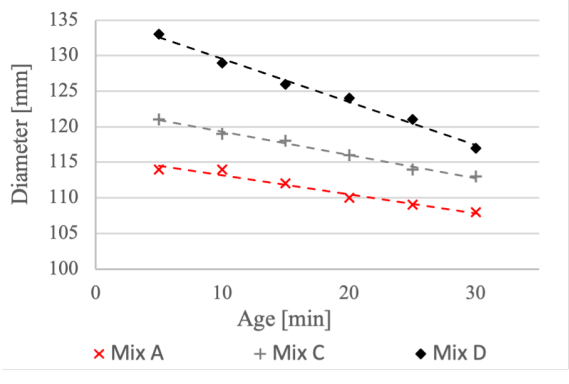

Figure 5.8: Slump flow Diameter of Mix A, C and D

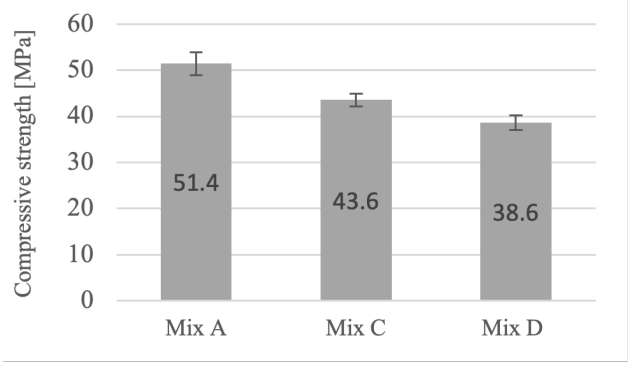

Figure 5.9: Cast compressive strength of Mix A, C and D

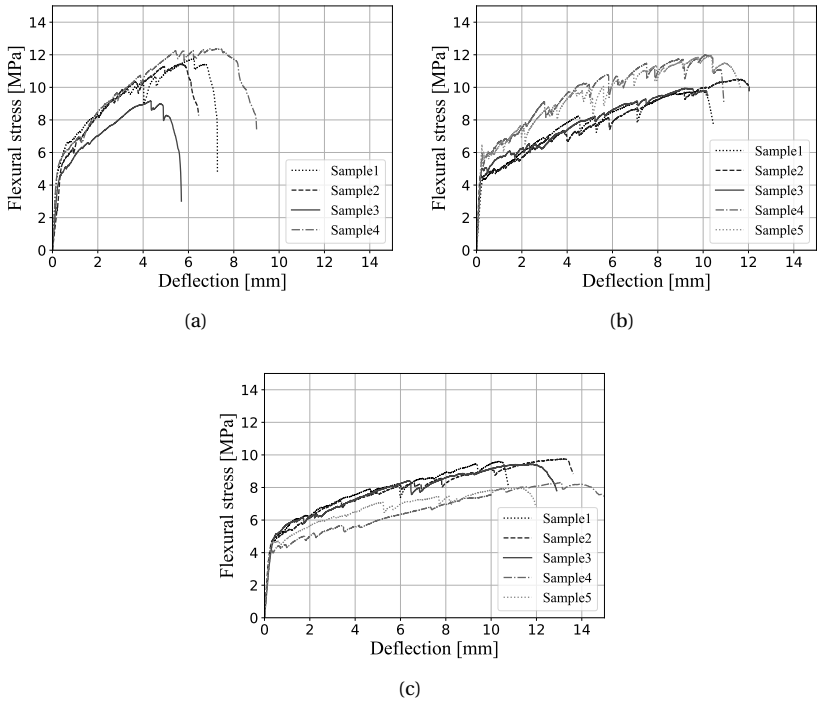

Figure 5.10: Flexural stress - Deflection curves of the cast specimens of (a) Mix A, (b) Mix C and (c) Mix D

5.6. RESULTS AND DISCUSSION PHASE 2

5.6.1. UNCONFINED UNIAXIAL COMPRESSION TEST

The evolution of the compressive strength over time has been acquired by performing the UUCT at various time intervals. The outcomes for Mix C and Mix D, together with their trendline and that of the original Mix A, are presented in figure 5.11a. The apparent Young's moduli were calculated by post-processing the fresh state compression stress values and the associated strain. The results can be seen in figure 5.11b. The linear trendlines for Mix A, Mix C and Mix D are represented in table 5.5.

	$\sigma_c(t)$ [kPa]	E(t) [kPa]
Mix A	0.49 t + 8.04	2.89 t + 66.26
Mix C	0.31 t + 2.27	1.35 t + 54.66
Mix D	0.24 t + 0.21	1.09 t + 13.25

Table 5.5: Linear trendline equations derived from UUCT, the parameter t is specified in minutes.

As expected from the slump flow test results, Mix C and Mix D have a reduced fresh compressive strength and apparent Young's modulus compared to Mix A. This indicates that they may perform better in the pumping phase of the printing routine, but will probably have lower buildability. Besides the overall lower values, figure 5.11b reveals that Mix C and Mix D have a signifi-

cantly slower Young's modulus development over time compared to Mix A. The same observation can be made for the compressive strength, only here, due to the high scatter of the results, the difference is not as pronounced. This can be related to the strongly reduced binder to filler ratio of Mix C and Mix D compared to mix A.

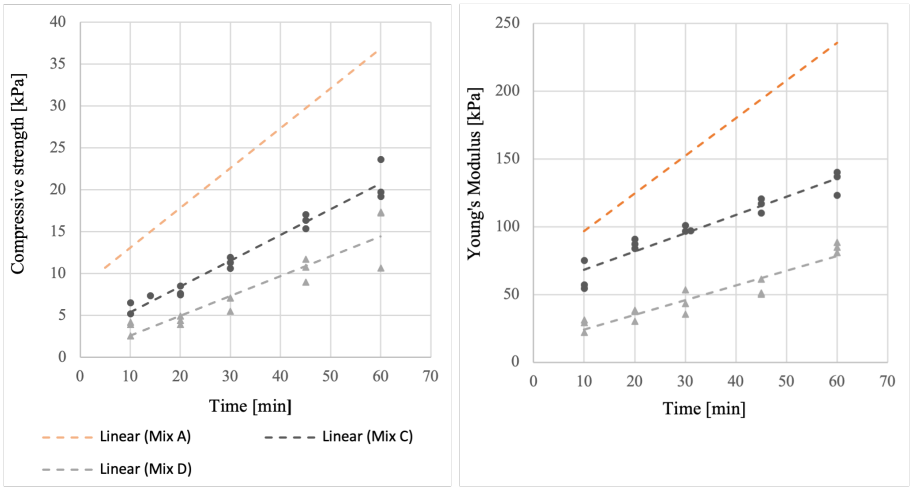

(a) (b)

Figure 5.11: Development over time of a) fresh compressive strength and b) Young's Modulus

The linear trendlines, together with the printing parameters (i.e., print speed, wall length, layer width and layer height) are used in the model proposed by Suiker [96] to predict the achievable building height during printing. For Mix C this results in an estimated building height of 13 layers, after which failure will occur due to elastic buckling. Buckling failure is also the predicted failure mode for Mix D, but here failure is expected to occur already after 10 layers.

When Mix A had been printed at the same speeds as for Mix C and Mix D, the predicted buckling failure would have occurred during the printing of the 16^{th} layer, for both speeds.

5.6.2. BUILDABILITY TEST AND PRINT QUALITY ASSESSMENT

Both Mix C and Mix D have successfully been printed at TU/e. Prior to printing, a nozzle speed test was carried out on the selected mixtures to determine the printing speed for optimal shape retention of the layer. Based hereon, Mix C and Mix D were printed with a nozzle speed of 33 and 30 mm/s, respectively.

Mix C showed good print quality, with consistent material flow and stable layer shape, as can be seen in figure 5.12. The mixture showed excellent buildability and achieved a height of 23 layers, after which the wall failed due to elastic buckling. The pumpability of Mix C, when used with the M-tech P20 pump, presented certain challenges. One of the issues observed was arching of the material within the pump reservoir. This arching phenomenon hindered the smooth flow of the material towards the Archimedes transport screw and into the rotor-stator, thus not fulfilling the full pumpability requirement, despite the good print quality after extrusion. It is worth noting that the slump flow table tests results displayed in section 3.1 had already indicated that Mix C (there referred as Mix X_3) did not meet the requirements for minimal flow conditions, as proposed by Cho et al. [177].

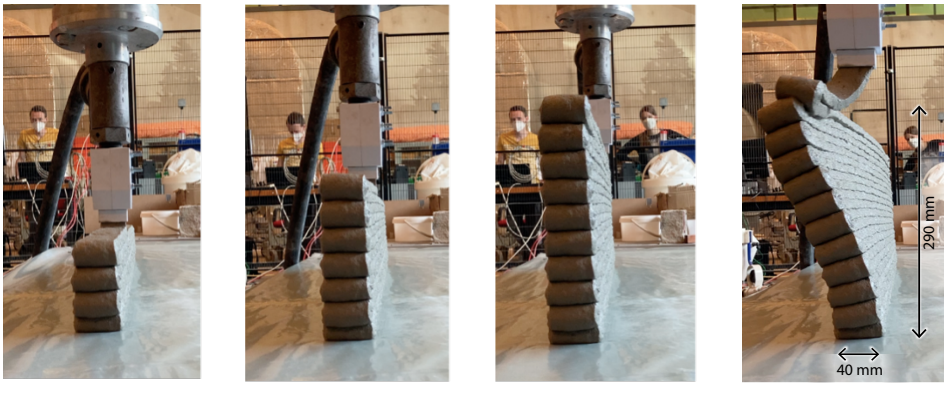

(a) (b) (c) (d)

Figure 5.12: Buildability test Mix C, failure after 23 layers

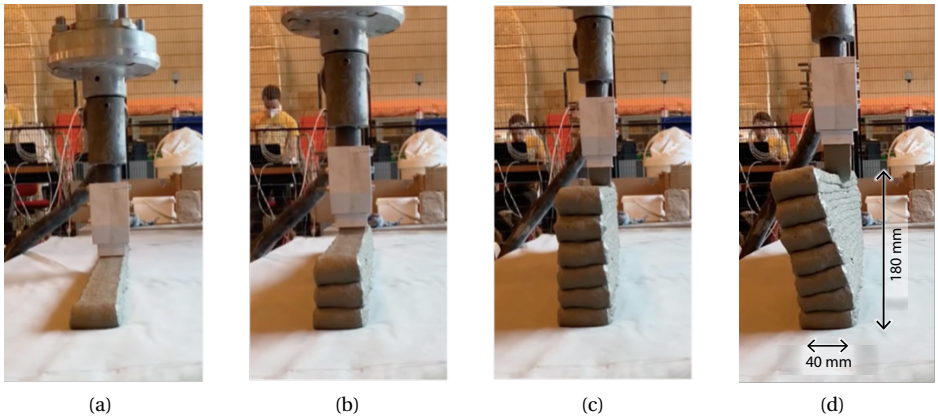

(a) (b) (c) (d)

Figure 5.13: Buildability test Mix D, failure after 15 layers

Throughout the printing session, including the printing of the additional beams, Mix D presented very good pumpability. This is in accordance with the findings in section 5.4.1, where Mix D (Mix L_4) complied with the minimal flow diameter as described by Cho et al [177]. Furthermore, it showed good extrudability and constant material flow. However, the buildability of Mix D was somewhat lower than that of Mix C, which is in correspondence with the UUCT results. The wall failed due to elastic buckling during the printing of the 15th layer, as can be observed in figure 5.13 When we compare the actual buildability height with the expected buildability height that was retrieved from the unconfined uniaxial compression test using Suiker's model [96], we find that both Mix C and Mix D perform significantly better (77% and 50%, respectively) than predicted. This result was also previously found for Mix A [95], and it is expected that this is due to additional stiffening of the material during pumping and extrusion. Note, again, that the model uses UUCT results as input, and these tests are performed on cast, not printed, specimens.

5.6.3. COMPRESSION TEST

The results of the compression tests, as illustrated in figure 5.14, indicate that the average compressive strength of the printed specimens tested in orientation **v** was 5% higher than that of specimens tested in orientation **w**. Furthermore, it was observed that the compressive strengths of the printed specimens were superior to those of the cast specimens (shown in figure 5.9). This trend was particularly pronounced for Mix D, where the compressive strength increased from 38.6 MPa for cast to 41.2 MPa for printed in orientation w and 43.6 MPa in orientation v. This finding is in contradiction with research conducted on mixtures without fibre reinforcement where a reduction in compressive strength is often reported for printed specimens in respect to cast specimens [114, 115]. However, research on 3DP-SHCC specimens have more often shown a higher compressive strength for the printed specimens [10, 15, 95].

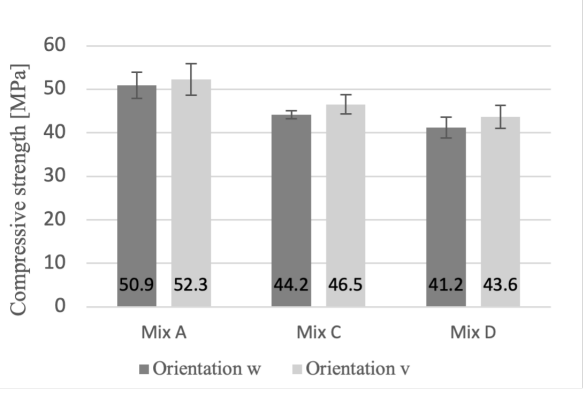

Figure 5.14: Compressive strength results (with standard deviation) of Mix A, C and D in orientation ***w*** and orientation ***v***

One possible explanation for enhanced compressive strength is the potential mix compaction during the printing process. In the process of pumping the material through the printing hose and additionally squeezing the mixture through a nozzle it is plausible that the material can get further compacted. This could also account for the increased buildability performance that was observed for both mixtures.

5.6.4. 4-POINT BENDING TEST

The 4-point bending tests were conducted on the printed specimens of Mix C and D in the orientation v.u. The flexural stress - deflection curves of these tests are shown in figure 5.15. The printed specimens of Mix C and Mix D demonstrate a significant improvement in deflection capacity when compared to Mix A, showing increases of 59% and 239%, respectively. Despite this significant improvement, the average maximum flexural stress remains approximately constant for all three printed materials, around 8.5 MPa.

Simultaneously, it stands out that the cast composites have a higher flexural strength and a higher associated ductility (see figure 5.10 and table 5.6) compared to their printed counterparts. The average flexural strength of the printed specimens was reduced by 25.1% and 6.2% for Mix C and Mix D, respectively. The average values for the deflection at maximum stress with 3.41 mm and 5.25 mm provide an even bigger reduction of 65.4% and 55.9%. During the early flexural behaviour, the printed materials exhibit a higher flexural stress at first crack, approximately 10% higher than the cast materials. Additionally, the deflection at first crack in the printed composites is signifi-

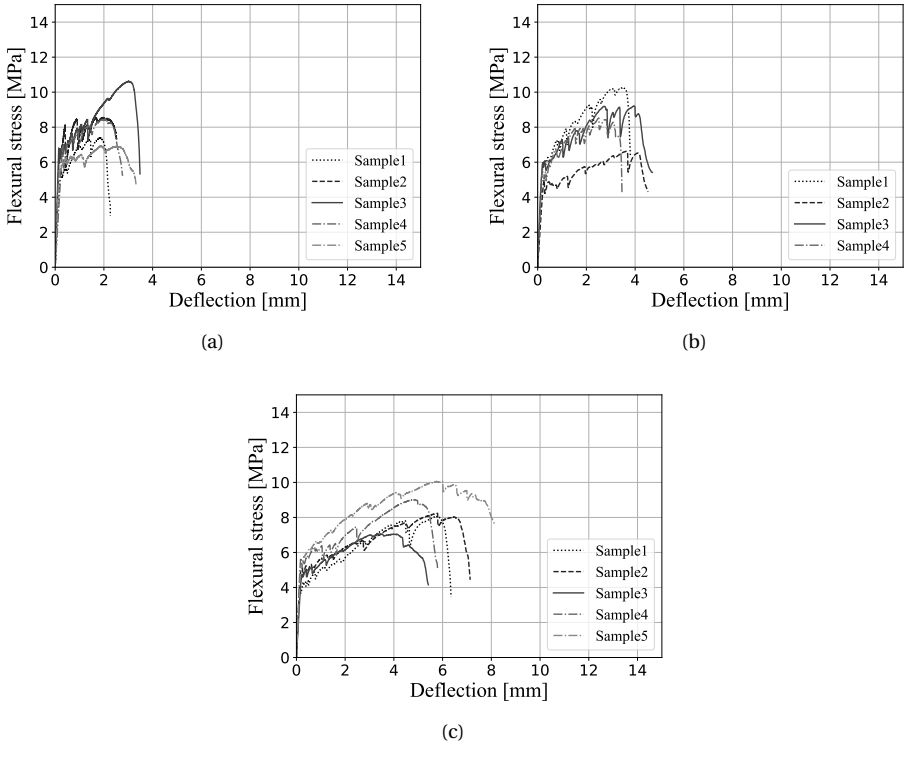

Figure 5.15: Flexural stress - Deflection curves of the printed specimens of (a) Mix A, (b) Mix C and (c) Mix D

cantly lower. These two observations suggest that the matrices of the printed composites have a higher E-modulus, indicating increased stiffness in comparison to the cast composites.

	Flexural stress at first crack [MPa]	Deflection at first crack [%]	Maximum flexural stress [MPa]	Deflection at max flexural stress [%]	$T_{f,LOP}$ [Nm (x10-2)]	$T_{f,MOR}$ [Nm (x10-2)]
Cast Mix A	5.37 ± 0.43	0.34 ± 0.04	11.18 ± 1.41	5.8 ± 1.13	1.45 ± 0.22	81 ± 25.1
Cast Mix C	5.28 ± 0.89	0.31 ± 0.07	10.83 ± 1.07	9.85 ± 0.38	1.27 ± 0.13	136.6 ± 19.6
Cast Mix D	4.9 ±0.42	0.36 ± 0.04	9.02 ± 0.81	11.91 ± 1.25	1.4 ± 0.08	235.7 ± 34.2
Printed Mix A	5.89 ± 0.57	0.23 ± 0.03	8.68 ± 1.57	2.14 ± 0.49	1.09 ± 0.21	24.3 ± 9.2
Printed Mix C	5.69 ± 0.59	0.25 ± 0.06	8.66 ± 1.53	3.41 ± 0.63	1.15 ± 0.29	37.9 ± 10.5
Printed Mix D	5.31 ± 0.52	0.3 ± 0.08	8.49 ± 1.13	5.25 ± 0.86	1.26 ± 0.16	56.4 ± 17.2

Table 5.6: Average results with standard deviations of the 4-point bending test

		Tensile stress at first crack [MPa]	Tensile strain at first crack [%]	Maximum tensile stress [MPa]	Strain at max. tensile stress [mm]	$T_{t,MOR}$ [N*mm^2]	Cracks [-]
Cast	Mix C	2.51 ± 0.20	0.043 ± 0.007	2.72 ± 0.19	1.75 ± 0.70	4.45 ± 1.86	11 ± 3
	Mix D	2.40 ± 0.43	0.028 ± 0.011	3.52 ± 0.47	2.84 ± 1.79	9.15 ± 6.2	20 ± 4
Printed	Mix C	2.61 ± 0.25	0.031 ± 0.006	3.16 ± 0.34	1.09 ± 0.31	3.04 ± 1.03	7 ± 2
	Mix D	2.48 ± 0.12	0.029 ± 0.013	2.97 ± 0.18	1.79 ± 0.52	4.06 ± 1.94	13 ± 3

Table 5.7: Average results with standard deviations of the uniaxial tensile tests

The flexural toughnesses, $T_{f,LOP}$, and $T_{f,MOR}$, presented in table 5.6, were computed to assess the overall performance of the six composites. The results of $T_{f,LOP}$ indicate that the energy stored in the materials up to the point of non-linearity shows a small but significant reduction for the printed composites. This is in line with the hypothesis that the matrices of the printed composites have a higher E-modulus. The impact of the printing process on the different composites becomes redundantly clear when reviewing the values of $T_{f,MOR}$. Where the energy storage capacity is reduced with 70, 72 and 76 percent, for Mix A, Mix C and Mix D, respectively.

Overall, it can be concluded that the alterations made in Phase 1 resulted in improved performance under flexural loading. Mix C and Mix D outperform the original Mix A both in the cast and printed form.

5.6.5. UNIAXIAL TENSILE TEST

The uniaxial tensile tests were conducted on cast and printed specimens of both Mix C and Mix D. The stress-strain curves acquired from these tests are presented in figure 5.16 for the cast specimens and in figure 5.17 for the specimens that were extracted from the printed beams. The figures present only the curves of the specimens where the final fracture occurred within the reduced cross-sectional area (see figure 3.7 in chapter 3), therefore the number of specimens shown per mixture varies. In table 5.7 the average values with the associated standard deviation are shown for all four specimen types.

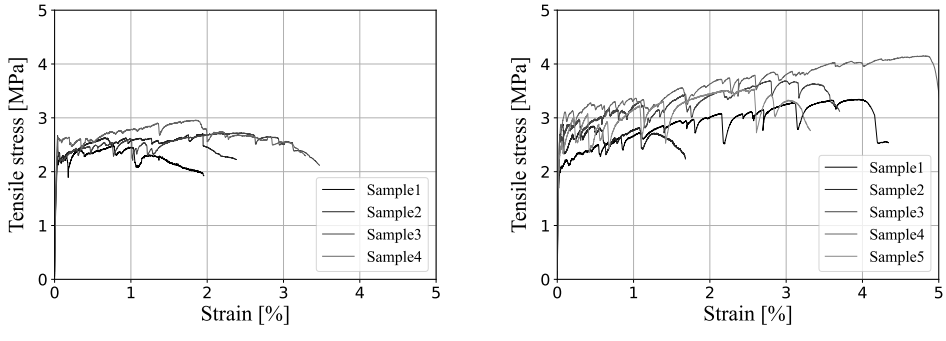

Figure 5.16: Tensile stress – strain curves of the cast specimens a) Mix C b) Mix D

The findings obtained from the cast composites indicate that Mix D surpasses Mix C concerning both tensile strength by 29% and strain hardening capacity by 62%. For the printed composites no significant difference was found in the tensile strength; however, Mix D still performs better in terms of final strain by 64%. It is important to note that the cast material consistently exhibits superior strain hardening performance compared to the printed material. Specifically, Mix C experiences a reduction in tensile strain capacity by 38%, and Mix D experiences a reduction of 37% when printed compared to cast specimens.

The tensile toughness at the maximum tensile stress ($T_{t,MOR}$), which represents the energy absorption capacity per unit volume, was calculated for all four composites. The tensile toughness is an important indicator when assessing the efficiency of strain- hardening cementitious composites [181]. The values demonstrate the superior strain- hardening capacity of Mix D in comparison with Mix C. In the case of cast composites, Mix D exhibits more than double the tensile toughness of Mix C, while for the printed specimens, Mix D displays 33% higher toughness. As

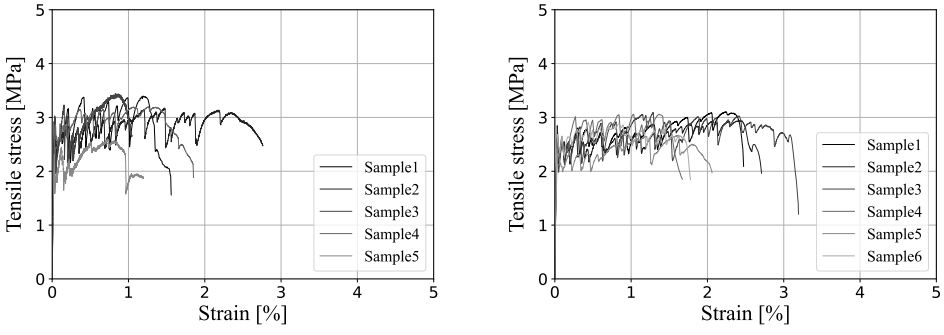

Figure 5.17: Tensile stress – strain curves of the printed specimens a) Mix C b) Mix D

with the flexural toughness a reduction of the tensile toughness of 42% (Mix C) and 56% (Mix D) was found for the printed composites.

From the shape of the stress-strain curves it can be observed that Mix D, both cast and printed, has a stable slope throughout the tensile test. This indicates a proper fibre/matrix interlayer bond and results in the stability of cracks that are formed during the cracking phase [6]. After the crack is formed, the fibres effectively distribute the load from the crack plane back into the matrix and cause the formation of another crack at a similar or slightly higher tensile stress. On the other hand, the printed specimens of Mix C show stress-strain curves with clear signs of unstable cracks.

The number of cracks and the distribution of these cracks is closely associated with the tensile strain capacity of the composite [7]. After analyses of the crack patterns (figure 5.18) it was concluded that the printed Mix C specimens displayed a smaller number of cracks and that these were more localised over the length of the reduced cross-sectional area. Where the crack patterns of Mix D, both cast and printed, were evenly dispersed throughout the reduced cross-section, in accordance with the observation made from the stress-strain curves.

Furthermore, it can be concluded that the printed composites developed fewer cracks in comparison to the cast counterparts. For both Mix C and Mix D the number of cracks was reduced with ± 35%.

In early publications on 3DP-SHCC, the general consensus was that printed SHCC elements performed better than cast elements under tensile loading due to the favourable alignment of fibres [9, 11, 182]. However, a recent publication of Zhou et al. [118] reported reductions in tensile strength and tensile strain capacity after printing, of up to 10% and 25%, respectively, depending on the printing parameters. The primary reasons for the reduction in the mechanical properties are proposed to be unfavourable fibre orientation and pore distribution due to the pumping system. In chapter 3, loss in tensile strength and strain capacity was observed as well, also here the effect of the pumping system on the material properties was proposed as a plausible explanation.

5.7. CONCLUSIONS

This study set out to improve the printability and strain hardening capacity of a previously developed 3DP-SHCC mix composition by altering multiple parameters. Indeed, for two 3DP-SHCC designs (Mix C and D), significant improvements in strain hardening capacity were achieved while printability was also improved. From the conducted research, the following conclusions can be

(a) Mix C, cast (b) Mix D, cast (c) Mix C, printed (d) Mix D, printed

Figure 5.18: Tensile test cracking patterns of representative specimens

drawn:

- For the development of 3DP-SHCC, the silica fume content and the W/S ratio are relevant parameters to simultaneously optimise workability and strain hardening properties.
- The study highlights the importance of tailoring the initial stiffness for optimising pumpability and avoiding issues like arching as observed for Mix C.
- The printing sessions of the two developed mix designs confirm the applicability of the minimal slump flow diameter criteria proposed by Cho et al. [177] for 3D printable SHCC.
- The extrudability requirements were met by both developed mix designs, resulting in a good print quality with a stable layer shape and without extrusion flaws such as tearing and overprinting.
- The buildability performance of Mix C and Mix D exceed the expectations derived from the UUCT test. Both mix designs are sufficiently buildable and have elastic buckling as main failure mechanism.
- The reduction of the compressive strength and simultaneously reducing the matrix fracture toughness, has proven to be a good approach to improve the energy balance of SHCC and to satisfy the energy requirement.
- Mechanical properties measured using cast and printed specimens of the same mixture are different. On the one hand, the hardened mechanical strength (flexural and tensile) and strain capacity (in bending and in tension) are reduced in printed compared to cast specimens; on the other hand, the buildability test and unconfined uniaxial compression test resulted in higher values for green strength and compressive strength.

The presented research makes clear that the printing process influences the material and mechanical properties of the SHCC, and this can have implications on the structural integrity of printed elements when they are designed based on casted mechanical properties. However, currently there are no established codes or standards for the designing and testing of printed concrete elements and materials. Existing codes, such as NEN EN-206, are not applicable in this context, as they do not account for the unique characteristics of printed elements, namely the lack of compaction (vibration) during printing and the anisotropic nature resulting from the layered build-up. As a result, the development of printed load-bearing structures, demands a comprehensive preliminary experimental investigation to provide robust support for the structural design throughout

all its phases [41]. The industry thus relies on conducting structural tests on 3D printed prototypes [49] to verify the structural integrity of printed elements. This approach would also apply for load bearing elements printed with fibre-reinforced concretes or SHCCs. Nevertheless, the impact of the printing process on the mechanical properties of 3DP-SHCC is a relevant and interesting subject for future investigation. To comprehend the influence of the printing process, research into the effect of specific printing phases on the mechanical properties is conducted and presented in chapter 6 section 6.2. This approach will facilitate the identification of the principal bottleneck within the printing process concerning SHCC.

6

THE INTERACTION OF 3DP-SHCC WITH THE PRINTING SYSTEM

The previous chapters have shown that the material and mechanical properties are affected during the printing process. The following chapter dives into this phenomenon by means of two investigations. The first study is related to the reproducibility of 3D printed SHCC, and studies the consistency of hardened mechanical properties of materials printed during three separate but nominally identical printing sessions. The mechanical tests included the compressive strength, the flexural strength with its associated deflection, and the tensile strength with its corresponding strain. The research shows that with 3DP-SHCC, significant variations in mechanical properties between printing sessions can be expected.

The second study evaluates the effect of each successive phase of the printing process on the mechanical properties of the composite. To this end, the material was collected at three different stages in the printing process and subsequently cast in specimen moulds. The mechanical properties of the specimens were obtained and juxtaposed with the mechanical properties of the specimens derived from a fully printed 3DP-SHCC element. The findings indicated that, while the density and the compressive strength are not significantly influenced by the printing process, the flexural and tensile strength, with their associated deflection and strain, are strongly affected. Additionally, the research identifies the pumping phase as the primary phase that influences the mechanical properties during the printing process.

* The two studies presented in this chapter have to a large extent been published in a joined conference paper presented at the Digital Concrete 2022 conference in Loughborough (EN) [183], and in a journal paper published in "Buildings" [184]

6.1. CONSISTENCY OF MECHANICAL PROPERTIES OF 3D PRINTED STRAIN HARDENING CEMENTITIOUS COMPOSITES WITHIN ONE PRINTING SYSTEM

6.1.1. INTRODUCTION

As the material development of 3DP-SHCC continued, several researchers reported a significant effect of the printing process on the quality of the 3D printed SHCC [11, 56, 118].

An initial study on the effect of different printing systems on the mechanical properties of 3DP-SHCC was investigated with the material developed by Figueiredo et al. [10]. The results of this study can be consulted in Appendix A. It was found that the mechanical and physical properties of 3DP-SHCC specimens manufactured at Delft University of Technology (TUD) and Eindhoven University of Technology (TU/e) were significantly different. For instance, an average difference of 45% was found for the flexural strength (as can be observed in figure A.5), and the air void content differed from 6.7-8.0 % (TUD) to 15.2-19.7 % (TU/e). These differences were mainly attributed to the differences in equipment (geometries, brands, types, specifications).

However, to the best of the author's knowledge, no research has been published on the reproducibility of hardened mechanical properties of 3DP-SHCC within one printing facility. This section therefore aims to investigate the consistency of mechanical properties of 3DP-SHCC elements printed on the same printing system but over different printing sessions.

6.1.2. METHODOLOGY

MATERIALS

The Mix D 3DP-SHCC composite, as developed in chapter 5 was used for the experimental study. The material composition is presented in table 6.1. The material is mixed in batches with a Hobart A200N mixer. Due to the maximum torque capacity of the mixer, the batches were limited to a volume of 3.5 litres. A detailed description of the mixing procedure can be found in chapter 5.

Table 6.1: Mix D composition in [grams/l], with RECS15 fibres (PVA),viscosity modifying agent (VMA), super plasticizer (SP)

BFS	CEM I 42,5 N	SF	LS	Sand <250 um	Water	PVA vol%	VMA	SP
263	470	33	584	318	400	2	3.06	2.68

PRINTING SESSION

Three nominally identical printing sessions were performed at the printing facilities of the Eindhoven University of Technology (TU/e) [156]. The sessions that will be referred to as printing sessions ''A", ''B" and ''C", were conducted within a time span of 10 days. The ambient conditions for each of these printing sessions were similar: 21.4 °C with a

relative humidity (RH) of 44.5%, 21.7 °C with an RH of 37.0%, and 21.4 °C with an RH of 35.5%, respectively. These printing sessions were followed by an experimental program to assess the consistency of the mechanical properties in the hardened state. Each printing session resulted in 10 beams with a length of 800 mm and a height of 6 layers. Printing was done with a downflow nozzle (40 × 12 mm^2) at a speed of 28.5 mm/s. Due to small deformations after the deposition of the material, an effective layer cross-section of approximately 40 × 11 mm^2 was achieved, resulting in an effective cross-section of the beam of 66 × 40 mm^2. The printed objects were covered with plastic. Wet cloths were placed inside to keep the relative humidity close to 100%. After 1 day of curing, the beams were submerged in water. On the 7th day, the beams were sawn into the specific specimens required for each test. Afterwards, the specimens were placed back into the water and were taken out again one day before testing.

COMPRESSION TEST AND APPARENT DENSITY

Compression tests were performed 14 and 28 days after the printing session. The compression test specimens with a size of 35 × 35 × 35 mm^3 (±1 mm) were sawn from the printed beams. The tests were performed on an Automax 5 test rig according to NEN-EN 196-1 [185], applying a compression rate of 2400 N/s. The compressive strength was determined in orientation **w** (load perpendicular to printing plane), orientation **v** (load perpendicular to the printing direction) and orientation **u** (load in printing direction), see figure 3.2. For each of the cubes, the weight and dimensions were measured directly before the tests were performed.

4-POINT BENDING TEST

The four-point bending test was conducted on 5 specimens per orientation at 14 and 28-29 days after printing. The applied test methodology is identical to section 3.4.3, with the adjustment of the deflection rate of the test apparatus which was set to 0.005 mm/s.

UNIAXIAL TENSILE TEST

The uniaxial tensile strength and deformation capacity were determined by performing an uniaxial tensile test in orientation **u**. Per printing session, six dogbone specimens were tested 27-28 days after printing. A detailed description of the specimen preparation and testing procedure is presented in section 3.4.5. A small modification was made to avoid failure of the adhesive bond between the specimen and the test set-up. For this purpose, steel plates were attached at two sides of the specimens to increase the adhesive area.

6.1.3. STATISTICAL METHODS

Due to the limited number of specimens available for the compression test (per curing age) (18), 4-point bending test (per curing age) (5) and uniaxial tensile test (6), the statistical distribution of the test results is not immediately obvious. To establish the statistical significance of the difference in results from specimens prepared from different printing sessions, the results were subjected to two statistical tests. Firstly, the Shapiro-Wilk [186] test method was used on the 28-day test results, to assess whether the results from a single printing session were normally distributed. The Shapiro-Wilk test method has two

outcome parameters: W and p. A W value close to 1 suggests that the data set is consistent with a normal distribution. The p-value is the probability that the observed data would occur if the data is indeed normally distributed. A high p-value (close to 1) implies that the data is not significantly different from a normal distribution. On the other hand, a low p-value (here the threshold is chosen to be 5%) suggests that the data significantly deviates from a normal distribution.

Subsequently, it was evaluated whether the results from individual sessions could originate from the same normal distribution. For this analysis, the Student T-test was deployed with a threshold for statistical significance (p-value) of 5%. Implying that when p value > 0.05, it is probable that the individual sessions are from the same distribution.

6.1.4. RESULTS AND DISCUSSION

COMPRESSIVE STRENGTH AND APPARENT DENSITY

The average compressive strength results at 14 days and 28 days after printing are presented in figure 6.1 for each of the three directions (u, v and w).

After 14 days of curing the average (over all directions), compressive strength obtained from printing session B is, respectively, 9.2% and 10.2% lower than those of printing sessions A and C, respectively. The average compressive strength at 14 days was measured to be 35.2 MPa, with a standard deviation of 2.02 MPa (5.6%).

For the 28 days specimen, the compressive strength obtained from printing session A stands out. The tested specimens from this printing session presented 11.69% and 10.59% higher compressive strength than those from printing sessions B and C. Here, an average compressive strength was measured to be 41.7 MPa, with a standard deviation of 2.59 MPa (6.2%).

When regarding the different test directions it was found that direction ***v*** generated the highest compressive strength, for both the 14-day and 28-day specimens. This is in line with previous research on 3DP-SHCC, [10, 15, 95]. However, this is not the case for the 28-day tested specimen of session B, here direction ***w*** gives the maximal average compressive strength. Note further that for session B, the standard deviation of the compressive strength is the highest in all three directions.

A more stable trend is observed in the apparent density results, displayed in figure 6.2. At 14 days after printing, the apparent density is stable, with less than 1% difference between printing sessions. For the 28 days the differences between the printing sessions become more significant. Here, the average apparent density of printing session A specimens is 1971 kg/mm^3, 2.2% and 1.1% higher than printing session B and C, respectively.

4-POINT BENDING TEST

The average maximum flexural stress and corresponding deflection, obtained from the 4-point bending tests are shown in table 6.2. The flexural stress-deflection curves of all printing sessions are presented in figures 6.3 and 6.4, for the ages of 14 days and 28 days, respectively.

There are two elements that stand out from these test results. Firstly, it can be observed that the specimens from printing session B show a significantly lower average maximum flexural stress and corresponding deflection capacity when compared to the specimens from printing sessions A and C. For the 14 days specimens the decrease in

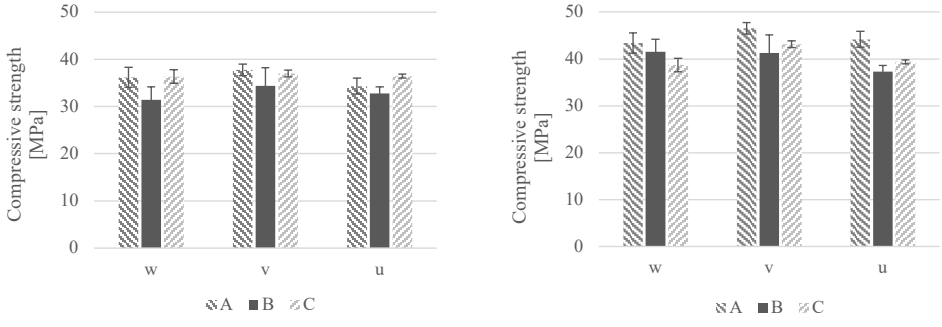

(a) 14 days (b) 28 days

Figure 6.1: Compressive strength for specimens from printing session A, B and C

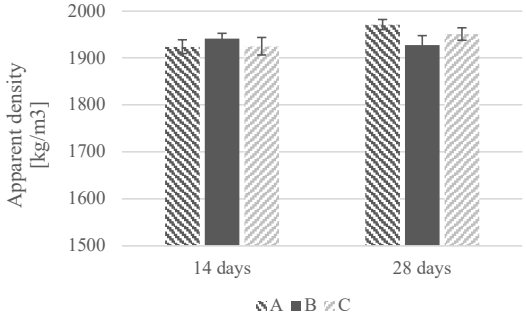

Figure 6.2: Apparent density for specimens from printing session A, B and C, 14 and 28 days after curing

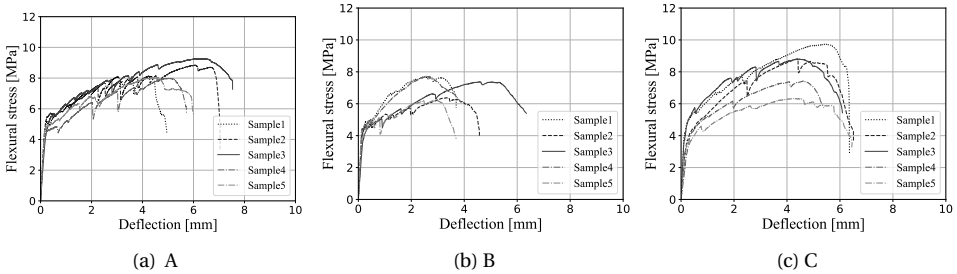

(a) A (b) B (c) C

Figure 6.3: Flexural stress-deflection curves for printing sessions A, B and C, at 14 days

flexural strength was 17% and 14% compared to A and C respectively, for the 28 days test this increased to a reduction of 29% and 21%.

Secondly, when comparing the 14-day and 28-day test results, it can be concluded that both the flexural strength and the deflection capacity are slightly reduced over time.

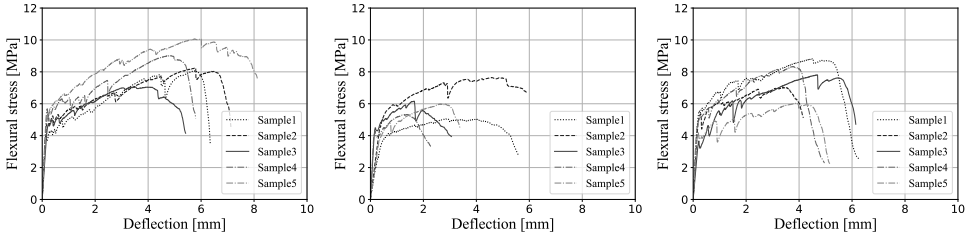

(a) A (b) B (c) C

Figure 6.4: Flexural stress-deflection curves for printing sessions A, B and C, at 28 days

	14 days		**28 days**	
Printing session	Maximum flexural stress	Deflection at max flexural stress	Maximum flexural stress	Deflection at max flexural stress
	MPa ± STD	mm ± STD	MPa ± STD	mm ± STD
A	8.45 ±0.58	5.22 ±0.96	8.49 ±1.13	5.12 ±1.10
B	7.07 ±0.74	3.09 ±0.91	6.03 ±1.01	2.63 ±1.26
C	8.23 ±1.34	4.66 ±0.49	7.61 ±1.10	4.09 ±0.50

Table 6.2: Average maximum flexural stress and deflection (14 and 28-29 days),

This finding is consistent with previous studies evaluating the performance of SHCC over time [187]. Together with this decrease, a higher standard deviation was reported for the older specimens.

UNIAXIAL TENSILE TEST

Figure 6.5 illustrates the stress-strain curves measured in the uniaxial tensile test on a specimen from each of the three printing sessions. The average maximum uniaxial stress and average maximum strain at the maximal stress are listed in table 6.3. Similar to the 4-point bending test, the uniaxial tensile tests show a lower strength for the specimen from session B, and further a considerably lower deformation (i.e. strain). The measured strain capacity, with differences >50% between printing sessions, is clearly less robust than the measured strength with differences <23%.

Printing session	Tensile stress at first crack	Strain at first crack	Maximum tensile stress	Strain at max tensile stress
	MPa ± STD	% ± STD	MPa ± STD	% ± STD
A	2.54 ± 0.24	0.047 ± 0.017	2.92 ± 0.17	0.86 ± 0.43
B	2.02 ± 0.42	0.038 ± 0.008	2.24 ± 0.38	0.41 ± 0.52
C	2.35 ± 0.41	0.031 ± 0.006	2.86 ± 0.13	1.15 ± 0.73

Table 6.3: Average maximum uniaxial tensile stress and strain (27-28 days).

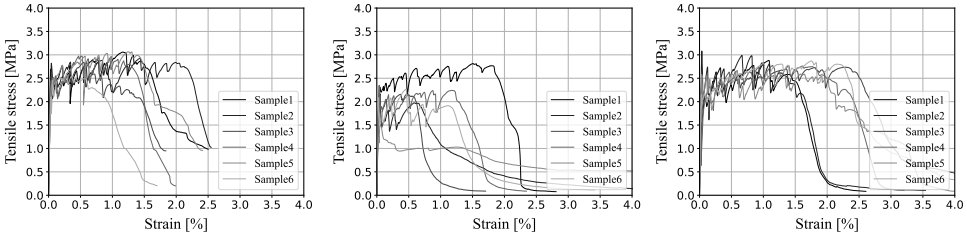

(a) A (b) B (c) C

Figure 6.5: Tensile stress-strain curves of the uniaxial tensile test, for printing sessions A, and B and C.

STATISTICAL ANALYSIS

The mechanical property values obtained from the 28 days old specimens, were subjected to the Shapiro-Wilk [186] test method. The statistical values for W and p, for the compressive strength, flexural strength and tensile strength are presented in table 6.4. The found values for W are all close to 1, and no p-value below 0.05 was found, therefore the method shows that the measured compressive strength, flexural strength and tensile strength from specimens within one printing session can be considered normally (Gaussian) distributed.

Printing Session	Compressive strength		Flexural strength		Tensile strength	
	W	p	E	p	W	p
A	0.979	0.94	0.971	0.82	0.956	0.52
B	0.983	0.95	0.909	0.46	0.969	0.87
C	0.877	0.25	0.921	0.51	0.943	0.68

Table 6.4: Shapiro-Wilk test statistical values for measured strength values

Printing Session	Deflection at maximum stress		Tensile strain at maximum stress	
	W	p	W	p
A	0.829	0.170	0.893	0.386
B	0.925	0.712	0.739	0.026
C	0.93	0.749	0.985	1.000

Table 6.5: Shapiro-Wilk test statistical values for measured deformation values

The Shapiro-Wilk test was also performed on the deformation property values of the 28 day old specimens namely, the deflection at maximum flexural stress and the strain at maximum tensile stress. The W and p-values of these tests can be found in 6.5. The tensile strain properties obtained from the specimens of printing session B, report a p-value below 0.05, proving that the session results display a significant departure from normality. Furthermore, printing session A reports low W and P-values for both the deflection (W=0.829 & p=0.17)and the tensile strain (W=0.893 & p=0.386), these values however are

not below the threshold value of p (p=0.05) and therefore there is no significant proof that these measurements are not normally distributed.

Based on these findings, the Student's t-test was performed for those mechanical properties that displayed normal distribution within their printing session. table 6.6 presents the outcome of this test for the strength properties and indicates which results are likely to originate from the same distribution and which are not.

For both flexural strength and tensile strength, sessions A and C demonstrate a high likelihood of originating from the same normal distribution. It can also be observed that neither session A nor C aligns with the distribution of session B. A different finding is obtained for the compressive strength, here the Student t-test indicates that the values for the compressive strength from printing sessions B and C are likely to come from the same underlying distribution. This statistical agreement was not found for the combined values of A and C nor A and B.

Printing session	T-test (Compressive strength)			T-test (Flexural strength)			T-test (Tensile strength)		
	A	B	C	A	B	C	A	B	C
A	-	x	x	-	x	v	-	x	v
B	x	-	v	x	-	x	x	-	x
C	x	v	-	v	x	-	v	x	-

Table 6.6: Comparison of the distribution of results from different printing sessions with the use of the Student's t-test (green/v; probably from the same distribution (p value > 0.05), (red/x; probably not from the same distribution (p value < 0.05)).

Printing session	T-test (Flexural deflection)			T-test (Tensile strain)		
	A	B	C	A	B	C
A	-	x	v	-	-	v
B	x	-	x	-	-	-
C	v	x	-	v	-	-

Table 6.7: Comparison of the distribution of results from different printing sessions with the use of the Student's t-test (green/v; probably from the same distribution (p value > 0.05), (red/x; probably not from the same distribution (p value < 0.05)).

Table 6.7 presents the outcome of this Student t-test for the deformation properties. The results on the distribution of flexural displacement, aligns with the results of the flexural strength, namely that the values of sessions A and C are likely originating from the same normal distribution, but the values of sessions A and B and sessions C and B display no such alignment. Also, the tensile strain values of sessions A and C are likely to come from the same distribution. No comparison could be made with the tensile strain data of session B, as these values were proven to be not normally distributed they were not included.

6.1.5. CONCLUSION

This study aimed to evaluate the consistency of mechanical properties of 3DP-SHCC, obtained from separate but apparently identical printing sessions. It may be concluded that:

- Objects printed in separate printing sessions can display significant differences in their mechanical properties.
- Compressive strength and apparent density show good consistency throughout different printing sessions.
- Mechanical properties related to deformation capacity (i.e., 4-point bending tests and uniaxial tensile tests) do not show consistent values throughout different printing sessions. Notably, the deformation in bending and strain in uniaxial tension are quantitatively more strongly affected by the printing session than flexural- and uniaxial tensile strength properties.
- The consistency between different printing sessions (i.e., whether results may have originated from the same statistical distribution) is not the same for compressive and (bending and uniaxial) tensile strength properties.

From the above results, it is concluded that several separate printing sessions and sufficient sample size are required to make unambiguous quantitative statements about the mechanical properties of 3DP-SHCC (e.g. in the context of standardised strengths and deformation capacities). Further research into the effect of the printing procedure on the mechanical properties is necessary to understand the cause of the high variation found in the presented study.

6.2. EFFECTS OF 3-DIMENSIONAL CONCRETE PRINTING PHASES ON THE MECHANICAL PERFORMANCE OF PRINTABLE STRAIN HARDENING CEMENTITIOUS COMPOSITES

6.2.1. INTRODUCTION

Numerous phenomena have the potential to influence the material and its mechanical properties throughout the printing process. Consequently, cast specimens do not necessarily provide a reliable indication of the actual behaviour of printed material. In the field of 3D concrete printing it is generally agreed that the interlayer between the subsequently extruded filaments can affect the mechanical performance of the printed element. The quality of the adhesion between two subsequent layers depends on both the fresh material properties and printing setting such as time-gap (interlayer time), [114, 115, 119], print speed [115] nozzle height [120], moisture content [121] and the structuration rate of the material [122, 123].

The pumping phase can also influence the material and mechanical properties of a printed element. The study presented in appendix A found a high variance in mechanical and material properties when the same mixture was printed at two different printing facilities while maintaining the same printing settings.

The influence of pumping on the material and mechanical properties of concrete has been the subject of a considerable number of studies [124–126]. The overview given by Li et al. [124] on the effect of pumping on concrete mixtures reports changes in rheological properties and air void content. Shen at al. [126] concludes that pumping may accelerate the hydration process causing a reduction in both the dormant period and the setting period up to 27 and 28 %, respectively. Shen argues that this is the main cause for the increase in the dynamic yield stress observed in pumped concrete.

In the domain of printable fibre- reinforced composites (FRC), which includes SHCC, the micro-fibres may also play a substantial role in the observed variations of mechanical properties between cast and printed composites.

Hambach and Volkmer [13] found that fibre alignment within a printed fibre-reinforced element can be achieved when the ratio of fibre length / nozzle diameter is larger than one. Similar to this approach, Me et al. [14] printed FRC using a nozzle with a small diameter, ensuring that the fibres were positioned vertically within the nozzle before extrusion. The evaluation of the mechanical properties was done in the three principal orthogonal directions and compared to conventionally cast specimens created from the identical FRC mix. In the cast specimen, they assumed that the fibres are randomly distributed. The research concludes that fibre alignment was achieved and that it strongly affected the mechanical properties in different directions. Figueiredo et al. [15] investigated the orientation of the fibres from a beam which was printed with a nozzle bigger that the maximum fibre length, (fibre length: 8 mm, rectangular nozzle size: 10x50 mm). In this scenario, it was found that the extrusion process orientated the fibres diagonally outwards in respect to the printing direction.

In addition to fibre orientation, also fibre agglomeration, the clustering or grouping together of individual fibres within a material, has been reported for printable SHCC [95, 127, 128]. Fibre agglomeration can strongly affect the robustness of SHCC performance,

especially its tensile strain capacity [7, 129].

In order to understand the difference between the cast and printed 3DP-SHCC specimens, this study researches the mechanical properties of 3DP-SHCC throughout the printing process. The printing of a concrete element can generally be seen as a succession of four phases: Mixing of material, pumping of material, extrusion of material and finally the printing of the material. The objective of this study is to determine the influence of each of these printing phases on mechanical properties and to identify potential bottlenecks within this process.

6.2.2. MATERIAL

For this study, Mix D was used, as developed in chapter 5. The material composition can be found in table 6.1. Information on the mixing routine and the fibre specification can be found in chapter 5.

6.2.3. RESEARCH METHODOLOGY

To research the effect of each printing phase on the hardened properties, this experimental program collects the material after each subsequent printing phase, referred to as phases A - C. In Phase A, material is collected directly after mixing, the material for Phase B is collected directly after the rotor/stator of the pump, and for Phase C the material is collected after the material is pumped through the hose and extruded from the nozzle. The collected material is then cast in moulds, without applying any additional compaction technique to the material. The filled moulds were covered with plastic foil. Wet cloths were placed underneath the foil to keep the relative humidity close to 100%. The specimens were demoulded after 24 hours of curing after which they were cured in water at a constant temperature of 20 °C. In addition to the cast specimens, beams with a length of 800 mm and a height of 6 layers were printed. Directly after printing, wet cloths were divided over the printing bed and all was covered with plastic foil. Beams were sawn to test specific specimen sizes after 7 days of curing. The specimens retrieved from these beams are referred to as Phase D. Curing took place under the same conditions as the cast specimens from Phases A-C. All specimens were taken out of the curing condition one day prior to testing.

Both the printing of the composite and the material collection and casting took place within one printing session.

Phase A—Cast: Mixed
Phase B—Cast: Mixed and pumped
Phase C—Cast: Mixed, pumped and extruded
Phase D—Printed: Mixed, pumped, extruded and printed

For the printing of the composite and the material collection, the printing facilities of the Eindhoven University of Technology (TU/e) were used [156]. The material was mixed with a A200-N Hobart planetary mixer. For pumping a M-Tec P20 Connect progressive cavity pump was employed, featuring a D8-2 Rotor/stator configuration capable of accommodating particles up to 3 mm in maximum size. The pump was equipped with a bespoke Archimedes transport screw. Consult chapter 4 to review all pump specifications.

A 5-meter long hose with a 25.4 mm diameter connects the pump to a downflow extrusion nozzle with a rectangular cross-section of 40 x 12 mm^2. The cross-sectional opening of the nozzle was chosen to be significantly larger than the fibre length of 8 mm, in order to minimise the fibre alignment as reported by [13–15]. The beams of Phase D were printed with a nozzle speed of 28.5 mm/s.

6.2.4. EXPERIMENTAL PROGRAM

To be able to assess the hardened mechanical properties, specimens were subjected to three types of mechanical tests: compression tests, four-point bending tests and uniaxial tensile tests.

COMPRESSION TEST

Twenty-seven days after casting and printing of the specimens the compression tests were conducted. Prior to testing the cubed specimens, with edges of 35 mm (± 1 mm), were weighed to determine their density. The test method is identical to the description in 6.1.2. Seven specimens were tested for each of the cast Phases A-C. The Phase D specimens were extracted from the 6-layer high beams. During specimen preparation, it was ensured that all cubes consisted of three layers and two interlayer zones. Six specimens were tested per orientation **u**, **v** and **w** [113].

4-POINT BENDING TEST

The four-point bending test was conducted on 5 specimens per orientation 29 days after casting and printing. The applied test methodology is identical to 3.4.3, with the adjustment of the deflection rate of the test apparatus which was set to 0.005 mm/s.

The results of the 4-point bending test were used to analyse the flexural toughness of the specimens in the different phases. The average flexural toughness (T_f) was calculated for two specific points on the load-deflection curve; the limit of proportionality (LOP) and the modulus of rupture (MOR), where MOR is defined as the point where deflection softening initiates subsequent to reaching the maximum load. A detailed description of this analysis can be found in chapter 5.3.3.

UNIAXIAL TENSILE TEST

To determine the tensile strength and strain hardening capacity of the composites the uniaxial tensile test was conducted. The cast specimens of Phases A-C were directly cast into the dogbone-shape moulds as presented in figure 3.6b. For the printed specimens an elaborate description of the specimen preparation can be found in the author's previous work [150]. The dogbone-shaped specimens were tested in printing direction; orientation **u**, according to the test protocol as described in paragraph 3.4.5.

Based on the results the tensile toughness values were quantified in accordance with the methodology described in 5.3.6.

6.2.5. RESULTS AND ANALYSIS

6.2.6. COMPRESSION TEST

Seven individual specimens were tested for each phase of the printing process. The average values of compressive strength for each phase are graphically depicted in figure 6.6.

The compressive strength of 41.5 Mpa for Phase D represents the average of the three orientations with compressive strengths of **u** (42.0 MPa), **v** (43.3 MPa) and **w** (39.0 MPa).

The observations reveal a consistent compressive strength across all four phases, with a noticeable but slight increase between Phase A and Phases B-D. However, it's important to consider the values of the corresponding relative standard deviations (RSTD), which remain consistent at approximately 6.5% to 8% for all phases. As the increase between Phases A and B falls within these error margins, no solid conclusion can be drawn based on these results.

This small increase in compressive strength between cast and printed composites is commonly encountered in the context of 3DP-SHCC, as presented in chapters 3 and 5 and documented in previous research [9, 10, 15, 188]. However, these outcomes are in contrast with the prevailing consensus for "plain" printable mortars, which often reported that printed specimen exhibit reduced compressive strength when compared to their cast counterparts [114, 115, 117].

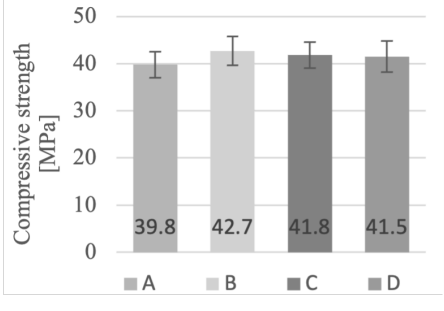

Figure 6.6: Compressive strength from printing phases A, B, C and D

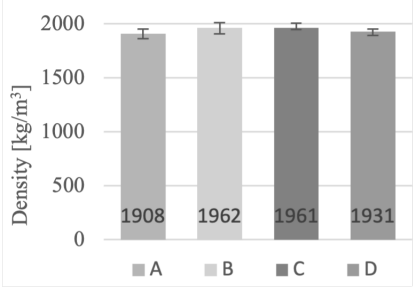

Figure 6.7: Apparent density for specimens from printing phases A, B, C and D,

The average apparent density measurements are presented in figure 6.7. The compressive strength presented for Phase D, presents the average of the three orientations **u** (41.5), **v** (42.2) and **w** (39.6). Similar to the compressive strength findings, the material density reports relatively stable values throughout the four phases of the printing process. Interestingly, a distinct increase in density of 3% is noted between Phase A

and Phase B, which can be related to the reduction of air voids, commonly observed in pumped concrete [124].

Considering that both the compressive strength and density display a distinct increase between Phase A and Phase B, it is reasonable to declare that the pumping phase plays a role in the increase of the material density, consequently leading to an increase in the compressive strength.

6.2.7. 4-POINT BENDING TEST

Five specimens per phase were tested on their flexural strength and displacement capacity in a four-point bending test. The flexural stress-deflection curves are presented in figure 6.8, in which a clear distinction is observable between Phase A and Phases B-D. While Phase A demonstrates an extended phase of deflection hardening with a consistent and linear slope from LOP (limit of proportionality) to MOR, Phases B-D exhibit more restricted deflection capacity and display increased variability among the specimens.

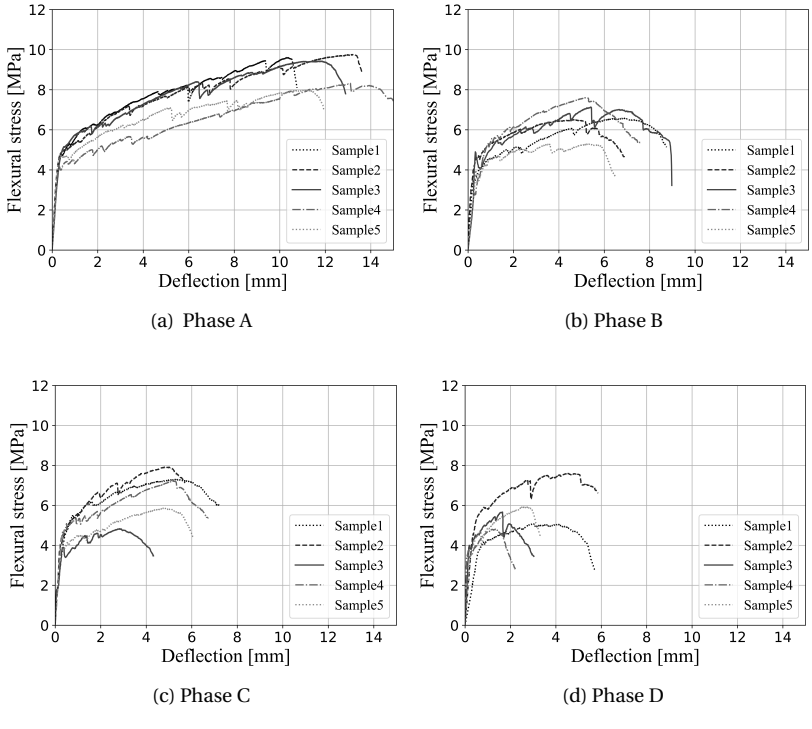

(a) Phase A (b) Phase B

(c) Phase C (d) Phase D

Figure 6.8: Flexural stress-deflection curves for printing phases A, B, C and D at 28 days

The average results of the 4-point bending tests, along with their standard deviations, are presented in table 6.8. From this table, three observations can be made. In regard to the flexural stress at LOP and its corresponding deflection, it can be observed that these values don't significantly deviate over the phases. This is in contrast with the

values found for the maximum flexural strength, which displays a significant decrease of 27% between Phase A (9.02 MPa) and Phase B (6.62 MPa). Following this, the flexural strength remains relatively consistent for Phases B and C, before experiencing a further 10% decline between Phases C and D. The same general trend can be seen for the deflection at maximum flexural stress. Reductions of 54%, 16% and 43% are measured between the subsequent printing Phases. Additionally significant is the finding that overall the flexural deflection was reduced by an astonishing 78% between cast and printed composites.

The development of the flexural toughnesses, $T_{f,LOP}$ and $T_{f,MOR}$, throughout the four printing phases is presented in figure 6.9. $T_{f,LOP}$ is fairly stable with 1.0 ± 0.12 (x 10^{-2}) Nm, although it exhibits high variance within all four phases. $T_{f,MOR}$ undergoes more pronounced changes over the four phases. Here, a significant drop of 61% is present between Phase A (1.37 Nm) and Phase B (0.54 Nm). This is significantly higher than the observed decrease for the one-dimensional values of maximal flexural stress and its corresponding deflection. The impact of the pumping phase becomes abundantly clear when reviewing the values of $T_{f,MOR}$.

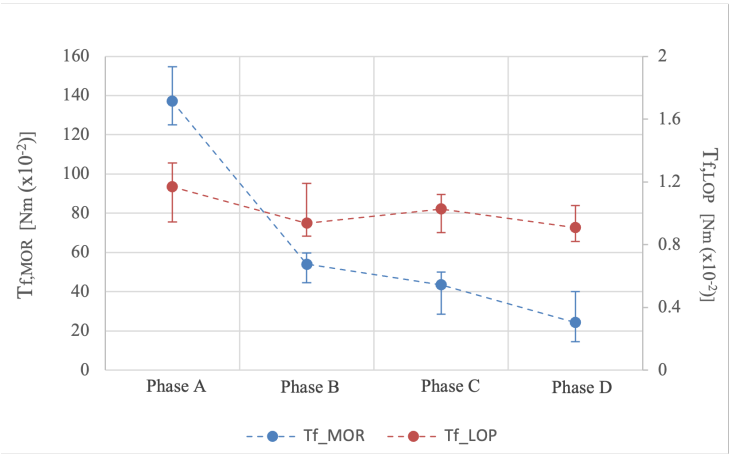

Figure 6.9: Development of flexural toughness over the four printing phases

Another reduction in flexural toughness was observed between the cast specimens from Phase C (0.43 Nm) and the printed specimens of Phase D (0.24 Nm). When reviewing these results, it is worth considering that both the printed and the cast specimens that were tested in the 4-point bending test are without an interlayer. Consequently, the reduction in mechanical performance between Phase C and Phase D cannot be attributed to this. Nevertheless, the cast specimens of Phases A-C are cast in a mould with a predetermined height of 8 mm height, ensuring all fibres are fully embedded within this height. This is not the case for Phase D specimens extruded from the printed beams,

Table 6.8: The average results with standard deviations of the 4-point bending tests

	Flexural stress at LOP		Deflection at LOP		Maximum flexural stress		Deflection at max. flexural stress	
	[MPa]	STD	[mm]	STD	[MPa]	STD	[mm]	STD
Phase A	3.99	± 0.65	0.26	± 0.05	9.02	± 0.81	11.91	± 1.25
Phase B	3.94	± 0.84	0.31	± 0.06	6.62	± 0.87	5.48	± 0.83
Phase C	4.06	± 0.35	0.28	± 0.03	6.62	± 1.25	4.62	± 1.01
Phase D	3.89	± 0.29	0.31	± 0.18	6.03	± 1.01	2.63	± 1.26

Table 6.9: The average results with standard deviations of the uniaxial tensile test

	Tensile stress at LOP		Tensile strain at LOP		Maximum tensile stress		Strain at max. tensile stress	
	MPa	STD	%	STD	MPa	STD	%	STD
Phase A	2.61	± 0.08	0.039	± 0.009	3.39	± 0.40	3.051	± 1.166
Phase B	2.26	± 0.27	0.051	± 0.041	2.88	± 0.16	0.870	± 0.411
Phase C	1.83	± 0.24	0.042	± 0.007	2.20	± 0.09	0.580	± 0.294
Phase D	2.27	± 0.16	0.040	± 0.013	2.58	± 0.12	0.898	± 0.534

here fibres may be partially embedded due to the sawn edges. This difference in specimen preparation could possibly have affected the mechanical results and be the cause of the strong reduction between Phase C and D flexural hardening capacity.

Throughout the full printing process, from mixed (cast) to printed, $T_{f,MOR}$ was reduced with 82%.

6.2.8. UNIAXIAL TENSILE TEST

The uniaxial tensile test was conducted on four specimens per phase. The tensile stress - strain curves of each phase are depicted in figure 6.10. The average results with their standard deviations are summarised in table 6.9. The total reduction of mechanical performance over the full printing process was found to be 24% and 71%, for the tensile strength and tensile strain capacity, respectively. In correspondence with the 4-point bending test results, the most significant decrease in tensile strength and strain was found to be between Phase A and B, where the average tensile strength dropped 15% and the tensile strain capacity decreased 70%.

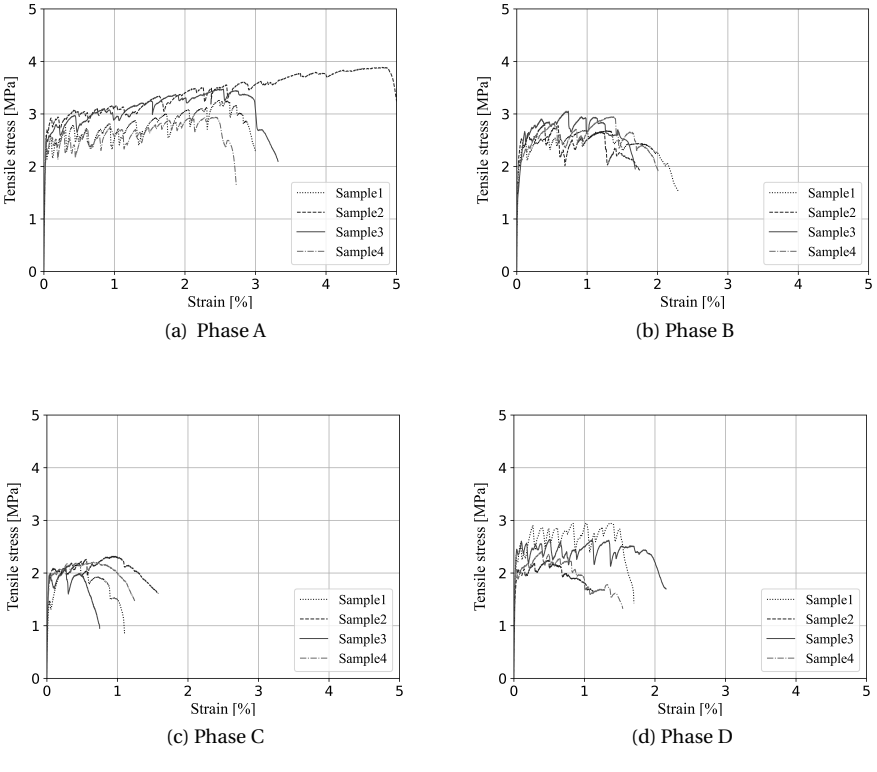

(a) Phase A (b) Phase B

(c) Phase C (d) Phase D

Figure 6.10: Tensile stress - strain curves a) Phase A, b) Phase B, c) Phase C, d) Phase D

The values measured for the LOP data points are constant over the four successive phases, with the exception of Phase C, which clearly showed reduced tensile stress at LOP.

The tensile toughness values, $T_{t,LOP}$ and $T_{t,MOR}$, are presented in figure 6.11. $T_{f,LOP}$ shows a small and steady reduction throughout the printing process of overall 10%. The values are combined with a relatively high variance between the test specimens. The tensile toughness at MOR presents a different trend with a significant reduction throughout the printing process. As with the 4-point bending a substantial drop is observed between Phase A (9.61 N/mm^2) and Phase B (3.68 N/mm^2), a reduction of 62%.

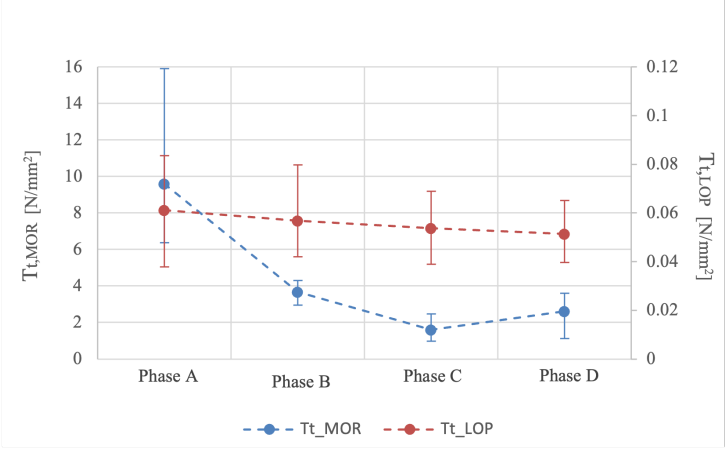

Figure 6.11: Development of tensile toughness over the four printing phases

In addition to the tensile stress and strain values, the $T_{t,MOR}$ specimens of Phase D have increased mechanical performance compared to those of Phase C, with 2.61 and 1.61 N/mm^2 respectively. This finding is in contrast with the observation of the 4-point bending results, which reported a reduction between Phase C and Phase D. A possible explanation for this is the observed change in rheological properties after pumping through a hose. It's worth mentioning that the material collected at Phase C, directly after the nozzle, was challenging to cast into the deep dog-bone mould as it was significantly stiffer than the material collected from Phase A and Phase B. This is in accordance with the literature on how the rheology (yield stress and viscosity) could be affected by a pumping process (including transport through the hose) [124, 126].

It is plausible that the stiffer material in combination with the mould shape (deep and with angular edges) caused initial specimen flaws within the dog-shaped specimens, such as entrapped air voids, which have led to reduced tensile strength and strain capacity.

The tensile toughness at MOR, $T_{t,MOR}$ experienced a reduction of 83% throughout the full printing process.

6.2.9. DISCUSSION

From the conducted research and data analysis, two findings stand out. Firstly, the pumping phase is a crucial phase when printing fibre-reinforced concretes, such as 3DP-SHCC. Following this phase, the investigated material experiences changes in all measured parameters. These changes include not only small increases observed in density and compression strength but also significant reductions in flexural deformation capacity and tensile strain capacity.

Secondly, the most substantial alteration in mechanical performance is observed in the deformation capacity of specimens subjected to the 4-point bending test and the uniaxial tensile test. Notably, the values for the compressive strength, apparent density and the LOP values of the 4-point bending test and tensile tests remain stable throughout the four printing phases. Consequently, it is reasonable to assume that the main cause of the reduced deformation capacity lies in the fibre bridging capacity of the material during the cracking phase.

One possible explanation for the drop in deformation capacity directly in Phase B, is the formation of fibre agglomerations in the pumping phase. The presence of fibre agglomerations have been found within printed 3DP-SHCC elements [95, 127] and even within the rotor/stators of cavity pumps by Xu et al. [128]. Fibre agglomerations reduce the uniform fibre distribution in the composite and therewith reduces the deformation capacity of the composite.

A second hypothesis involves a potential alteration in the fibre/matrix bond, which could affect the energy criteria of SHCC. Consequently, the fibre bridging capacity of the composite is reduced. Pumping can be associated with high friction forces which can lead to a significant temperature rise of the cavity pump and the pumped material [189]. Elevated temperatures can accelerate the hydration process, which can significantly impact the mechanical properties of the cement-based matrix due to altered hydration products and increased porosity [190, 191]. The alteration in the cementitious matrix may have resulted in a weaker fibre/matrix bond, which has caused the reduced deformation capacity.

6.2.10. CONCLUSIONS

The present study was designed to determine the influence of different printing phases on the mechanical properties of 3DP-SHCC. From the elaborate experimental investigation the following conclusions can be drawn:

- The compressive strength and apparent density are slightly increased after pumping (Phase B) by 7% and 3% respectively. After pumping, these two parameters stay stable throughout the remaining printing process.
- The flexural and tensile strength and particularly their associated deformation, (i.e. deflection and strain) are strongly decreased by the printing process.
- The flexural toughness at Limit of Proportionality remains unaltered throughout the printing process, where the tensile toughness displays a small and steady decrease, up to 10% over the full printing process.

- The flexural and tensile toughness at Modulus Of Rupture present the clearest values to analyse the reduced mechanical performance, with overall reductions of 82 and 83% respectively. $T_{f,MOR}$ and $T_{t,MOR}$ displayed the most significant drop directly after pumping of 61 and 62%.
- From the four investigated phases, the pumping phase has the most significant influence on the mechanical properties of 3DP-SHCC.

To determine the exact cause of the decrease in deformation capacity of 3DP-SHCC and how this can be overcome, further investigation into the microstructure and the hydration products of the composite after subsequent printing phases is recommended. This endeavour was not pursued, as it was outside the scope of this PhD thesis.

7

EFFECT OF FIBRE TYPE ON THE MECHANICAL PROPERTIES OF 3DP-SHCC

The distinctive tensile strain hardening behaviour of SHCC results from the optimal design between fibre, matrix, and fibre–matrix interface. This chapter presents research into the fresh and hardened mechanical properties of six 3DP-SHCC materials, in which two different matrix designs were combined with three fibre types. The fibres include two types of oil-coated polyvinyl alcohol (PVA) fibres and a high-density polyethylene (HDPE) fibre. The research concludes, that for the same volume percentage shorter fibres decrease the workability of the 3DP-SHCC and that HDPE fibres present the most favourable results in terms of tensile strain hardening capacity and crack width control.

7.1. INTRODUCTION

The characteristic features of SHCC are derived from the addition of microfibres into the mortar matrix. However, achieving strain hardening behavior in SHCC requires more than simply increasing the fibre volume in the mixture. The development of SHCC is based on the micro-mechanical concept, where the interaction and cooperation between the fibres and the matrix are fundamental. The fibre properties (such as aspect ratio, stiffness, mechanical properties, and chemical composition), along with matrix properties (packing density, mechanical properties, initial flaw size), and fibre/matrix interface properties (chemical bond, frictional bond, and fibre orientation) collectively contribute to the attainment of strain hardening behaviour [6].

SHCC is tailored correctly when it complies with two micro-mechanical requirements; the strength criterion and the energy criterion. These criteria can be found in section 2.2.1 of chapter 2.

Due to the importance of the fibre within this material concept, considerable research has been conducted on different fibre types and their applicability for SHCC. Typically, SHCCs are reinforced with a relatively small amount (around 2% by volume) of polyvinyl alcohol (PVA) fibres [56, 57] or polyethylene (PE) fibres [58, 59].

PVA is a hydrophilic material, as can be seen from the chemical composition shown in figure 7.2. The hydroxyl group in the base element of PVA is able to form intermolecular interactions through hydrogen bonds with the cement surfaces [192]. As a consequence, PVA fibres can have a (too) high bond strength, which results in a very high bridging stress combined with a low complimentary energy and consequently a low strain hardening capacity [6]. To overcome this, PVA fibres used for SHCC get surface treatment, to moderate the chemical bond of the fibres with the cement matrix [7]. This surface treatment is also beneficial for the fibre dispersion in the wet mix. It should be emphasised that this surface treatment reduces the number of hydrogen bonds, but it does not fully prevent it.

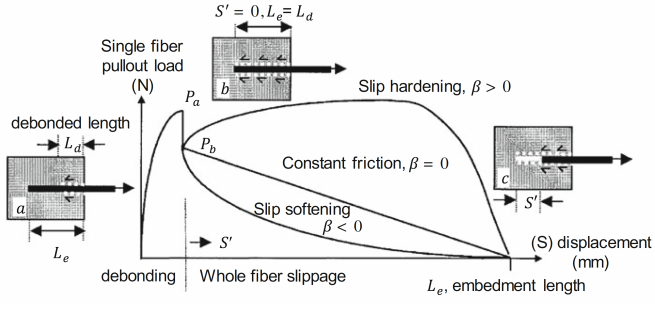

Figure 7.1: Typical single PVA fibre pull-out curve [193]

A typical test curve from a single PVA fibre pull test is presented in figure 7.1. When the fibre is put under tension it initially goes through a debonding phase in which the hydrogen bonds between the fibre and the matrix are broken. Afterwards a sudden load drop is observed to P_b, corresponding to the friction the fibre experiences in the matrix. From this point on there are three possibilities, reduced friction (slip softening), constant

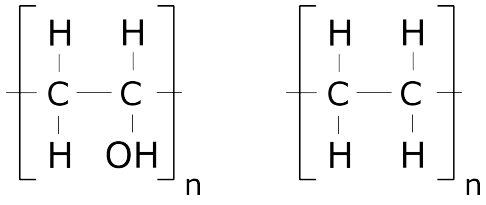

(a) (b)

Figure 7.2: Chemical composition of fibres a) Untreated PVA b) HDPE

friction, and increasing resistance, with increasing slip (slip hardening) [7]. To comply with the energy criterion 2.2 presented in chapter 2, slip hardening behaviour of the fibres is required.

In contrast to PVA fibres, HDPE (High-Density Polyethylene) fibres exhibit inherent hydrophobicity, leading to the absence of chemical bonding between the fibres and the cement matrix. Consequently, the anchorage of HDPE fibres within the matrix relies solely on frictional forces [194]. The frictional bond between fibres and matrix could be optimised by increasing the packing density of the matrix. The ability to use these fibres in combination with very dense particle packing, makes them suitable for high-strength strain hardening materials, commonly known as strain hardening Ultra high-performance concrete (SH-UHPC), or Ultra high-performance SHCC (UHP-SHCC) [59, 195–197].

Besides these two commonly used fibres, research has also been conducted on other types of polymer fibres such as poly(p-phenylene-2,6-benzobisoxazole) (PBO) and aramide fibres [59, 60], steel fibres, [61, 62] and natural fibres [63, 64]. Finally, research has also been carried out on hybrid fibre mix designs [65–68]. Hybrid fibre mixtures combine steel fibres with synthetic and/or natural fibres within one SHCC material design, and are mainly used in SH-UHPC and UHP-SHCC.

Research on fibre types is still relevant, especially now that SHCC has found its way into the world of automated manufacturing. In the field of 3D concrete printing the composite has been proposed as a self reinforcing material under the name 3DP-SHCC or 3DP-ECC [9–11, 95, 118, 152, 182].

As with conventional strain hardening cementitious composites, 3DP-SHCC's are mostly designed with PVA and HDPE fibres. And even though literature provides a wide range of publications on 3DP-SHCC, the different studies use only one type of fibre throughout their experimental trials. This study aims to research the effect of different fibre types on the workability and hardened mechanical properties of 3DP-SHCC. Therefore, this chapter presents a comparative research of six mix designs in which three fibre types are combined with two different matrix designs. The six mix designs are subjected to a slump flow table test, to assess their workability and to get an indication of their suitability for 3D concrete printing. Subsequently, the hardened properties of cast specimens are assessed by means of a compression test, a 4-point bending test and a uniaxial tensile test.

7.2. MATERIAL

To investigate different fibre types for their applicability to 3DP-SHCC, three fibre types were selected, of which two types of polyvinyl alcohol (PVA) fibres and a high-density polyethylene (HDPE) fibre. The PVA fibres used in this research, RMS702 and RECS15, both have had surface treatment to improve their fresh and hardened mechanical behavior. Additional information on the fibres geometry and mechanical properties can be found in table 7.1.

The three fibre types were combined with two matrix designs, namely the matrices of Mix C and Mix D, as developed in chapter 5. The two mix designs, (when combined with PVA 8 fibres) differ in compressive strength (43.6 MPa and 38.6 MPa), respectively. The composition of the two matrices can be found in table 7.2. In total six fibre-reinforced mix designs were tested, all with a 2% volume fraction of fibres.

Table 7.1: Fibre specifications

		PVA 8 (RECS15)	PVA 6 (RMS702)	HDPE
Tensile strength	GPa	1.6	1.6	3.0
Modulus of elasticity	GPa	42.5	37	80
Length	mm	8	6	6
Diameter	μm	39	26	20
Aspect ratio (L/D)		205	231	300
Water absorption (by weight)	%	<1	<1	<0.2

Table 7.2: Material composition, values in g/dm^3

Material	Matrix C	Matrix D
BFS	263	263
Cem 1 42.5 N	470	470
Silica Fume	33	33
Limestone	584	584
Sand 125-250	318	318
Water	367	400
VMA	3.43	3.06
SP	3.05	2.68

When discussing the results of the different mix designs, they will be referred to as "Matrix"-"fibre type". For example, the combination of Matrix C with the PVA 6 mm fibre will be named as: C-PVA6.

All the tests were conducted on material from 3.5-liter batches mixed with an A200N Hobart planetary mixer. For the preparation of the materials, the mixing procedure as described in section 5.2.2 of chapter 5 was used.

7.3. METHODOLOGY

In order to determine the effect of the fibres on the mechanical properties of the different composites four mechanical tests were conducted.

- Fresh state: Slump flow table test (SFTT)
- Hardened state: Uniaxial compression test (UCT)
- Hardened state: Four-point bending test (4PBT)
- Hardened state: Uniaxial tensile test (UTT)
- Fresh state: Buildability test and shape retention analysis

After one day of curing, the specimens utilised for the hardened state tests were demoulded and moved to a fog room with a temperature of 20 °C and a relative humidity of 97%. The specimens were sawn into the specimen size that is required by the test, one week after casting, after which they were placed back in the fog room. Finally, a day before testing, the specimens were taken out of the fog room.

7.3.1. SLUMP FLOW TABLE TEST

The workability of the fresh materials was evaluated using a flow table test according to EN 1015-3 [176]. A full description of the test set-up and the deployed methodology can be found in paragraph 5.3.1

This test is conducted at several ages to assess the workability of fresh 3DP-SHCC mortars over time. Specifically, the tests were performed at t= 10, 15, 20, 25, 30 and 40 minutes, with t=0 being the time of water addition during the mixing process.

To be able to analyse the effect of the fibre on the mortar, the slump flow table test was also conducted on Matrix C and Matrix D, without the addition of fibres.

7.3.2. UNIAXIAL COMPRESSION TEST

The compressive strength of the six composites was measured at 14 and 28 days after casting. For comparative purposes, the compressive strength test was also conducted on Mix C and Mix D without the addition of fibres. The results that are displayed in the result section are the averages of five specimens (14 days) and four specimens (28 days). A full description of the Uniaxial compression test can be found in 3.4.4.

7.3.3. FOUR POINT BENDING TEST

In order to assess the flexural strength and deflection capacity of the 3DP-SHCC's, a 4-point bending test was performed, in accordance with the procedure described in 3.4.3. The effective displacement was measured during testing by employing two linear variable differential transformers (LVDT) that were mounted on the two steel rods of the test set-up. Due to the position of the LVDTs, the measurement of the vertical displacement relates to the average displacement of these two rods. When we assume a perfect parabolic shape of the bent specimen, the maximum displacement in the middle of the span will be ± 5.7% higher than the measured value. The test set-up can be viewed in figure 3.4. The results that are presented in the result section are the averages of three specimens (14 days) and four specimens (28 days).

7.3.4. UNIAXIAL TENSILE TEST (UTT)

The strain hardening capacity under tensile loading was measured by means of a uniaxial tensile test. The four mixtures that showed strong deflection capacity in the 4 point bending test were subjected to this test. The test was performed on dog-bone-shaped specimens which were made by casting fibre-reinforced concrete (FRC) 'feet' around a rectangular beam with an average dimension of 20 mm [w] x 40 mm [h] x 250 mm [l]. To eliminate irregular orientation of the fibres at the edges of the specimens, the rectangular beams were sawn from a larger cast element that measured 100 mm [w] x 100 mm [h] x 300 mm [l]. A full description of the specimen preparation can be found in a previous article from the author [150].

Tests were conducted on an Instron 8872 servo hydraulic testing system making use of the strain-controlled mode. The displacement rate was set to 0.5 μm/s, resulting in a strain rate of 5 microstrain/s. Two LVDT sensors were utilised to measure the vertical displacement, and the average value of the LVDTs was used to control the strain rate.

7.3.5. PRINTABILITY TEST

After evaluation of the mechanical properties two mix designs were subjected to a printability test at the printing facilities of the Eindhoven University of Technology (TU/e) [156]. For this research the gantry system 3D printer was equipped with an M-Tech P20 cavity pump containing an Archimedes transport screw as described in Chapter 4. The pump was connected to a 5-meter long hose and a downflow nozzle with a rectangular cross-section of 40 * 14 mm^2. The material was mixed in batches of 3.5 litres with an A200-N Hobart planetary mixer. The two mix designs were assessed on Buildability and Shape retention.

BUILDABILITY

A slender wall in subsequent layers of 800 mm length and 40 mm width was printed to assess the buildability of the materials. The wall was printed in a back-and-forth printing routine. The main failure types for buildability tests are plastic collapse and elastic buckling, but literature has also reported that a combination of these two mechanisms can lead to failure [76, 147].

SHAPE RETENTION

The geometry of the slender wall was meticulously examined using an in-line measurement system developed by Versteege et al. [198]. This measuring equipment utilises two laser profile scanners that are connected to the printing nozzle, and scans the printed element directly after deposition. The first scanner is orientated vertically and scans the geometry of the top layer while simultaneously measuring the vertical distance of the top layer from the printing nozzle. The second scanner is orientated under a 45-degree angle and scans the top layer and the side profile of the printed element. The set-up of the in-line measurement system is presented in figure 7.3. Examples of the geometric profiles are presented in figure 7.4.

Laser scanner 2 only provides the geometric profile of one side of the beam (figures 7.4b and 7.4d). Additionally, this tilted laser scanner has a limited scanning range, which with the given layer height results in a maximum profile scan of three full layers, as can be

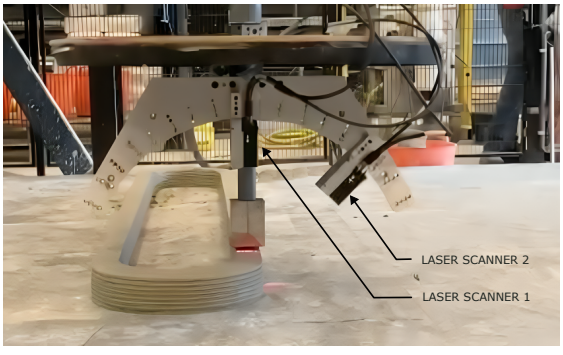

Figure 7.3: Set-up in-line geometry measuring device, with the courtesy of Jelle Versteege [198]

viewed in figure 7.4d. Due to the shadows cast by overlying layers onto underlying ones, the resulting geometric profiles can exhibit discontinuities caused by the shadow effect. From the data derived from the laser scanner, the total element height can be derived. Furthermore, and under the assumption that the printed layers are symmetrical, the width of the printed layers is retrieved. Due to the back-and-forth printing routine, every other layer can be scanned.

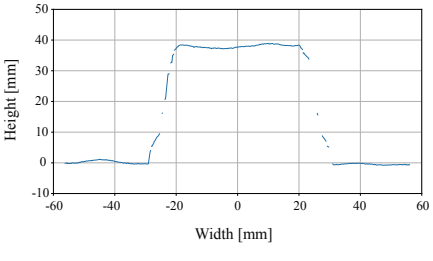

(a) Geometry after 3^{rd} layer with laser scanner 1

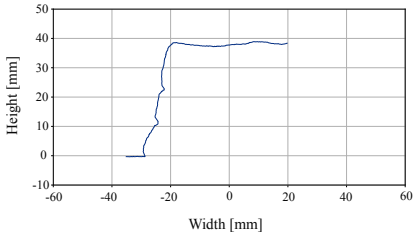

(b) Geometry after 3^{rd} layer with laser scanner 2

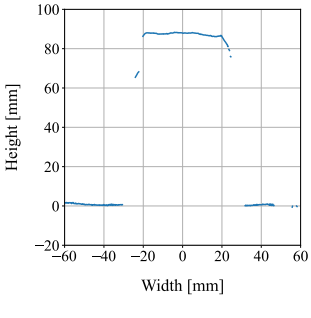

(c) Geometry after 7^{th} layer with laser scanner 1

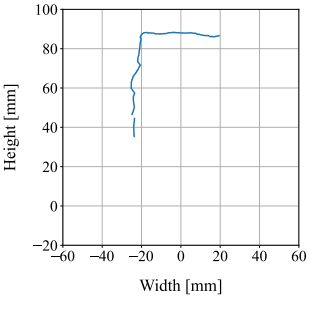

(d) Geometry after 7^{th} layer with laser scanner 2

Figure 7.4: Geometry profiles with a-c) Vertical laser scanner 1, b-d) Tilted laser scanner 2

The width measurement have been conducted on the third layer viewed from above. See figure 7.5 for clarification. These measurements were taken at three locations over the 800 mm long thin wall namely, at u = 100, 400 and 700. For further comparison of the two mix designs, the average total height of the wall was measured at 9 places over the wall. For the three locations along the thin wall, three measurements on the top layer were conducted at v = -10, 0 and 10. These points have been indicated with an X on figure 7.5.

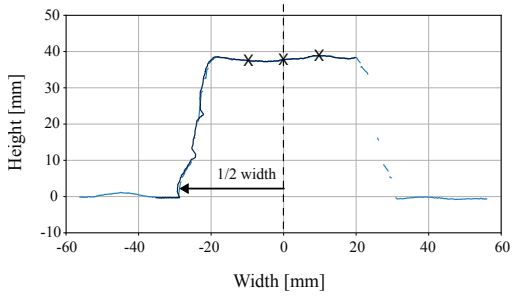

Figure 7.5: Methodology for width measurement and the locations (marked with x) for height measurements on laser scan profiles.

7.4. RESULTS AND DISCUSSION

7.4.1. SLUMP FLOW TABLE TEST

The slump flow table test gives an assessment of the effect of the fibres on the workability of the fresh mixture. From the graph shown in figure 7.6 it can be seen that fibres have a significant effect on the fresh behavior of the 3DP-SHCC. Furthermore, the results show that Matrix C has a lower spread diameter and thus lower workability than Matrix D, which is in line with previous research on these two material designs presented in chapter 5.

Two additional elements stand out from these results. Firstly, a clear distinction is found in the workability between the different fibre types. For both Matrix C and Matrix D it holds that the addition of 2 vol% PVA 6 fibres results in the lowest slump flow diameter, followed by the HDPE and PVA 8 fibres. When we compare the values measured to the guideline provided by Cho et al. [177], it stands out that all the fibre containing mixes combined with Matrix C are well bellow the 130 mm spread diameter. The same holds for mix D-PVA6. According to Cho, these materials are likely to be difficult to pump and can result in reduced printing quality by for instance filament tearing.

All fibre types are added at an equal volume, which means that the mixes containing the fibres with a smaller diameter or shorter length will have an increased fibre surface area and fibre content. These increases would generally lead to reduced workability. However, it is not the thin and short HDPE fibre (⌀=20 μm, l=6mm) that results in the lowest workability, but the PVA 6 fibre (⌀26 μm, l=6mm). This finding can also not be attributed to the Modulus of elasticity, which with 80 GPa, is much higher than those of PVA 6 and PVA 8, see table 7.1. Therefore, it is expected that the chemical composition of

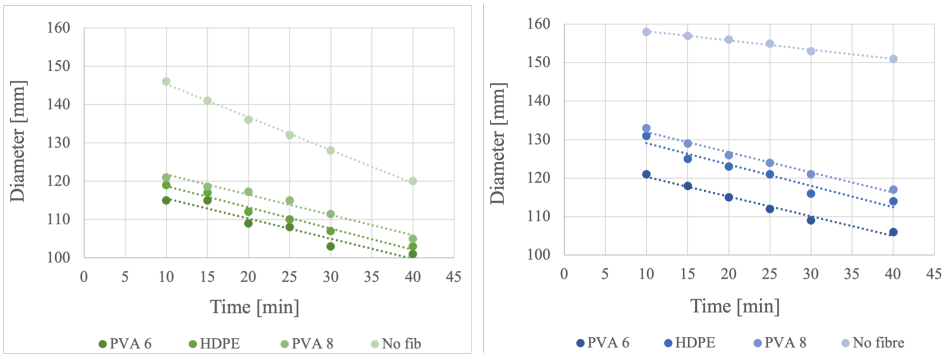

(a) Matrix C (b) Matrix D

Figure 7.6: Flow diameter results of the mini slump flow table test

these fibres plays a role. From HDPE fibres it is known that they have a lower water demand due to their hydrophobicity, which results in more free water in the fresh material and relatively higher workability.

Secondly, the results show that the workability of Matrix D was affected more significantly by the introduction of fibres than Matrix C. When we compare the slump flow diameter of Matrix D without fibres (for 10 minutes) with D-PVA8, the flow diameter was reduced by 35 mm, whereas the same comparison for Matrix C, yielded a reduction of 25 mm.

7.4.2. COMPRESSIVE STRENGTH

The results from the compressive strength tests, conducted at the age of 14 and 28 days, are presented in figure 7.7.

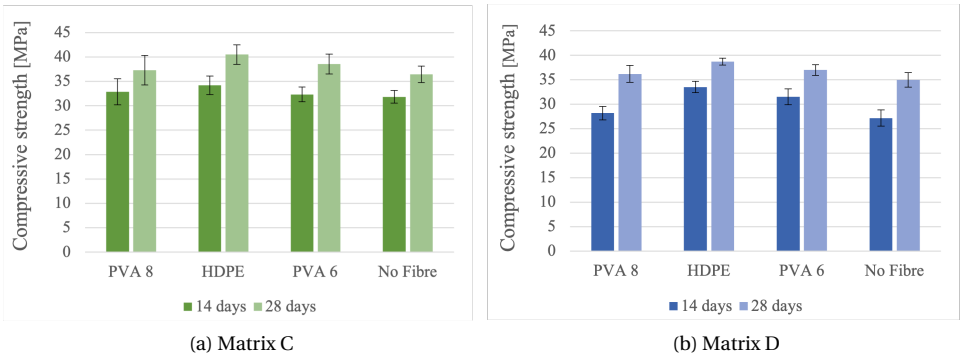

(a) Matrix C (b) Matrix D

Figure 7.7: Compressive strength

In general, it can be stated that the addition of synthetic fibres results in a small but significant increase in compressive strength, evident in both the 14-day and 28-day spec-

imens. This observation aligns with earlier studies conducted by Kamal et al [199] and Aydın and Baradanand [200], who both reported an increase in compressive strength for higher fibre volumes (0 vol% to 2 vol%).

Of all the fibres considered, the addition of the HDPE fibres resulted in the most substantial increase of compressive strength, while PVA 8 fibres showed the lowest improvement. There is one exception to this trend: in the case of Matrix C at 14 days, C-PVA8 shows a slightly higher compressive strength than C-PVA6, measuring 32.85 MPa compared to 32.33 MPa, though this exception falls within the margin of error. In the case of the HDPE fibres, the addition of the fibres in Matrix D yielded an increase in compressive strength of 23.3% and 10.6 % compared to the plain Matrix D (for 14 and 28 days respectively). The compressive strength of Matrix C increased with 7.4% and 11.1% for the 14 and 28 days old specimens, respectively.

Analyzing the results of the PVA 8 fibre, only a limited increase in compressive strength is found, compared to the plain matrix. For both Matrix C and Matrix D, the strength improvement is modest, ranging between 2% and 4%, falling within the margin of error.

In contrast with the slump flow test results, where the effect of fibre addition was more pronounced for Matrix D than Matrix C, the compressive strength results do not show a distinct difference between the two matrices.

7.4.3. FOUR POINT BENDING TEST

The bar charts in figure 7.8 present the average flexural strength and maximum displacement of the 3DP-SHCC mixes made with Matrix C. They contain both the average results with the associated standard deviations for the 14-day and 28-day specimens.

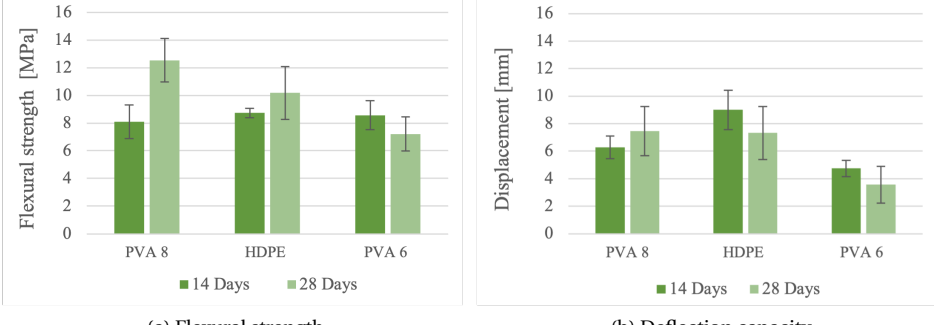

(a) Flexural strength

(b) Deflection capacity

Figure 7.8: 4-point bending test results for different fibre types combined with Matrix C at 14 days and 28 days

At the age of 14 days, the flexural stress retrieved from the 4-point bending tests is stable for all three fibre types, with an average value of 8.4 MPa and a relative standard deviation of 4%. The deflection capacity presents significantly more variation between the tested materials. Notably, the C-PVA6 mix shows the lowest average deflection at maximal flexural strength, measuring only 4.7 mm, while C-HDPE achieves 9.0 mm.

When reviewing the flexural hardening capacity of the Matrix C at the age of 28 days, it becomes clear the mixes reinforced with PVA 6 fibres lag behind compared to the other

two fibre types. Specifically, C-PVA6 achieves a flexural strength of 7.21 MPa, which is 29.2% lower than C-HDPE and 42.5% lower than C-PVA8. The related deflection capacities highlight the contrast further, as C-PVA6 records a deflection capacity of 3.6 mm, representing a 51.4% and 52.2% decrease compared to C-HDPE and C-PVA8, respectively.

Figure 7.9 shows the flexural strength and deflection capacity for the Matrix D composites. The same stable trend in flexural strength is observed for the 14-day specimens, with a value of 8.6 MPa and a relative standard deviation of 1%. However, in contrast to Matrix C specimens, there is a significant divergence in deflection capacity at 14 days among the three fibre types. Specifically, PVA6 fibres exhibit a deflection capacity of 5.5 mm, while HDPE and PVA8 fibres display 11.6 mm and 12.3 mm, respectively.

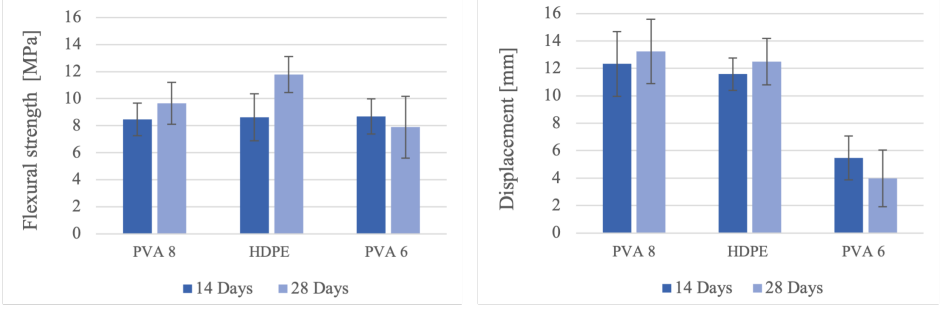

(a) Flexural strength

(b) Deflection capacity

Figure 7.9: 4-point bending test results for different fibre types combined with Matrix D at 14 days and 28 days

Also for 28-day specimens, D-PVA6 underperforms compared to the D-HDPE and D-PVA8 regarding its maximum displacement. Here, the low value found for D-PVA6 stands out even more, with a displacement capacity of 4.0 mm, which is a significant 68.1% and 69.9% lower than D-HDPE and D-PVA8. Here D-HDPE and D-PVA8 also perform significantly better than their Matrix C counterparts, with an increase of 77.6% and 70.5% respectively.

For completeness, all flexural stress-deflection curves for the composites ages of 14 and 28 days are presented in figures 7.10 and 7.11, respectively.

In figure 7.12, images of representative tested specimens for each mix design are presented. These images offer a useful insight into the crack patterns of the tested specimens, and therewith a complementary perspective on the ductility of materials. From the images, it becomes clear that all composites with Matrix C present limited ductility. This becomes evident by the presence of one prominent crack in the middle of the specimen. Although C-PVA8 does present some crack branches and C-HDPE presents a few additional micro-cracks, the characteristic of this prominent crack is consistent among all mixes with Matrix C. The Matrix D mixes demonstrate a different, more favorable cracking pattern. D-PVA6 exhibits two parallel cracks with a separation distance of 40mm, indicating that the specimen has cracked at the positions corresponding to the two centered rollers. Mix D-PVA8 displays a greater number of microcracks distributed

across the specimen surface, but like Mix D-PVA6, it also features two main cracks in the proximity of the centered rollers. Among the Matrix D mixes Mix D-HDPE stands out as it showcases a saturated distribution of cracks throughout the tested surface, indicating its ability to effectively distribute flexural stress across the specimen while maintaining a stable crack width.

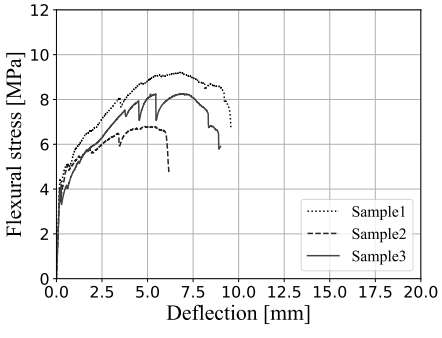

(a) C-PVA8

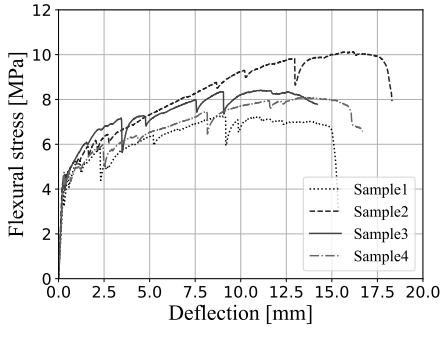

(b) D-PVA8

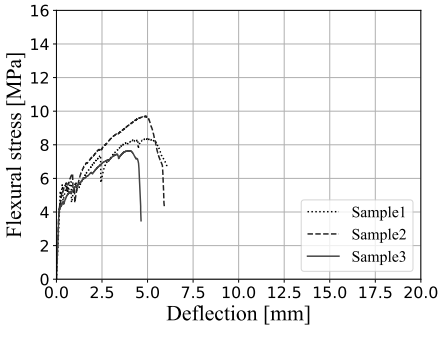

(c) C-PVA6

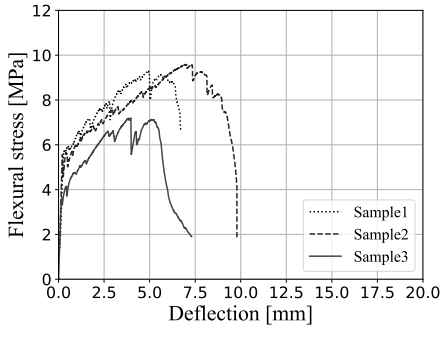

(d) D-PVA6

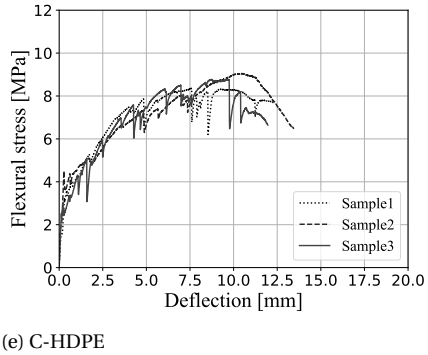

(e) C-HDPE

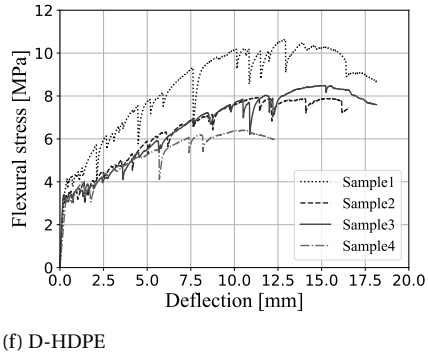

(f) D-HDPE

Figure 7.10: Flexural stress - deflection curves at 14 days

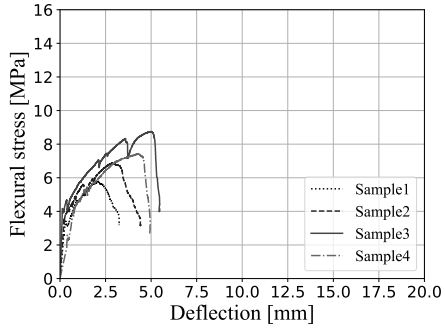

(a) C-PVA8

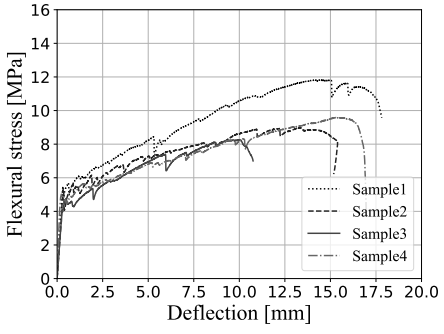

(b) D-PVA8

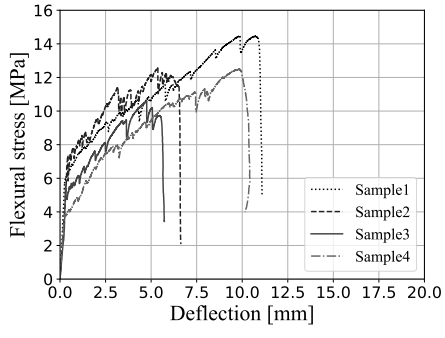

(c) C-PVA6

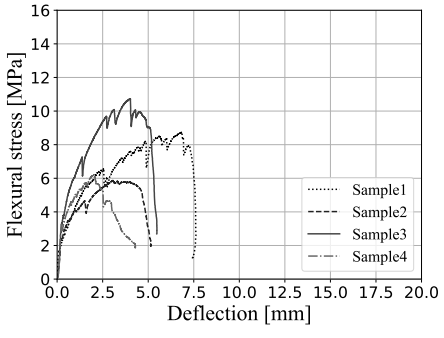

(d) D-PVA6

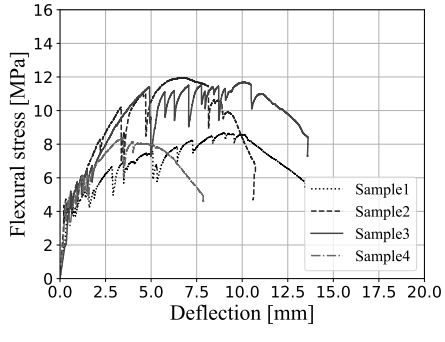

(e) C-HDPE

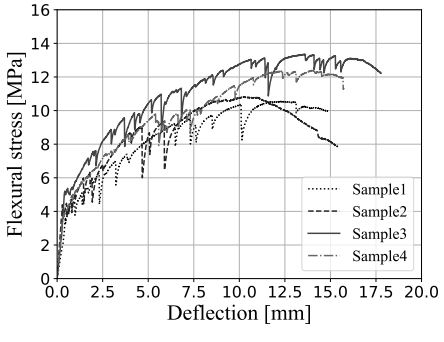

(f) D-HDPE

Figure 7.11: Flexural stress - deflection curves at 28 days

It's worth acknowledging that the limitations of the test setup, where the LVDTs effectively measure the average displacement between the two middle rollers, might have resulted in underestimating the true maximum displacement of the D-HDPE specimens. Given their well-distributed cracks throughout the tested surface and the nearly perfect

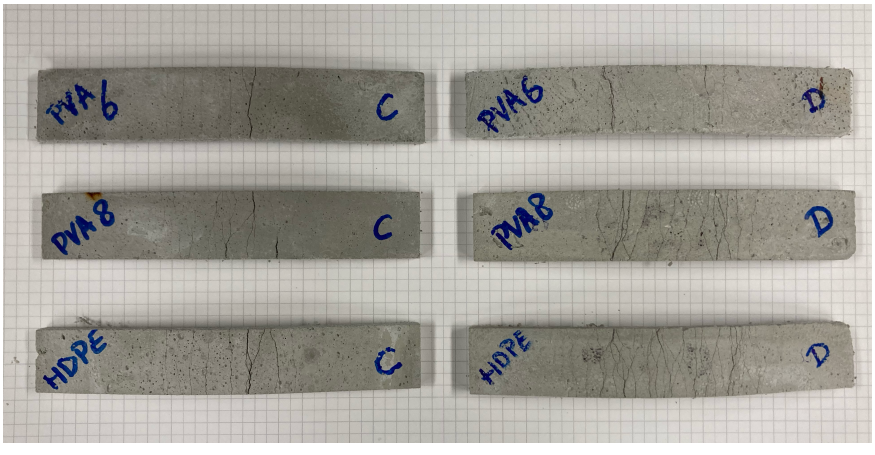

Figure 7.12: Crack patterns of representative 4-point bending specimens

parabolic shape post-testing, it is plausible that their effective displacement at mid-span is higher compared to that of D-PVA8.

Overall, it can be concluded that PVA 6 does not significantly contribute to achieving ductility. Furthermore, the HDPE and PVA8 fibres report the most optimal flexural hardening capacity in combination with Matrix D.

7.4.4. UNIAXIAL TENSILE TEST

In the final stage of the experimental program, mixes C-PVA8, D-PVA8, C-HDPE and D-HDPE were subjected to a tensile test. Due to the limited deflection capacity of mixes C-PVA6 and D-PVA6, these two mix designs were disregarded for this stage of the research.

The average tensile strength and strain, with the associated standard deviation, are presented in the bar chart presented in figure 7.3. The stress-strain curves acquired of the four tested composites are presented in figure 7.13.

Table 7.3: Average results of tensile tests

	Tensile strength		Strain at maximum stress	
	MPa	RSD [%]	[%]	RSD [%]
C-PVA8	2.72	7.1	1.75	39.9
D-PVA8	3.52	13.2	3.24	34.3
C-HDPE	3.17	13.8	1.93	45.2
D-HDPE	3.76	5.3	3.53	30.9

The tensile test results confirm the trends observed in the 4-point bending tests, indicating that mixtures combined with Matrix D exhibit more superior tensile strain hardening capacity. Specifically, in the case of PVA fibres, Matrix D demonstrates a notable 30% higher tensile strength and an impressive 85% increase in tensile strain compared to its Matrix C counterpart. For the HDPE fibres these values, with 19% and 83%, are

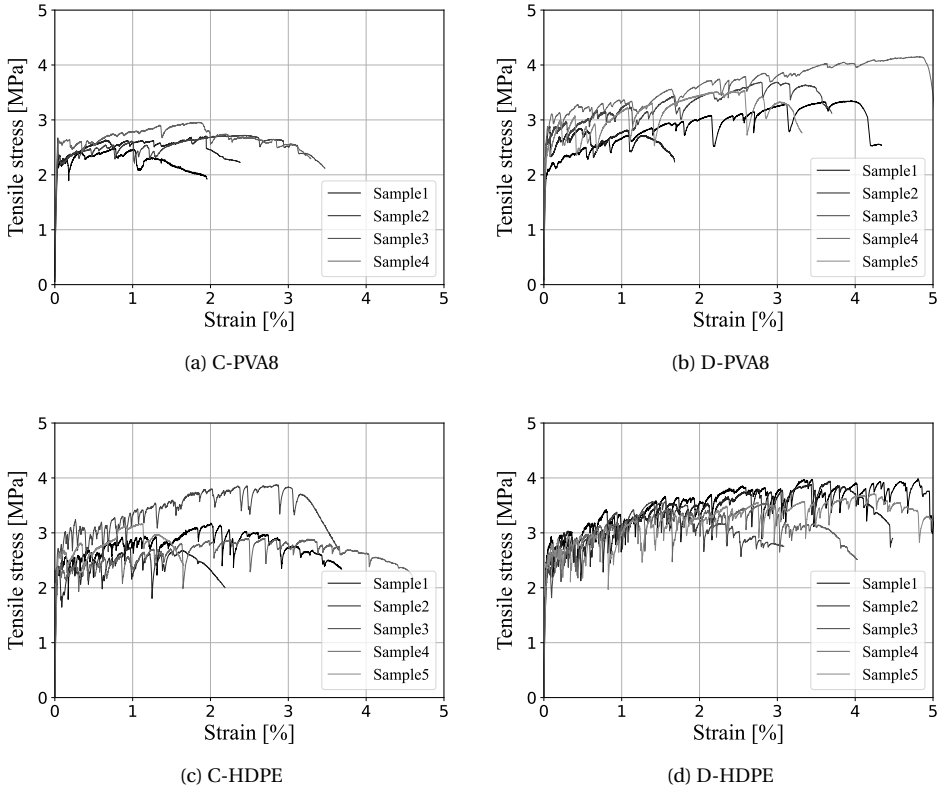

(a) C-PVA8

(b) D-PVA8

(c) C-HDPE

(d) D-HDPE

Figure 7.13: Tensile stress - strain curves at 28 days

relatively similar.

This result was unexpected as HDPE fibres are recognised for their compatibility with stronger matrices. Therefore, it was anticipated that the fibres would exhibit a comparable or slightly improved strain hardening capacity when combined with Matrix C in comparison to Matrix D.

The HDPE fibre demonstrates favorable results when compared to the PVA fibre, in both Matrix C and Matrix D. In comparison to the PVA fibres, the tensile strength is increased by 16.7% and 6.8% for Matrix C and D, respectively. Additionally, the strain hardening capacity also attained a significant increase with 10% and 8.9% for Matrix C and Matrix D, respectively.

The variety in tensile performance of the mixes becomes even more evident when reviewing representative tensile test specimens as presented in 7.14. The composites made with Matrix D consistently present a higher number of cracks, especially when combined with HDPE fibres. In the case of D-HDPE, a very fine and well-saturated crack pattern is observed across the entire reduced cross-section of the specimens.

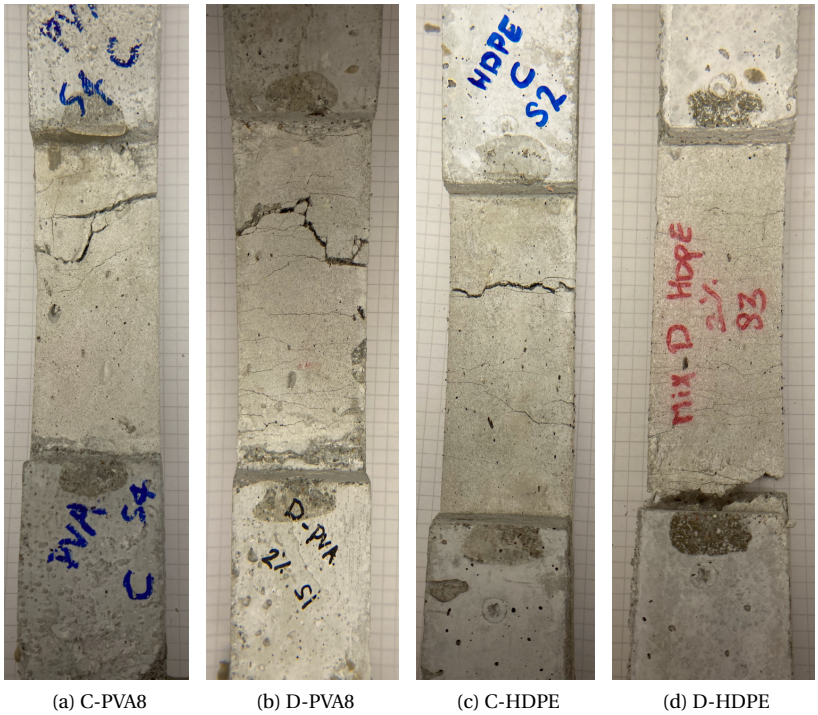

(a) C-PVA8 (b) D-PVA8 (c) C-HDPE (d) D-HDPE

Figure 7.14: Representative tensile test samples after testing

7.4.5. PRINTING TRIAL

The eight mix designs were assessed on their strain hardening capacity and their potential for 3d printing according to the slump flow table test results. Based on these two criteria Mix D-HDPE and D-PVA8 were selected for the printing trial.

BUILDABILITY

The materials were printed with a nozzle velocity of 20 mm/s. At higher pumping speeds, the arching phenomena occurred for mix D-HDPE. To facilitate comparison, the materials were printed with an equal pump and nozzle speed.

Both D-HDPE and D-PVA8 were successfully printed at TU/e and showed exceptionally good print quality with a consistent material flow. Mix D-HDPE showed excellent buildability and achieved a height of 38 layers, without failing.

The D-PVA 8 mix showed good buildability, it failed during the printing of the 30th layer due to elastic buckling (figure 7.15). The achieved height was almost 2 times higher than in chapter 5. This is the direct result of the reduced printing speed used for this buildability study, which was 2/3 of the printing speed previously deployed.

(a) (b) (c)

Figure 7.15: Buildability mix designs with a) D-HDPE b) D-PVA8 prior to collapse and c) D-PVA8 during collapse

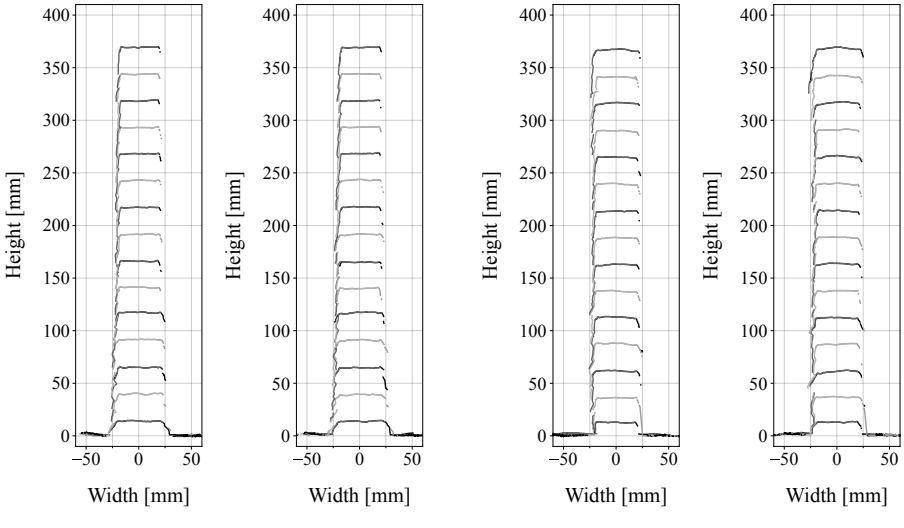

(a) D-HDPE mid wall (b) D-HDPE end wall (c) D-PVA8 mid wall (d) D-PVA8 end wall

Figure 7.16: Scanned thin wall geometry profiles

SHAPE RETENTION

The laser scanner was able to measure the geometry of the thin wall during printing. In figure 7.16 the mid and end cross sections of the two thin walls presented, up until layer 29.

The wall built with D-HDPE follows a straight vertical line while the buildup of D-PVA8 is more irregular, this is particularly clear in the end cross section of D-PVA8 in

figure 7.16d. Additionally, it is noticeable that the top corners of the D-HDPE layers keep a rectangular shape and that the top surface is straight and horizontal, in comparison with D-PVA8. From these observations it can be stated that D-HDPE is better able to keep its original nozzle shape, compared to the D-PVA8.

The average layer width is presented in figure 7.17. From the graph it stands out that the two mix designs follow the same trend for the first seven layers, with a relatively wide initial layer, slowly decreasing to a steady layer width from layer 9 and onwards. For D-PVA8 the steady layer width measures 45 mm (std= 0.94mm), where the width of D-HDPE with 42.5 mm (std=0.74 mm) is significantly lower.

Interesting to see is that the calculated layer width of D-PVA8 slowly increases again at the height of 25 layer. The methodology for the layer width measurement, which assumes symmetry, does not take into account the horizontal displacement that can be associated with buckling failure. It is expected that the increase in layer width measured for D-PVA8 actually represents the initial elastic deformations that finally resulted in the buckling failure.

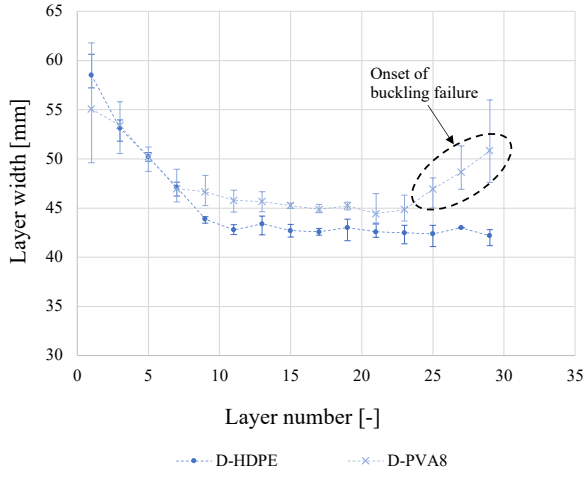

Figure 7.17: Layer width measured by the laser scanner

Although the difference in width is significant, the average total height at 29 layers was, was measured to be 369.1 mm and 367.5 for D-HDPE and D-PVA8, respectively. The standard deviation over the 9 height measurements was very low, with only 0.42 mm for the D-HDPE and 0.30 for the D-PVA8. If no deformations had occurred in the vertical direction, the thin wall would have been 406 mm high at this stage, meaning that a total height reduction of 36.86 mm and 38.40 mm has taken place for D-HDPE and D-PVA8 respectively. These findings indicate that the layers of D-PVA8 have a bigger cross sectional area than D-HDPE, as they have the same average height but a significantly larger width. Therewith it can be concluded that the material flow of D-PVA8, when printed with the same pump and nozzle speed, is higher than the material flow of D-HDPE.

Overall, mix D-HDPE and mix D-PVA8 show very good shape retention during the thin wall printing. The average layer width and overall height is very stable up until failure.

7.5. CONCLUSIONS

This chapter presents research into the effect of fibre types on the workability, buildability and hardened mechanical properties of 3DP-SHCC. Based on the experimental results and discussion, the following conclusions can be drawn:

1. The adaption of fibre type within 3DP-SHCC for the same volume fraction has a significant influence on the workability, as demonstrated in the slump flow table test. The PVA 6 (RMS702) fibre demonstrated the highest increase in resistance to flow.

2. The addition of fibres and the adaption of the fibre type has a limited effect on the hardened compressive strength, which is slightly higher for fibre-reinforced matrices compared to non-reinforced references. The increase in compressive strength was most pronounced for the HDPE fibres.

3. Due to the limited flexural hardening capacity and the strong reduction in workability, PVA 6 (RMS702) fibres are not suitable for application in 3DP-SHCC.

4. PVA 8 mm (RECS15) fibres and HDPE fibres are both suitable for 3DP-SHCC, where HDPE fibres provide the highest number of cracks combined with the most saturated crack dispersion under tensile loading.

5. Mixes D-HDPE and D-PVA8 have good buildability and shape retention properties, and therewith are suitable for large scale for 3D printing.

In the following chapter the two best performing materials (D-HDPE and D-PVA8) will be subjected to an elaborate fresh mechanical study, to evaluate which tests are applicable to determine the fresh mechanical properties of these printable 3DP-SHCC.

8

APPLICABILITY OF FRESH MECHANICAL TESTS FOR 3DP-SHCC MIXTURES

Fresh mechanical and rheological properties play a crucial role in the development of various concrete types, including shotcrete and self-consolidating concretes. However, with the emergence of additive manufacturing in the realm of concrete construction, rheology science has taken on added significance in the creation of 3D printable concretes. Key rheological properties such as static and dynamic yield stress are important in determining whether a material can meet the printing requirements: pumpability, extrudability, buildability, and open time. To evaluate these properties for 3D printable mortars, multiple traditional and innovative fresh mechanical and rheological tests have been proposed. However, not all test methods can be used to characterise all types of printable mortars. This holds particularly true for 3D printable strain hardening cementitious composites (3DP-SHCC), which contain a relatively high volume of synthetic microfibres. This gives the materials a higher initial static yield stress and higher viscosity, potentially making them incompatible with some established test methods. This chapter presents an extensive examination of six laboratory tests and their suitability for the fresh mechanical and rheological testing of 3DP-SHCC. It discusses the theoretical bases of the methods, their relevance in the context of 3DP-SHCC, and an assessment of their overall applicability for 3DP-SHCC.

8.1. INTRODUCTION

When one works with materials that flow, knowledge of the rheological properties is of great importance. Rheology is the scientific field that studies the flow phenomena of materials and takes into account time-dependent behaviour under the influence of stresses. Fresh-state cementitious materials show both liquid and solid-state properties that evolve rapidly over time. By understanding the rheological behaviour of cementitious materials, researchers can develop and optimise them to improve the quality and reliability of a product.

The first time rheology research became of interest to concrete developers was with the introduction of concrete pumping in the 1930s. Fundamental research on phenomena related to the pumping of concrete, such as the friction between the material and the pipe, came a few decades later. In the late 50s one of the first studies on the experimental testing of pumping friction was published by Ede [201]. He presented the "sliding compression test" as a method to determine the friction stress in relation to the pumping pressure. In more recent years, a variant of this method called the sliding pipe rheometer (SLIPER) was developed by Nerella et al. [202, 203].

Rheology research on concrete was further triggered by the introduction of self- consolidating concretes (SCC). This is a material concept that was developed in Japan in the late 80s, and covers the group of concrete materials that have self-compacting and levelling properties [204, 205]. The material was developed at a time when skilled labour was in limited supply, and therefore these new features of self-compaction and levelling were very much of interest. Over time, four key characteristics were defined that describe the stability and filling capacity of SCC in fresh state: Flowability, Viscosity, Passing ability (corners and rebars) and Segregation resistance. Tests were developed to assess these features, such as the slump flow test, L-box test, V-funnel test and the Sieve segregation resistance test [206–208].

The importance of rheology is once again emphasised with the emergence of three-dimensional concrete printing (3DCP). The four printability criteria, pumpability, extrudability, buildability and open time [33], impose strict requirements on the fresh properties of 3D printable mortar. Especially the contradicting requirements of the pumpability (which demands the material to be sufficiently fluid) and the buildability (which requires the material to be sufficiently strong) require good control of the fresh mechanical and rheological properties with respect to their evolution in time [77, 82, 209].

The fresh properties of printable mortars have therefore been intensively researched over the last decade. Multiple characterisation methods were developed and assessed for the correct analyses of the fresh properties of printable mortars[78, 85–89, 91, 97]. Interestingly, for the characterisation of 3DCP materials, rheological tests, traditional concrete tests and fresh mechanical tests, that have their basis in soil mechanics, have been used.

In the case of 3DP-SHCC, fibres are added to the printable mortars to achieve strain hardening behaviour. Fibres reduce the workability of the printable mortar depending on fibre content, fibre specifications and distribution. This leads to materials with even higher static/dynamic yield stress and plastic viscosity than conventional printable mortars. Consequently, fibre addition could potentially limit the amount of tests that can determine the fresh material properties of 3DP-SHCC [103]. This makes an investigation

into suitable fresh mechanical test methods for 3DP-SHCC even more challenging and significant.

The present study aims to research the applicability of fresh mechanical and rheological tests for 3DP-SHCC materials. The study consists of an extensive experimental program in which the following six laboratory tests were evaluated: the slump flow table test, the unconfined uniaxial compression test (UUCT), the ram extruder test, the continuous slow penetration test (SPT), the amplitude sweep test, and the flow curve test.

The tests were conducted on three mix designs, a non-fibre reinforced material, and the two 3DP-SHCC mix designs (D-HDPE and D-PVA8) that showed good printability in the previous chapter 7. The paper discusses the theoretical background of the tests, their applicability for 3DP-SHCC and their possible limitations.

8.2. THEORETICAL BACKGROUND

This chapter will address multiple tests that are based on the fundamentals of rheology, i.e. the study of flow behavior. Therefore, this section will provide a concise introduction to the field of rheology within the context of cementitious materials.

Fresh concrete can be thought of as a yield stress fluid, which means that it behaves as a liquid when a stress is applied above a critical yield stress and as a solid when the applied stress is below the critical yield stress [80, 130]. An overview of all common fluid types is given in figure 8.1.

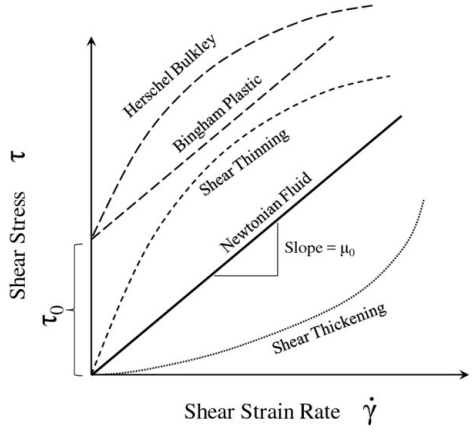

Figure 8.1: Presentation rheological models for fluid types [210]

The simplest type of rheological model that can be used to describe cementitious materials in the fresh state is the Bingham model [170]. It presents a linear relation between the applied shear rate and the shear stress as expressed in equation 8.1 [211].

$$\tau = \tau_0 + \eta \cdot \dot{\gamma} \tag{8.1}$$

The Bingham model however does not account for shear thickening (increasing viscosity for increasing shear rate) or shear thinning (decreasing viscosity with increasing

shear rate) of cementitious materials. This however, can be taken into account when the Herschel Buckley (H-B) model [212] is used, and therefore this model is generally considered to be a very good representation for fresh concrete[213]. Also for 3D printable mortars it has been found that these materials can be better described by the Herschel-Buckley law.[214]. The Herschel-Buckley model can be described by equation 8.2.

Here the parameter **y** represents the (possible) non-linear behaviour of the cementitious material. If y = 1, the model simplifies to the Bingham model, when y < 1 the model presents a shear-thinning material and for y > 1 the rheological curve presents a shear-thickening material.

$$\tau = \tau_0 + \eta \cdot \dot{\gamma}^y \tag{8.2}$$

Fresh concrete rheological properties are also influenced by the flow history of the material. For fresh concrete, it can be said that the static yield stress and viscosity increase with increasing time the material has been in a condition of rest. This results from the thixotropy phenomenon, which is the accumulation of a structure that transfers stress between particles. When testing fresh cementitious mixtures with thixotropic properties, it's essential to account for this property in the testing procedure to obtain accurate and representative results.

8.3. MATERIALS

To investigate the applicability of various fresh material tests for 3DP-SHCC, three mix designs were selected for the experimental trial. Two of these mixes, D-PVA8 and D-HDPE, have already demonstrated good printing results in chapter 7. In addition, D-PVA8 has proven good printability properties within multiple other printing projects, including those with alternating printing speeds and nozzle designs [72, 183]. D-PVA8 and D-HDPE are reinforced with 2 volume % of Polyvinyl alcohol (PVA) fibres and High-density polyethene (HDPE) fibres, respectively.

Table 8.1: Material composition, values in g/dm^3

Material	D-PVA8	D-HDPE	D-NoFib
BFS	262.8	262.8	262.8
Cem I 42.5 N	470.4	470.4	470.4
Silica Fume	32.9	32.9	32.9
Limestone	583.9	583.9	583.9
Sand 125-250	317.5	317.5	317.5
Water	400.2	400.2	400.2
PVA	26	-	-
HDPE	-	19.5	-
VMA	3.06	3.06	3.06
SP	2.68	2.68	2.68

For analyse and comparison purposes, D-NoFib has been selected for the experimental trial. This mix consists purely of the matrix design of D-PVA8 and D-HDPE, without the addition of fibres. For convenience the material composition can be found in

table 8.1.

All the tests were conducted on material from 0.8 liter batches unless specified differently in the specific test description. The deployed mixing routine was identical for all three mix designs and can be found in section 5.2.2.

8.4. METHODOLOGY

In this study the following fresh mechanical tests were selected:

1. Slump flow table test (SFTT)
2. Unconfined uniaxial compression test (UUCT)
3. Ram extruder test (RAM)
4. Slow penetration test (SPT)
5. Amplitude sweep test (AST)
6. Flow curve test (FCT)

The tests were performed three times per mix design over a period of, or with a sequence of one hour.

In literature, there is no universally agreed-upon framework regarding the criteria required to ensure the validity and reliability of tests. The American Society for Testing and Materials (ASTM) has presented some criteria that should be satisfied for a test to be considered applicable or appropriate [215]. This research will assess the tests based on the four main criteria that ASTM defined, namely: Reliability (by ASTM defined as applicable), explicit, unambiguous, and feasibility. In addition to these four, this research has added a fifth criterion: Repeatability, defined by ASTM as the variation in measurements taken by a single person or instrument on the same item and under the same conditions [216].

The definitions of the five evaluation criteria for fresh mechanical testing are given below:

- **Reliability**: The testing equipment can measure the mechanical or material properties as anticipated.
- **Explicit/Precise**: The test is able to supply accurate and precise data and this can clearly distinguish the different materials and material ages.
- **Unambiguous**: It is clear how to obtain the desired parameters from the retrieved raw data, this procedure is not open to multiple interpretations.
- **Repeatability**: Also called re-test reliability, is the variation in measurements taken by a single person or instrument on the same item and under the same conditions. For this study the coefficient of variation (CoV [%]) ((standard deviation/mean value) x 100%) is the chosen index for repeatability. There is no test independent guideline for CoVs, however from literature it can be deducted that a CoV <5% is regarded as excellent, and CoVs below <20% are considered good [216–218]. The test conducted in this study will be assessed as repeatable when the CoV is <20%.

- **Feasibility**: This covers multiple aspects such as: The ease of operating the test set-up, the time it takes to conduct the test, and the difficulty of data analyses.

8.4.1. SLUMP FLOW TABLE TEST

The slump flow table tests, due to the straightforward test apparatus and protocol is a suitable method for quickly assessing the printability of various fresh mixtures. Consequently, this approach has gained widespread adoption in the evaluation of 3D concrete printing (3DCP) materials [12, 177, 219–223]. The slump flow table test does not directly measure the yield stress nor does it provide information on the thixotropy of a material. However, the spread diameter offers insight into the workability, which can be related to the yield stress [180, 224, 225]. A concrete mixture with a large spread diameter is generally associated with a lower yield stress, and vice versa.

The workability of the three fresh materials was assessed using a slump flow table test following the guidelines of EN 1015-3 [176]. This test uses a circular rigid flow table, which is dropped 15 times without significant friction from a height of 12.7 mm. The material is filled into a smooth cone with dimensions of 60 mm in height, 70 mm in top diameter, and 100 mm in bottom diameter.

The flow table test was conducted at various time intervals to evaluate the workability over time. Specifically, the tests were performed at t=10, 15, 20, 25, 30, 40, 50 and 60 minutes, with t=0 representing the time of water addition during the mixing process. For analysis purposes, a recording camera was positioned above the test setup to capture the top view. The average spread diameter of the material during testing was accurately determined through image analysis. A more thorough description of the test set-up and test methodology is given in 5.3.1.

8.4.2. UUCT

In this research, the unconfined uniaxial compression test (UUCT) was used to determine the development of the green compression strength and the apparent Young's Modulus of the printable mortar. The UUC test is a fundamental method used in soil mechanics to assess the mechanical properties of soils, particularly cohesive soils such as clays. Since the mechanical behaviour of 3D printable mortars is assumed to be similar to that of soils, namely that its green strength can be attributed to a combined inter particle friction and cohesion [226], the UUC test is also used for the determination of fresh mechanical properties of printable mortars.

Based on the ASTM D2166 standard [146], and initial application of this test method on printable mortars by Di Carlo [227], the UUCT method has been further developed by Wolfs et al. [226]. This modified UUCT is well accepted in the industry for the quantification of fresh properties of 3DP mortars [78, 87, 91–94, 227–229].

The tests were conducted in displacement-controlled mode at a speed of 30 mm/min. The material underwent testing during the initial hour of hydration, with measurements taken at intervals of 10, 20, 30, 45, and 60 minutes, with t=0 minutes corresponding to the moment when water was added during the mixing process. Three specimens were tested for each time interval. The apparent Young's modulus was determined using the Hooke's law (equation 8.3), and calculated with the compression stress and strain of the elastic part of the stress-strain curve (measured at 5% strain).

$$E = \frac{\sigma}{\epsilon} \tag{8.3}$$

For the full description of the test set-up and the deployed methodology, please refer to section 5.3.4.

8.4.3. RAM EXTRUDER TEST

THEORY

A ram extruder, in the field of rheology known as a capillary rheometer, is widely deployed for determining the rheology properties of viscous materials, including 3D printable concretes [10, 230–235]. In this research the test is evaluated on its ability to obtain the yield stress values of the 3DP-SHCC materials. The test is performed with a piston that pushes the material from a larger reservoir through a small die, while the force that is needed to enforce this converging flow is measured by the connected load cell. The data acquired is generally analysed with the Benbow-Bridgwater model (BB) [143] or the Basterfield model [236].

The BB model is presented in chapter 3 equation 3.3. The BB model describes the overall pressure measured during the ram extrusion as the combination of two separate phenomena, the flow from the barrel into the die (P_1), and the flow through the die (P_2) [143]. The linear version of the BB model, in which the exponent parameters n and m are set equal to one, is also commonly applied for paste analysis [144]. To determine the fresh mechanical properties including the bulk yield stress, each mixture variant needs to be extruded through at least three different die lengths and four different speeds.

The equation for the Basterfield model is given in equation 8.4 [236]. The calculated bulk yield stress is directly related to the Herschel Buckley material model as presented in figure 8.1. In contrast to the BB model, the Basterfield model requires the material to be tested with only one short die.

$$P = 2\sigma_{Y,HB} \cdot ln(\frac{D}{d}) + Ak_{HB} \cdot (\frac{2V}{d})^n \cdot [1 - \frac{d}{D}]^{3n} \tag{8.4}$$

$$A = (2/(3 * n)) * (sin(\theta_{max})(1 + cos(\theta_{max})))^n \tag{8.5}$$

where,θ_{max} is the angle of the static zone at the end of the barrel in [deg], as presented by Basterfield [236].

P	= Total pressure drop [kPa]
$\sigma_H B$	= Bulk yield stress (Herschel-Buckley) [kPa]
A D	= Barrel diameter [mm]
d	= Die diameter [mm]
V	= Extrusion speed in the die land [mm/s]
n	= non linear fitting coefficients
θ_{max}	angle of the static zone at the end of the barrel in [deg]

Distance [mm]	Piston speed [mm/s]	Extrusion speed [mm/s]
0-13.5	2	18
13.5-27	1	9
27-40.5	0.5	4.5
40.5-54	0.25	2.25
54-67.5	2	18

Table 8.2: Speed program for piston

METHODOLOGY

The ram extrusion tests were performed with a laboratory ran extruder, with a barrel diameter of 38.4 mm and die diameter of 12.8 mm. The geometry is shown in figure 8.2.

One single ram extrusion test consists of a speed program with 4 different speeds on one fixed die length. The test has to be performed on three different die lengths to obtain the rheology properties of a material. A description hereof can be found in table 8.2. Due to the laborious nature of the test, only two batches of material were tested per die length, over the course of the first hour. To account for the reduction in material batches the time intervals were increased to: t= 8, 13, 28, 33, 43, 48 and 56 minutes. Where t=0 minutes is defined as the time of water addition in the mixing procedure. The three die lengths that were utilised have length over diameter ratios (L/D) of 1, 4 and 8.

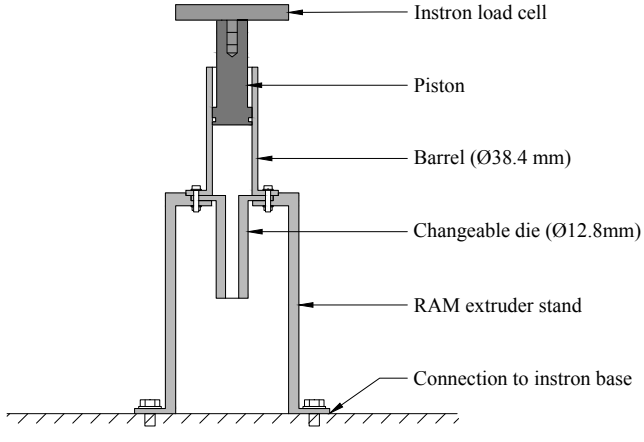

Figure 8.2: Cross section of ram extruder

During the test the normal force is measured that is needed to extrude the material from the barrel through the die, at a specific speed and die length. From the measured normal force and the barrel diameter the average pressure is calculated which is the required input for the BB and Basterfield model. From the research conducted in chapter 3 it is known that the measurements from the ram extruder test can be scattered. Therefore the measured data was analysed with two different strategies.

In the first strategy, a regression line of pressure over time is formulated based on the 14 data data points (2 specimens x 7 time steps), to represent the average pressure development over time, as illustrated in figure 8.3. Based on this regression line the average pressure of the material for timestamps t= 10, 30, 45 and 60 minutes, per speed and die length was determined. This post-processed data was then used as input for both the linear and the non linear BB models and the Basterfield model.

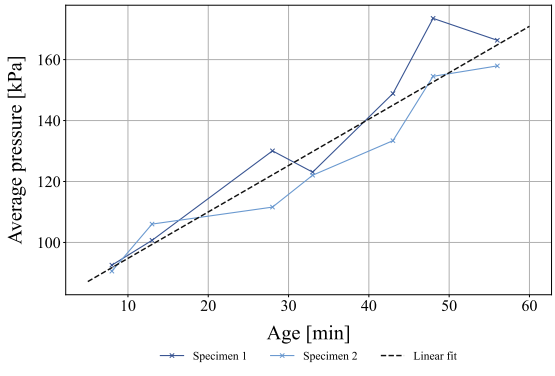

Figure 8.3: Strategy 1, ram extrusion linear fit (D-HDPE)

In the second strategy, the bulk yield stress was determined for all separate time stamps and specimens, by means of the two BB models (linear and non linear) and the Basterfield rheology model. Based on the values calculated with these models, a trendline was determined for the development of the bulk yield stress over time.

In total, the derived measured average pressure will be analysed in 6 methods, strategy 1 combined with linear BB, BB and Basterfield and strategy 2 combined with these same three material models.

It should be noted that the Basterfield model describes a material that is extruded through a tapered die [231] that has no effective die length. For the data analysis in this research this corresponds to a die with a L/d of 1 is deployed.

8.4.4. SLOW PENETRATION TEST

THEORY

The slow penetration test provides a systematic way to measure the development of rheological properties of 3D printable cementitious materials [89, 237, 238]

The slow penetration test deviates from the tests mentioned above as it is able to test the material continuously over time. In the test the required force to penetrate the material is measured and recorded continuously over the time frame of interest, normally until the final setting time of the material. Depending on the specific contact surface area of the penetration probe, the yield stress can be obtained from the recorded forces. The slow penetration test, as developed by Lootens et al, [89] prescribes a very low vertical velocity of 1 μm/s. Due to the low velocity of the probe the measurement is regarded

as quasi-static, and the yield stress that is obtained is regarded as the static yield stress of the material.

Penetration tests on cement pastes and mortars can be performed with probes of many different shapes (needles, conical, and (hemi)spherical) and sizes (5-15 mm) [89]. For a probe with a hemispherical tip in combination with the Bingham material model (see figure 8.1) and the Stokes' Law [89], the determination of the static yield stress is presented in equation 8.6.

$$\tau_0 = \frac{F}{3 \cdot \pi \cdot R_{probe}^2} \tag{8.6}$$

This equation is determined on the basis that the drag force acting on the penetration probe during testing is proportional to the yield stress, and under the assumption that Stokes' Law, originally derived for a sphere in a Newtonian fluid, can be extrapolated to this context [89]. Furthermore, it necessitates the mounting rod to be smaller than the sphere diameter (see figure 8.4b), and for the material to maintain constant surface contact with the bottom half of the penetration sphere. To achieve the latter, the material must exhibit sufficient stiffness to prevent the closure of the gap above the sphere, as depicted in the figure 8.4a. Additionally, the container holding the fresh material specimen should have a sufficiently large diameter for it not to intervene with the free material flow of the material, thus ensuring accurate test results.

Under these conditions, a good indication of the static yield stress development over time can be obtained from the slow penetration test.

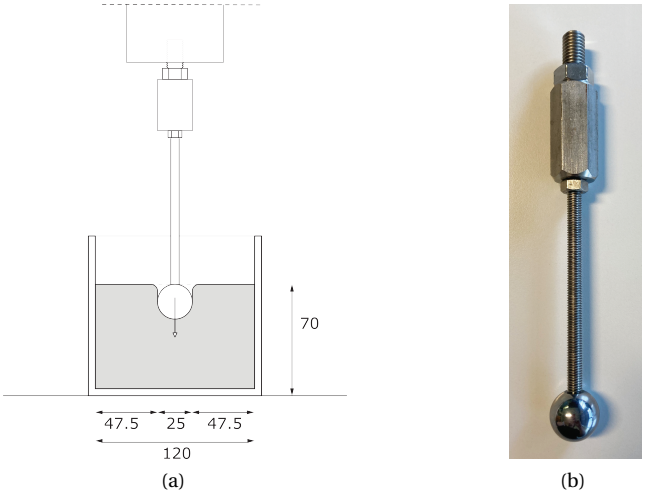

Figure 8.4: Slow penetration test a) Overall set-up, measurements in mm b) Penetration probe

METHODOLOGY

For this study, careful consideration was given to the design of the probe in accordance with the fibre geometries present in 3DP-SHCCs. A spherical tip was selected to prevent

the tip from cutting through the present network of fibres, as can be expected with a conical tip. Additionally, the diameter of the sphere was chosen to be at least three times the fibre length, in order to retrieve the bulk material properties. The slow penetration tests were therefore conducted with a 25 mm diameter spherical tip in combination with a cylindrical cup of 120 mm diameter. In figure 8.4 the setup of the slow penetration test is presented.

The vertical velocity of the probe was set to 1 μm/s, in order to achieve a quasi-static behavior. The associated static yield stress was calculated with equation 8.6. The displacement of the penetration probe and the exerted load are saved every second.

Two minutes prior to testing the spherical tip was fully submerged into the material in the cup, to achieve full surface covering of the bottom half of the sphere. This initial penetration was conducted with a speed of 1 mm/s, and from a height of 30 mm. For the remaining time, the material was kept at rest, while the cup was covered with plastic film to prevent moisture evaporation from the material during testing. The test was started at t=10, where t=0 minutes is defined as the time of water addition in the mixing procedure. Before testing, the load cell was set equal to zero.

8.4.5. STRAIN AMPLITUDE SWEEP

THEORY

Oscillating strain amplitude sweep is a rheological test method commonly used to study the viscoelastic behavior of (prinatble) materials that exhibit both viscous (liquid) and elastic (solid) characteristics [234, 239–241]. It involves subjecting a specimen to a range of strain amplitudes while measuring the torque exerted by the material. This strain is imposed by a measuring system, which can vary from e.g. plate-plate, vane and cup or ball measuring system.

A strain amplitude sweep test is performed by increasing the strain amplitude gradually, starting from a low value and incrementally increasing it until the material's response changes significantly. See figure 8.5a for the concept of a strain sweep. During the test, the rheometer measures the stress response (torque) of the material on the vane as a function of the applied strain amplitude. In the case of a vane and cup set-up the shear stress can be derived by the following equation:

$$\tau = \frac{T}{2 \cdot \pi \cdot h \cdot r^2} \tag{8.7}$$

In which T is the measured torque, r is the vane radius and h is the height of the rotating vane.

The stress response is represented in terms of an elastic modulus (G") and viscous modulus (G'), and is measured over a range of strain amplitudes. The relation of G" versus G' provides information about the material's ability to store and dissipate energy under deformation.

By plotting the stress response of G' and G" as a function of the shear strain, a rheological curve is obtained, see figure 8.5b. This curve exhibits distinct regions that provide valuable information about the material's behavior.

One of the outcomes of this test is the data on the linear visco-elastic region (LVR), where the material's response is predominantly elastic. In this region, the stress response is proportional to the strain amplitude, and the material exhibits a linear relationship between stress and strain. The shear stress that represents the end of the LVR is generally regarded as the dynamic yield stress τ_y.

The second interesting parameter that can be obtained is the flow stress (τ_f). The flow stress is measured at the intersection of the G' and G" and therefore represents the strain rate and stress at which the material behaves more like a fluid than like a solid.

The zone between τ_y and τ_f is called the yielding zone. The yield stress (τ_y) represents the lower bound value, and the flow stress (τ_f) the higher bound value. Therefore, in this paper the flow stress τ_f will be related to static yield stress of the material, where the yield stress (τ_y) will be regarded as the dynamic yield stress.

A typical rheological curve with the aforementioned parameters can be found in figure 8.5b.

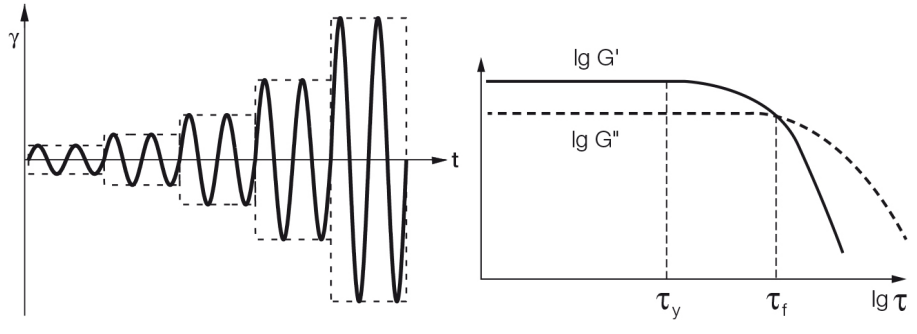

(a) Testing concept of Amplitude sweep test

(b) Yielding zone of amplitude sweep test between τ_y and τ_f

Figure 8.5: Amplitude sweep test method [242]

8

METHODOLOGY

The amplitude sweep test was conducted on an Anton Paar MCR 502 rheometer in combination with a (four-blade) vane (diameter: 22 mm; height: 40 mm) and a small ribbed cylindrical cup (inner diameter: 28.92 mm; depth: 68 mm). The cup and vane set-up is a widely used measuring tool, as the insertion of the vane causes minimal disturbance to the specimen in the cup and secondly because the setup is known to avoid wall slip [239, 243].

The test was conducted with a constant angular frequency of 10 ω/s and a variable oscillating shear strain γ with a logarithmic ramp starting from 0.01 to 1000 %. In total 25 data points were collected during the course of the test.

The ribbed cup was filled three minutes prior to testing, until testing height, which was equal to a total weight of 400 ($\pm$1) grams (cup: 315.2 grams and material: 94.8 grams). To ensure a constant material volume throughout the experimental program the material weight was kept constant throughout the testing program.

One minute prior to testing the vane was inserted into the material. For the remainder of the minute, the material was kept at rest. The surface of the material in the cup was covered with vaseline to prevent the material from dehydrating during testing.

The (dynamic) yield stress was determined as the shear stress at the limit of the linear visco-elastic region. The limit of the linear elastic region was set to a 5% drop from the average of the LVR plateau. The flow stress was quantified as the intersection of the G' and G" curves.

8.4.6. FLOW CURVE TEST

THEORY

The flow curve test, also known as a shear rate sweep test, is a test performed to evaluate the yield stress and viscosity of a material as a function of shear rate. The flow curve test is adopted to study the rheology properties of 3D printable mix [244–248].

In this test, which is commonly conducted using a rotational rheometer, the shear rate is increased from low to high values in a step-wise manner. The material is subjected to a shear rate for a predefined duration, allowing the material to reach a steady state response and ensure accurate and consistent data (figure 8.6a). The rheometer measures the torque required and calculates the corresponding shear stress as a function of the applied shear rate.

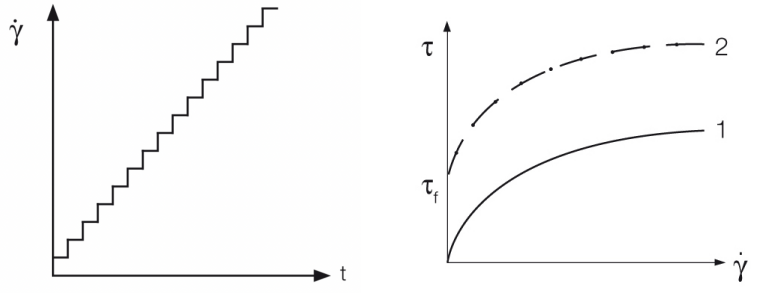

(a) Testing concept of Flow curve

(b) Flow curve results of two materials related to Herschel Bulkley

Figure 8.6: Flow curve test method [249]

For the calculation of the shear yield stress equation 8.7 is adopted. Under the assumption of a Bingham fluid the viscosity can be derived by the following equation:

$$\eta = \frac{\tau}{\dot{\gamma}} \tag{8.8}$$

In which $\dot{\gamma}$ is equal to the strain rate imposed by the rheometer.

Dependent on the size of the gap between the vane and the cup, the velocity profile inside the material may not be linear for non-Newtonian materials [243, 250]. Therefore it must be noted that the viscosity, for this specific vane-cup set-up (gap size = 6.9 mm), is derived by approximation.

METHODOLOGY

The flow curve test was deployed to retrieve the yield stress of the three mixes. The tests were performed on a Anton Paar MCR 502 rheometer equipped with the same vane and cup set-up as the amplitude sweep test. The measurements were conducted by executing a linear shear rate sweep, commencing at 0.4 s^{-1} and increasing by 0.4 s^{-1} every 30 seconds until reaching a maximum value of 4 s^{-1}. Subsequently, the shear rate decreased in the same incremental manner until a shear rate of 0.4 s^{-1} was achieved. For each shear rate, 10 data points were collected. The resulting flow curves were fitted to the Herschel-Bulkley model to obtain the yield stress values. The specimen preparation was identical to the amplitude sweep test.

8.5. RESULTS AND DISCUSSION

This section will systematically present and analyse the results obtained from each fresh mechanical or rheological test. Drawing from these results and the insights gained throughout the experimental trial, the test is evaluated based on the five predefined criteria.

8.5.1. SLUMP FLOW TABLE TEST

The average flow diameter results of the slump flow table test are presented in figure 8.7. The addition of fibres into the mix has a significant effect on the fresh behavior of the material, as had already been reported in chapter 7.

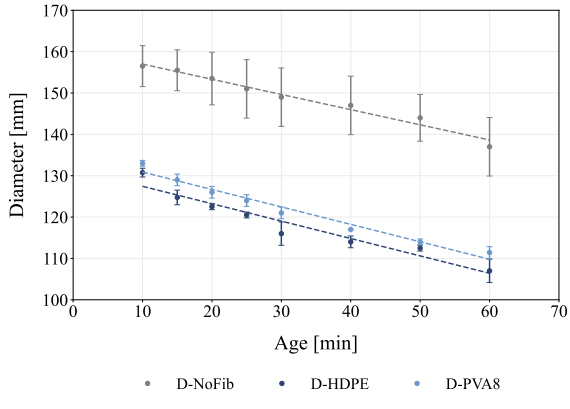

Figure 8.7: Average results with standard deviation obtained from the slump flow table test

D-NoFib has an initial spread flow of 158 mm. This reduces by 21 mm (12.5%) over the course of the first hour. Lower spread diameters are measured for Mix D-PVA8 and Mix D-HDPE, with initial values of 133 and 131, respectively. The spread diameter of the fibre-containing mixtures show higher reduction after an hour, with reductions of 16.2 and 18.2 %, respectively.

Noteworthy is the difference in standard deviation for the increase in spread, (i.e. the measured diameter - the initial diameter (100 mm)). The fibre reinforced mixes, D-PVA8 and D-HDPE, in general have a coefficient of variation lower than 10%, mix D-NoFib has

a significantly higher coefficient of variation which varies between 9-20%.

In terms of applicability for 3DP-SHCC the test is assessed on the following five criteria:

Reliability: The testing equipment is able to agitate the material sufficiently to initiate material flow, and therefore the anticipated flow diameter can be measured.
Explicit/ Precise: The test can distinguish the three different mix designs, but the measured difference between D-HDPE and D-PVA8 is relatively small. It is therefore doubtful if this test is precise enough to explicitly distinguish mixtures with smaller variations in material composition.
Unambiguous: As the measuring of the spread flow diameter is straightforward and highly tangible the test is regarded as unambiguous.
Repeatability: It is found that the 3DP-SHCC mixes D-HDPE and D-PVA8 have a lower margin of variability between the samples than the less viscous mix D-NoFib. For all mixes the CoV was found to be <20%, therefore the slump flow table test was found to be repeatable for 3DP-SHCC mix designs.
Feasibility: The test is very accessible, easy to use and as there is no data post-processing needed to obtain distinct results. The test is assessed to be very feasible.

The test is especially meaningful when suitable ranges of spread flow diameters have been empirically determined for the allocated printing system, as was done in the publications of Cho et al. and Tay et al. [177, 219]. These studies show that the region of printability is pump and print set-up dependent, as was confirmed by the printability of Mix C and D-HDPE in chapters 5 and 7, respectively.

8.5.2. UNCONFINED UNIAXIAL COMPRESSION TEST

The results of the UUC tests are presented in figures 8.8 and 8.9. The specimens of the D-NoFib mixture exhibited insufficient strength for testing at a 10-minute age, necessitating the exclusion of this timestamp from analysis for this specific mixture.

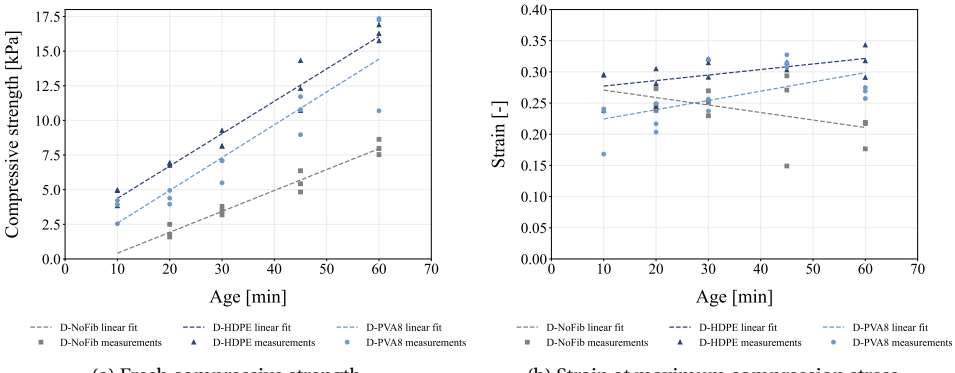

(a) Fresh compressive strength

(b) Strain at maximum compression stress

Figure 8.8: Development of fresh compressive strength and strain over time, derived from the UUCT

Among the tested mixtures, D-HDPE demonstrated the highest initial compression strength, followed by D-PVA8 and D-NoFib. Notably, the trend lines of the two fibre-reinforced mixtures ran in parallel, suggesting an equivalent rate of compression strength increase. The D-NoFib mix has significantly lower initial compression strength (at the 20 minute mark) and displays a slower strength increase over time. The same trend was found for the Young's modulus (figure 8.9). Remarkably, D-NoFib showed the most pronounced increase in Young's modulus development, indicating rapid stiffening of the mixture.

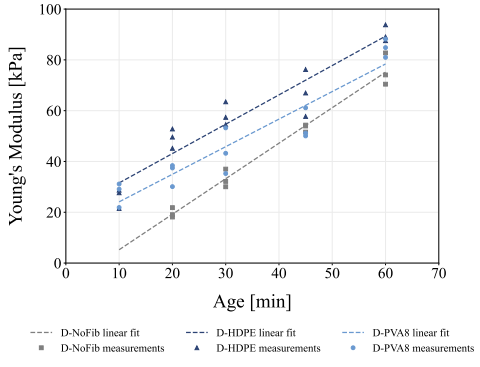

Figure 8.9: Development of Young's modulus over time, derived from the UUCT

As expected, the development of the strain at peak load presented the inverse trend for the mix without fibres in comparison to the two fibre reinforced mixes. Where D-NoFib becomes more brittle over time, D-PVA8 and D-HDPE show an increase in ductility over the course of the first hour and are thus able to deform significantly more before failure. This indicating that the incorporated fibres are already able to distribute some of the induced stresses in fresh state.

On average, the coefficient of variation for the compressive strength, strain and Young's modulus was measured to be 13.2 %, 10.8 % and 10.5 %, respectively. However the CoV measured for the individual materials and time stamps was occasionally relatively high, namely >20%. This has been reported in the recently published work of Pott et al. [93] who reviewed the test for non-fibre reinforced printable mortars. In the publication a list of recommendations is provided on, for example, specimen preparation, to keep the scatter low.

Reliability: The test is able to measure the compressive stress and deformation during testing.
Explicit/ Precise: The raw measurements are precise and enable the calculation of the three material properties. It is easy to distinguish the tested materials and the test provides valuable insight into the strain capacity of fibre reinforced mixtures in fresh state. As the cross-sectional area of the specimen changes during the test an additional camera (to measure the diameter of a additional side view) can benefit the precision of of the final compressive strength and Young's modulus results.
Unambiguous: Calculation of the three material properties is founded on the Hooke's

law material equation, and therewith is unambiguous.
Repeatability: Careful specimen preparation is needed to keep scatter between test results low and to make the test reproducible. A sufficient number of specimens is needed to achieve reliable output parameters.
Feasibility: The testing procedure of the UUC test is relatively simple and does not require the use of high-end equipment. Nonetheless, the process of acquiring real-time specimen diameters from the camera images and subsequently correlating them to the stress-deformation curve can be a labour intensive task. With additional equipment and specialised software this part of the data analysis can be automated, significantly enhancing the feasibility of the test method.

8.5.3. RAM EXTRUSION TEST

The measured data obtained from the ram extrusion tests were analysed with two strategies each deploying the three material methods: the linear and non-linear Benbow-Bridgwater models, and the Basterfield model. As only two batches of materials were tested over the course of an hour, a valuable CoV could not be obtained for this test. To give an impression of the repeatability of the test, figure 8.10 presents the individual data points and their trendlines of the two material batches. The presented materials were tested with an extrusion speed of 9 mm/s and a die with L/d equal to 4.

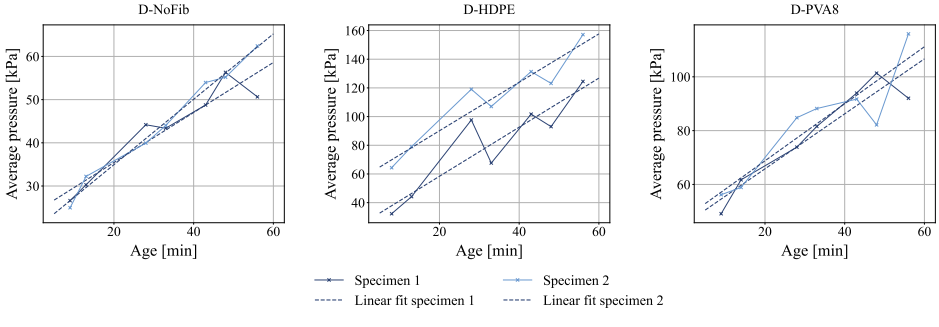

Figure 8.10: Pressure measurements and trend lines for two material batches (speed = 9 mm/s and L/d = 4)

Based on strategy one, the bulk yield stress calculated based on the average pressure-over-time trend lines are illustrated in figure 8.10. The development of the bulk yield stress over time per material for each the three material methods are presented in figures 8.11a - 8.11c.

The figures show that the difference between the material models, within strategy 1, is very low. When the values derived from the three deployed methods are averaged, the yield stress of D-NoFib increases from 4.4 kPa to 14.4 kPa from 10 to 60 minutes. The highest yield stress is measured for D-HDPE with 30.4 kPa to 65.0 kPa, which is almost double the values of D-PVA8, which increased from 15.2 kPa to 26.3 kPa.

In strategy 2, the bulk yield stress of the individual timestamps and specimens was calculated directly from the measured average pressure, using the three material models. Subsequently, a trend line was constructed based on the derived bulk yield stresses. The results can be viewed in figures 8.12a - 8.12c, that present the yield stress develop-

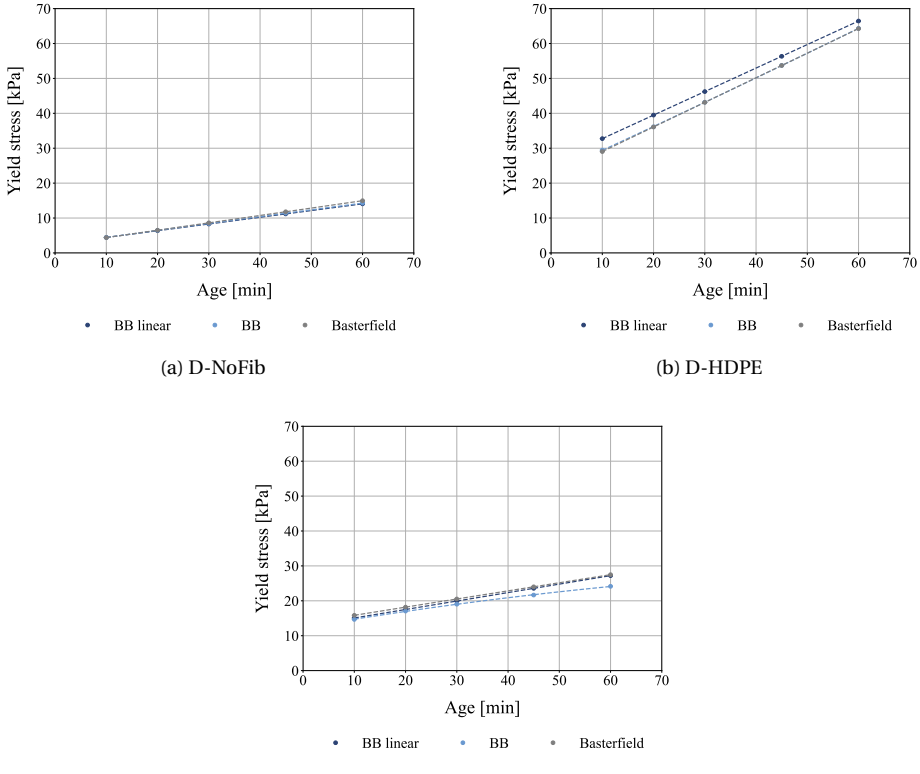

(a) D-NoFib

(b) D-HDPE

(c) D-PVA8

Figure 8.11: Bulk yield stress retrieved with strategy 1 for a) D-NoFib b) D-HDPE and c) D-PVA8

ment over time of the materials per material model. To facilitate comparison, figure 8.13 includes the yield stress of the materials for each fitting method for specific time stamps, namely 10, 30 and 60 minutes.

Upon examination of the results, it becomes evident that strategy 2 demonstrates notable variation across the three material models. Particularly noteworthy is the variability observed in the values obtained for D-HDPE, which display significant fluctuations across the models. This is combined with high scatter for the calculated singular yield stresses for each specimen, that additionally exhibits an irregular evolution over time. This observation is especially evident when employing the BB models, as the data points resulting from the Basterfield model are less scattered.

When analysing the underlying data, an anomaly emerges in the pressure measurements when the test is conducted with an L/d ratio of 4. For specimen 2 the pressure needed to extrude the material through a L/d=1 die is higher than that of a L/d =4. Additional graphs confirming this measurement have been added in appendix B section B.3.2. Since the Basterfield model only considers measurements obtained from the L/d ratio of 1 die, the deviating measurements for the L/d ratio of 4 are disregarded. Conse-

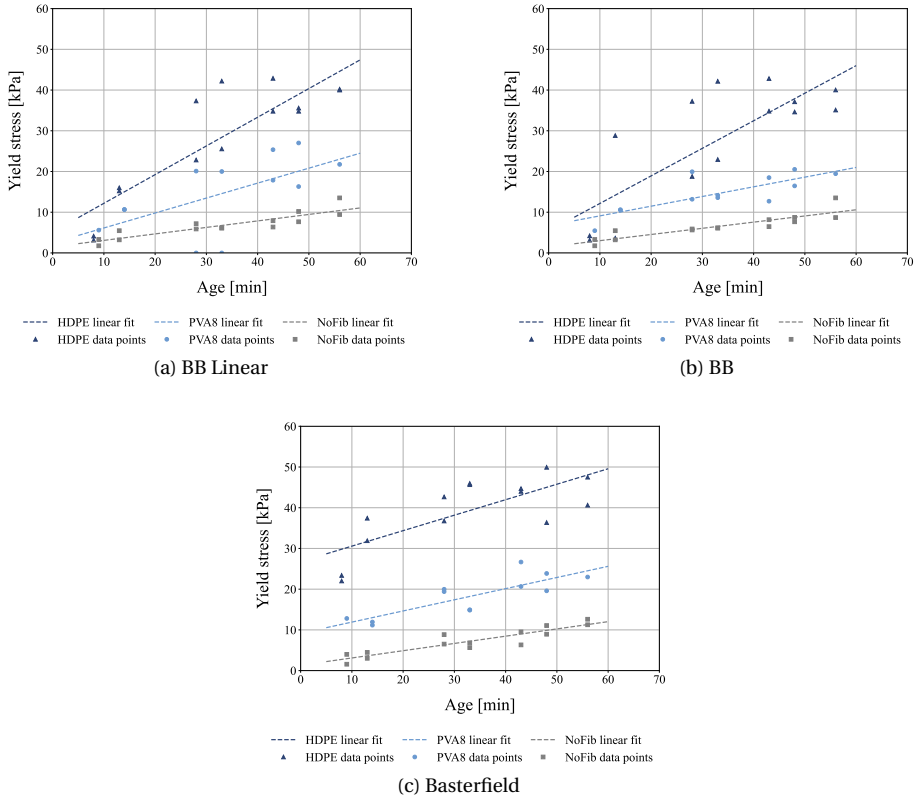

Figure 8.12: Bulk yield stress retrieved with strategy 2 for a) BB Linear model b) BB model and c) Basterfield model

quently, this simplifies the task for the models to ascertain the corresponding yield stress and formulate a plausible linear fit over the data points to depict the yield stress development. Furthermore, by deploying the Basterfield model the number of ram extrusion tests that needs to be performed reduces with 2/3.

The results and data analysis show that 3DP-SHCC materials are much more sensitive for ambiguity between the different material methods than the non fibre containing mix D-NoFib, as mix D-NoFib presented hardly any variance in its general trend line between the material models within the two deployed strategies.

Reliability: The method is able to extrude all the materials through the die and measure the required pressure to do so. However, for the fibre reinforced materials inconsistency was measured for the pressure needed for the different die lengths.
Explicit/ Precise: The data output is very precise and explicit.
Unambiguous: From the performed research it has become clear that the ram extruder test combined 3DP-SHCC is ambiguous. High variance was found between the different

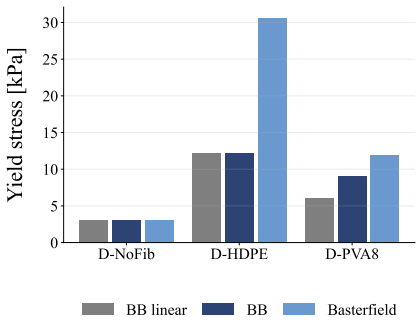

(a) 10 minutes

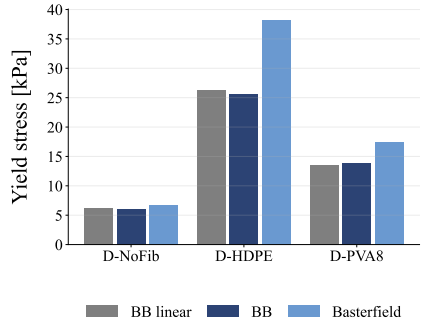

(b) 30 minutes

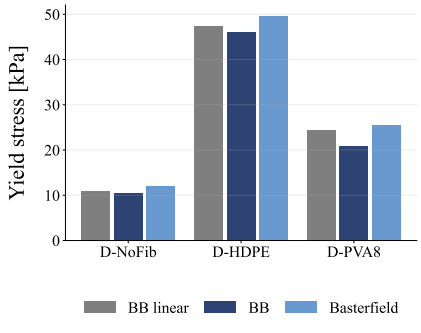

(c) 60 minutes

Figure 8.13: Static yield stress values for the time stamps 10, 30 and 60 minutes derived from trend lines

8

material analysing methods, where clear overlap was found for mix D-NoFib.
Repeatability: No CoV could be determined for this test. However, from the pressure over time trend lines and the pressure over die length ratio high deviations can be observed between the individual material batches. Because the BB models depend on the input of three individual tests (3 die length), this scatter can result in unreliable model fits and rheology properties.
Feasibility: The test demands thorough data-analysis to obtain the rheology properties and intense labor, as cleaning of the barrel between measurements is needed for accurate pressure measurements. The test is feasible but demanding, especially when performed over a time sequence.

8.5.4. SLOW PENETRATION TEST

The findings from the slow penetration test are presented in figure 8.14. From the test results, we can conclude that mix D-HDPE develops the highest static yield stress over the course of the first 100 minutes, followed by D-PVA8 and D-NoFib.

Due to test method, the test begins with a zero value for the static yield stress. The

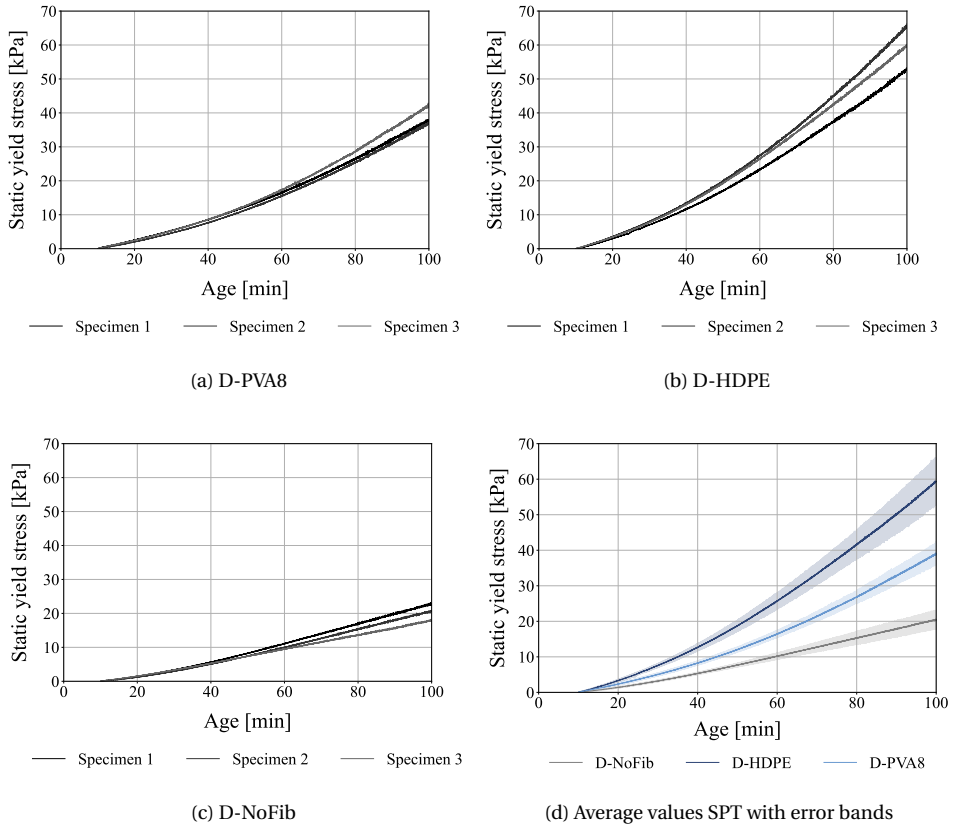

(a) D-PVA8

(b) D-HDPE

(c) D-NoFib

(d) Average values SPT with error bands

Figure 8.14: Static yield stress development over time, SPT

test therefore is only applicable to measure the development of the static field stress over time, with the assumption that $\sigma_y = 0$ at the time the test is initiated, which in this case was at 10 minutes after adding of the water. With this in regard, mix D-NoFib develops over the course of 50 minutes (timestamp = 60) to 10.2 ±0.83 kPa. Mix D-HDPE develops towards 25.70±2.14 kPa, and D-PVA8 towards 16.4±0.90 kPa. Resulting in a coefficient of variation <10% for all three materials. Due to the assumption that $\sigma_y = 0$ at the start of the test (t=10) direct comparison of the static yield stress values with yield stress properties obtained from other tests is not evident. However, the measured yield stress developments are in the same order of magnitude as was found for the ram extruder, when data was analysed with strategy 1 or strategy 2 + Basterfield.

Reliability: The slow penetration test is able to measure the static yield stress over time, without the introduction of flaws. Due to the assumption that $\sigma_y = 0$ at the start of the test, one should be aware that the test only provides an accurate value for the static yield stress development, but not the absolute values.

Explicit/ Precise: When enabling a precise load cell and measuring the load on the pen-

etration probe and the displacement frequently, the slow penetration test can clearly distinguish the tested mix designs and report precise values.
Unambiguous: The post-processing of the raw data is straightforward and unambiguous.
Repeatability: With a coefficient of variation <10% the test is regarded as repeatable.
Feasibility: The testing procedure and specimen preparation of the slow penetration test is straightforward and does not require any high-end equipment.

8.5.5. AMPLITUDE SWEEP TEST

The derived dynamic yield stress and flow stress are presented in figures 8.15a and 8.15b. Notably, D-HDPE exhibits the highest values for both parameters, followed by D-PVA8 and D-NoFib. The average dynamic yield stress curves show (slight) exponential growth over time, indicating that the dynamic yield stress develops slightly faster at later age. The static yield stress (i.e. flow stress) does not show this slightly exponential curve. Specifically, the D-NoFib values demonstrate nearly linear behaviour. Contrarily, for the self-reinforced mixtures, the average static yield stress curves gradually flatten at later ages, a trend inconsistent with previous findings in this research and with the literature on the evolution of yield stress in cement-based materials [251–253].

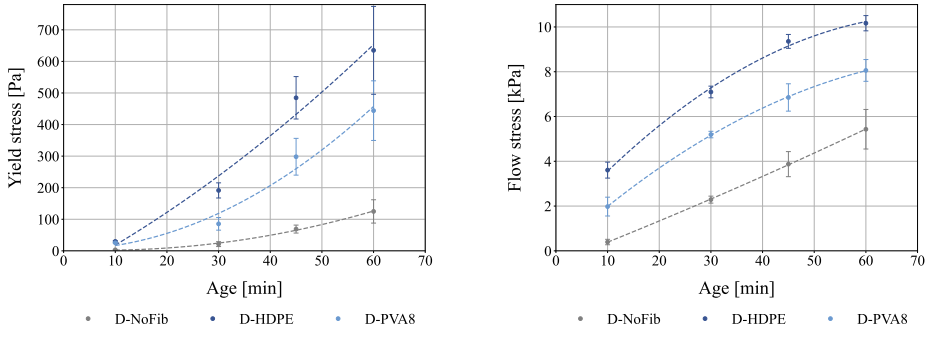

Figure 8.15: Amplitude test results with a) Average (dynamic) yield stress values with standard deviation and b) Average flow stress values with standard deviation.

In figure 8.16 the average curves obtained from the amplitude sweep test are presented in logarithmic scale. Here, it can be observed that the linear viscoelastic regions are longer and more stable for older materials, resulting in a higher dynamic yield stress.

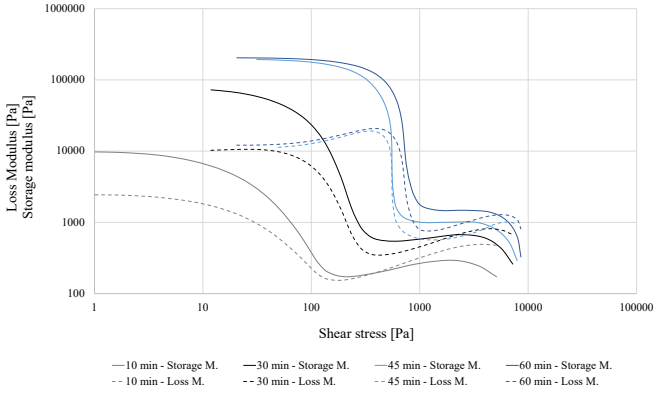

(a) D-NoFib

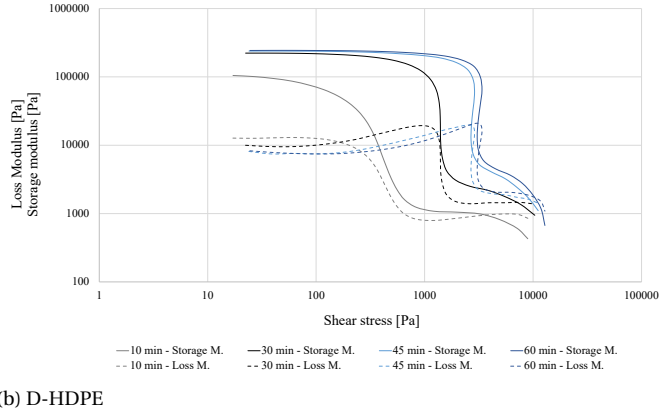

(b) D-HDPE

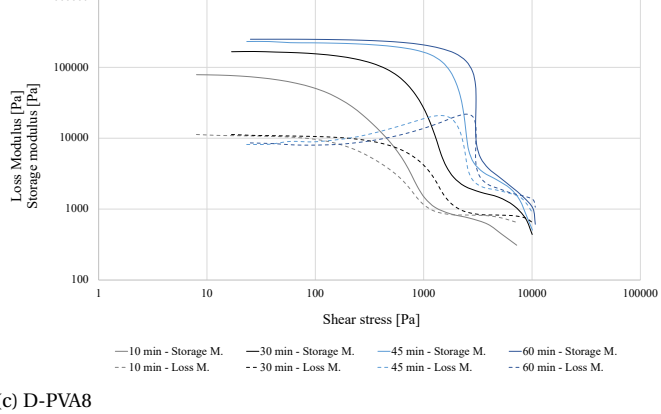

(c) D-PVA8

Figure 8.16: Average rheology curves of Amplitude sweep (log scale)

This trend is observed for both the non-fibre reinforced material as the two 3DP-SHCC materials.

The results regarding the static yield stress align with findings from a previous study involving a ball measuring system [103]. In that study, the material exhibited low recovery during testing, leading to the formation of a channel-shaped void behind the ball. The data on static yield stress suggests that with increasing viscosity of fresh material, the amplitude sweep test is less capable of measuring the material's rheology properties.

To investigate this hypothesis further, amplitude sweep tests were conducted on half-full cups containing mix D-NoFib and mix D-HDPE. Note that the boundary conditions in these tests differed from those in a full cup of material, where the vane is fully submerged into the material, with a one-centimeter layer of material covering the top of the vane. This configuration limits the material's freedom of movement compared to a half-full cup. Nevertheless, these tests provided valuable insights into the suitability of the test method itself. Figures 8.17a and 8.17b depict the material behavior during these high-amplitude tests for D-NoFib and D-HDPE, respectively.

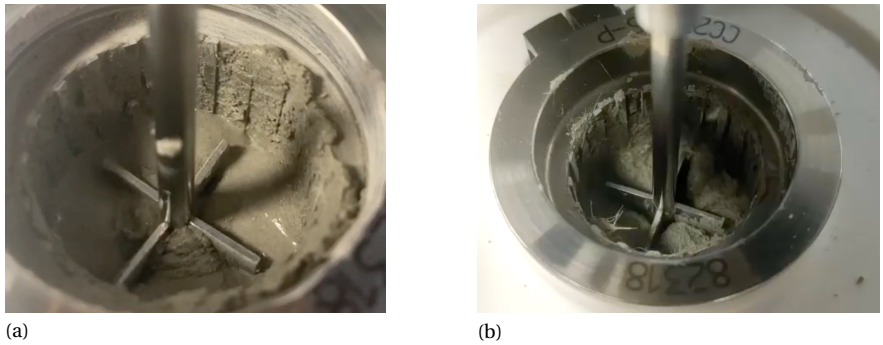

(a) (b)

Figure 8.17: Amplitude sweep on half-full cups with a) D-NoFib b)D-HDPE, which shows dead zones behind the vane.

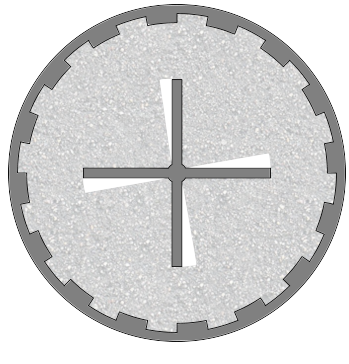

Figure 8.18: Dead zones during testing of 3DP-SHCC mixtures

In the case of D-NoFib, the material remains in contact with the vane throughout the

entire testing procedure. However, for Mix D-HDPE, this contact is lost as the amplitudes increase. The measuring system, however, calculates the reported values under the assumption that the vane remains in full contact with the material throughout the entire range of amplitudes. Given that this is likely not the case for fibre-reinforced materials, it raises questions about the reliability of the flow stress values obtained.

Further visual observations during the half-full tests suggest that the material maintains contact with the vane during the initial part of the test, when amplitudes are still relatively small. This observation makes the values found for the dynamic yield stress more plausible, especially considering the dynamic yield stress (see in figure 8.15a) presents the expected (exponential) increase over time. However, it is also apparent that the error margin is high, six out of the twelve averaged values (per material and timestamp) have a coefficient of variation that exceeds 20%.

Reliability: The amplitude sweep test is unable to correctly measure the flow stress and dynamic yield stress of the material, due to insufficient material recovery between the amplitude rotations of the vane.
Explicit/ Precise: The rheometer is able to measure very accurately the resistance the material imposes on the vane during rotations.
Unambiguous: If the material would behave in accordance with the assumptions of the test, the data analysis is straight forward and unambiguous. However, it does take a critical view and additional analysis to uncover any underlying complexities or deviations from these assumptions.
Repeatability: The material behaviour during testing results in relatively high scatter. This is particularly the case for the dynamic yield stress where 50% of the average values have a CoV > 20%.
Feasibility: The amplitude sweep test, when coupled with the cup and vane set-up, offers notable advantages in terms of ease of use and efficiency. Its testing duration is relatively brief, facilitating swift experimentation. Moreover, the rheometer's automated data processing capability minimises the time needed for analysis.

8.5.6. FLOW CURVE TEST

The flow curve test presented severe issues in determining the fresh mechanical properties of 3DP-SHCC. While conducting the tests of mix D-PVA8 and mix D-HDPE the specimen in the vane cup failed on shear around the edges of the vane, after which the rheometer recorded no values. The shear plane occurred early on in the test, at a maximum of two full vane rotations, which makes data analysis of the retrieved measurements meaningless. In figure 8.19 a specimen of mix D-PVA8 at the age of 10 minutes is presented, directly after testing. This tested specimen consists of two parts. The first part is at the top above the white line and shows the ribs of the cup. The second part, below the white line, is internally completely disconnected from the first part and covers the full length of the vane.

Based on these findings the flow curve test was excluded from the full experimental trial.

Figure 8.19: D-PVA8 specimen that failed on shear during testing at the age of 10 minutes

8.6. DISCUSSION

The objective of the conducted research was to evaluate the applicability of six fresh mechanical and rheological tests for 3D printable strain hardening cementitious composites. Table 8.3 presents the overall findings of this assessment.

Criteria	SFTT	UUCT	RAM	SPT	AST		FCT
					Dyn. yield stress	Flow stress	
Reliability	xx	xxx	x	xxx	o	o	o
Explicit/ Precise	x	xx	x	xx	xx	xx	o
Unambiguous	xxx	xxx	o	xx	xx	xx	o
Repeatability	xx	x	o	xxx	o	x	o
Feasibility	xxx	xx	x	xxx	xx	xx	o
Overal	xx	xx	o	xx	o	o	o

Table 8.3: Results on test assessment, with xxx = very good, xx = good, x = sufficient and o = poor or could not be assessed

Upon examination, it becomes evident that bulk material tests, including the slump flow table test, UUC test, and slow penetration test, prove applicable for determining the fresh mechanical properties of 3DP-SHCC. These tests effectively measure material properties of all three mix designs as expected, while demonstrating sufficient repeatability and precision, and exhibit low ambiguity. Moreover, their execution is very feasible, with clear procedures for testing and specimen preparation, and no requirement for high-end testing devices.

In contrast, fresh mechanical test methods that assess the material on a smaller scale, such as the ram extrusion test, the amplitude sweep test and the Flow curve test, show lower applicability for 3DP-SHCC. With the ram extruder, challenges arise regarding repeatability, this holds particularly true for mix D-HDPE. This inconsistency may stem from shear failure of the material when it converges under pressure from the barrel to the die. This failure type was visually observed during a preliminary ram extrusion test

(a) (b)

Figure 8.20: Shear failure during ram extrusion of mix D-PVA6 a) during extrusion b) after extrusion

conducted on mix D-PVA6, (specification of this mix design are presented in chapter 7). This test was performed outside of context of this chapter but yields interesting results. In figures 8.20a and 8.20b images of the material during and after extrusion are presented in which the shear failure of the material is visible. Notably, this material failure was only observed when the mix design was extruded with the short die. Although similar failures were not visually observed during the extrusion of D-HDPE and D-PVA8, the risk of material segregation is known for 3DP-SHCC [84]. Therefore, it should be considered a plausible factor contributing to the found high variation.

The flow curve test presented a similar material failure, here the material in and around the vane was sheared off from the material in the cup. The Amplitude sweep test proved inadequate for accurately measuring the mechanical properties of the fibre reinforced materials as expected. The limited material recovery of mix D-HDPE and mix D-PVA8 made it impossible for the rheometer to measure the material's resistance during vane oscillation.

The ram extruder and rheometer test methods may suffer from limitations in applicability due to their small-scale nature. Both setups feature narrow gaps (the ram extruder with a 12.8 mm die and the vane and ribbed cup with a 6.9 mm gap size) particularly noteworthy when considering the length of the incorporated fibres. The identified shortcomings of these tests in this study suggest that the physical dimensions of the testing set-up may significantly influence the reliability of the test results for 3DP-SHCC.

8.7. CONCLUSIONS

This research was conducted with the goal of assessing the suitability of various methods for testing fresh properties of 3DP-SHCC materials. A comprehensive experimental program was carried out, encompassing a range of tests commonly employed in the field of 3DCP. From the obtained results it can be concluded that the fresh mechanical testing of 3DP-SHCC is not evident and poses unique challenges, primarily due to the material's high viscosity and susceptibility to segregation under shear forces. In general the following statement can be made:

Bulk material tests, including the slump flow table test, UUCT, and slow penetration tests, are better suited for quantifying the properties of 3DP-SHCC. Unlike small scale tests like ram extrusion, amplitude sweep and flow curve tests, these bulk material tests are less susceptible to high variations stemming from local material effects and failures.

The conclusions regarding the test assessments are presented here below.

- The slump flow table test can be used as a quick verifying method to determine the general suitability for 3DP-SHCC. It is especially meaningful when a range of spread flow diameters have been determined for the associated printing system.
- The unconfined uniaxial compression test can determine the green compression strength and yield stress over time for 3D printable SHCC's. When a sufficient sample size and accurate specimen preparation is taken into account, the test is very applicable for determining the fresh properties of 3DP-SHCC mix designs.
- The ram extrusion test presents repeatability issues in extrusion pressure for specific die length and speed combinations, for 3DP-SHCC. This inconsistency complicates the fitting of material models and leads to significant scatter in the generated mechanical properties, rendering the test unsuitable for 3DP-SHCC assessment.
- The slow penetration test is a feasible test that is able to provides precise measurements of the static yield stress development over time of 3DP-SHCC. The test has its limitations, since it is not able to obtain a single timestamp yield stress from the test.
- The amplitude sweep test is not able to reliably measure the fresh mechanical properties due to insufficient recovery of the material between subsequent vane rotations.
- The flow curve test is not applicable to 3DP-SHCC due to early shear failure between the material around the vane and the material in the cup.

9

CONCLUSIONS AND RECOMMENDATIONS

The PhD project had as objective to systematically develop a printable strain hardening cementitious composite for structural applications. To do so, the research presented in this thesis aimed to combine two recent innovations, namely SHCC and 3D concrete printing.

This chapter presents the main findings resulting from the thesis and will be presented in four main domains:

- Development of a printable SHCC material.
- The printing system design for SHCC and its material interaction.
- Influence of fibres on hardened mechanical properties.
- Rheology testing methods for 3DP-SHCC.

9.1. MATERIAL DEVELOPMENT

During the material development conducted in this thesis, the importance of the boundary conditions was evident. Both the fresh state requirements (i.e. the printability) and the hardened state requirements (i.e the criteria to obtain strain hardening capacity) needed to be met.

Building on this knowledge, research was conducted on the particle packing to achieve a solid structural buildup of the material during printing. It was shown that optimisation of the particle size distribution can contribute to the buildability performance of 3DP-SHCC, resulting in sufficiently high initial yield and compressive strength and therewith showing no plastic failure during buildability tests. The Young's modulus was found to be the critical fresh mechanical parameter for 3DP-SHCC, and therewith buckling failure is the most likely failure mode in buildability tests and printing trials.

In continuation, multiple parameters (BFS/LS, SF/CEM, W/S and additives) were researched for tailoring the fresh and hardened mechanical properties. It can be concluded that the silica fume content and water/solid ratio are relevant parameters for tailoring the fresh and hardened mechanical properties simultaneously. Altering the BFS/LS ratio proved to be a good parameter for fine-tuning the hardened properties, such as the compressive strength and the strain hardening capacity, without altering the workability of the material in the fresh state.

From the material development and subsequent printing trials, it was found that 3DP-SHCC is sensitive to dynamic segregation in the pumping phase, leading to the formation of fibre agglomerates. This results in inconsistent fibre distribution throughout the specimens, causing high variance in mechanical properties and also limiting the strain hardening capacity.

9.2. INFLUENCE OF THE PRINTING PROCESS

Extensive research has been conducted on the impact of the printing system on the material and mechanical properties. The research and analyses undertaken on this topic yield the following conclusions:

The pumping system has a strong influence on the flow rate and the material stability of 3DP-SHCC. Evaluation of four pump types reveals that the progressive cavity pump is the most suitable for pumping 3DP-SHCC. Its ability to handle highly viscous materials and generate sufficient material flow for 3DP-SHCC printing positions it as the optimal choice. Moreover, the progressive cavity pump offers versatility by allowing the exchange of specific components such as the transport screw and rotor/stator, to align with the requirements of a specific material design.

Further investigations indicate that the design of the transport screw significantly influences the entrapment of air voids and the formation of fibre agglomerates. The design of the rotor-stator has a significant influence on the flow rate of the material. In terms of fibre agglomerates, the rotor-stator displayed a smaller role than the design of the transport screw.

To further investigate the influence of the printing process, the consistency of mechanical properties of 3DP-SHCC, obtained from three distinct yet ostensibly identical printing sessions was evaluated. It was found that the compressive strength and apparent density of the printed 3DP-SHCC exhibit good consistency throughout different printing sessions. In contrast, the mechanical properties related to deformation capacity, as retrieved from the 4-point bending tests and the uniaxial tensile tests, do not show consistent values throughout the three printing sessions. Notably, the deformation capacities are quantitatively more strongly affected by the printing session than flexural- and uniaxial tensile strength properties.

This yields the overall conclusion that unambiguous quantitative statements about the mechanical properties of 3DP-SHCC, can only be drawn based on the data of several separate printing sessions and sufficient sample size.

In continuation, a research program was designed to determine the influence of

different printing phases (mixing, pumping, extruding and printing) on the mechanical properties of 3DP-SHCC. From the elaborate experimental investigation, it can be concluded that compressive strength and apparent density are slightly increased after pumping, after which they stay stable throughout the remaining printing process. This is in contrast with the flexural and tensile strength and particularly their associated deformation, (i.e. deflection and strain) which are all strongly reduced throughout the four phases of the printing process. Here it was found that the flexural toughness at the first crack (Limit of proportionality) remains unaltered throughout the printing process, while the toughness at final failure (Modulus of rupture) shows an overall reduction of >80% from mixing to printing. From the evaluated phases within the printing system, it can be concluded that the pumping phase has the most significant influence on the mechanical properties of 3DP-SHCC.

9.3. FIBRE TYPES

Chapter 7 investigates the influence of fibre types on the workability and hardened mechanical properties of 3DP-SHCC. Firstly, the study revealed that fibre type adaptation significantly affects workability, in which 6 mm fibres exhibiting higher resistance to flow in the slump flow table test compared to 8 mm fibres. Additionally, the study found that fibre type has a limited effect on hardened compressive strength, resulting in only a slight increase when compared to non-reinforced references. Among the studied fibre types, PVA 6 (RMS702) fibres are noted for their limited flexural hardening capacity and lower workability, rendering them unsuitable for 3DP-SHCC application. In contrast, both PVA 8 mm (RECS15) fibres and HDPE fibres demonstrate good flexural and strain hardening capacity, with HDPE fibres displaying the highest crack dispersion under tensile loading. Moreover, in the conducted printing trial, both mixes D-HDPE and D-PVA8 exhibit robust buildability, high print quality, and good shape retention properties, making them suitable candidates for large-scale 3D printing.

9.4. FRESH MECHANICAL TESTING

One of the objectives of the thesis was to determine the fresh mechanical properties required to achieve printable SHCC. To determine these requirements an extensive research program was performed to assess which fresh mechanical tests are applicable for evaluating 3DP-SHCC. From the research presented in chapter 8 it can be concluded that fresh mechanical testing for 3PD-SHCC is not straightforward. The material poses unique challenges, primarily due to its high viscosity and susceptibility to segregation under shear. In general, it can be concluded that bulk material tests, such as slump flow table test, unconfined uniaxial compression test, and slow penetration test are applicable for 3DP-SHCC.

Fresh mechanical tests that stress the material on a more local scale (mm-scale), such as the RAM extrusion test and the Flow curve test, may be sensitive shear failure during testing. This can result in test failure in the case of the flow curve test or high variation leading up to unreliable material model fits in case of the RAM extrusion test. Additionally, it was found that oscillating tests (such as the Amplitude sweep test), that depend on material recovery for reliable measurements, can result in unreliable data.

In the end, bulk material tests combined with pumpability and buildability tests are the most effective way to assess whether the 3DP-SHCC material is suitable for 3d printing on a given printing system.

9.5. RECOMMENDATIONS

The PhD research trajectory aimed to systematically develop a 3DP-SHCC (3D printable strain hardening cementitious composite) for structural applications. Throughout this research, several critical topics were investigated, including the development of various materials, the tailoring of printing systems, and the evaluation of fresh material testing methods. Nevertheless, in order to integrate this material within the 3D printing industry, there are still certain aspects that require further exploration.

As presented in chapter 3, the fresh 3DP-SHCC must meet multiple requirements to establish good printability and maintain material stability. However, to make optimal use of this narrow playing field, a case study research on a structural engineering level is recommended. This critical investigation should assess the required technical specifications of the material, particularly the requirements for flexural bending and tensile strain capacity. Additionally it should consider the specific applications for which this material may be intended. By conducting such research, structural engineers can outline the mechanical properties that are essential for the material in their specific structural designs.

The investigation shown in chapters 4 and 6 (and Appendix A), demonstrates the significant influence of the printing process, especially the pumping phase, on the hardened mechanical properties. This reduction in hardened mechanical properties and the found inconsistency between printing sessions poses considerable challenges when conducting structural design calculations.

In light of these findings, two recommendations are made. Firstly, as proposed in chapter 6, it is highly recommended to further investigate the micro-structure and hydration products of the composite following successive printing phases. This research will provide information on specific material alterations that caused the reduction in mechanical performance.

Secondly, it is advisable to conduct fundamental research into the progressive cavity pump and its mechanical interactions with fibre-reinforced composites. When combined with the aforementioned additional investigation, this comprehensive study will provide information on how to adjust the printing system to achieve minimal material change during printing and enhance the overall performance of the 3D printed SHCC structure.

Initial studies on set-on demand materials have shown promising results and multiple companies and research institutes are already working with the so-called 2K systems [254–258]. Due to the high mixing energy needed for 3DP-SHCC, in order to sufficiently disperse the fibres throughout the mix, the printed works presented in this dissertation are all manufactured with the batch mixing approach. This approach has multiple limitations, such as the high labor intensity and the inconsistent hydration time of the material over a printing session.

Therefore it is advised to start a comprehensive research study into a 2K system in combination with 3DP-SHCC, in which a dormant SHCC is mixed with an accelerating slurry just before extrusion. If successful, this methodology would ensure constant hydration time and fresh mechanical properties of the material throughout the printing session. Additionally, it would give greater flexibility in the design of 3DP-SHCC materials, as the contradicting requirements of pumpability and buildability are resolved at a later stage in the printing process.

For further developments in 3DCP, especially on the side of building codes and quality control, standardisation of printing systems should be aimed for. The printing system has a strong influence on the printability of fibre reinforced mortars and for this constructive technology to be embedded in the build environment adoption of safety codes is essential.

To take the manufacturing technique to a mature state a comprehensive study is needed on the durability performance of 3DP-SHCC. From literature it is known that both 3d printable mortars[40, 259] and SHCC [187, 260] suffer from time dependent physical mechanisms such as shrinkage and creep. It is therefore advised to investigate these phyisical mechanisms and how they may affect the material and its mechanical performance, specifically the tensile strain hardening capacity over time.

A

MECHANICAL PROPERTIES OF A 3DP-SHCC MIXTURE PRINTED AT TWO DIFFERENT PRINTING FACILITIES

Over the past few years, several studies have shown the potential of three-dimensional concrete printing (3DCP) for applications in building and civil engineering. However, only a few studies have compared the properties of the fresh printing material and the quality of the printed elements from different printing facilities. Variations in the manufacturing conditions caused by the mixing procedures, the pumping device and the nozzle shape and/or dimensions may influence the quality of the printed elements. This study investigates the differences in the fresh and hardened properties of a printing material tested in two different printing facilities. The pump pressure and temperature experienced by the printing material during the printing session are monitored real-time. Hardened properties are measured for the printed elements, such as the bending capacity, the apparent density, and the air void content. The research shows that two different printing facilities may result in printed elements with relative differences in flexural strength and volumetric density of 49% and 7%, respectively.

** The research presented in this paragraph was done in collaboration with Karsten Nefs and Stefan Chavez Figueiredo from the Eindhoven University of Technology. The content of this chapter has largely been published in a joined paper presented at the Digital Concrete 2020 conference in Eindhoven (NL) [151].*

A

A.1. INTRODUCTION

The influence of the printing system first became evident from two unrelated studies that employed an identical 3DP-SHCC material on different 3D printing systems [10, 150]. A comparative analysis of the research results reveals a significant difference in the mechanical properties. For instance, the compressive strength exhibited a significant divergence of 29%.

It is therefore that the primary objective of this research is to thoroughly investigate the influence of the printing facility on the mechanical properties of hardened SHCC specimens manufactured by 3D printing. Accordingly, printing sessions were conducted with two different printing facilities, one located at the Delft University of Technology and one located at the Eindhoven University of Technology. The mix design, mixing procedure, and printing routine were kept the same, and the temperature and pumping pressure were monitored during the printing session. After hardening, the printed elements were subjected to a three-point bending test with crack mouth opening control in order to characterize the fracture response and determine the fracture properties. Furthermore, the apparent density was measured and the air void content was analysed.

A.2. PRINTING FACILITIES

The printing facilities at the technical universities of Eindhoven and Delft both use a gantry system for creating the contour of the printed elements. The gantry systems in Eindhoven and Delft are illustrated in figure A.1, and are able to print volumes of [9 x 4.5 x 2.8] m^3 and [1 x 0.6 x 0.35] m^3, respectively. The printing facilities are equipped with a mixing device and a pump, which are connected to a 5 m hose and a down flow nozzle. The hose has a diameter of 25 mm, and the nozzle has a rectangular cross-section of [40 x 14] mm^2.

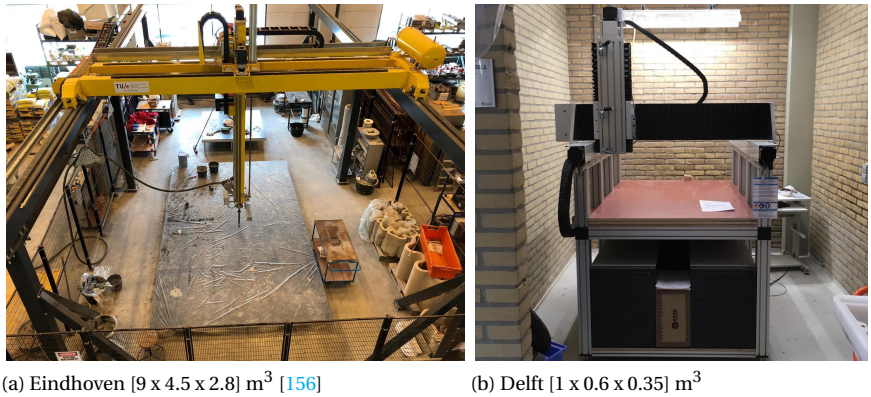

(a) Eindhoven [9 x 4.5 x 2.8] m^3 [156] (b) Delft [1 x 0.6 x 0.35] m^3

Figure A.1: Gantry system used in both printing facilities.

The mixing devices are both of the planetary type, but differ in volume capacity, engine power and operating speed. The mixing device in Eindhoven uses a TMV 75 pan mixer fabricated by Van der Zalm Nuth B.V., and is characterized by a capacity of 75 litres,

Table A.1: Mix proportion [kg/m^3]

Raw materials	
CEM I 42.5	259.2
Blast furnace slag	604.9
Limestone powder	894.1
PVA fibres (Kuraray REC15)	26
Viscosity modifier admixture (VMA)	5.1
Superplasticizer	17.3
Water	345.6

an engine power of 2.2 kW, and a single rotational speed. In Delft, an A120N Hobart planetary mixer is used, characterised by a volume capacity of 12 litres, an engine power of 0.27 kW, and three rotational speeds. Figures A.2a and A.2b illustrate the mixers used in both facilities. Due to the different specifications of the engine power and printing volume, the mixing procedure in Delft was carried out in 7 batches of 3 liters each, while in Eindhoven a total volume of 28 litres was mixed in one batch. At the TUD the PFT Swing M pump, as described in chapter 3, was deployed. For the printing session at the TUe, the M-tec duo-mix connect was used, which has briefly been described in chapter 4. The M-tec duo-mix connect is a different pump type than the one used throughout the rest of this thesis. The main differences between the two PFT Swing M and the M-tec duo-mix connect is the design of the rotor-stator and the transport screws that collect the material from the reservoir and transport it through the rotor-stator. Furthermore, the material flow of the M-tec duo-mix connect is vertically orientated, while for the PFT Swing M the transport screw and the rotor-stator are horizontally orientated.

The pump components are illustrated in figures A.2c - A.2f.

A.3. METHODOLOGY

Materials and specimen preparation The mix design used in the research was developed at the TUD, see [10] for more details. The specific composition can be found in Table A.1.

The mixing procedure adopted in Delft was as follows:

- All dry materials were mixed for two minutes at a relatively low rotational speed of 60 rpm.
- During approximately one minute, water mixed with a superplasticizer was added.
- Next, the wet powders were mixed for two minutes, whereby a significant change in the mixture‘s viscosity was observed.
- The dough-like mixture was further mixed for four minutes at a moderate rotational speed of 124 rpm.

The same mixing procedure was adopted in Eindhoven. However, due to the larger material volume and the use of a single rotational speed in the mixing device, the mixing

A

(a) Mixer in Eindhoven.

(b) Mixer in Delft.

(c) Transport screw in Eindhoven

(d) Transport screw in Delft

(e) Rotor-stator in Eindhoven

(f) Rotor-stator in Delft

Figure A.2: Comparison of the components of the printing facilities used at the Technical Universities of Eindhoven and Delft.

time after the inclusion of the liquid ingredients was taken somewhat longer in order to achieve the same visual mix consistency as in Delft.

Initially, a single layer filament was printed at different speeds and constant pumping pressure, whereby the width of the filaments was measured to select the optimal printing speed. Subsequently, two objects were printed with a height of five layers. The objects were kept on the printing table for 24 hours, after which they were cured in water for 13 days. Subsequently, specimens of [40 x 40 x 160] mm^3 were sawn from the hardened object, see figure A.3, which were subjected to mechanical testing the next day (day 14).

A.3.1. FRESH STATE

During the printing session, the pressure in the hose and the temperature of the printing material were monitored continuously. Pressure drops may indicate potential failures in the extruded material due to the development of large air pockets, and temperature changes in the printing material may lead to significant alterations in its rheological properties and hydration speed. The pumping pressure was measured by installing analogical manometers directly behind the pump and just before the printing nozzle. The pressure measured by the sensors was recorded and the values were read off after completing the printing of the object. The heat development was monitored by means of two thermocouples installed on the manometers. Accordingly, the temperature reached in the printing facilities could be determined, and the origin of the heat generated during the pumping process could be identified.

A.3.2. FRACTURE BEHAVIOUR

The fracture behaviour of the hardened specimens was determined by means of a Crack Mouth Opening Displacement (CMOD) test: a 3-point bending test on notched beams in which the load point displacement is controlled by the gradually increasing opening of the notch, known as the CMOD value.

All the tests were performed on an Instron universal test rig of the Eindhoven University of Technology. The applied CMOD experiment is a variant of the test detailed in EN 14651 [261]. The test was adapted to accommodate the standard prism size used for the characterization of cementitious mortars ([i.e. 40 x 40 x 160] mm^3, cf. EN 196 [185]) as this specimen size is more appropriate in the context of slender 3DCP structures. This adaption in specimen size resulted in a scale factor of approximately 0.27. More extensive descriptions and a discussion on the potential size effect of this scaled-down CMOD test are provided in [262].

The CMOD tests were performed with an initial crack mouth opening rate of 0.05 mm/min until an opening of 0.1 mm was reached. The test was continued at 0.10 mm/min of CMOD until the opening reached 2.6 mm at which point the test was discontinued. The bending test span was 130 mm. A 3 mm wide, 7 mm (± 0.5 mm) deep notch was sawn into each specimen, leaving an effective section height at the notch of h_{sp} = 33 mm.

Specimens were sawn with an accuracy of ± 2 mm from rectangular objects printed in Eindhoven ('E') and Delft ('D'). The printed specimens were tested in orientation **v.u.**. The notches were made across the width of the specimen in the direction of the bending moment. This implies that specimens tested in orientation **v.u.** have a notch in the **v-**

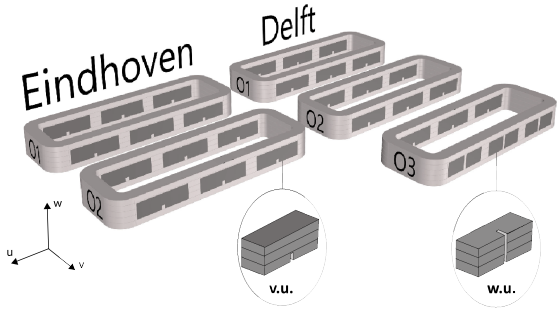

Figure A.3: Printed objects in Delft and Eindhoven with indicated specimen orientation **v.u.**

direction (within the **v.u.** plane).

Figure A.3 provides an overview of printed objects, obtained specimens (six per object) and direction definitions.

A.3.3. APPARENT DENSITY AND AIR VOID CONTENT

The apparent density of the hardened specimens was assessed by measuring their weight and volume after the CMOD test. Based on the apparent density of the SHCC, the printing quality can be estimated. Additionally, a single core of 13.6 mm diameter was drilled from one object printed by the facilities in Delft and Eindhoven. This core was subjected to a micro-computed tomography scanning procedure (μCT-scan). An acceleration voltage of 130 kV and beam current of 220 μA were applied. The pictures obtained from the scans were created from an average of two radiographs with an exposure time of 0.5 s, each generating a total of 1441 pictures. In this way, pictures with a resolution of 8.33 μm/pixel were obtained.

The software phoenix datos | x 2.0 was used for reconstructing the three-dimensional specimen volume. The software centralizes the radiographs generated during the scan. Additionally, a beam hardening correction of 8 was used to correct for artefacts. With the help of the software VGStudio MAX 2.0, the image stack from the top and the right side view were obtained from the three-dimensional specimen volume and a median filter of 3 pixels in all directions was applied to the images. For analyzing the air void content and distribution in the image stack, the software ImageJ was employed. A grey value threshold was imposed in order to distinguish and isolate the air voids from the original images. In the new images of the void distribution, the size and content of the air voids with an area bigger than 40 pixel^2 and a circularity between 0.3 and 1.0 were counted. These filter values were applied to minimize the effect of the voids surrounding the fibres.

A.4. RESULTS AND DISCUSSION

A.4.1. ASSESSMENT OF THE 3D PRINTING PROCESS

The variation in temperature and pump pressure, as measured during the sequential printing of all objects, is summarized in figures A.4a and A.4b for the 3D printing facilities

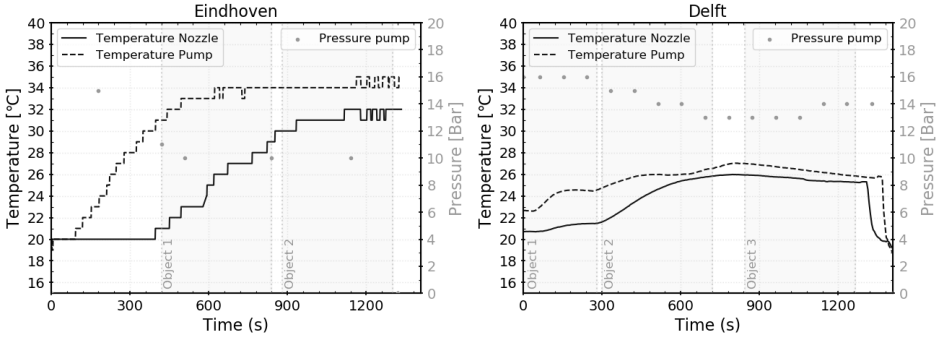

(a) Eindhoven (b) Delft

Figure A.4: Temperature and pressure profiles measured during the sequential printing of the objects.

in Eindhoven and Delft, respectively. The pressure values obtained from the manometers installed close to the nozzle turned out to be very low, and therefore could not be read with sufficient accuracy. The pump pressure measured in the Eindhoven 3D printing facility on average is smaller than the pump pressure measured in the Delft 3D printing facility. Such pressure differences may be ascribed to various effects, such as differences in temperature, air void content, and alterations in static pressure height caused by moving the hose during the 3D printing process. In both printing facilities, the temperature rose from the moment the printing process started, whereby after some time a constant, stable temperature was reached.

In Eindhoven, the measuring of the pump pressure started from the very beginning of the 3D printing process, i.e., as soon as the material was pumped through the system, while in Delft the measuring started after the printing of 1.5 layers. This explains why the initial temperatures measured at the nozzle and in the pump are slightly different in figures A.4a and A.4b. Observe further that the temperature of the printing material used in Eindhoven went up to 35°C, while in Delft the maximal temperature was approximately 27°C. This rise in temperature is believed to be due to frictional effects, between the rotor and the inner part of the stator. Moreover, the observed difference in temperature rise between the two printing facilities can originate from the geometries of the rotor-stator, as has been illustrated in figures A.2e and A.2f. It can be further observed that the temperature at the pump is higher than at the nozzle, which is due to heat being dissipated during material transport through the hose. In general, a printing material used in relatively long printing sessions is clearly exposed to a significant temperature increase, which will change its rheological properties, such as the buildability, see [76] for more details on this aspect. It is also noted that a temperature increase of the fresh printing material can accelerate water evaporation, which eventually might cause cracking due to shrinkage.

A

A.4.2. FAILURE RESPONSE IN CMOD TEST

The obtained flexural strength vs Crack Mouth Opening Displacement (CMOD) curves are presented in figure A.5. On the horizontal CMOD axis, the values of 0.135 mm, 0.405 mm, 0.675 mm, and 0.945 mm have been indicated. These values correspond to 0.27 times the $CMOD_1$ to $CMOD_4$ values, as predefined by the EN 14651 [261]. Table A.2 lists the average values of the (residual) strength parameters derived from the CMOD test. These parameters include:

- f_t: Maximum flexural strength.
- f_{LOP}: Limit of Proportionality as defined by [185]
- $f_{R,1} * 0.27$: Residual strength at the predefined CMOD value $CMOD_1$.
- $f_{R,3}$*0.27: Residual strength at the predefined CMOD value $CMOD_3$.

Furthermore, the table provides the classification according to the fib Model Code 2010 [263] that characterises the residual strength. This classification is determined based on the ratio of $f_{R,3}$*0.27/ $f_{R,1}$*0.27.

Table A.2: Average results of the CMOD tests.

	f_t [MPa]	f_{LOP} [MPa]	$f_{R,1}$*0.27 [MPa]	$f_{R,3}$*0.27 [MPa]	$f_{R,3}$*0.27 / $f_{R,1}$*0.27	Class
Eindhoven - Object 1	5.29	3.52	4.06	4.59	1.13	c – e
Eindhoven - Object 2	4.99	3.14	3.87	4.83	1.25	d – e
Delft - Object 1	7.32	4.03	5.03	6.92	1.39	d - e
Delft - Object 2	7.56	4.41	5.48	7.27	1.33	d - e

Figures A.5a and A.5b depict the results of the specimens sawn from the first object printed in Eindhoven and Delft, respectively. It can be seen that, after the initial stiff response that lasts until crack initiation, the load increases to a maximum that is reached at some point between the $CMOD_1$ and $CMOD_4$ values (i.e. strain hardening), depending on the individual specimen. After reaching the maximum strength, the flexural stress gradually drops with deformation, showing a rather ductile softening response. The failure behaviour can clearly be ascribed to the bridging of the cracks by the fibres. Remarkably, the average maximum flexural strength f_t of the Delft specimens is 38.4% higher than that of the Eindhoven specimens. For the specimens sawn from the second object printed, this difference is even larger, namely 51.4%, see figures A.5c and A.5d. The residual strength classication of the Delft specimens is also slightly better, ranging from 'd' to 'e', while the Eindhoven specimens vary from 'c' to 'e' (details on this classification can be found in [263]).

When comparing specimens sawn from different objects printed at the same 3D printing facility, the differences in maximum flexural strength are not substantial. As can be observed in figure A.6, the relative difference in strength of specimens from the first and second objects printed is 5.6% (Eindhoven) and 3.3% (Delft), and 5.9% (Delft)

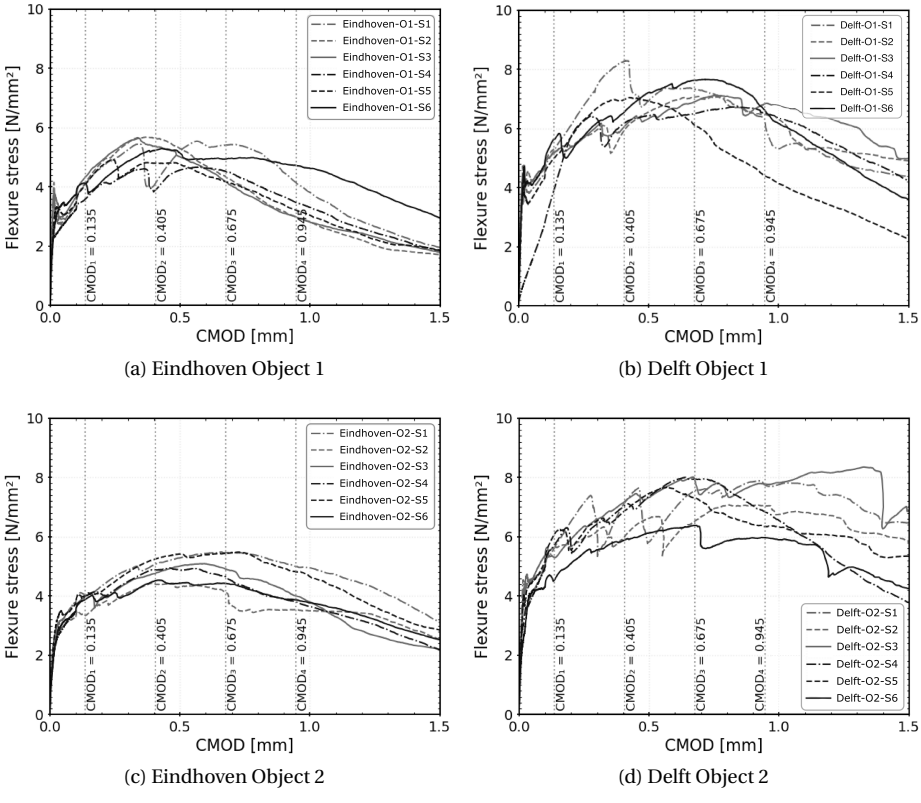

(a) Eindhoven Object 1

(b) Delft Object 1

(c) Eindhoven Object 2

(d) Delft Object 2

Figure A.5: Flexural stress versus CMOD of all specimens.

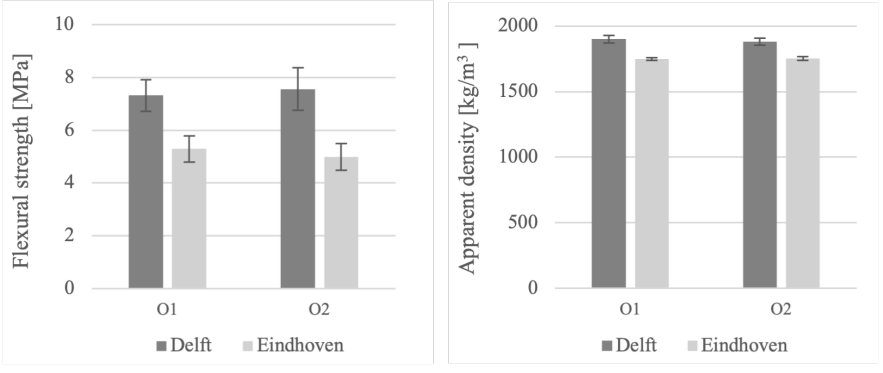

(a) (b)

Figure A.6: a) Average flexural strength b) Average apparent density of the specimens manufactured in Delft and Eindhoven.

for specimens from the first and third object printed. Also, the notch orientation (and associated specimen orientation during testing) did not significantly influence the failure response. The significant differences in the flexural strength of the specimens printed in Eindhoven and Delft may be associated with differences in the internal material structure, which will be analyzed in more detail in the section below.

A.4.3. APPARENT DENSITY AND AIR VOID CONTENT

After the CMOD experiments were performed, the apparent density of the specimens was measured. The results summarised in figure A.6 show that the average apparent densities, did not change significantly during the printing sessions. Furthermore, the specimens manufactured in Delft have an average density that is approximately 7% higher than those manufactured in Eindhoven, which explains their higher flexural strength.

The cross-sectional images obtained from the μCT-scan of the specimen indicate a significant variation in air void content within the layers, see figures A.7 and A.8. Moreover, the distribution of the air void sizes across the specimen height shows that the interfaces between printed layers show a local increase in air void size. For the Delft specimen the average air void content within the layers ranges from 6.7% to 8%, while for the Eindhoven specimen it ranges from 15.2 up to 19.7%. This explains why the density and flexural strength of the Delft specimens are higher than those of the Eindhoven specimens. Furthermore, the layer interfaces of the Delft specimen show to have a higher average air void content than within the layers, while the Eindhoven specimens show the opposite trend.

In addition, for both the Delft and Eindhoven specimens the void size within the layers is in the range of 0.01 to 0.016 pixel^2. However, for the Delft specimen the voids at the layer interface range from 0.016 – 0.031 pixel^2, which is larger than the range of 0.016 to 0.026 pixel^2 measured for the Eindhoven specimen. Hence, the layer interfaces of the objects printed in the Delft facility contain larger air voids than the layer interfaces of the objects printed in Eindhoven. Figure A.9 shows an example of relatively large air voids

found within the printed layers in a Delft specimen.

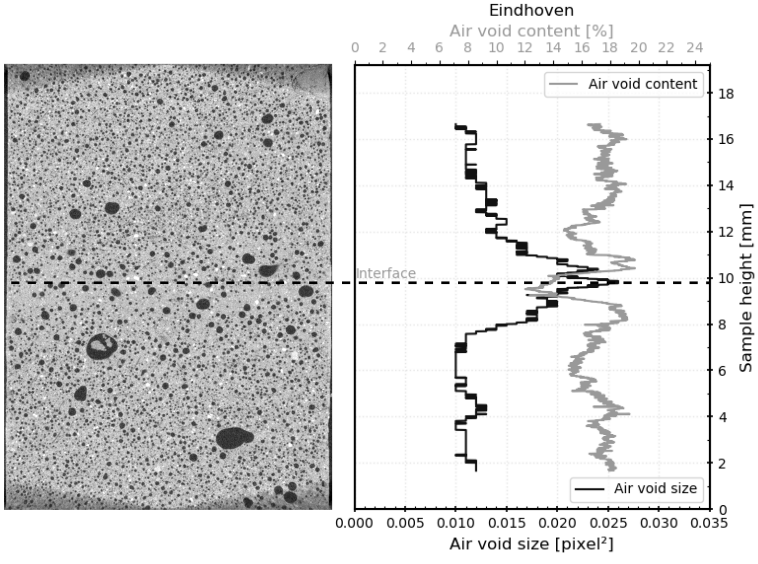

Figure A.7: Air void content and size across the height of a specimen printed in Eindhoven. The dashed line designates the interface between the printed layers.

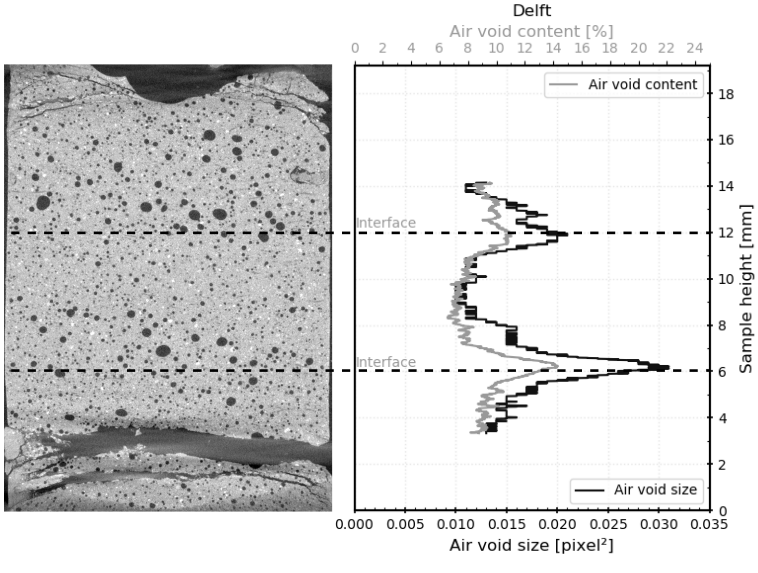

Figure A.8: Air void content and size across the height of a specimen printed in Delft. The dashed line designates the interface between the printed layers.

The differences in the properties observed for hardened specimens may originate from the mixing characteristics of the fresh concrete, such as the dissolution time from the VMA or superplasticizer, the fibre dispersion, and the air entrapment or entrainment

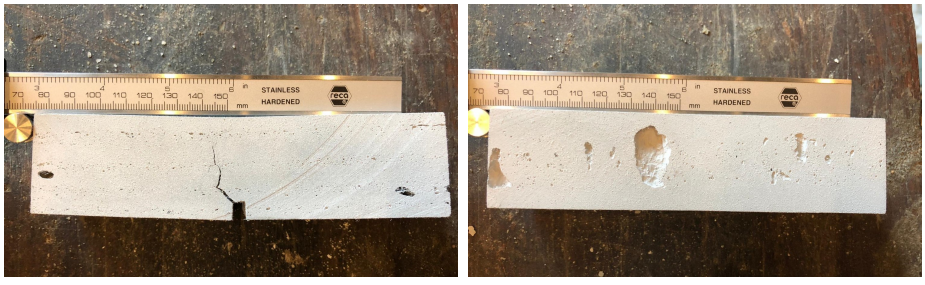

(a) Top-view (b) Side-view

Figure A.9: Large air voids in specimen printed in Delft and tested in direction **v.u.**.

during mixing. Previous work by Figueiredo et al [264] has demonstrated that VMA can influence the total air void content of the cement paste. Additionally, it is important to emphasize that the mixer in Eindhoven is significantly more powerful than the one in Delft, and that the mixing time in Eindhoven was adapted to reach the same visible consistency. Therefore, it may be reasonably expected that the mixing procedure has a strong effect on the total air void content of the printed material.

The relatively large air voids found in specimens from Delft is in accordance with the findings reported in chapter 3 and findings in authors previous publication [150] and could be explained by the pumping mechanism. The coarse transport screw design from Delft, exemplified in figure and A.2d, rotate to collect the material from the reservoir and push it towards the rotor-stator. Due to the high viscosity of printable SHCCs, some air pockets might have been created during this stage. It is hypothesised that a coarse rotor-stator system (Delft) can transport these large air pockets as a whole, whereas a fine rotor-stator system (Eindhoven) might break these large air voids down into smaller voids. However, more research is needed to explore such differences in more detail.

A.5. CONCLUSIONS

- The mechanical and physical properties of the specimens manufactured in the 3D printing facilities in Delft and Eindhoven were significantly different. In order to reduce these differences, standardization of printing methods and full understanding of printing variables is of crucial importance.

- The mixing time and intensity have a strong influence on the quality of dough-like mixtures. Longer mixing times introduce the entrainment of air voids in the fresh state, which causes a reduction in mechanical properties.

- The coarse transport screw design can introduce large entrapped air voids in the printed composite.

- Based on the collected data no significant differences were found in the mechanical results in relation to the temperature history of each object.

- The total air content found in specimens mixed and printed at different 3D printing facilities may vary significantly. This turns out to have a considerable effect on the mechanical properties in the hardened state.

B

ADDITIONAL DATA ANALYSIS ON RAM EXTRUSION CHAPTER 8

In this appendix additional data analysis is provided to support the analysis of the RAM extrusion tests, presented in chapter 8.

B.1. PARAMETER RANGES

To fit the measured data to the material three material models an optimisation routine was used. For ranges used for the model parameters are presented in table B.1.

	$\sigma_y[kPa]$	α	**m**	τ_0	β	**n**	$A*k$
BB	0-100	0-5	0-1	0-100	0-5	0-1	-
BB Linear	0-100	0-5	-	0-100	0-5	-	-
Basterfield	0-100	-	-	-	-	0-1	1-1000

Table B.1: Set ranges for parameters

B.2. STRATEGY 1

Here below the static yield stress versus time curves are presented for all researched materials, per material model.

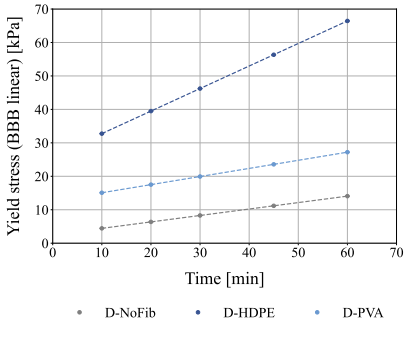

(a) Linear BBB model

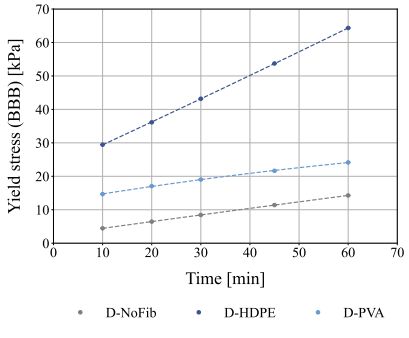

(b) BBB model

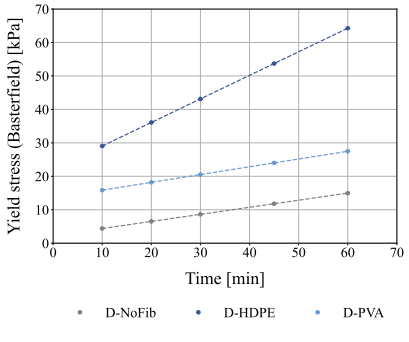

(c) Basterfield model

Figure B.1: Static yield stress development over time.

B.3. PRESSURE OVER DIE LENGTH CURVES

The following section presents the the measured pressure vs. die length curves are presented for all four speeds, per specimen and timestamp, followed by a 3d representation of the non-linear Benbow-Bridgwater model fit on the measured mean pressure points.

B.3.1. MIX D-NOFIB

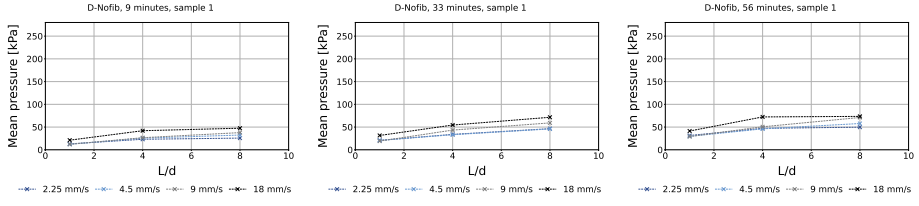

(a) (b) (c)

Figure B.2: Mean Pressure - L/D graphs measured for D-NoFib specimen 1 for the four extrusion speeds. For time stamps 9, 33 and 56 minutes

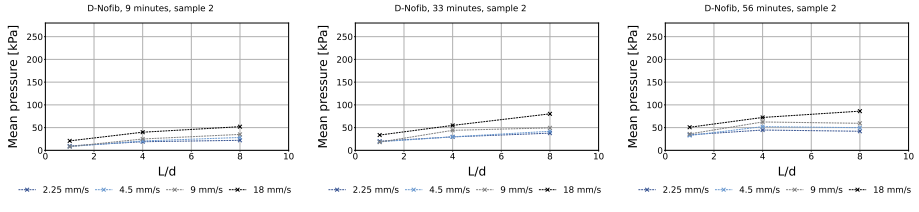

(a) (b) (c)

Figure B.3: Mean Pressure - L/D graphs measured for D-NoFib specimen 2 for the four extrusion speeds. For time stamps 9, 33 and 56 minutes

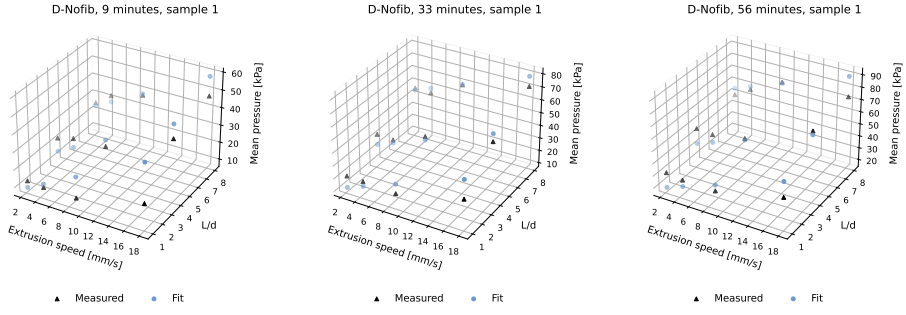

(a) (b) (c)

Figure B.4: 3D BBB-linear fit for D-NoFib specimen 1 for time stamps 9, 33 and 56 minutes

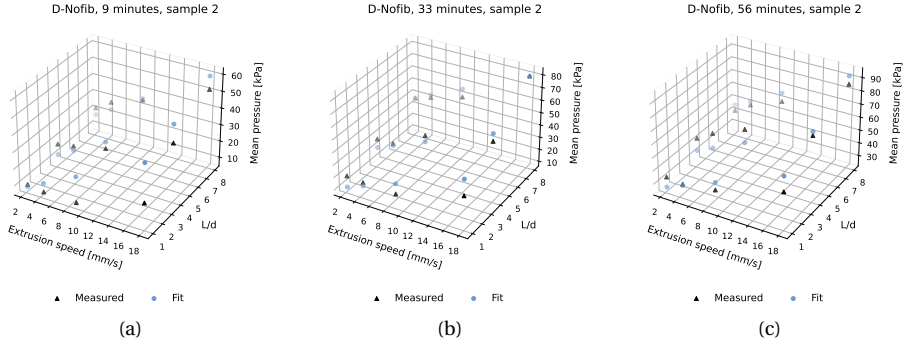

(a) (b) (c)

Figure B.5: 3D BBB-linear fit for D-NoFib specimen 2 for time stamps 9, 33 and 56 minutes

B.3.2. MIX D-HDPE

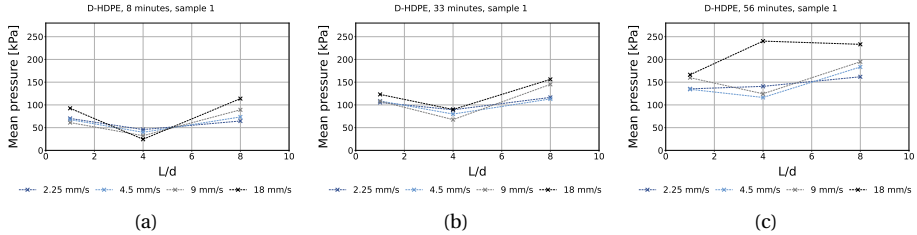

(a) (b) (c)

Figure B.6: Mean Pressure - L/D graphs measured for D-HDPE specimen 1 for the four extrusion speeds. For time stamps 8, 33 and 56 minutes

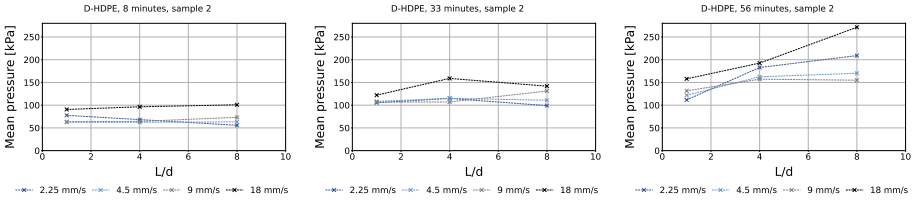

(a) (b) (c)

Figure B.7: Mean Pressure - L/D graphs measured for D-HDPE specimen 2 for the four extrusion speeds. For time stamps 8, 33 and 56 minutes

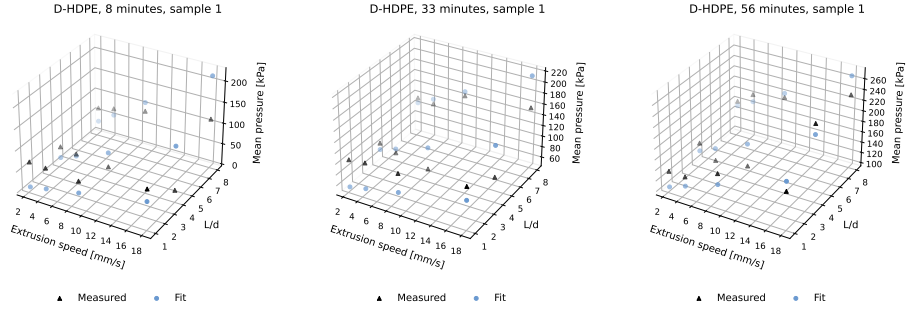

(a) (b) (c)

Figure B.8: 3D BBB-linear fit for D-HDPE specimen 1 for time stamps 8, 33 and 56 minutes

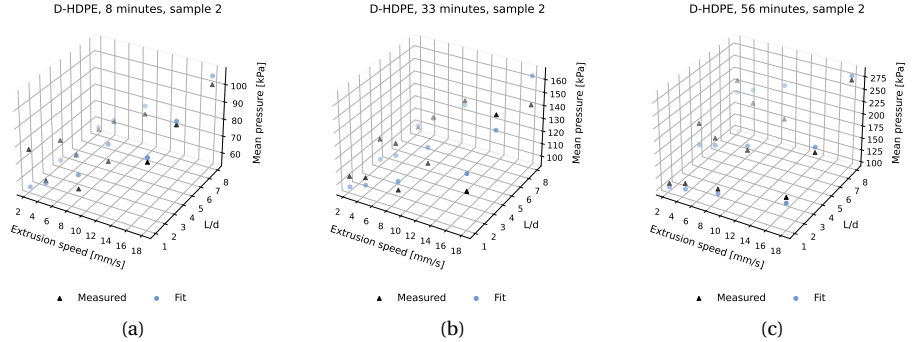

(a) (b) (c)

Figure B.9: 3D BBB-linear fit for D-HDPE specimen 2 for time stamps 8, 33 and 56 minutes

B

B.3.3. MIX D-PVA

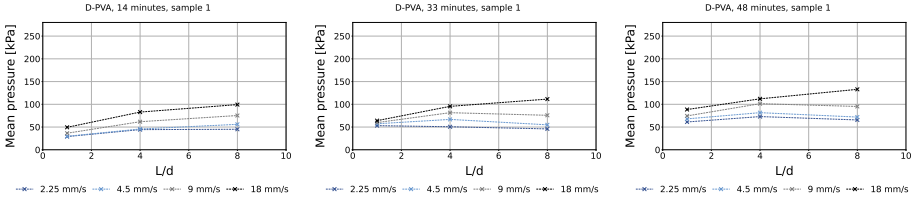

(a) (b) (c)

Figure B.10: Mean Pressure - L/D graphs measured for D-PVA specimen 1 for the four extrusion speeds. For time stamps 14, 33 and 48 minutes

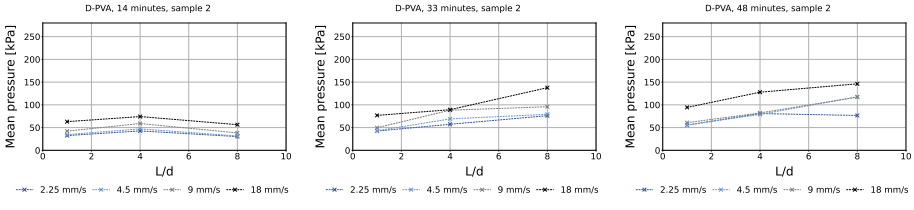

(a) (b) (c)

Figure B.11: Mean Pressure - L/D graphs measured for D-PVA specimen 2 for the four extrusion speeds. For time stamps 14, 33 and 48 minutes

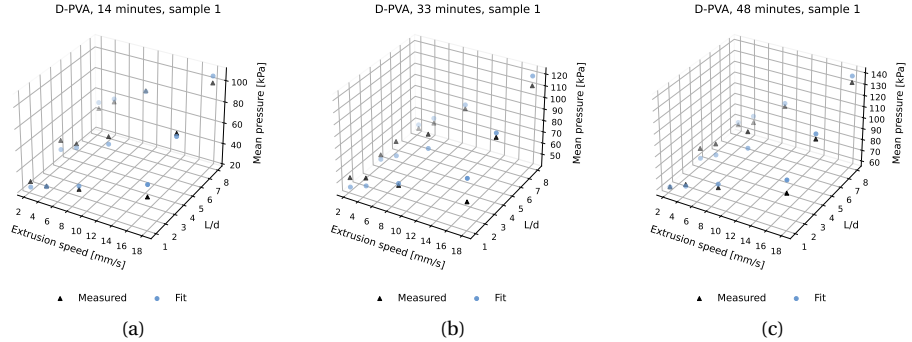

(a) (b) (c)

Figure B.12: 3D BBB-linear fit for D-PVA specimen 1 for time stamps 14, 33 and 48 minutes

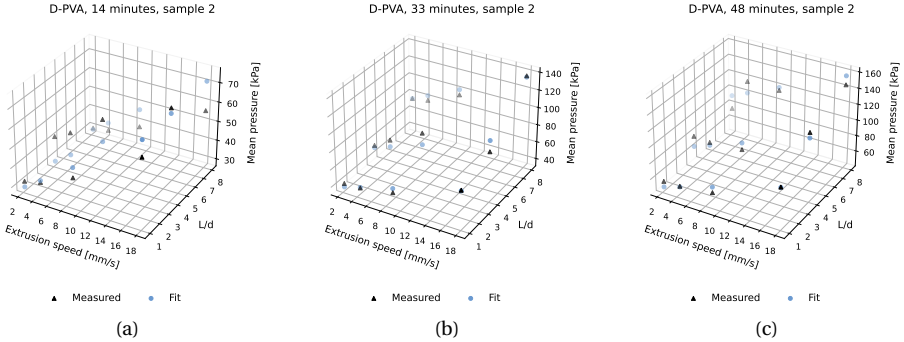

(a) (b) (c)

Figure B.13: 3D BBB-linear fit for D-PVA specimen 2 for time stamps 14, 33 and 48 minutes

BIBLIOGRAPHY

[1] T. Wangler, E. Lloret, L. Reiter, *et al.*, "Digital concrete: Opportunities and challenges", *RILEM Technical Letters*, vol. 1, pp. 67–75, 2016. DOI: 10.21809/rilemtechlett.2016.16.

[2] G. De Schutter, K. Lesage, V. Mechtcherine, *et al.*, "Vision of 3d printing with concrete technical, economic and environmental potentials", *Cement and Concrete Research*, vol. 112, pp. 25–36, 2018. DOI: 10.1016/j.cemconres.2018.06.001.

[3] R. A. Buswell, W. L. de Silva, S. Jones, and J. Dirrenberger, "3d printing using concrete extrusion: A roadmap for research", *Cement and Concrete Research*, vol. 112, pp. 37–49, 2018. DOI: 10.1016/j.cemconres.2018.05.006.

[4] S. Lim, R. Buswell, T. Le, *et al.*, "Development of a viable concrete printing process", *Proceedings of the 28th International Symposium on Automation and Robotics in Construction, ISARC 2011*, Jan. 2011. DOI: 10.22260/ISARC2011/0124.

[5] https://www.bridgeproject.nl, Accessed on 15-12-2023.

[6] V. C. Li, "On engineered cementitious composites (ecc)", *Journal of advanced concrete technology*, vol. 1, no. 3, pp. 215–230, 2003. DOI: 10.3151/jact.1.215.

[7] V. Li, *Engineered Cementitious Composites (ECC)*. Springer, 2019, ISBN: 978-3-662-58437-8.

[8] *4-point bending test*, https://www.ducon.eu, Accessed on 06-10-2019.

[9] Y. Bao *et al.*, "Three-dimensional printing multifunctional engineered cementitious composites (ecc) for structural elements", in *RILEM International Conference on Concrete and Digital Fabrication*, Springer, 2018, pp. 115–128. DOI: 10.1007/978-3-319-99519-9_11.

[10] S. C. Figueiredo, C. R. Rodriguez, Z. Y. Ahmed, *et al.*, "An approach to develop printable strain hardening cementitious composites", *Materials & Design*, vol. 169, 2019. DOI: 10.1016/j.matdes.2019.107651.

[11] H. Ogura, V. Nerella, and V. Mechtcherine, "Developing and testing of strain-hardening cement-based composites (shcc) in the context of 3d-printing", *Materials*, vol. 11, no. 8, 2018. DOI: 10.3390/ma11081375.

[12] B. Zhu, J. Pan, B. Nematollahi, *et al.*, "Development of 3d printable engineered cementitious composites with ultra-high tensile ductility for digital construction", *Materials & Design*, vol. 181, p. 108 088, 2019. DOI: 10.1016/j.matdes.2019.108088.

[13] M. Hambach, M. Rutzen, and D. Volkmer, "Properties of 3d-printed fiber-reinforced portland cement paste", in *3D Concrete Printing Technology*, Elsevier, 2019, pp. 73–113. DOI: 10.1016/j.cemconcomp.2017.02.001.

[14] G. Ma, Z. Li, L. Wang, *et al.*, "Mechanical anisotropy of aligned fiber reinforced composite for extrusion-based 3d printing", *Construction and Building Materials*, vol. 202, pp. 770–783, 2019. DOI: 10.1016/j.conbuildmat.2019.01.008.

[15] S. Chaves Figueiredo *et al.*, "Mechanical behavior of printed strain hardening cementitious composites", *Materials*, vol. 13, May 2020. DOI: 10.3390/ma13102253.

[16] *Reinventing construction: A route to higher productivity*, Accessed on 2023-12-01. [Online]. Available: chrome-extension://efaidnbmnnnibpcajpcglclefindmkaj/https://www.mckinsey.com/~/media/mckinsey/business%20functions/operations/our%20insights/reinventing%20construction%20through%20a%20productivity%20revolution/mgi-reinventing-construction-a-route-to-higher-productivity-full-report.pdf.

[17] J. Lehne and F. Preston, *Making Concrete Change: Innovation in Low-carbon Cement and Concrete*. Londen. UK: The Royal Institute of International Affairs, 2018, ISBN: 978-1-78413-272-9.

[18] J. Olivier, G. Janssens-Maenhout, M. Muntean, and J. Peters, "Trends in global co2 emissions", Netherlands Environmental Assessment Agency (PBL), Tech. Rep., 2016.

[19] P. Fonta and F. Birol, "Technology roadmap low-carbon transition in the cement industry", International Energy agency (IEA) and World Business Council on Sustainable Development (WBCSD), Tech. Rep., 2018.

[20] D. Lowke, E. Dini, A. Perrot, D. Weger, C. Gehlen, and B. Dillenburger, "Particle-bed 3d printing in concrete construction – possibilities and challenges", *Cement and Concrete Research*, vol. 112, pp. 50–65, 2018. DOI: 10.1016/j.cemconres.2018.05.018.

[21] N. Hack and H. Kloft, "Shotcrete 3d printing technology for the fabrication of slender fully reinforced freeform concrete elements with high surface quality: A real-scale demonstrator", in *Second RILEM International Conference on Concrete and Digital Fabrication*, F. P. Bos, S. S. Lucas, R. J. Wolfs, and T. A. Salet, Eds., Springer International Publishing, 2020, pp. 1128–1137. DOI: 10.1007/978-3-030-49916-7_107.

[22] F. Heidarnezhad and Q. Zhang, "Shotcrete based 3d concrete printing: State of art, challenges, and opportunities", *Construction and Building Materials*, vol. 323, p. 126 545, 2022. DOI: 10.1016/j.conbuildmat.2022.126545.

[23] D. Weger, D. Talke, D. Lowe, and K. Henke, "3d-betondruck, variante'paste intrusion'", *Herstellung eines mit inneren Streben ausgesteiften Rohres. Gefördert durch Informationszentrum Beton GmbH*, 2017.

[24] D. Weger and C. Gehlen, "Particle-bed binding by selective paste intrusion—strength and durability of printed fine-grain concrete members", vol. 14, p. 586, 2021. DOI: 10.3390/ma14030586.

[25] E. Lloret-Fritschi *et al.*, "From smart dynamic casting to a growing family of digital casting systems", *Cement and Concrete Research*, vol. 134, p. 106 071, 2020. DOI: 10.1016/j.cemconres.2020.106071.

[26] E. Lloret-Fritschi, "Smart dynamic casting - a digital fabrication method for non-standard concrete structures", Ph.D. dissertation, ETH Zürich, 2016. DOI: ttps://doi.org/10.3929/ethz-a-010800371.

[27] E. Lloret *et al.*, "Complex concrete structures: Merging existing casting techniques with digital fabrication", *Computer-Aided Design*, vol. 60, pp. 40–49, 2015. DOI: 10.1016/j.cad.2014.02.011.

[28] J. Burger *et al.*, "Design and fabrication of a non-standard, structural concrete column using eggshell: Ultra-thin, 3d printed formwork", in *Rilem, Second RILEM International Conference on Concrete and Digital Fabrication*, 2020. DOI: 10.1007/978-3-030-49916-7_105.

[29] B. Khoshnevis, "Automated construction by contour crafting—related robotics and information technologies", *Automation in Construction*, vol. 13, no. 1, pp. 5–19, 2004. DOI: 10.1016/j.autcon.2003.08.012.

[30] F. P. Bos, Z. Y. Ahmed, R. J. Wolfs, and T. A. Salet, "3d printing concrete with reinforcement", in *High Tech Concrete: Where Technology and Engineering Meet*, Springer, 2018, pp. 2484–2493. DOI: 10.1007/978-3-319-59471-2_283.

[31] W. Leal da Silva, *3d concrete printing - technological issues in concrete mix design and extrusion*, 2017.

[32] H. Chen, Z. Daobo, P. Chen, N. Li, and A. Perrot, "A review of the extruder system design for large-scale extrusion-based 3d concrete printing", *Materials*, vol. 16, p. 2661, Mar. 2023. DOI: 10.3390/ma16072661.

[33] T. T. Le, S. A. Austin, S. Lim, *et al.*, "Mix design and fresh properties for high-performance printing concrete", *Materials and structures*, vol. 45, no. 8, pp. 1221–1232, 2012. DOI: 10.1617/s11527-012-9828-z.

[34] F. Faleschini, D. Trento, M. Masoomi, C. Pellegrino, and M. Zanini, "Sustainable mixes for 3d printing of earth-based constructions", *Construction and Building Materials*, vol. 398, p. 132 496, 2023. DOI: 10.1016/j.conbuildmat.2023.132496.

[35] T. S. Rushing *et al.*, "Chapter 7 - investigation of concrete mixtures for additive construction", in *3D Concrete Printing Technology*, J. G. Sanjayan, A. Nazari, and B. Nematollahi, Eds., Butterworth-Heinemann, 2019, pp. 137–160. DOI: 10.1016/B978-0-12-815481-6.00007-5.

[36] V. Mechtcherine *et al.*, "Extrusion-based additive manufacturing with cement-based materials – production steps, processes, and their underlying physics: A review", *Cement and Concrete Research*, vol. 132, p. 106 037, 2020. DOI: 10.1016/j.cemconres.2020.106037.

[37] Y. A. Al-Noaimat, S. H. Ghaffar, M. Chougan, and M. J. Al-Kheetan, "A review of 3d printing low-carbon concrete with one-part geopolymer: Engineering, environmental and economic feasibility", *Case Studies in Construction Materials*, vol. 18, e01818, 2023. DOI: 10.1016/j.cscm.2022.e01818.

B

[38] L. Dong *et al.*, "Microstructure and mechanical behaviour of 3d printed ultra-high performance concrete after elevated temperatures", *Additive Manufacturing*, vol. 58, p. 103 032, 2022. DOI: 10.1016/j.addma.2022.103032.

[39] J. D. Malan, A. S. van Rooyen, and G. P. A. G. van Zijl, "Chloride induced corrosion and carbonation in 3d printed concrete", *Infrastructures*, vol. 7, no. 1, 2022. DOI: 10.3390/infrastructures7010001.

[40] J. Van Der Putten, "Mechanical properties and durability of 3d printed cementitious materials", Ph.D. dissertation, 2021.

[41] F. Bos *et al.*, "The realities of additively manufactured concrete structures in practice", *Cement and Concrete Research*, vol. 156, p. 106 746, 2022, ISSN: 0008-8846. DOI: 10.1016/j.cemconres.2022.106746.

[42] *Milestone house*, https://www.3dprintedhouse.nl/en/project-info/project-milestone/, Accessed on 06-10-2019.

[43] A. Dell'Endice, S. Bouten, T. Van Mele, and P. Block, "Structural design and engineering of striatus, an unreinforced 3d-concrete-printed masonry arch bridge", *Engineering Structures*, vol. 292, p. 116 534, 2023. DOI: 10.1016/j.engstruct.2023.116534.

[44] D. Asprone, C. Menna, F. P. Bos, *et al.*, "Rethinking reinforcement for digital fabrication with concrete", *Cement and Concrete Research*, vol. 112, pp. 111–121, 2018. DOI: 10.1016/j.cemconres.2018.05.020.

[45] F. Bester, M. van den Heever, J. Kruger, and G. van Zijl, "Reinforcing digitally fabricated concrete: A systems approach review", *Additive Manufacturing*, vol. 37, p. 101 737, 2021. DOI: 10.1016/j.addma.2020.101737.

[46] V. Mechtcherine, J. Grafe, V. N. Nerella, *et al.*, "3d-printed steel reinforcement for digital concrete construction–manufacture, mechanical properties and bond behaviour", *Construction and Building Materials*, vol. 179, pp. 125–137, 2018. DOI: 10.1016/j.conbuildmat.2018.05.202.

[47] V. N. Nerella, H. Ogura, and V. Mechtcherine, "Incorporating reinforcement into digital concrete construction", in *Proceedings of IASS annual symposia*, International Association for Shell and Spatial Structures (IASS), vol. 2018, 2018, pp. 1–8.

[48] D. Asprone, F. Auricchio, C. Menna, and V. Mercuri, "3d printing of reinforced concrete elements: Technology and design approach", *Construction and Building Materials*, vol. 165, pp. 218–231, 2018. DOI: 10.1016/j.conbuildmat.2018.01.018.

[49] T. A. Salet, Z. Y. Ahmed, F. P. Bos, and H. L. Laagland, "Design of a 3d printed concrete bridge by testing", *Virtual and Physical Prototyping*, vol. 13, no. 3, pp. 222–236, 2018. DOI: 10.1080/17452759.2018.1476064.

[50] T. Marchment and J. Sanjayan, "Mesh reinforcing method for 3d concrete printing", *Automation in Construction*, vol. 109, p. 102 992, 2020. DOI: 10.1016/j.autcon.2019.102992.

[51] D.-Y. Yoo and N. Banthia, "High-performance strain-hardening cementitious composites with tensile strain capacity exceeding 4%: A review", *Cement and Concrete Composites*, vol. 125, p. 104 325, 2022. DOI: 10.1016/j.cemconcomp.2021.104325.

[52] Y. Ding, K. Yu, and M. Li, "A review on high-strength engineered cementitious composites (hs-ecc): Design, mechanical property and structural application", *Structures*, vol. 35, pp. 903–921, 2022. DOI: 10.1016/j.istruc.2021.10.036.

[53] M. Lukovic, "Influence of interface and strain hardening cementitious composite (shcc) properties on the performance of concrete repairs", Ph.D. dissertation, Technische Universiteit Delft, Faculty of Civil Engineering and Geosciences, 2016.

[54] J. Wei, H. Liu, and C. K. Leung, "Application of high-strength strain-hardening cementitious composites (shcc) in the design of novel inter-module joint", *Construction and Building Materials*, vol. 359, p. 129 491, 2022. DOI: 10.1016/j.conbuildmat.2022.129491.

[55] K. Rokugo, T. Kanda, H. Yokota, and et al, "Applications and recommendations of high performance fiber reinforced cement composites with multiple fine cracking (hpfrcc) in japan", *Material structures*, vol. 42, pp. 1197–1208, 2009. DOI: 10.1617/s11527-009-9541-8.

[56] J. Zhou, S. Qian, M. Guadalupe Sierra, *et al.*, "Development of engineered cementitious composites with limestone powder and blast furnace slag", *Materials and Structures*, vol. 43, pp. 803–814, 2010. DOI: 10.1617/s11527-009-9549-0.

[57] V. Li and C. Wang S.and Wu, "Tensile strain-hardening behavior or polyvinyl alcohol engineered cementitious composite (pva-ecc)", *ACI Materials Journal*, vol. 98, no. 6, pp. 483–492, 2001.

[58] S. Zhou, L. Xie, Y. Jia, and C. Wang, "Review of cementitious composites containing polyethylene fibers as repairing materials", *Polymers*, vol. 7, p. 2624, 2020. DOI: 10.3390/polym12112624.

[59] I. Curosu, M. Liebscher, V. Mechtcherine, C. Bellmann, and S. Michel, "Tensile behavior of high-strength strain-hardening cement-based composites (hs-shcc) made with high-performance polyethylene, aramid and pbo fibers", *Cement and Concrete Research*, vol. 98, pp. 71–81, 2017. DOI: 10.1016/j.cemconres.2017.04.004.

[60] A. Ramezani, S. Modaresi, P. Dashti, M. R. GivKashi, F. Moodi, and A. A. Ramezanianpour, "Effects of different types of fibers on fresh and hardened properties of cement and geopolymer-based 3d printed mixtures: A review", *Buildings*, vol. 13, no. 4, 2023.

[61] J.-I. Choi, S. Y. Jang, S.-J. Kwon, and B. Y. Lee, "Tensile behavior and cracking pattern of an ultra-high performance mortar reinforced by polyethylene fiber", *Advances in Materials Science and Engineering*, p. 5 383 982, 2017. DOI: 10.1155/2017/5383982.

B

[62] A. E. N. D.-J. Kim and S. El-Tawil, "High performance fiber reinforced cement composites with innovative slip hardending twisted steel fibers", *International Journal of Concrete Structures and Materials*, vol. 3, no. 2, pp. 119–126, 2009. DOI: 10.4334/IJCSM.2009.3.2.119.

[63] D. G. Soltan, P. das Neves, A. Olvera, H. S. Junior, and V. C. Li, "Introducing a curauá fiber reinforced cement-based composite with strain-hardening behavior", *Industrial crops and products*, vol. 103, pp. 1–12, 2017. DOI: 10.1016/j.indcrop.2017.03.016.

[64] B. Zukowski, F. de Andrade Silva, and R. D. Toledo Filho, "Design of strain hardening cement-based composites with alkali treated natural curauá fiber", *Cement and Concrete Composites*, vol. 89, pp. 150–159, 2018. DOI: 10.1016/j.cemconcomp.2018.03.006.

[65] J. Li and Z. Deng, "Tensile behavior of hybrid fiber-reinforced ultra-high performance concrete", *Frontiers in Materials*, vol. 8, 2021. DOI: 10.3389/fmats.2021.769579.

[66] B.-T. Huang, K.-F. Weng, J.-X. Zhu, Y. Xiang, J.-G. Dai, and V. Li, "Engineered/strain-hardening cementitious composites (ecc/shcc) with an ultra-high compressive strength over 210 mpa", *Composites Communications*, vol. 26, p. 100 775, 2021. DOI: 10.1016/j.coco.2021.100775.

[67] L. Li, B. Li, Z. Wang, Z. Zhang, and O. Alselwi, "Effects of hybrid pva–steel fibers on the mechanical performance of high-ductility cementitious composites", *Buildings*, vol. 12, p. 1934, 2022. DOI: 10.3390/buildings12111934.

[68] H. Zhong, M. Chen, and M. Zhang, "Engineering properties of sustainable engineered cementitious composites with recycled tyre polymer fibres", *Construction and Building Materials*, vol. 370, p. 130 672, Mar. 2023. DOI: 10.1016/j.conbuildmat.2023.130672.

[69] S. Muzenski, I. Flores Vivian, K. Sobolev, and V. Mechtcherine, "Hydrophobic and superhydrophobic strain-hardening cement-based composites", *BFT international*, vol. 82, pp. 48–56, 2016.

[70] Z. He, J. Chen, L. Z., and Z. Ma, "Analytical approach for bursting cracking analysis of post-tensioned anchorage zone", *Structures*, vol. 52, pp. 401–409, 2023. DOI: 10.1016/j.istruc.2023.04.010.

[71] L. Hass, F. Bos, and T. Salet, "Characterizing the bond properties of automatically placed helical reinforcement in 3d printed concrete", *Construction and Building Materials*, vol. 355, p. 129 228, 2022. DOI: 10.1016/j.conbuildmat.2022.129228.

[72] L. Hass, K. Nefs, F. Bos, and T. Salet, "Application potential of combining strain hardening cementitious composites and helical reinforcement for 3d concrete printed structures: Case study of a spiral staircase", *Journal of Building Engineering*, vol. 80, 2023. DOI: 10.1016/j.jobe.2023.107926.

[73] Y. Chen, J. Yu, H. Younas, and C. Leung, "Experimental and numerical investigation on bond between steel rebar and high-strength strain-hardening cementitious composite (shcc) under direct tension", *Cement and Concrete Composites*, vol. 112, p. 103 666, 2020. DOI: 10.1016/j.cemconcomp.2020.103666.

[74] J. P. M. Deng and H. Sun, "Bond behavior of steel bar embedded in engineered cementitious composites under pull-out load", *Construction and Building Materials*, vol. 168, pp. 705–714, 2018. DOI: 10.1016/j.conbuildmat.2018.02.165.

[75] J. Kruger, S. Zeranka, and G. van Zijl, "Rheo-mechanics modelling of 3d concrete printing constructability", Ph.D. dissertation, Stellenbosch University, Dec. 2019. DOI: 10.13140/RG.2.2.16259.04649.

[76] R. J. M. Wolfs and A. S. J. Suiker, "Structural failure during extrusion-based 3D printing processes", English, *International Journal of Advanced Manufacturing Technology*, vol. 104, no. 1-4, pp. 565–584, 2019. DOI: 10.1007/s00170-019-03844-6.

[77] J. Kruger, S. Zeranka, and G. van Zijl, "Quantifying constructability performance of 3d concrete printing via rheology-based analytical models", in *Rheology and Processing of Construction Materials*, Springer, 2019, pp. 400–408. DOI: 10.1007/978-3-030-22566-7_46.

[78] R. Wolfs, "Experimental characterization and numerical modelling of 3d printed concrete: Controlling structural behaviour in the fresh and hardened state", English, Ph.D. dissertation, Technische Universiteit Eindhoven, 2019, ISBN: 978-90-386-4819-4.

[79] D. Marchon, S. Kawashima, H. Bessaies-Bey, S. Mantellato, and S. Ng, "Hydration and rheology control of concrete for digital fabrication: Potential admixtures and cement chemistry", *Cement and Concrete Research*, vol. 112, pp. 96–110, 2018. DOI: 10.1016/j.cemconres.2018.05.014.

[80] N. Roussel *et al.*, Eds., *Understanding the rheology of concrete* (Woodhead Publishing Series in Civil and Structural Engineering). Woodhead publishing, 2012, ISBN: 978-0-85709-028-7. DOI: 10.1016/B978-0-85709-028-7.50015-7.

[81] N. Roussel, H. Bessaies-Bey, S. Kawashima, D. Marchon, K. Vasilic, and R. Wolfs, "Recent advances on yield stress and elasticity of fresh cement-based materials", *Cement and Concrete Research*, vol. 124, p. 105 798, 2019. DOI: 10.1016/j.cemconres.2019.105798.

[82] J. Kruger, S. Zeranka, and G. van Zijl, "An ab initio approach for thixotropy characterisation of (nanoparticle-infused) 3d printable concrete", *Construction and Building Materials*, vol. 224, pp. 372–386, 2019. DOI: 10.1016/j.conbuildmat.2019.07.078.

[83] N. Roussel, G. Ovarlez, S. Garrault, and C. Brumaud, "The origins of thixotropy of fresh cement pastes", *Cement and Concrete Research*, vol. 42, no. 1, pp. 148–157, 2012. DOI: 10.1016/j.cemconres.2011.09.004.

[84] M. Li and V. C. Li, "Rheology, fiber dispersion, and robust properties of engineered cementitious composites", *Materials and Structures*, vol. 46, no. 3, pp. 405–420, 2013. DOI: 10.1617/s11527-012-9909-z.

[85] R. Nicolas *et al.*, "Assessing the fresh properties of printable cement-based materials: High potential tests for quality control", *Cement and Concrete Research*, vol. 158, p. 106 836, 2022. DOI: 10.1016/j.cemconres.2022.106836.

[86] Y. Chen, S. He, Y. Gan, O. Çopuroğlu, F. Veer, and E. Schlangen, "A review of printing strategies, sustainable cementitious materials and characterization methods in the context of extrusion-based 3d concrete printing", *Journal of Building Engineering*, vol. 45, p. 103 599, 2022. DOI: 10.1016/j.jobe.2021.103599.

[87] F. Bos, P. Kruger, S. Lucas, and G. van Zijl, "Juxtaposing fresh material characterisation methods for buildability assessment of 3d printable cementitious mortars", *Cement and Concrete Composites*, vol. 120, p. 104 024, 2021. DOI: 10.1016/j.cemconcomp.2021.104024.

[88] S. K. Kaliyavaradhan, P. Ambily, P. R. Prem, and S. B. Ghodke, "Test methods for 3d printable concrete", *Automation in Construction*, vol. 142, p. 104 529, 2022. DOI: 10.1016/j.autcon.2022.104529.

[89] D. Lootens, P. Jousset, L. Martinie, *et al.*, "Yield stress during setting of cement pastes from penetration tests", *Cement and Concrete Research*, vol. 39, no. 5, pp. 401–408, 2009. DOI: 10.1016/j.cemconres.2009.01.012.

[90] Z. Toutou, N. Roussel, and C. Lanos, "The squeezing test: A tool to identify firm cement-based material's rheological behaviour and evaluate their extrusion ability", *Cement and Concrete Research*, pp. 1891–1899, Oct. 2005. DOI: 10.1016/j.cemconres.2004.09.007.

[91] Y. Chen, Z. li, S. Chaves Figueiredo, O. Çopuroğlu, F. Veer, and E. Schlangen, "Limestone and calcined clay-based sustainable cementitious materials for 3d concrete printing: A fundamental study of extrudability and early-age strength development", *Applied Sciences*, vol. 9, 2019. DOI: 10.3390/app9091809.

[92] B. Panda, J. Lim, and M. Tan, "Mechanical properties and deformation behaviour of early age concrete in the context of digital construction", *Composites Part B: Engineering*, vol. 165, pp. 563–571, 2019. DOI: 10.1016/j.compositesb.2019.02.040.

[93] U. Pott, C. Wolf, Y. Petryna, and D. Stephan, "Evaluation of the unconfined uniaxial compression test to study the evolution of apparent printable mortar properties during the early age transition regime", *Cement and Concrete Research*, vol. 161, p. 106 956, 2022. DOI: 10.1016/j.cemconres.2022.106956.

[94] R. Wolfs, F. Bos, and T. Salet, "Correlation between destructive compression tests and non-destructive ultrasonic measurements on early age 3d printed concrete", *Construction and Building Materials*, vol. 181, pp. 447–454, 2018. DOI: 10.1016/j.conbuildmat.2018.06.060.

[95] A. L. van Overmeir, S. C. Figueiredo, B. Šavija, F. P. Bos, and E. Schlangen, "Design and analyses of printable strain hardening cementitious composites with optimized particle size distribution", *Construction and Building Materials*, vol. 324, p. 126 411, 2022. DOI: 10.1016/j.conbuildmat.2022.126411.

[96] A. Suiker, "Mechanical performance of wall structures in 3d printing processes: Theory, design tools and experiments", English, *International Journal of Mechanical Sciences*, vol. 137, pp. 145–170, Jan. 2018. DOI: 10.1016/j.ijmecsci.2018.01.010.

[97] N. Ducoulombier *et al.*, "The "slugs-test" for extrusion-based additive manufacturing: Protocol, analysis and practical limits", *Cement and Concrete Composites*, vol. 121, p. 104 074, 2021. DOI: 10.1016/j.cemconcomp.2021.104074.

[98] M. Santos De Franca, "Rheological behaviour of engineered cementitious composites reinforced with pva fibers", M.S. thesis, Politechnical University of Sao Paulo, 2018.

[99] C. J. Petrie, "The rheology of fibre suspensions", *Journal of Non-Newtonian Fluid Mechanics*, vol. 87, no. 2, pp. 369–402, 1999. DOI: 10.1016/S0377-0257(99)00069-5.

[100] E. Secrieru, V. Mechtcherine, C. Schröfl, and D. Borin, "Rheological characterisation and prediction of pumpability of strain-hardening cement-based-composites (shcc) with and without addition of superabsorbent polymers (sap) at various temperatures", *Construction and Building Materials*, vol. 112, pp. 581–594, 2016. DOI: 10.1016/j.conbuildmat.2016.02.161.

[101] M. Şahmaran, Z. Bilici, E. Ozbay, *et al.*, "Improving the workability and rheological properties of engineered cementitious composites using factorial experimental design", *Composites Part B: Engineering*, vol. 45, no. 1, pp. 356–368, 2013. DOI: 10.1016/j.compositesb.2012.08.015.

[102] S. B. Lindström and T. Uesaka, "A numerical investigation of the rheology of sheared fiber suspensions", *Physics of fluids*, vol. 21, no. 8, p. 083 301, 2009. DOI: 10.1017/S0022112010003885.

[103] M. S. de França, B. Cazacliu, T. Kränkel, and H. Savastano Jr., "Influence of measuring system on rheological behavior of pva-fiber reinforced mortars", *Construction and Building Materials*, vol. 314, p. 125 613, 2022, ISSN: 0950-0618. DOI: 10.1016/j.conbuildmat.2021.125613.

[104] *Testing hardened concrete*, European Committee for Standardization (CEN), 2021.

[105] V. Mechtcherine and J. Schulze, "Testing the behaviour of strain hardening cementitious composites in tension", *International RILEM Workshop on HPFRCC in Structural Applications, Honolulu, USA*, vol. 49, pp. 37–46, Jan. 2005. DOI: 10.1617/2912143942.005.

[106] K. Yu, L. Li, J. Yu, Y. Wang, J. Ye, and Q. Xu, "Direct tensile properties of engineered cementitious composites: A review", *Construction and Building Materials*, vol. 165, pp. 346–362, 2018. DOI: 10.1016/j.conbuildmat.2017.12.124.

B

[107] D. Kim, A. Naaman, and S. El-Tawil, "Comparative flexural behavior of four fiber reinforced cementitious composites", *Cement and Concrete Composites*, vol. 30, no. 10, pp. 917–928, 2008. DOI: 10.1016/j.cemconcomp.2008.08.002.

[108] K. Turk and M. Nehdi, "Flexural toughness of sustainable ecc with high-volume substitution of cement and silica sand", *Construction and Building Materials*, vol. 270, p. 121 438, 2021. DOI: 10.1016/j.conbuildmat.2020.121438.

[109] V. C. Li, C. Wu, S. Wang, A. Ogawa, and T. Saito, "Interface tailoring for strain-hardening polyvinyl alcohol-engineered cementitious composite (pva-ecc)", *Materials Journal*, vol. 99, no. 5, pp. 463–472, 2002. DOI: 10.14359/12325.

[110] A. Katz and V. C. Li, "A special technique for determining the bond strength of micro-fibres in cement matrix by pullout test", *Journal of Materials Science Letters*, pp. 1821–1823, 1996. DOI: 10.1007/BF00275353.

[111] G. Guinea, J. Planas, and M. Elices, "Measurement of the fracture energy using three-point bend tests: Part 1—influence of experimental procedures", *Materials and Structures*, vol. 25, pp. 212–218, 1992. DOI: 10.1007/BF02473065.

[112] *NEN-EN 14651 Test Method for Metallic Fibered Concrete – Measuring theFlexural Tensile Strength (Limit of Proportionality (LOP),Residual)*, Delft: NEN, 2007.

[113] V. Mechtcherine, K. v. Tittelboom, F. P. Bos, *et al.*, "A roadmap for quality control of hardening and hardened printed concrete", *Cement and Concrete Research*, vol. 157, p. 106 800, 2022. DOI: 10.1016/j.cemconres.2022.106800.

[114] T. Le *et al.*, "Hardened properties of high-performance printing concrete", *Cement and Concrete Research*, vol. 42, no. 3, pp. 558–566, 2012. DOI: 10.1016/j.cemconres.2011.12.003.

[115] R. Wolfs, F. Bos, and T. Salet, "Hardened properties of 3d printed concrete: The influence of process parameters on interlayer adhesion", *Cement and Concrete Research*, vol. 119, pp. 132–140, 2019.

[116] E.-A. Seo, W.-W. Kim, S.-W. Kim, H.-K. Kwon, and H.-J. Lee, "Mechanical properties of 3d printed concrete with coarse aggregates and polypropylene fiber in the air and underwater environment", *Construction and Building Materials*, vol. 378, p. 131 184, 2023, ISSN: 0950-0618. DOI: 10.1016/j.conbuildmat.2023.131184.

[117] S.-J. Woo, J.-M. Yang, H.-J. Lee, and H.-K. Kwon, "Comparison of properties of 3d-printed mortar in air vs. underwater", *Materials (Basel, Switzerland)*, vol. 14, Oct. 2021. DOI: 10.3390/ma14195888.

[118] W. Zhou, Y. Zhang, L. Ma, and V. Li, "Influence of printing parameters on 3d printing engineered cementitious composites (3dp-ecc)", *Cement and Concrete Composites*, vol. 130, p. 104 562, 2022. DOI: 10.1016/j.cemconcomp.2022.104562.

[119] Y. W. D. Tay, G. H. A. Ting, Y. Qian, B. Panda, L. He, and M. J. Tan, "Time gap effect on bond strength of 3d-printed concrete", *Virtual and Physical Prototyping*, vol. 14, no. 1, pp. 104–113, 2019. DOI: 10.1080/17452759.2018.1500420.

[120] B. Panda, N. A. N. Mohamed, Y. W. D. Tay, and M. J. Tan, "Bond strength in 3d printed geopolymer mortar", in *RILEM International Conference on Concrete and Digital Fabrication*, Springer, 2018, pp. 200–206. DOI: 10.1007/978-3-319-99519-9_18.

[121] J. G. Sanjayan, B. Nematollahi, M. Xia, and T. Marchment, "Effect of surface moisture on inter-layer strength of 3d printed concrete", *Construction and Building Materials*, vol. 172, pp. 468–475, 2018. DOI: 10.1016/j.conbuildmat.2018.03.232.

[122] B. Panda, N. A. Noor Mohamed, S. C. Paul, G. Bhagath Singh, M. J. Tan, and B. Šavija, "The effect of material fresh properties and process parameters on buildability and interlayer adhesion of 3d printed concrete", *Materials*, vol. 12, no. 13, 2019. DOI: 10.3390/ma12132149.

[123] N. Roussel and F. Cussigh, "Distinct-layer casting of scc: The mechanical consequences of thixotropy", *Cement and Concrete Research*, vol. 38, no. 5, pp. 624–632, 2008. DOI: 10.1016/j.cemconres.2007.09.023.

[124] F. Li, W. Shen, Q. Yuan, X. Hu, Z. Li, and C. Shi, "An overview on the effect of pumping on concrete properties", *Cement and Concrete Composites*, vol. 129, p. 104 501, 2022. DOI: 10.1016/j.cemconcomp.2022.104501.

[125] K. Jang, S. Kwon, and M. Choi, "Experimental observation on variation of rheological properties during concrete pumping", *International Journal of Concrete Structures and Materials*, vol. 12, 79 2018. DOI: 10.1186/s40069-018-0310-3.

[126] W. Shen *et al.*, "Influence of pumping on the resistivity evolution of high-strength concrete and its relation to the rheology", *Construction and Building Materials*, vol. 302, p. 124 095, 2021. DOI: 10.1016/j.conbuildmat.2021.124095.

[127] M. Chen *et al.*, "Rheological behaviors and structure build-up of 3d printed polypropylene and polyvinyl alcohol fiber-reinforced calcium sulphoaluminate cement composites", *Journal of Materials Research and Technology*, vol. 10, pp. 1402–1414, 2021. DOI: 10.1016/j.jmrt.2020.12.115.

[128] N. Xu and Y. Qian, "Effects of fiber volume fraction, fiber length, water-binder ratio, and nanoclay addition on the 3d printability of strain-hardening cementitious composites (shcc)", *Cement and Concrete Composites*, vol. 139, p. 105 066, 2023. DOI: 10.1016/j.cemconcomp.2023.105066.

[129] V. Alamshahi, A. Taeb, R. Ghaffarzadeh, and M. A. Rezaee, "Effect of composition and length of pp and polyester fibres on mechanical properties of cement based composites", *Construction and Building Materials*, vol. 36, pp. 534–537, 2012. DOI: 10.1016/j.conbuildmat.2012.06.005.

[130] L. Reiter, T. Wangler, N. Roussel, and R. J. Flatt, "The role of early age structural build-up in digital fabrication with concrete", *Cement and Concrete Research*, vol. 112, pp. 86–95, 2018. DOI: 10.1016/j.cemconres.2018.05.011.

[131] Y. Zhang, Y. Zhang, W. She, *et al.*, "Rheological and harden properties of the high-thixotropy 3d printing concrete", *Construction and Building Materials*, vol. 201, pp. 278–285, 2019. DOI: 10.1016/j.conbuildmat.2018.12.061.

[132] Z. Quanji, "Thixotropic behavior of cement-based materials: Effect of clay and cement types", M.S. thesis, Iowa State University, 2010.

[133] H. Brouwers and H. Radix, "Self-compacting concrete: The role of the particle size distribution", *Transactions of The Society for Modeling and Simulation International - SIMULATION*, Jan. 2005. DOI: 10.1617/2912143624.010.

[134] S. Kumar and M. Santhanam, "Particle packing theories and their application in concrete mixture proportioning: A review", *Indian Concrete Journal*, vol. 77, pp. 1324–1331, Sep. 2003.

[135] D. D. J.E. Funk, "Predictive process control of crowded particulate suspensions: Applied to ceramic manufacturing", 1994. DOI: 10.1007/978-1-4615-3118-0.

[136] X. Wang, K. Wang, P. Taylor, and G. Morcous, "Assessing particle packing based self-consolidating concrete mix design method", *Construction and Building Materials*, vol. 70, pp. 439–452, 2014, ISSN: 0950-0618. DOI: 10.1016/j.conbuildmat.2014.08.002.

[137] K. Ragalwar, W. F. Heard, B. A. Williams, *et al.*, "Significance of the particle size distribution modulus for strain-hardening-ultra-high performance concrete (sh-uhpc) matrix design", *Construction and Building Materials*, vol. 234, p. 117 423, 2020. DOI: 10.1016/j.conbuildmat.2019.117423.

[138] K. A. Ragalwar, H. Nguyen, R. Ranade, W. F. Heard, and B. A. Williams, "Influence of distribution modulus of particle size distribution on rheological and mechanical properties of ultra-high-strength shcc matrix", in *Strain-Hardening Cement-Based Composites*, Springer Netherlands, 2018, pp. 221–229. DOI: 10.1007/978-94-024-1194-2_26.

[139] S. Fennis and J. Walraven, "Using particle packing technology for sustainable concrete mixture design", *Heron*, vol. 57, 2012, ISSN: 0046-7316.

[140] A. R. Arunothayan, B. Nematollahi, R. Ranade, S. H. Bong, and J. Sanjayan, "Development of 3d-printable ultra-high performance fiber-reinforced concrete for digital construction", *Construction and Building Materials*, vol. 257, p. 119 546, 2020. DOI: 10.1016/j.conbuildmat.2020.119546.

[141] A. Andreasen and J. Andersen, "Ueber die beziehung zwischen kornabstufung und zwischenraum in produkten aus losen körnern mit einigen experimenten", *Kolloid-Zeitschrift*, vol. 50, pp. 217–228, 1930. DOI: 10.1007/BF01422986.

[142] D. Kumar, K. Ragalwar, W. Heard, B. Williams, and R. Ranade, "Influence of maximum aggregate size and distribution modulus on uhpc matrix properties", in *Ultra-High Performance Concrete and High Performance Construction Materials*, Mar. 2020. DOI: 10.17170/kobra-202002271026.

[143] J. Benbow and J. Bridgwater, "Paste flow and extrusion", *Oxford Series on Advanced Manufacturing*, 1993.

[144] J. Benbow, S. Jazayeri, and J. Bridgwater, "The flow of pastes through dies of complicated geometry", *Powder Technology*, vol. 65, no. 1, pp. 393–401, 1991. DOI: 10.1016/0032-5910(91)80201-S.

[145] J. Benbow, E. Oxley, and J. Bridgwater, "The extrusion mechanics of pastes—the influence of paste formulation on extrusion parameters", *Chemical Engineering Science*, vol. 42, no. 9, pp. 2151–2162, 1987. DOI: 10.1016/0009-2509(87)85036-4.

[146] *ASTM D2166-00, Standard Test Method for Unconfined Compressive Strength of Cohesive Soil*, ASTM International, www.astm.org, 2000.

[147] P. Kruger, S. Zeranka, and G. v. Zijl, "3d concrete printing: A lower bound analytical model for buildability performance quantification", *Automation in Construction*, vol. 106, p. 102 904, 2019. DOI: 10.1016/j.autcon.2019.102904.

[148] A. L. van Overmeir, B. Šavija, F. P. Bos, and E. Schlangen, "3d printable strain hardening cementitious composites (3dp-shcc), tailoring fresh and hardened state properties", *Construction and Building Materials*, vol. 403, 2023. DOI: 10.1016/j.conbuildmat.2023.132924.

[149] *ASTM C39/C39M-17, Standard Test Method for Compressive Strength of Cylindrical Concrete Specimens*, ASTM International, www.astm.org, 2017.

[150] A. L. van Overmeir, "Designing an interlayer reinforcement solution for printable strain-hardening cement-based composites", M.S. thesis, Delft University of Technology, 2020. [Online]. Available: https://repository.tudelft.nl/islandora/object/uuid%3A3e397363-4749-47e3-8f9a-201639ab74f2.

[151] S. Chaves Figueiredo, A. L. van Overmeir, K. Nefs, *et al.*, "Quality assessment of printable strain hardening cementitious composites manufactured in two different printing facilities", in *Second RILEM International Conference on Concrete and Digital Fabrication*, Springer International Publishing, 2020, pp. 824–838, ISBN: 978-3-030-49916-7. DOI: 10.1007/978-3-030-49916-7_81.

[152] V. C. Li *et al.*, "On the emergence of 3d printable engineered, strain hardening cementitious composites (ecc/shcc)", *Cement and Concrete Research*, vol. 132, p. 106 038, 2020. DOI: 10.1016/j.cemconres.2020.106038.

[153] L. Hermens, "Strength development of concrete used for 3d concrete printing determination of the influence of temperature on the development of concrete strength properties before initial set and the applicabillity of maturity methods", M.S. thesis, Eindhoven University of Technology, 2018. [Online]. Available: https://research.tue.nl/en/studentTheses/strength-development-of-concrete-used-for-3d-concrete-printing.

[154] S. Grünewald, "9 - fibre reinforcement and the rheology of concrete", in *Understanding the Rheology of Concrete*, N. Roussel, Ed., Woodhead Publishing, 2012, pp. 229–256, ISBN: 978-0-85709-028-7. DOI: 10.1533/9780857095282.2.229.

[155] L. Woo, S. Wansom, N. Ozyurt Zihnioğlu, B. Mu, S. Shah, and T. Mason, "Characterizing fiber dispersion in cement composites using ac-impedance spectroscopy", *Cement and Concrete Composites*, vol. 27, Jul. 2005. DOI: 10.1016/j.cemconcomp.2004.06.003.

B

[156] F. Bos, R. Wolfs, Z. Ahmed, and T. Salet, "Additive manufacturing of concrete in construction: Potentials and challenges of 3d concrete printing", *Virtual and Physical Prototyping*, vol. 11, pp. 209–225, 2016. DOI: 10.1080/17452759.2016.1209867.

[157] Veder, https://www.verderliquids.com/, Accessed on 2021-03-21.

[158] PFT, https://www.pft.net/, Accessed on 2020-09-10.

[159] M-Tec, https://m-tec.com/, Accessed on 2021-08-10.

[160] A. Aql, "Dimensional and empirical modeling of fluid flow in progressing cavity pumps", https://www.researchgate.net/publication/324175995-Dimensional-and-Empirical-Modeling-of-Fluid-Flow-in-Progressing-Cavity-Pumps, Accessed on 2023-09-3, M.S. thesis, Kuwait University, 2016.

[161] M. Volk, *Pump Characteristics and Applications* (Mechanical Engineering). CRC Press, 2013, ISBN: 9781466563094. [Online]. Available: https://books.google.nl/books?id=QFjSBQAAQBAJ.

[162] S. Khan, M. Kamal, F. Khan, *et al.*, "Performance evaluation of the fresh and hardened properties of different pva-ecc mixes: An experimental approach", *Case Studies in Construction Materials*, vol. 18, e01764, 2023. DOI: 10.1016/j.cscm.2022.e01764.

[163] Z. Pan, C. Wu, J. Liu, *et al.*, "Study on mechanical properties of cost-effective polyvinyl alcohol engineered cementitious composites (pva-ecc)", *Construction and Building Materials*, vol. 78, pp. 397–404, 2015. DOI: 10.1016/j.conbuildmat.2014.12.071.

[164] A. Drescher, A. Waters, and C. Rhoades, "Arching in hoppers: I. arching theories and bulk material flow properties", *Powder Technology*, vol. 84, no. 2, pp. 165–174, 1995. DOI: 10.1016/0032-5910(95)02981-7.

[165] G. Enstad, *A novel theory on the arching and doming in mass flow hoppers*. Norwegan technical university, 1981.

[166] R. Buswell, J. Xu, D. D. Becker, *et al.*, "Geometric quality assurance for 3d concrete printing and hybrid construction manufacturing using a standardised test part for benchmarking capability", *Cement and Concrete Research*, vol. 156, p. 106 773, 2022. DOI: 10.1016/j.cemconres.2022.106773.

[167] H. Zhang, J. Wang, Y. Liu, *et al.*, "Effect of processing parameters on the printing quality of 3d printed composite cement-based materials", *Materials Letters*, vol. 308, no. Part B, p. 131 271, 2022. DOI: 10.1016/j.matlet.2021.131271.

[168] S. Bhattacherjee, S. Jain, and M. Santhanam, "Developing 3d printable and buildable limestone calcined clay-based cement composites with higher aggregate content", *Construction and Building Materials*, vol. 376, p. 131 058, 2023. DOI: 10.1016/j.conbuildmat.2023.131058.

[169] C. Zhang *et al.*, "Mix design concepts for 3d printable concrete: A review", *Cement and Concrete Composites*, vol. 122, p. 104 155, 2021. DOI: 10.1016/j.cemconcomp.2021.104155.

[170] C. Ferraris, K. Obla, and R. Hill, "The influence of mineral admixtures on the rheology of cement paste and concrete", *Cement and Concrete research*, vol. 31, no. 2, pp. 245–255, 2001. DOI: 10.1016/S0008-8846(00)00454-3.

[171] Z. Geng *et al.*, "Layer-interface properties in 3d printed concrete: Dual hierarchical structure and micromechanical characterization", *Cement and Concrete research*, vol. 138, p. 106 220, 2020. DOI: 10.1016/j.cemconres.2020.106220.

[172] C. Liu *et al.*, "Influence of hydroxypropyl methylcellulose and silica fume on stability, rheological properties, and printability of 3d printing foam concrete", *Cement and Concrete Composites*, vol. 122, p. 104 158, 2021. DOI: 10.1016/j.cemconcomp.2021.104158.

[173] R. Banar, P. Dashti, A. Zolfagharnasab, A. Ramezanianpour, and A. Ramezanianpour, "A comprehensive comparison between using silica fume in the forms of water slurry or blended cement in mortar/concrete", *Journal of Building Engineering*, vol. 46, p. 103 802, 2022. DOI: 10.1016/j.jobe.2021.103802.

[174] M. Ashraf *et al.*, "Developing a sustainable concrete incorporating bentonite clay and silica fume: Mechanical and durability performance", *Journal of Cleaner Production*, vol. 337, p. 130 315, 2022. DOI: 10.1016/j.jclepro.2021.130315.

[175] M. Hou, D. Zhang, and V. Li, "Crack width control and mechanical properties of low carbon engineered cementitious composites (ecc)", *Construction and Building Materials*, vol. 348, p. 128 692, 2022. DOI: 10.1016/j.conbuildmat.2022.128692.

[176] *EN 1015-3 - Methods of test for mortar for masonry. Determination of consistence of fresh mortar (by flow table)*, European Committee for Standatization, CEN, 1999.

[177] S. Cho, J. Kruger, F. Bester, M. van den Heever, A. van Rooyen, and G. van Zijl, "A compendious rheo-mechanical test for printability assessment of 3d printable concrete", in *Second RILEM International Conference on Concrete and Digital Fabrication*, Springer International Publishing, 2020, pp. 196–205. DOI: 10.1007/978-3-030-49916-7_20.

[178] S. Shamir, S. Raman, A. Kaish, and A. M. Azrul, "Calibration of astm c230 cone for measuring flow diameter of self-flowing mortar according to the efnarc recommendation", 2020. DOI: 10.1007/978-3-030-22566-7_31.

[179] N. Roussel and P. Coussot, "Fifty-cent rheometer" for yield stress measurements: From slump to spreading flow", *Journal of Rheology*, vol. 49, 2005. DOI: 10.1122/1.1879041.

[180] T. Shin and J. Kim, "First step in modelling the flow table test to characterize the rheology of normally vibrated concrete", *Cement and Concrete Research*, vol. 152, 2022. DOI: 10.1016/j.cemconres.2021.106678.

[181] B. Tahmouresi, P. Nemati, M. Asadi, A. Saradar, and M. Moein, "Mechanical strength and microstructure of engineered cementitious composites: A new configuration for direct tensile strength, experimental and numerical analysis", *Construction and Building Materials*, vol. 269, p. 121 361, 2021. DOI: 10.1016/j.conbuildmat.2020.121361.

[182] K. Yu, W. McGee, T. Ng, H. Zhu, and V. Li, "3d-printable engineered cementitious composites (3dp-ecc): Fresh and hardened properties", *Cement and Concrete Research*, vol. 143, p. 106 388, 2021. DOI: 10.1016/j.cemconres.2021.106388.

[183] K. Nefs *et al.*, "Consistency of mechanical properties of 3d printed strain hardening cementitious composites within one printing system", in *Third RILEM International Conference on Concrete and Digital Fabrication*, Springer International Publishing, 2022, pp. 145–151. DOI: 10.1007/978-3-031-06116-5_22.

[184] A. van Overmeir, B. Šavija, F. Bos, and E. Schlangen, "Effects of 3d concrete printing phases on the mechanical performance of printable strain-hardening cementitious composites", *Buildings*, vol. 13, p. 2483, 2023.

[185] *EN 196-1:2016 Methods of testing cement - Part 1: Determination of strength*, European Comitee for Standatization, CEN.

[186] S. S. Shapiro and M. B. Wilk, "An analysis of variance test for normality (complete samples)", *Biometrika*, vol. 52, p. 591, 1965. DOI: 10.2307/2333709.

[187] V. Li, "Engineered cementitious composites (ecc) – material, structural, and durability performance", in *Concrete Construction Engineering Handbook*, E. Nawy, Ed., Oxford: CRC Press, 2008, ch. 24.

[188] D. G. Soltan and V. C. Li, "A self-reinforced cementitious composite for building-scale 3d printing", *Cement and Concrete Composites*, vol. 90, pp. 1–13, 2018. DOI: 10.1016/j.cemconcomp.2018.03.017.

[189] E. Secrieru, D. Cotardo, V. Mechtcherine, L. Lohaus, C. Schröfl, and C. Begemann, "Changes in concrete properties during pumping and formation of lubricating material under pressure", *Cement and Concrete Research*, vol. 108, pp. 129–139, 2018. DOI: 10.1016/j.cemconres.2018.03.018.

[190] E. Gallucci, X. Zhang, and K. Scrivener, "Effect of temperature on the microstructure of calcium silicate hydrate (c-s-h)", *Cement and Concrete Research*, vol. 53, pp. 185–195, 2013. DOI: 10.1016/j.cemconres.2013.06.008.

[191] B. Lothenbach, F. Winnefeld, C. Alder, E. Wieland, and P. Lunk, "Effect of temperature on the pore solution, microstructure and hydration products of portland cement pastes", *Cement and Concrete Research*, vol. 37, no. 4, pp. 483–491, 2007. DOI: 10.1016/j.cemconres.2006.11.016.

[192] F. Liu, B. Wang, Y. Xing, K. Zhang, and W. Jiang, "Effect of polyvinyl alcohol on the rheological properties of cement mortar", vol. 25(3), p. 754, 2020. DOI: 10.3390/molecules25030754.

[193] C. Redon, V. Li, C. Wu, H. Hoshiro, T. Saito, and A. Ogawa, "Measuring and modifying interface properties of pva fibers in ecc matrix", *Journal of Materials in Civil Engineering*, vol. 13, Dec. 2001. DOI: 10.1061/(ASCE)0899-1561(2001)13:6(399).

[194] A. Bashiri Rezaie *et al.*, "Enhancing the interfacial bonding between pe fibers and cementitious matrices through polydopamine surface modification", *Composites Part B: Engineering*, vol. 217, p. 108 817, 2021. DOI: 10.1016/j.compositesb.2021.108817.

[195] V. Li and T. Kanda, "Engineered cementitious composites for structural applications", *Journal of Materials in Civil Engineering*, vol. 10, pp. 66–69, 1998. DOI: 10.1061/(ASCE)0899-1561(1998)10:2(66).

[196] X. Zhao, X. Cai L.and Ji, W. Zeng, and J. Liu, "Mechanical properties of polyethylene fiber reinforced ultra high performance concrete (uhpc)", *Materials*, vol. 15, p. 8734, 2022. DOI: 10.3390/ma15248734.

[197] J.-X. Zhu, L.-Y. Xu, B.-T. Huang, K.-F. Weng, and J.-G. Dai, "Recent developments in engineered/strain-hardening cementitious composites (ecc/shcc) with high and ultra-high strength", *Construction and Building Materials*, vol. 342, p. 127 956, 2022. DOI: 10.1016/j.conbuildmat.2022.127956.

[198] J. Versteege, R. Wolfs, and T. Salet, "In-line measurement systems for 3dcp quality control", Third RILEM International Conference on Concrete and Digital Fabrication, 2022. [Online]. Available: https://www.digitalconcrete2022.com/.

[199] M. Kamal, S. Khan, K. Shahzada, and M. Alam, "Experimental investigation of the mechanical properties of engineered cementitious composites (ecc)", *International Journal of Advanced Structures and Geotechnical Engineering*, vol. 05, pp. 40–45, Apr. 2016.

[200] S. Aydın and B. Baradan, "The effect of fiber properties on high performance alkali-activated slag/silica fume mortars", *Composites Part B: Engineering*, vol. 45, no. 1, pp. 63–69, 2013, ISSN: 1359-8368. DOI: 10.1016/j.compositesb.2012.09.080.

[201] A. Ede, "The resistance of concrete pumped through pipelines", *Magazine of Concrete research*, vol. 9, no. 27, pp. 129–140, 1967. DOI: 10.1680/macr.1957.9.27.129.

[202] V. Mechtcherine, V. N. Nerella, and K. Kasten, "Testing pumpability of concrete using sliding pipe rheometer", *Construction and Building Materials*, vol. 53, pp. 312–323, 2014. DOI: 10.1016/j.conbuildmat.2013.11.037.

[203] V. N. Nerella and V. Mechtcherine, "Virtual sliding pipe rheometer for estimating pumpability of concrete", *Construction and Building Materials*, vol. 170, pp. 366–377, 2018. DOI: 10.1016/j.conbuildmat.2018.03.003.

[204] K. Ozawa, "High performance concrete based on the durability design of concrete structures", in *The Second East Asia-Pasific Conference on Structural Engineering & Construction*, 1989.

[205] H. Okamura, "Self-compacting high-performance concrete", *Concrete international*, vol. 19, no. 7, pp. 50–54, 1997. DOI: 10.2749/101686696780496292.

[206] *The European Guidelines for Self-Compacting Concrete: Specification, Production and Use*, EFNARC, 2005. [Online]. Available: http://www.efnarc.org/pdf/SCCGuidelinesMay2005.pdf.

[207] P. Bartos, M. Sonebi, and A. Tamimi, *Workability and Rheology of Fresh Concrete: Compendium of Tests*. Jan. 2002, ISBN: 2-912143-32-2.

[208] S. Pandey, A. Dalvi, A. Patel, B. Chaurasia, and N. Mishra, "A review on the study of principle characteristics, composition mixture and durability of self compacting concrete with different techniques", *nternational Journal of Scientific Engineering and Science*, vol. 2, pp. 10–13, 1 2018, ISSN: 2456-7361.

[209] A. Perrot, D. Rangeard, and A. Pierre, "Structural built-up of cement-based materials used for 3d-printing extrusion techniques", *Materials and Structures*, vol. 49, no. 4, pp. 1213–1220, 2016. DOI: 10.1617/s11527-015-0571-0.

[210] D. Burt, "Improved design of settling tanks using an extended drift flux model", Ph.D. dissertation, Jan. 2010. DOI: 10.13140/RG.2.1.5109.2082.

[211] E. Bingham, *Fluidity and Plasticity*. 1922, p. 440.

[212] W. Herschel and R. Bulkley, "Konsistenzmessungen von gummi-benzollösungen", *Kolloid-Zeitschrift*, vol. 39, pp. 291–300, 1926. DOI: 10.1007/BF01432034.

[213] F. de Larrard, C. Ferraris, and T. Sedran, "Fresh concrete: A herschel-bulkley material", *Materials and structures*, vol. 31, pp. 494–498, 1998. DOI: 10.1007/BF02480474.

[214] W. Wu, X. Huang, Y. Li, C. Fang, and X. Jian, "A modified lbm for non-newtonian effect of cement paste flow in 3d printing", *Rapid Prototyping Journal*, vol. 25, pp. 22–29, 2019. DOI: 10.1108/RPJ-06-2017-0124.

[215] *ASTM manual for conducting an interlaboratory study of a test method by American Society for Testing and Materials*, ASTM, 1963.

[216] *Standard Practice for Use of the Terms Precision and Bias in ASTM Test Methods*, ASTM, 1961.

[217] WHO, ""who" - library cataloguing-in-publication data laboratory quality management system: Handbook", 2011.

[218] E. M. Asif, I.-U.-H. Col, A. Mangrio, N. Mustafa, and B. Iqbal, "Analysis of application uniformity and pressure variation of microtube emitter of trickle irrigation system", *Net Journal of Agricultural Science*, vol. 3, pp. 14–22, Jan. 2015.

[219] Y. W. D. Tay, Y. Qian, and M. J. Tan, "Printability region for 3d concrete printing using slump and slump flow test", *Composites Part B: Engineering*, vol. 174, p. 106 968, 2019. DOI: 10.1016/j.compositesb.2019.106968.

[220] Y. Chen, S. He, Y. Z., Z. Wan, O. Çopuroglu, and E. Schlangen, "3d printing of calcined clay-limestone-based cementitious materials", *Cement and Concrete Research*, vol. 149, p. 106 553, 2021. DOI: 10.1016/j.cemconres.2021.106553.

[221] Y. Chen *et al.*, "Improving printability of limestone-calcined clay-based cementitious materials by using viscosity-modifying admixture", *Cement and Concrete Research*, vol. 132, p. 106 040, 2020, ISSN: 0008-8846. DOI: 10.1016/j.cemconres.2020.106040.

[222] G. Ma, Z. Li, and L. Wang, "Printable properties of cementitious material containing copper tailings for extrusion based 3d printing", *Construction and Building Materials*, vol. 162, pp. 613–627, 2018. DOI: 10.1016/j.conbuildmat.2017.12.051.

[223] V. Nerella, M. Näther, A. Iqbal, M. Butler, and V. Mechtcherine, "Inline quantification of extrudability of cementitious materials for digital construction", *Cement and Concrete Composites*, vol. 95, pp. 260–270, 2019. DOI: 10.1016/j.cemconcomp.2018.09.015.

[224] A. Laskar, "Correlating slump, slump flow, vebe and flow tests to rheological parameters of high-performance concrete", *Materials Research-ibero-american Journal of Materials*, vol. 12, Mar. 2009. DOI: 10.1590/S1516-14392009000100009.

[225] S. Chidiac, F. Habibbeigi, and D. Chan, "Slump and slump flow for characterizing yield stress of fresh concrete", *ACI Materials Journal*, vol. 103, pp. 413–418, Nov. 2006.

[226] R. Wolfs, F. Bos, and T. Salet, "Early age mechanical behaviour of 3d printed concrete: Numerical modelling and experimental testing", *Cement and Concrete Research*, vol. 106, pp. 103–116, 2018. DOI: 10.1016/j.cemconres.2018.02.001.

[227] T. Di Carlo, B. Khoshnevis, and A. Carlson, "Experimental and numerical techniques to characterize structural properties of fresh concrete", in *ASME International Mechanical Engineering Congress and Exposition*, American Society of Mechanical Engineers, vol. 56383, 2013, V009T10A062.

[228] T. Ding, J. Xiao, F. Qin, and Z. Duan, "Mechanical behavior of 3d printed mortar with recycled sand at early ages", *Construction and Building Materials*, vol. 248, p. 118 654, 2020. DOI: 10.1016/j.conbuildmat.2020.118654.

[229] L. Casagrande, L. Esposito, C. Menna, D. Asprone, and F. Auricchio, "Effect of testing procedures on buildability properties of 3d-printable concrete", *Construction and Building Materials*, vol. 245, p. 118 286, 2020. DOI: 10.1016/j.conbuildmat.2020.118286.

[230] A. Perrot, D. Rangeard, V. N. Nerella, and V. Mechtcherine, "Extrusion of cement-based materials-an overview", *RILEM Technical Letters*, vol. 3, pp. 91–97, Jan. 2018. DOI: 10.21809/rilemtechlett.2018.75.

[231] X. Zhou, Z. Li, M. Fan, and H. Chen, "Rheology of semi-solid fresh cement pastes and mortars in orifice extrusion", *Cement and Concrete Composites*, vol. 37, pp. 304–311, 2013. DOI: 10.1016/j.cemconcomp.2013.01.004.

[232] R. Jayathilakage, P. Rajeev, and J. Sanjayan, "Extrusion rheometer for 3d concrete printing", *Cement and Concrete Composites*, vol. 121, p. 104 075, 2021. DOI: 10.1016/j.cemconcomp.2021.104075.

[233] Y. Chen, S. Chaves Figueiredo, Ç. Yalçinkaya, O. Çopuroğlu, F. Veer, and E. Schlangen, "The effect of viscosity-modifying admixture on the extrudability of limestone and calcined clay-based cementitious material for extrusion-based 3d concrete printing", *Materials*, vol. 12, no. 9, 2019. DOI: 10.3390/ma12091374.

[234] R. Jayathilakage, P. Rajeev, and J. Sanjayan, "Rheometry for concrete 3d printing: A review and an experimental comparison", *Buildings*, vol. 12, no. 8, 2022. DOI: 10.3390/buildings12081190.

[235] A. Fasihi and N. A. Libre, "From pumping to deposition: A comprehensive review of test methods for characterizing concrete printability", *Construction and Building Materials*, vol. 414, p. 134 968, 2024. DOI: 10.1016/j.conbuildmat.2024.134968.

[236] R. Basterfield, C. Lawrence, and M. Adams, "On the interpretation of orifice extrusion data for viscoplastic materials", *Chemical Engineering Science*, vol. 60, no. 10, pp. 2599–2607, 2005. DOI: 10.1016/j.ces.2004.12.019.

[237] L. Reiter, T. Wangler, N. Roussel, and R. J. Flatt, "Slow penetration for characterizing concrete for digital fabrication", *Cement and Concrete Research*, vol. 157, p. 106 802, 2022. DOI: 10.1016/j.cemconres.2022.106802.

[238] U. Pott and D. Stephan, "Penetration test as a fast method to determine yield stress and structural build-up for 3d printing of cementitious materials", *Cement and Concrete Composites*, vol. 121, p. 104 066, 2021. DOI: 10.1016/j.cemconcomp.2021.104066.

[239] T. Mezger, *The Rheology Handbook: For Users of Rotational and Oscillatory Rheometers* (Coatings compendia). Vincentz Network, 2006, ISBN: 9783878701743. DOI: 10.1515/9783748603702. [Online]. Available: https://books.google.nl/books?id=N9FdnOMEIDIC.

[240] A. L. Lima *et al.*, "Oscillatory shear rheology as an in-process control tool for 3d printing medicines production by fused deposition modeling", *Journal of Manufacturing Processes*, vol. 76, pp. 850–862, 2022. DOI: 10.1016/j.jmapro.2022.03.001.

[241] Y. Chen *et al.*, "Can superabsorbent polymers be used as rheology modifiers for cementitious materials in the context of 3d concrete printing?", *Construction and Building Materials*, vol. 371, p. 130 777, 2023. DOI: 10.1016/j.conbuildmat.2023.130777.

[242] *Amplitude sweeps*, https://wiki.anton-paar.com/en/amplitude-sweeps/, Accessed on 2023-06-05.

[243] G. Ovarlez, "2 - introduction to the rheometry of complex suspensions", in *Understanding the Rheology of Concrete*, ser. Woodhead Publishing Series in Civil and Structural Engineering, N. Roussel, Ed., Woodhead Publishing, 2012, pp. 23–62, ISBN: 978-0-85709-028-7. DOI: 10.1533/9780857095282.1.23.

[244] G. Giridhar, P. R. Prem, and D. Jiao, "Effect of varying shear rates at different resting times on the rheology of 3d printable concrete", *Materials Today: Proceedings*, 2023. DOI: 10.1016/j.matpr.2023.03.027.

[245] M. Chen *et al.*, "Rheological parameters, thixotropy and creep of 3d-printed calcium sulfoaluminate cement composites modified by bentonite", *Composites Part B: Engineering*, vol. 186, 2020. DOI: 10.1016/j.compositesb.2020.107821.

[246] Y. Zhang, Z. Jiang, Y. Zhu, J. Zhang, Q. Ren, and T. Huang, "Effects of redispersible polymer powders on the structural build-up of 3d printing cement paste with and without hydroxypropyl methylcellulose", *Construction and Building Materials*, vol. 267, 2021. DOI: 10.1016/j.conbuildmat.2020.120551.

[247] Z. Duan, L. Li, Q. Yao, S. Zou, A. Singh, and H. Yang, "Effect of metakaolin on the fresh and hardened properties of 3d printed cementitious composite", *Construction and Building Materials*, vol. 350, 2022. DOI: 10.1016/j.conbuildmat.2022.128808.

[248] E. M. Aydin, B. Kara, Z. B. Bundur, N. Ozyurt, O. Bebek, and M. Ali Gulgun, "A comparative evaluation of sepiolite and nano-montmorillonite on the rheology of cementitious materials for 3d printing", *Construction and Building Materials*, vol. 350, p. 128 935, 2022. DOI: 10.1016/j.conbuildmat.2022.128935.

[249] *Flow curve and yield point determination with rotational viscometry*, https://wiki.anton-paar.com/en/flow-curve-and-yield-point-determination-with-rotational-viscometry, Accessed on 2023-06-05.

[250] E. Chaparian, C. E. Owens, and G. H. McKinley, "Computational rheometry of yielding and viscoplastic flow in vane-and-cup rheometer fixtures", *Journal of Non-Newtonian Fluid Mechanics*, vol. 307, p. 104 857, 2022. DOI: 10.1016/j.jnnfm.2022.104857.

[251] Q. Yuan, D. Zhou, K. H. Khayat, D. Feys, and C. Shi, "On the measurement of evolution of structural build-up of cement paste with time by static yield stress test vs. small amplitude oscillatory shear test", *Cement and Concrete Research*, vol. 99, pp. 183–189, 2017. DOI: 10.1016/j.cemconres.2017.05.014.

[252] A. Papo and B. Caufin, "A study of the hydration process of cement pastes by means of oscillatory rheological techniques", *Cement and Concrete Research*, vol. 21, no. 6, pp. 1111–1117, 1991. DOI: 10.1016/0008-8846(91)90071-O.

[253] J. Liu, W. Zhao, T. Jiang, Q. Wang, and B. Sun, "Rheology and yield stress evolution of highly flowable cementitious grouting materials: Mechanisms and modeling", *Construction and Building Materials*, vol. 421, p. 135 686, 2024. DOI: 10.1016/j.conbuildmat.2024.135686.

[254] C. Gosselin, R. Duballet, P. Roux, N. Gaudillière, J. Dirrenberger, and P. Morel, "Large-scale 3d printing of ultra-high performance concrete – a new processing route for architects and builders", *Materials & Design*, vol. 100, pp. 102–109, 2016. DOI: 10.1016/j.matdes.2016.03.097.

[255] A. Anton, A. Yoo, P. Bedarf, L. Reiter, T. Wangler, and B. Dillenburger, "Vertical modulations: Computational design for concrete 3d printed columns", Oct. 2019. DOI: 10.52842/conf.acadia.2019.596.

[256] L. Reiter, T. Wangler, A. Anton, and R. J. Flatt, "Setting on demand for digital concrete – principles, measurements, chemistry, validation", *Cement and Concrete Research*, vol. 132, p. 106 047, 2020. DOI: 10.1016/j.cemconres.2020.106047.

[257] V. Esnault, A. Labyad, M. Chantin, and F. Toussaint, "Experience in online modification of rheology and strength acquisition of 3d printable mortars", in *First RILEM International Conference on Concrete and Digital Fabrication – Digital Concrete 2018*, T. Wangler and R. J. Flatt, Eds., Springer International Publishing, 2019, pp. 24–38. DOI: 10.1007/978-3-319-99519-9_3.

[258] T. Wangler, R. Pileggi, S. Gürel, and R. J. Flatt, "A chemical process engineering look at digital concrete processes: Critical step design, inline mixing, and scaleup", *Cement and Concrete Research*, vol. 155, p. 106 782, 2022. DOI: 10.1016/j.cemconres.2022.106782.

[259] D. S. Kurup, M. K. Mohan, K. Van Tittelboom, G. De Schutter, M. Santhanam, and A. Rahul, "Early-age shrinkage assessment of cementitious materials: A critical review", *Cement and Concrete Composites*, vol. 145, p. 105 343, 2024. DOI: 10.1016/j.cemconcomp.2023.105343.

[260] F. Wittmann and G. V. Zijl, *Durability of Strain-Hardening Fibre-Reinforced Cement-Based Composites (SHCC)*. Springer, 2011.

[261] *EN 14651:2005+A1:2007(E) Test method for metallic fibre concrete – measuring the flexural tensile strength (limit of proportionality (LOP), residual)*, European Comitee for Standatization, CEN.

[262] F. P. Bos, E. Bosco, and T. A. M. Salet, "Ductility of 3d printed concrete reinforced with short straight steel fibers", *Virtual and Physical Prototyping*, vol. 14, no. 2, pp. 160–174, 2019. DOI: 10.1080/17452759.2018.1548069.

[263] *fib Model Code for Concrete Structures 2010*, ISBN: 978-3-433-03061-5, International Federation for Structural Concrete, Ernst & Sohn GmbH & Co. KG, 2013.

[264] S. C. Figueiredo, O. Çopuroğlu, and E. Schlangen, "Effect of viscosity modifier admixture on portland cement paste hydration and microstructure", *Construction and Building Materials*, vol. 212, pp. 818–840, 2019. DOI: 10.1016/j.conbuildmat.2019.04.020.

"Love travels on smiles"

ACKNOWLEDGEMENTS

I would like to express my gratitude to everyone who has contributed to my PhD journey over the past years, in any way, shape, or form. Pursuing a PhD is a team effort, and the work I have done and the joy I have experienced, would not have been possible without a wonderful group of inspiring, loving, and motivating individuals.

First and foremost, I extend my sincere appreciation to my supervisors, whose guidance has been crucial in the successful completion of this thesis.
To my promoter, Erik Schlangen, I am deeply grateful for the opportunity to pursue a PhD in your research group. Your constructive guidance, unwavering support, and genuine kindness have been invaluable, making this journey immensely rewarding.
Branko Savija, my daily supervisor and co-promoter, your addition to my committee was a stroke of good fortune. Your relaxed demeanor, combined with strong analytical skills, critical thinking, and delightful sense of humor, has made this time truly a blessing. I sincerely hope our paths will cross again in the future.
To my "co-promotor", Freek Bos, your dedication to and interest in the project made the collaboration with the Technical University of Eindhoven very smooth, and fruitful. Your guidance in project design and writing has been essential, keeping our endeavors focused and productive. I'm especially thankful for the inspiration you provide beyond the professional realm; the way you strive to integrate all your passions in life is truly inspiring.

My gratitude goes out to the independent committee members who meticulously reviewed my PhD thesis. Thank you, Gideon van Zijl, Max Hendriks, Jolien Van Der Putten, and Vera Popovich, for the time and effort you invested in reading my work and providing valuable feedback. I also extend my thanks to the NWO User Committee members for their support of the broader NWO project and, in particular, for their guidance throughout my PhD project.

During my PhD, I had the pleasure of collaborating with colleagues from various universities, and therefore I want to extend my gratitude to:

The Technical University of Eindhoven and all its staff, for opening your doors to me and making me feel so welcome. Stefan Chaves, for your guidance and support in the first year, this was so valuable to me. And a special thanks to Karsten Nefs for the smooth collaboration and your strong muscles during our seemingly endless printing sessions. Most importantly for your friendship, unwavering ambition, and genuine curiosity.
Max Herschl at the Technical University of Munich (TUM), thank you for welcoming me into your lab, assisting me during testing, and providing me with solid German food.

Joshua Dijkman at the University of Wageningen (WUR), for introducing me to the field of rheology and advising me during my initial experimental trials.

My dear colleagues at the Technical University of Delft have of course been an essential contributor to my PhD journey. Thank you, Ameya Kamat, for your creativity and kindness. Most of all, your playful teasing which has helped me to embrace my architectural background and re-appreciate the education that I obtained. Room 6.26! Thank you, Minfei, Patrick, and Chen, for cre- ating the best office atmospher. I wish you all the best in your future endeavors and I look forward to our office dinner reunions. And a heartfelt thank you to all my other dear Microlab colleagues: Marija, Albina, Claudia, Yading, Ze, Luiz, Shan, Guilherme, Irving, Zhi, Mohammed, Ali, Jinbao, Bart, Jaap, Jacqueline, Maiko, Ton, Arjan, John and many more.
A special thank you to Evelien Dorresteijn. The time we spent working while giggling in the lab remains one of my fondest memories. Your energy, hard work, and friendship made this project truly joyful.
Thank you Mariska and Rein for providing me with a home away from home during my experimental trials in Munich. That my PhD research led to the strengthening of our family bonds was a very delightful benefit.
Peter Katgert and Jet Merkelijn †, without knowing it, you opened up a world for me that I never knew existed. Thank you for your unwavering support and confidence in me. To my dear family —Peter, Anke, Tamar, Martje, Mare, and co.— who don't quite un- derstand my addiction to learning, thank you for the support and for sticking with me. I promise to embrace my "normal" job now!
Ceciel, thank you for always being there, supporting me, lending an ear, and being the wonderful friend that you are. Without your friendship I would be forever lost.
And finally, Michiel, thank you for your countless read-throughs, your invaluable programming lessons and your eye for cover design. But most importantly, thank you for allowing me to retract in times of focus and for unconditionally being there in times of need. The way you have adapted and moved with me during this journey is remark- able. I am truly blessed to have you in my life and I am looking forward to the adventures that await us in the future.

List of Publications

Journal publications

3. **A.L. van Overmeir**, B. Šavija, F.P. Bos & E. Schlangen, *Effects of 3D Concrete Printing Phases on the Mechanical Performance of Printable Strain-Hardening Cementitious Composites* Buildings , **13 (10)**, 2483 (2023)

2. **A.L. van Overmeir**, B. Šavija, F.P. Bos & E. Schlangen, *3D printable strain hardening cementitious composites (3DP-SHCC), tailoring fresh and hardened state properties* Construction and Building Materials , **403**, 132924 (2023)

1. **A.L. van Overmeir**, S.C. Figueiredo, B. Šavija, F.P. Bos & E. Schlangen, *Design and analyses of printable strain hardening cementitious composites with optimized particle size distribution* Construction and Building Materials , **324**, 126411 (2022)

Conference publications

2. S. C. Figueiredo, **A.L. van Overmeir**, K. Nefs, E. Schlangen, T. A. M. Salet, B. Šavija, A.S.J. Suiker &F.P. Bos.*Quality Assessment of Printable Strain Hardening Cementitious Composites Manufactured in Two Different Printing Facilities*, RILEM Bookseries: Second RILEM International Conference on Concrete and Digital Fabrication, 824–838 (2020)

1. K. Nefs, **A.L. van Overmeir**, E. Schlangen, T. A. M. Salet, B. Šavija, A.S.J. Suiker, *Consistency of Mechanical Properties of 3D Printed Strain Hardening Cementitious Composites Within One Printing System.*, RILEM Bookseries: Third RILEM International Conference on Concrete and Digital Fabrication, 145-151 (2022)